Open Research Online

The Open University's repository of research publications
and other research outputs

Exoplanet Transit Observations with Small Aperture Ground-Based Telescopes

Thesis

How to cite:

Salisbury, Mark (2021). Exoplanet Transit Observations with Small Aperture Ground-Based Telescopes. PhD thesis The Open University.

For guidance on citations see FAQs.

© 2021 Mark Salisbury

https://creativecommons.org/licenses/by-nc-nd/4.0/

Version: Version of Record

Link(s) to article on publisher's website:
http://dx.doi.org/doi:10.21954/ou.ro.00013d4d

Copyright and Moral Rights for the articles on this site are retained by the individual authors and/or other copyright owners. For more information on Open Research Online's data policy on reuse of materials please consult the policies page.

oro.open.ac.uk

Exoplanet Transit Observations with Small Aperture Ground-Based Telescopes

Mark A Salisbury BSc (Open)

A thesis presented for the Degree of

Doctor of Philosophy

School of Physical Sciences

The Open University

Supervisors: Dr U. Kolb,

Prof A. Norton, Prof C. Haswell

June 2021

Abstract

In this thesis I investigate using small aperture ground-based telescopes to contribute to transiting exoplanet science. 95 transits were obtained of three case study systems, HAT-P-23b, WASP-12b and WASP-52b over multiple seasons, using three (~ 0.4m) telescopes. Observations were made either side of GPS timing control installation at the OU Open-Science Observatories and its impact quantified. The transit lightcurves were analysed using open-source applications combined with published data providing precise timing and system parameters. HAT-P-23 and WASP-12 were monitored separately outside of transits.

Transit timing analysis confirms and refines the linear ephemeris for HAT-P-23b and quadratic ephemeris for WASP-12b. Transit timing of WASP-52b indicates preference for a previously unreported non-linear ephemeris.

HAT-P-23 monitoring revealed variability with a period of 7.015d, interpreted as stellar rotation due to surface spots. No variability was unambiguously detected for WASP-12 over 4 seasons. J0630+2942, located $2'$ from WASP-12 and commonly used as a comparison star for observations of WASP-12b was discovered to be variable with an amplitude that declined over four seasons. The results show OSO PIRATE telescope can achieve a monitoring precision better than 0.01Magnitude over multiple seasons.

I confirm the disputed eccentricity for HAT-P-23b is consistent with zero and determine a planetary radius and mass of $1.157^{+0.023}_{-0.022}\mathrm{R}_{\odot}$ and $1.063^{+0.063}_{-0.060}\mathrm{M}_{\odot}$, 3.8% and 5.9% smaller respectively than reported at discovery. WASP-52b lightcurves exhibit no detectable spot crossings as seen in previous seasons while the star remains variable, indicating the spot latitude has likely migrated from the transit chord.

The effects of different observing modes are quantified and general best practice identified for photometry of transiting exoplanets with small aperture ground-based telescopes. This includes observing transits using the CCD in 1×1 binning mode and an ideal minimum Transit SNR (TSNR) of 10-12. GPS implementation at the OSO halved the transit timing measurement scatter. The results demonstrate the capability and efficiency of small aperture ground-based telescopes to contribute to our understanding of transiting hot Jupiter systems.

Acknowledgements

Firstly I would like to thank my supervisors, Dr Ulrich Kolb, Prof Andrew Norton and Prof Carole Haswell for their tireless support, encouragement and guidance while working on my PHD and during my years of part time undergraduate study with the Open University.

I thank my wife, Diane, for your boundless love, support and understanding, providing me the space and encouragement to follow my dream. To my boys Daniel and Thomas, even though you never understood my endless fascination with "*squiggly lines on a computer screen*", I hope you have the same opportunities to follow your dreams in life.

Finally, to my parents for always believing in me.

I wish to acknowledge the following resources which I have made regular use of during my research.

- The NASA Exoplanet Archive, which is operated by the California Institute of Technology, under contract with the National Aeronautics and Space Administration under the Exoplanet Exploration Program.
- The Exoplanet Transit Database, provided and supported by the Variable Star and Exoplanet section of the Czech Astronomical Society (Poddaný et al., 2010).
- Astropy (`http://www.astropy.org`) a community-developed core Python package for Astronomy (Robitaille et al., 2013; Price-Whelan et al., 2018).
- The AAVSO Photometric All-Sky Survey. APASS is a public service to the astronomical community, and was funded through generous contributions from the Robert Martin Ayers Sciences Fund, the National Science Foundation (NSF AST 1412587) and the AAVSO endowment.

This thesis is entirely my own work. Chapter 3 is based on work previously published in collaboration with my thesis supervisors, U. Kolb, A. Norton and C. Haswell as Salisbury et al. (2021).

Foreword

It has long been a source of fascination for me that, armed with a just modest aperture commercial telescope, it is possible to observe the signature of planets around other stars across the galaxy from my back garden in a small Kent village. These planets are often very different to anything we have in our solar system or that we could even have imagined prior the first discovery by the Nobel prize winning Michael Mayor and Didier Queloz in 1995 (Mayor and Queloz, 1995). Since then we have discovered over 4000 planets around other stars, many hundreds of which are so called hot Jupiters, planets the size of Jupiter but so close to the parent stars they orbit in a matter of days rather then the leisurely 12 years Jupiter takes to orbit the Sun. As is often the way, it is these unexpected discoveries that drive huge leaps in our understanding and the field of exoplanet research has grown into a dynamic and diverse community over the last 26 years. Planets are a familiar topic that the general public, young students and amateur astronomers can grasp and thus they provide a unique opportunity for public engagement and inspiring the next generation of scientists.

In making the observations used in this thesis I have been fortunate to have the opportunity to make extensive use of the Open Universities telescope facilities. When I started my PHD journey the OU Physics Innovations Robotic Telescope Explorer (PIRATE) telescope was also on a journey, first from it's home on the island of Mallorca to a temporary base in Mammendorf, Germany and then on to the superb Observatorios de Canarias on the island of Tenerife where it was joined by a second telescope, the COmpletely Autonomous Service Telescope (COAST). It was fascinating to be involved in the testing and commissioning of this fantastic facility for teaching and research in astronomy and on several occasions to to be able to support students using the observatory on their own journey's of discovery.

The future of Exoplanet science is bright with dedicated missions TESS[1] and CHEOPS[2] currently in orbit and PLATO[3] and Ariel[4] scheduled for launch in the coming decade the field is transitioning from discovery to characterisation and understanding. These dedicated

[1] https://tess.mit.edu/

[2] https://www.esa.int/Science_Exploration/Space_Science/Cheops

[3] https://sci.esa.int/web/plato

[4] https://arielmission.space/

missions will be supported by the next generation of observatories including Webb space telescope[5] and ground based extremely large telescopes currently under construction[6], all of which will be focusing a significant proportion of their available time on Exoplanet research. These grand projects will undoubtedly provide giant steps forward in our understanding of exoplanetary systems but to do so they require support to both plan and help place the detailed observations they make in context. An excellent example of this is the Exoclock project[7] bringing together amateur and student observers to refine the ephemerides of Ariel's target star list and monitor for host star activity, both important for efficient scheduling of valuable space telescope time.

[5] https://www.nasa.gov/mission_pages/webb/main/index.html

[6] E.g. https://elt.eso.org/telescope/

[7] https://www.exoclock.space/

Contents

Introduction

In this era of having a large and rapidly growing catalogue of planetary systems but limited resources available to make all the observations astronomers desire, I demonstrate the science value that observations made using small aperture telescopes can bring to the field of exoplanet science. Transit photometry of selected hot Jupiters was undertaken with the aim of measuring transiting timing variations, refining orbital ephemerides and providing high precision system parameters. To place these observations in context I also undertake long term monitoring of the host stars to search for variability and better understand these host stars, a critical step in better understanding the planets that orbit them. This type of monitoring is often overlooked in published studies of transiting exoplanet systems as it is telescope time intensive and is therefore well suited to small aperture robotic observatories.

In the Summer of 2018 a series of upgrades were made to the OpenScience Observatories, including the installation of GPS time controllers. I undertook observations of two selected transiting exoplanets both before and after these changes, the results of which form the first research chapter in this thesis (Chapter 3). This was also the subject of a paper published in New Astronomy (Salisbury et al., 2021) and a poster presentation at the Ariel community conference in January 2020.

Studying transiting exoplanets over extend time periods provides the opportunity to detect long term changes occurring such as orbital decay or apsidal precession. This is the subject of the second research chapter (Chapter 4) where transit and host star monitoring observations of the WASP-12 system were undertaken over four observing seasons between 2016 and 2020.

In the final chapter I look at the performance and capabilities of the small aperture telescopes used in this study before finishing by summarising my key findings, developing best practice guidance and looking forward to some of the exciting future opportunities for observing transiting exoplanets with small aperture telescopes.

Chapter 1

Exoplanet Transit Timing

1.1 Introduction

In the absence of any perturbing force a planet orbiting its host star will do so following the laws of Keplerian motion. For a transiting exoplanet following a strictly Keplerian orbit the transits should occur exactly periodically, any deviation from this strictly periodic orbital motion will manifest as variations in the measured transit timing. There are a number of external forces that can act on the star-planet system to drive deviations from the expected periodic orbit, including;

- Another body in the system interacting gravitationally with the planet, the star or both.
- Gravitational tides raised on the planet, star or both as a result of their small orbital separation.
- Precession of the line of apsides in systems where the planetary orbit is not circular.
- Changes in the magnetic moment of the host star, the Applegate effect (Applegate, 1992).

There are also astrophysical effects that can degrade our ability to accurately measure transit times and in some cases mimic changes in transit timing such as stellar surface activity (star spots). Measuring and understanding these transit timing variations can inform us about the planetary system, E.g. if there are additional planets or moons present and can provide information to inform theories on the formation and dynamical history of the planetary system. Variations in transit mid-times arising from any of the effects above can be seen when the observed transit time is plotted against the calculated time of transit in an observed minus calculated (O-C) diagram. An O-C diagram provides a plot of the residuals

of the timing data arising from fitting the data with a calculated ephemeris and serves to highlight deviations from the expected behaviour (Steffen et al., 2007; Southworth, 2014).

In this section I look first at the periodic transit timing variations (TTVs) that can arise from the presence of another planetary body in the system followed by how other processes can lead to periodic TTVs. I then look at how other processes can lead to non-periodic changes such as tidal interactions finishing with a look at how the presence (or otherwise) of these timing variations can inform us about the planetary system.

1.2 Transit Timing Variations

In this section I look at the mathematical descriptions and physical principles underlying the causes of transit timing variations (TTVs) resulting from interaction with companion planets. I focus on three main scenarios. The first is where the perturbing planet on an orbit interior to the transiting planet. Secondly the scenario where the perturbing planet on an eccentric orbit exterior to the transiting planet and finally the case of an exterior perturbing planet in or close to mean motion resonance. The discussion of these scenarios relies heavily on the seminal work by Agol et al. (2005) and its subsequent description in "Transiting Exoplanets", Haswell (2010). I then look at the related transit duration variations and the methods for inverting TTV measurements to physical parameters along with possible sources of bias in these measurements. Finally, I consider all these points in the context of this project to measure TTVs of hot Jupiter systems with multiple small aperture ground-based telescopes.

1.2.1 Inner perturbers

In this case the host star of a transiting planet is also orbited by a planet on an interior orbit to that of the transiting planet. The star and planets all orbit the system barycentre. It is assumed that both planets are in coplanar circular orbits and thus any timing variations are due to the reflex motion of the host star around the system barycentre. The assumption of circular orbits is reasonable for hot Jupiter systems where the inner planet would have a very small semi-major axis and is therefore highly likely to have had its orbit tidally circularised (Howard 2013). This is confirmed from the orbital eccentricity of 241 known transiting hot Jupiters with masses between 0.5-15 Jupiter masses (M_J) and period (P) < 10 days where 197 (81.7%) have an orbital eccentricity less than 0.1 and 219 (90.9%) have an orbital eccentricity below 0.2[1]. The inner planet displaces the host star as they orbit their barycentre thus the line of sight from the observer to star when the outer planet is in transit will be seen to move, changing the time of the mid transit. The displacement x of the host star as a function of

[1]NASA Exoplanet Archive, December 2019.

time is given by Equation 8 from Agol et al. (2005);

$$x_t = -a\mu_1 \sin\left[\frac{2\pi(t-t_0)}{P_1}\right] \tag{1.1}$$

where a_1 and P_1 are the semi major axis and period of the inner planet and μ_1 is the reduced mass of the inner planet-star system;

$$\mu_1 = \frac{M_1}{M_\star + M_1} \approx \frac{M_1}{M_\star} \tag{1.2}$$

where $M_\star$ and M_1 are the stellar and planetary mass respectively. As the semi major axis of a planet interior to a hot Jupiter will be small, significant perturbations would only be expected for high mass inner planets orbiting low mass stars. This is shown schematically in Figure 1, also adapted from Agol et al. (2005).

Equation 9 from Agol et al. (2005) provides the expected amplitude of the timing variation for the n^{th} transit of the outer planet;

$$\delta t_2 = -\frac{P_2 a_1 \mu_1 \sin\left[2\pi(nP_2 - t_0)/P_1\right]}{2\pi a_2} \tag{1.3}$$

The maximum amplitude in the variation will occur when the value of the sine function is at its greatest or smallest (± 1) which allows us to calculate the maximum expected TTV amplitude for a given scenario. HAT-P-44b has an orbital period of 4.3 days. Using Equation 1.3 to calculate the TTV generated by an interior $0.5M_J$ planet on a 1.3d orbit shows the maximum TTV to be a little over 13 seconds. For an Earth mass inner planet on the same orbit the maximum variation amplitude is just a few hundredths of a second. This maximum variation amplitude is significantly below the typical ± 50 seconds timing precision possible with small aperture telescopes from the ground, Salisbury (2015), see also Tables 3.3 and 3.5. Unseen inner perturbing planets would be expected to be uncommon as, following the assumption of circular co-planar orbits, the inner planet would be expected to create a detectable transit signature. Multi-planet systems containing hot Jupiters are known to be rare, of the 241 systems in the NASA Exoplanet database only 7 are known to be members of multi-planet systems. Of these seven, three have inner orbiting planets also known through their own transits. It can be seen from Equation 1.3 that for a given system only the sine term will vary from one orbit to the next. If the two planets are in a resonant orbital configuration such that $P_2 = jP_1$ and j is an integer, then the value of the sine function will be the same for each orbit and no variation in the timing of transits for the outer planet would occur.

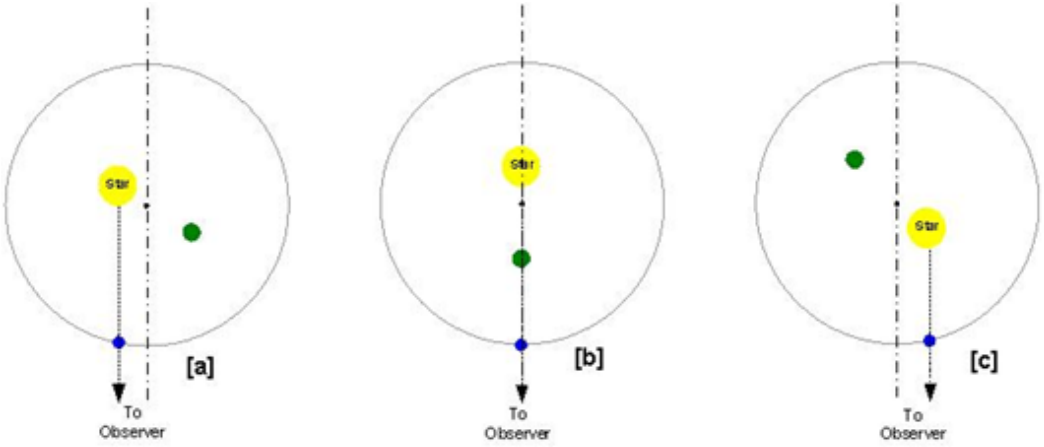

Figure 1.1: A simple sketch (not to scale) of TTV geometry for an inner perturber shown in plan view, adapted from (Agol et al., 2005). All the bodies in the system orbit the common barycentre. In [a] the presence of the inner planet has caused the transit of the outer planet to occur early. In [b] the system is aligned to the observer and the transit is on time. In [c] the transit occurs later.

1.2.2 Outer perturbers on eccentric orbits

An outer companion to a hot Jupiter could cause a measurable TTV if it is in a non-circular orbit. This is a planet-planet interaction whereas the previous case was a planet-star interaction. As the outer planets' orbit is eccentric the distance between the two planets varies with time causing a varying acceleration of the inner planet on the timescale of the outer planet's orbit. The amount of acceleration at a given time depends on the location of the outer planet in its orbit, the true anomaly, which would generally not be known. Following (Haswell, 2010, Eq. 7.29) it is possible to calculate an approximate maximum TTV of an inner transiting planet for a given system.

$$\delta t_1 \approx \mu_2 e_2 \left(\frac{a_1}{a_2}\right)^3 P_2 \tag{1.4}$$

Again using the example of the HAT-P-44b system but this time with an exterior Jupiter mass planet in a 100 day orbit and an eccentricity of 0.6 we can calculate that the maximum transit timing variation will be just 5.1 seconds. As with the previous example this is also well below the detection threshold for ground-based timing with small telescopes. Despite these very small potential TTVs a growing number of hot Jupiter systems have been found through trends in their RV residuals to harbour massive planets in long period orbits around transiting systems (Knutson et al., 2014).

1.2.3 MMR or close to MMR systems

So far the chances of detecting TTVs seem poor however a much more interesting opportunity for TTV detection arises if two planets in a system are in a mean motion resonance (MMR). For a first order MMR with j+1:j the two planets will undergo a conjunction at the same longitude for each j^{th} orbit of the outer planet. This repeated alignment cumulatively tugs on the orbit of the inner planet creating an eccentricity which adds coherently over subsequent orbits. As the conjunction precesses over time the longitude of the conjunction and thus the semi major axis of the inner planet shifts through 360°known as a libration cycle. It is this libration that leads to a change in the transit timing over time, betraying the presence of the MMR companion. Agol et al. (2005) calculated an approximate analytical expression for the amplitude of the timing variation as (their equation 33)

$$\delta t_2 \approx \frac{P_2}{4.5j} \frac{M_1}{M_1 + M_2} \tag{1.5}$$

where δt_2, P_2 and M_2 are the timing variation, period and mass of the inner transiting planet and M_1 is the mass of the outer perturbing planet. Unlike Equations 1.3 and 1.4, the timing variation does not depend on the mass of the star, only on the masses of the planets. As the stellar mass is often of the order of a thousand times that of the planet we should expect a much larger maximum amplitude for the timing variation. The downside is that the variation occurs over the libration cycle period not the orbital period of the perturbing planet which is approximately given by Agol et al. (2005), Eq 34.

$$P_{Lib} \approx 0.5 j^{-4/3} \mu_2^{-2/3} P_2 \tag{1.6}$$

To consider an example again based on the HAT-P-44b system but this time with a terrestrial mass companion planet in an outer 3:2 MMR orbit where j=2 the δt_{max} would be 5.9 minutes. The libration period over which this variation would occur would be approximately 165 days, over 25 times the outer planet's orbital period. As j increases δt_{max} and the libration period decrease. Agol et al. (2005) compared the results of these analytical expressions to numerical modelling and found them to be accurate to within 10% for j≥2 but only to about 40% for j=1.

1.2.4 Near Resonant Systems

The above discussion considers systems in exact MMR configurations expected to be stable for significant periods of time. Analysis of TTVs from Kepler data has showed a large fraction of systems exhibiting TTVs are in a near MMR configuration (Lithwick et al., 2012; Steffen et al., 2013). These systems will be stable over long periods but may be far enough

from resonance that the libration period is significantly shortened, increasing the chances of monitoring full or multiple cycles (Jontof-Hutter et al., 2016). The duration of the "super period" (P_j) in a near resonance system was shown by Lithwick et al. (2012) to be;

$$P_j = \frac{P_{\text{Outer}}}{j+1 \times \Delta j} \tag{1.7}$$

Where Δj is given by Lithwick et al. (2012) Eq. 6, and is equal to half the ratio difference from MMR where the near resonance is given by $(j+1) : j$. Thus for a system with a period ratio of 2.02:1, $\Delta j = 0.01$. Taking the example again of HAT-P-44b but this time assuming the outer planet is in a 3.04:2 near resonance then the super period would be approximately 17 times the outer planet's orbital period (rather than 25 times for the MMR libration period).

Also in their 2012 paper Lithwick et al. (2012) separate the eccentricity of the perturbing planet into a free component unrelated to the resonance and a component forced by the closeness to resonance. They discuss how both components of eccentricity can be damped away but how the forced component is replenished by the planet-planet interaction reducing orbital energy and helping explain the increase in the number of planets found in orbits just wide of resonance.

The free component of the eccentricity can be determined from the phase of the two sets of TTVs in a dual planet system where both planets transits can be measured. If they are in phase (i.e. crossing zero at the same time) then free eccentricity is zero and mass can be uniquely determined. The amount of free eccentricity can also be informative for formation and dynamical history theories.

1.2.5 Transit Duration Variations

Another potentially measurable variation is the duration of the transit. TDV's that are in or close to phase with the timing variations can be caused by interactions between companion planets on or close to MMR. The effect of an outer perturbing planet is to alter the orbital velocity of the inner transiting planet leading to duration variations E.g. (Nesvorny et al., 2013). For a planet in a non-circular orbit, variations in the transit duration could be caused by apsidal precession where the ellipse of the orbit rotates in its own plane thus varying the orbital speed of the planet across the face of the star from the observers view point. Nodal variations lead to changes in the orbital plane varying the impact parameter and thus the transit duration and would be detectable for planets in circular orbits. Nodal variation would be expected to be most profound for planets in grazing transits where changes to the orbital plane could even move a planet out of transit. Additional possible causes or TDV's include exomoons orbiting a planet. An exomoon could be the cause of both transit time

and duration variations which would be $\pi/2$ out of phase with one another which is a unique identifier for the presence of an Exomoon Kipping (2011).

1.2.6 Solving the Inverse problem

As can be seen from the calculations in previous sections even very small terrestrial mass planets difficult to detect by RV or transit methods can cause significant TTVs in resonant or near resonance systems. The conversion of a measured TTV amplitude and period to parameters for the perturbing planet is not straight forward due to a number of parameter degeneracies principally between mass, eccentricity and longitudes of pericentre of the perturbing planet and is known as the inverse problem. On the assumption that the perturbing planet does not itself transit or is not detectable in transit the parameters we would hope to determine are the planet's mass, period (semi-major axis) and eccentricity. In order for these to be uniquely determined we require to also find the orbital phase (true anomaly), longitude of pericentre and apsidal precession so a total of 6 free parameters just for the perturbing planet (more if the perturbing planet is not co-planar). The same parameters also need to be defined for the transiting planet leading to 12 free parameters and only 2-3 are constrained by observations. Numerical n-body calculations are very computationally intensive but provide the most accurate method to recover the desired parameters. Codes such as TTVFast (Deck et al., 2014), TTVFaster (Agol and Deck, 2016) and TRADES (Borsato et al., 2014) have been developed to invert TTV data to planet parameters, for example in the discovery of the only hot Jupiter system (WASP-47) with known short period companions (Becker et al., 2015). Analytical methods have been developed to approximate the perturbing planet parameters using simplifying assumptions such as circular and co-planer orbits (Nesvorný and Morbidelli, 2008). These methods enable us to understand the underlying physical processes and can be used to refine priors before n-body calculations e.g.(Hadden and Lithwick, 2016). These analytical methods have been extended to cover the first and second order close to resonance eccentric type systems that are prevalent in the Kepler data set (Lithwick et al., 2012; Agol and Deck, 2016; Deck and Agol, 2016).

1.2.7 Bias in TTV measurements

When considering any aspect of astronomical data analysis it is vital that sources of potential bias are fully explored, of which there are many for transit variations. The first and most obvious bias is that variations can only be determined for transiting planets. This has become less of an issue as the number of transiting planets has increased significantly beyond that detected via other methods, due largely to the Kepler satellite observatory, allowing statistically significant samples to be tested to high precision Mazeh et al. (2013). A drawback

of many of the Kepler targets is that they are too faint for radial velocity follow up and so rely on the TTV measurements for mass determination. An interesting aspect of bias caused by TTVs was highlighted by García-Melendo et al. (2011) who discuss how systems with TTVs could be missed by planet search algorithms altogether. They highlight three possible scenarios where the period variations due to TTVs could lead to transits being missed, thus explaining the lack of hot Jupiter systems with significant TTVs. Firstly the transits folded over the wrong period can be individually smeared into the background noise resulting in non-detection in the first place. Secondly the transit is detected but with the wrong Period (P) or epoch (T_0) leading to non-detection in follow up observations, and lastly the transit shape can be deformed leading to rejection as a blended or binary star source.

1.2.8 Exomoons

Moons orbiting transiting exoplanets are another potential source of TTVs and TDV's (Kipping, 2013). The reflex motion of a planet orbiting the planet-moon barycentre will change the timing from successive orbits which would be detectable as periodic TTVs. Additionally the duration of the planetary transit can be varied by this orbital motion around the barycentre. Following equations 3.1 and 3.2 in Kipping (2013) it is straightforward to calculate the TTV and TDV effects of an exomoon for circular co-planar orbits. These calculations show that for an Earth mass exomoon orbiting WASP-48b at the same distance as Io orbits Jupiter the maximum timing variation amplitude would be ~ 48 seconds whist the effect on the transit duration would be only 3.6 seconds. A Europa mass exomoon orbiting WASP-48b at Europa's distance from Jupiter the TTV amplitude would be just 0.6 seconds and the TDV 0.02 seconds.

A TTV amplitude of 48 seconds is in principle within the detection range of small aperture ground-based telescopes and the existence of exomoons would need to be considered for any suspected TTV. The phase of TDV's with the TTVs would be $\pi/2$ which would enable confirmation or rejection of an exomoon hypothesis but TDV detection is extremely difficult and well beyond that achievable with small aperture telescopes from the ground.

The difficulty of detecting exomoons is highlighted by the recent case of Kepler-1625b-i, the first credible (but still not confirmed) detection of of a Neptune radius moon orbiting a Jupiter radius planet (Teachey and Kipping, 2018). Three Kepler observations of Kepler 1625b show $\simeq 25$ minute TTVs and HST observations of a fourth transit show a decrease in the out of transit flux at the location expected from the TTV phase. Together the evidence of the first Exomoon detection is compelling however the authors caution that the quality of the detection is highly dependent on the HST lightcurve detrending methodology applied and the Neptuanian size and inclined orbit around the host planet require explanation. With an

orbital period of ~ 287 days, further follow up observations are complicated by the difficulty of forward predicting the moons location from the TTV phase.

1.3 Orbital decay

A possible cause of departure from strictly Keplerian orbit is orbital decay where a planet orbit is spiralling in towards its host star. This change in orbital radius would manifest as a continuous reduction in the orbital period resulting in a quadratic departure from the expected linear ephemeris, Equation 1.8 (Maciejewski et al., 2016);

$$\mathrm{T_C(E)} = \mathrm{t_0} + \mathrm{PE} + 0.5\frac{\delta \mathrm{P}}{\delta \mathrm{E}}\mathrm{E}^2 \tag{1.8}$$

where $\mathrm{T_C(E)}$ is the calculated transit mid-time, t_0 is the reference epoch, P is the period and E is the number of periods since the reference epoch. This is the same as a linear ephemeris, the quadratic component $0.5\frac{\delta P}{\delta E}E^2$ accounts for the change in period with each epoch (assuming a constant period change). From measurements of the period derivative it is simple to calculate the period change per day and thus the cumulative annual change;

$$\frac{\delta P}{\delta t} = \frac{1}{P}\frac{\delta P}{\delta E} \tag{1.9}$$

This quadratic ephemeris is discernible from other causes of transit time variations due to the unique non-periodic shape of the fit to the measured transit times in an O-C diagram. Another test for the presence of orbital decay is occulation timing which should be correlated with the transit timing. As the baseline of observations of hot Jupiters over many epochs has grown it has become possible to test for orbital decay in the systems where this could be expected.

In systems where the orbital period is shorter than the stellar rotation period the most commonly proposed mechanism driving orbital decay is dissipation due to dynamical tides raised within the host star. This leads to the raising of a tidal bulge on the stellar surface (much like the Moon does for the Earth) but as the orbital angular velocity is greater than the stellar rotational velocity this tidal bulge lags behind the orbit of the planet and exerts a tidal torque on the planet. Angular momentum is transferred from the planets orbit to the stellar rotation resulting in an increased rotational velocity for the star and a reduction in the orbital period, which we see as orbital decay and potentially increased stellar activity (Poppenhaeger, 2016).

In this model, the rate of period decay is dependant on the stellar tidal dissipation rate, often expressed as the dimensionless reduced tidal quality factor, Q'_*. With the simplifying assumptions that the planetary orbit is circular, the stellar rotation angular velocity $\ll$ the

orbital angular velocity and that we can neglect tidal dissipation in the planet, the rate of decay is given by (Patra et al., 2020);

$$\frac{\delta \mathrm{P}}{\delta \mathrm{t}} = -\frac{27\pi}{2Q'_*}\frac{M_\mathrm{P}}{M_*}\left(\frac{R_*}{a}\right)^5 \tag{1.10}$$

where $Q'_* = {}^{1.5Q_*}/_{\kappa_{*,2}}$, with Q_* being the stellar tidal quality factor and $\kappa_{*,2}$ is the Love number, a measure of the central condensation of the star (Patra et al., 2020). Orbital decay has only been detected or is suspected in a very small number of hot Jupiter exoplanet systems (see Section 1.3.1) limiting our ability to identify the full range of Q'_* values we should expect for these systems so alternative approaches have been sought to bound the expected values of Q'_* for exoplanet host stars. Penev et al. (2016) used the tidal spin up of two hot Jupiter host stars to infer Q'_* in the range $10^{6.4-7.4}$ which was extended to 188 host stars where the range of Q'_* was found to increase from 10^5 to 10^7 as the tidal forcing frequency increased (Penev et al., 2018). Hamer and Schlaufman (2019) used Gaia DR2 results to show hot Jupiter hosts have a lower galactic velocity dispersion than field stars of similar population without a known hot Jupiter. As galactic velocity dispersion is correlated with age they conclude that the known hot Jupiters systems are young and that this is best explained by engulfment while the host stars are on the main sequence, in turn requiring Q'_* to be $\lesssim 10^7$.

The stability, or otherwise, of planetary systems to tidal decay has been considered by Levrard et al. (2009) who find that for a system in which angular momentum is conserved but energy is dissipated there are two possible end states defined by the ratio between the systems total angular momentum (L_tot) and a critical angular momentum value (L_c). L_c depends on the masses and polar moments of inertia of the planet and star (their Eq.1). Where $L_\mathrm{tot} < L_c$, i.e. where the total angular momentum is less than the critical value, the system is unstable to tidal decay regardless of the model for the tidal dissipation. Alternatively where $L_\mathrm{tot} > L_c$ there are two possible equilibrium states, the further distance which is greater than the orbital distance for $L_\mathrm{tot} = L_c$ is stable. The other where the orbital distance is less than the equilibrium orbital distance for $L_\mathrm{tot} = L_c$ is unstable. Of the 26 transiting systems known at the time of of the study by Levrard et al. (2009), only one, HAT-P-2b, has $L_\mathrm{tot} > L_c$ and thus the remaining systems will be expected to undergo orbital decay towards their host stars. HAT-P-2b on the other-hand has an orbital distance slightly greater than the equilibrium orbital distance for $L_\mathrm{tot} = L_c$ and will decay asymptotically towards the equilibrium orbital distance.

1.3.1 Period Decay in the Literature

As the baseline of timing observations for many exoplanet systems approaches decade long durations we can now start to search for orbital period decay. With their close proximity and

high orbital angular velocity the ultra short period hot Jupiters with periods $\lesssim$ a few days should provide the best candidates to test for this effect.

WASP-43b is a 1.81M_J ultra short period hot Jupiter on a 0.81 day orbit around a low ($0.58M_\odot$) star. Using Spitzer observations of secondary eclipses combined with primary transits taken from the Exoplanet Planet Transit Database (ETD), a database of mainly amateur observations made with small aperture telescopes, Blecic et al. (2014) tentatively reported an orbital decay rate -0.095 ± 0.036 syr^{-1}. This was later revised down by a factor of 3 (Jiang et al., 2016) and subsequently called into question altogether following further refinements of the ephemeris (Hoyer et al., 2016). With an orbital period of 0.79 days, WASP-19b is a another ultra short period Jupiter mass ($M_P = 1.11M_J$) planet orbiting a solar type ($M_* = 0.9M_\odot$) star predicted to show a period shift of at least 34 seconds after 10 years for tidal quality factors $10^6 - 10^8$ (Valsecchi and Rasio, 2014). Analysis of 60 transit times by Espinoza et al. (2019) suggested detection of a high significance approximately -40 second timing change between 2014 and 2017. Petrucci et al. (2020) undertook a homogeneous reanalysis of 74 transit data sets and find that a linear ephemeris is the best fit to the data with an upper limit to any period change $\dot{P} = -2.294$ ms yr^{-1}.

Kepler-1658b was the first planet discovered (KOI-4.01) by the Kepler space mission and is a massive planet orbiting a evolved sub-giant star on a longer period orbit than the examples above ($M_* = 1.45M_\odot, M_P = 5.88M_J, P = 3.85$ days). Using all 4 years data from the Kepler main mission Chontos et al. (2019) find a 3σ upper limit to an orbital decay rate of $\dot{P} = -0.42$ ms yr^{-1}, though the authors note their result is consistent with a linear ephemeris at 1σ.

The hot Jupiter WASP-4b ($M_* = 0.865M_\odot, M_P = 1.19M_J, P = 1.33$ days) was observed for 18 transits by the TESS mission which occurred 81.6 ± 11.7s earlier than predicted from the linear ephemeris (Bouma et al., 2019). The authors calculated a decay rate of $\dot{P} = -12.6 \pm 1.2$ ms yr^{-1} though were unable to conclusively distinguish between orbital decay or apsidal precession as the cause. Baluev et al. (2019) reported a homogeneous analysis of 56 published transit times and 10 new observations, excluding those from TESS, and were unable to support the period decay seen by Bouma et al. (2019). When the authors included the TESS transit times and other published transit times where the original data was not available for reanalysis the quadratic ephemeris becomes significant, though with a reduced decay rate. Southworth et al. (2019) added 22 new transit times spanning almost 3000 epochs and find a quadratic ephemeris is best fit to the data though with rate of change of $\dot{P} = -9.2 \pm 1.1$ ms yr^{-1}, 3σ lower than reported by (Bouma et al., 2019). The result implies a modified tidal quality factor (Q'_*) somewhat lower than expected from values reported in the literature, so both orbital decay and apsidal precession are consistent with the data but

each is not without its drawbacks.

Probably the most secure and best studied example of orbital period decay is that of WASP-12b, a $1.47M_{\rm J}$ planet orbiting a $1.4M_{\odot}$ star every 1.09 days (Hebb et al., 2009). WASP-12b is known to be losing mass via Roche overflow of its extended exosphere (Haswell et al., 2012; Haswell, 2018). Period change was first reported by Maciejewski et al. (2016) and subsequently extensively studied by a large number of authors (Patra et al., 2017; Maciejewski et al., 2018; Öztürk and Erdem, 2019; Baluev et al., 2019; Yee et al., 2019). Both orbital period decay and apsidal precession have been proposed as viable drivers of the period change observed. The most robust way to determine between these two hypothesis is with occlutation measurements which, in the case of apsidal precession will be $\pi/2$ out of phase with the transit times whereas for period decay the occultations and transits will be in phase. Yee et al. (2019) have reported four additional occultation measurements separated by 16 epochs obtained with the Spitzer space telescope, along with ten new ground-based transit measurements. Their analysis indicates the occulations are in phase thus preferring the orbital decay hypothesis for the measured period change of $\dot{P} = -29.9 \pm 2$ ms yr^{-1} (Yee et al., 2019). WASP-12b was observed by TESS between December 2019 and January 2020 and the results from the timing analysis of the 21 transits obtained support the orbital decay model (Turner et al., 2021).

A different approach using radial velocity measurements to detect the radial velocity of the tidally raised bulge on the surface of WASP-12 has been investigated by Maciejewski et al. (2020). The period of this RV signal would be half the orbital period and its phase is related to the planetary orbital motion such that it cam mimic non-zero orbital eccentricity with a longitude of periastron (ω) of 270°. The authors separate the orbital and tidally induced RV semi amplitudes and determine a value of 7.5 ± 1.2ms^{-1} for the latter with ω close to 270°. This is the first such detection of tidally induced RV variations which may be detectable in other systems which exhibit a non zero eccentricity with $\omega \sim 270$°such as WASP-18b (Maciejewski et al., 2020).

1.4 Apsidal and nodal precession.

Apsidal precession is the rotation of the point of periastron of an elliptical orbit around the orbital plane while nodal precession is the precession of an orbit around the rotation axis which can be different to the orbital plane. Taking a star-planet system if both bodies were completely spherical and the orbit circular there would be no precession. As the stars and planets themselves rotate they generate rotational flattening and this departure from a purely spherical state creates a gravitational quadrupole field which causes the line of apsides

to rotate (precess) around the orbit. For an exoplanet with an eccentric orbit this results in changes in the transit time over the period of the precession.

The rotation periods of hot Jupiter's would be expected to be synchronised to the orbital period, reducing the planets rotational flattening and thus the precession. However the same proximity between star and planet can lead to the raising of tidal bulges on both components. Ragozzine and Wolf (2009) showed [their equation 13] that the total precession is a linear summation of all the contributing components and that for hot Jupiters this planetary tidal bulge is the most significant contributor to apsidal precession.

$$\bar{\omega}_{\text{total}} = \bar{\omega}_{tide_P} + \bar{\omega}_{gr} + \bar{\omega}_{rot_P} + \bar{\omega}_{tide_*} + \bar{\omega}_{rot_*} + \bar{\omega}_{P2} \tag{1.11}$$

Equation 1.11 lists the contributing components in order of importance for a hot Jupiter where $\bar{\omega}_{tide_P}$ and $\bar{\omega}_{rot_P}$ are the contribution from the planets tidal and rotation bulges, $\bar{\omega}_{tide_*}$ and $\bar{\omega}_{rot_*}$ are the contribution from the stellar tidal and rotational bulges. $\bar{\omega}_{gr}$ is the component due to relativistic precession and $\bar{\omega}_{P2}$ is that due to a second planet in the system. An excellent summary of the relative contribution of these components to the apsidal precession total is given in Perryman (2014), chapter 6.4.13.

Unless the orbit of the planet around the star is eccentric then apsidal precession will not have any effect on transit timing. Ragozzine and Wolf (2009) calculated apsidal precession rates for a number of hot Jupiters known at the time and showed that for WASP-12b the precession of perastron could be as much as $19.9°\text{yr}^{-1}$, completing a full 360°rotation of the line of apsides in just over 18 years with a maximum timing variation amplitude of ~ 25 minutes over the apsidal rotation period. This is significant and well within the detection limits for small aperture, ground-based, telescopes.

Apsidal precession of an eccentric orbit would also be expected to exhibit transit duration variations and variations in the timing between primary and secondary eclipses. In the latter case the timing variation of the transits and occultations would occur $\pi/2$ degrees out of phase with each other, providing a mechanism to determine between timing changes due to apsidal precession and those due to other effects such as tidal decay.

Non detection of TTVs caused by apsidal precession also allows tight upper limits to be placed on the planet's orbital eccentricity. Measuring orbital precession is not only important to exclude from possible companion planet discovery but it also allows the planet Love number κ_2 to be determined, providing information on the central concentration of mass within the planet (Ragozzine and Wolf, 2009). This allows us a 'view' inside the planetary structure without being able to see the planet.

The departure from a pure sphere for the star and the consequent quadrupole gravitational field also means the gravitational force on the planet is not directly toward the centre of the

host star, but is offset toward the equator. If the planet is not orbiting in the rotational plane of the star it will experience a pull toward the stellar equator causing a precession of the line of nodes. As also calculated by Ragozzine and Wolf (2009) this nodal precession effect is an order of magnitude less than for apsidal precession and is not detectable even with Kepler quality photometry. We can therefore safely ignore nodal precession in timing measurements made with ground-based small telescopes.

Apsidal precession has been considered as the cause of the non linear ephemeris for WASP-12b (Maciejewski et al., 2016; Patra et al., 2017) where the observed quadratic ephemeris is simply part of a longer sinusoidal apsidal precession with a period of 14 ± 2 years (Patra et al., 2017). Subsequent observations of occultations Yee et al. (2019) indicates they occur in phase with the primary transits, ruling out apsidal precession as a cause of the observed non-linear ephemeris for WASP-12b.

1.5 Applegate effect

The Applegate effect (Applegate, 1987, 1992) was proposed to explain the changes in the observed orbital periods of binary stars that could not be attributed to mass transfer or loss. In this model, as applied to exoplanets, changes in the stellar quadrupole moment lead to changes in the oblateness of the star which in turn impacts the non-spherical component of the gravitational field experienced by the orbiting planet. The planet in turn has to react to the changing gravitational field by changing its orbital velocity and thus in order to conserve angular momentum the orbital period will change (Watson and Marsh, 2010). In this way an increase in oblateness will lead to an increased velocity and reduced orbital period while a reduction in oblateness will lead to a reduced velocity and an increased orbital period.

The mechanism proposed to drive the change in the quadrupole moment is internal angular momentum transfer from the stellar core to the envelope (and back again) driven by changes in the magnetic field of the star (Applegate, 1992). Thus the changes will occur on the quasi-periodic timescales of the stellar magnetic activity cycle and will apply for relatively low mass stars with a convective envelope capable of dynamo generation of a magnetic field. It happens that, largely through selection effects, many detected exoplanets orbit this type of star.

Theoretical Applegate effect TTV amplitudes for a number of exoplanet host stars known at the time have been calculated by Watson and Marsh (2010) for theoretical magnetic cycle periods of 11, 22 and 50 years. These show amplitudes ranging from 0.1 seconds over 11 years to more than 6 minutes over a 50-year period. The size of potential O-C variations is calculated in equation 13 of Watson and Marsh (2010) where it can be seen that the

two parameters least well constrained are the stellar rotational velocity and the luminosity (due to distance uncertainties). The rotation velocity enters the equations linearly whereas luminosity enters as the square root so the uncertainties in the rotational velocity of the star have the greatest impact. Uncertainties on luminosity are greatly reduced with the availability Gaia DR2 parallax data allowing more precise distance determination to many exoplanet host stars (Brown and Gaia Collaboration., 2016; Stassun et al., 2017; Stassun and Torres, 2018)

The timing variation caused by the Applegate effect decreases with the square root of the orbital seperation so will only be applicable to short period systems. It should therefore be easily distinguishable from TTVs caused by interior companion planets due to their much shorter periods, and from planets in or close to exterior mean motion resonance due to their larger TTV amplitudes. The Applegate effect however can occur on timescales similar to that of apsidal precession or light travel time delays (Rømer effect, section 1.6) caused by long period planetary or stellar companions. As the variations due to the Applegate effect are expected to be quasi-periodic, monitoring over extended periods would be required to determine if the variations follow a strict periodicity expected from apsidal precession or the Romer effect.

1.6 Light travel time, the Rømer effect.

Well known from the studies of close binary systems the variation in light travel time in exoplanet systems is caused by the reflex orbital motion of the star around the barycentre. The component of this acceleration along our line of sight to the host star is called the Rømer effect and it is related to the orbital period change observed by;

$$\frac{\dot{P}}{P} = \frac{\dot{\nu}_r}{c} \tag{1.12}$$

where P and $\dot{P}$ are the period and period derivative, $\dot{\nu}_r$ is the line of sign acceleration and c is the speed of light. An acceleration towards the observer will cause successive transits to appear to occur earlier than expected while an acceleration away from the observer will have the opposite effect making transit appear to occur later than expected. The sign and upper limits for $\dot{\nu}_r$ can be provided by precise radial velocity measurements allowing an easy test against any measured timing variation.

The amplitude of the timing variation caused by this effect can be calculated for companion planets (Watson and Marsh, 2010, Eq. 15));

$$\delta_{t(s)} = \frac{a}{c}\frac{M_P}{M_*} \approx \left(\frac{M_P}{M_J}\right)\left(\frac{a_P}{AU}\right) \tag{1.13}$$

where M_P and a_P are the mass and semi-major axis of the outer perturbing companion. Thus for a Jupiter mass planet in a Jupiter wide orbit of 5AU around a solar mass star, the amplitude of the timing variation due to light travel effects is 5 seconds. This variation will be strictly periodic over successive 12-year orbital periods. Large amplitude variations caused by massive companions on wide orbits can be ruled out through high precision radial velocity measurements

1.7 Exoplanet Host Star Variability

Intrinsic stellar variability can arise in many forms including periodic or quasi-periodic variations due to stellar pulsations, surface spots caused by magnetic activity tracking the stellar rotation and stochastic events such as flares. Stellar magnetic variability driven by the dynamo effect in F, G, K and M type stars is of particular interest to the study of exoplanets, especially the short period hot Jupiters. Surface spots and faculae on these stars can affect the shape of the transit lightcurve with the resulting asymmetry leading to an offset in the measured transit mid-time. This effect can result in a false transit timing variation without appropriately inflating the fitted errors, emphasising the importance of a complete understanding of exoplanet host stars when determining planetary parameters. In this section I look at how star spots occur (1.7.1), how they are used to measure stellar rotation (1.7.2) and finally how they affect exoplanet transit measurements (1.7.3).

1.7.1 Star Spots and Activity Cycles

Star spots are dark regions that rotate with the stellar surface at the latitude at which they form. They are best studied for the Sun where they can be as large as 30,000km and are often made up of groups of smaller spots. The central region of a spot, called the umbra, appears dark because of its lower effective temperature which, for the Sun, can be as low as 3900K compared to the normal photospheric temperature of around 5780K (Carroll and Ostile, 2007). This in turn leads to a flux from the umbria region that is $(5780\text{K}/3900\text{K})^4 = 4.8$ times lower than the normal photosphere flux level which makes the spot appear dark against the photosphere even though it has a high (by Earth standards) temperature, Figure 1.2.

Solar spots are well studied because the Suns proximity, it is the only star on which we can currently clearly resolve the spot regions. Spectral studies have revealed Zeeman line splitting in the dark umbria showing that they are regions of intense magnetic fields, thought to be formed when buoyant magnetic flux 'tubes' break through the photosphere surface. The intense magnetic fields in starspots can inhibit the convective flow of energy to the

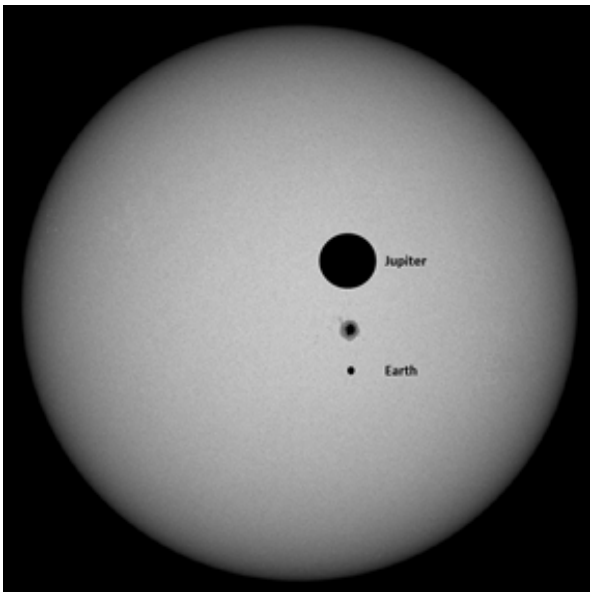

Figure 1.2: . SOHO MDI image from 21st May 2016 showing sunspot 2546 near the centre of the solar disk. Added above is Jupiter's disk to scale and below the spot is the Earths disk to scale. Solar disk image, SOHO 2016 http://sohowww.nascom.nasa.gov/sunspots/

surface leading to the lower temperatures in spots than the surrounding photosphere. This interpretation is supported by the observation that Sun spots and spot groups form in pairs that trail one another with opposite magnetic polarity. Star spots (and Sun spots) are not simple dark structures, the umbria is surrounded by the penumbria, a region of intermediate flux that shows linear structures indicative of a strong magnetic field. In contrast to the darker spots bright plages are regions of increased brightness associated with spots and spot groups on the solar photosphere and are brightest when viewed in Hα emission.

Bright faculae are another manifestation of magnetic activity in the photosphere appearing as large bright regions best observed closer to the limb. Faculae and plages are often associated with Sunspots and can remain after the spot themselves have disappeared. Faculae are best seen near the limb where we can see into the hotter side walls of the granules which can, in principle, lead to an overall brightening of the local stellar limb in contrast to the expected limb darkening (Herrero et al., 2012).

At first glance the spot activity on the Sun appears random and unordered however when looked at over long timescales it becomes obvious that the activity levels are in fact structured and even predictable. Solar spot activity waxes and wanes with an 11-year period which is half the 22-year solar magnetic cycle period. This creates maximums in spot activity every 11 years with minimums 5.5 years later. The spot coverage, or filling factor, many times greater at maximum than at minimum when the solar surface can be spot free for extended periods of time while at solar maximum spots coverage can reach as high as 0.5% of the projected solar disk Figure 1.3 (bottom).

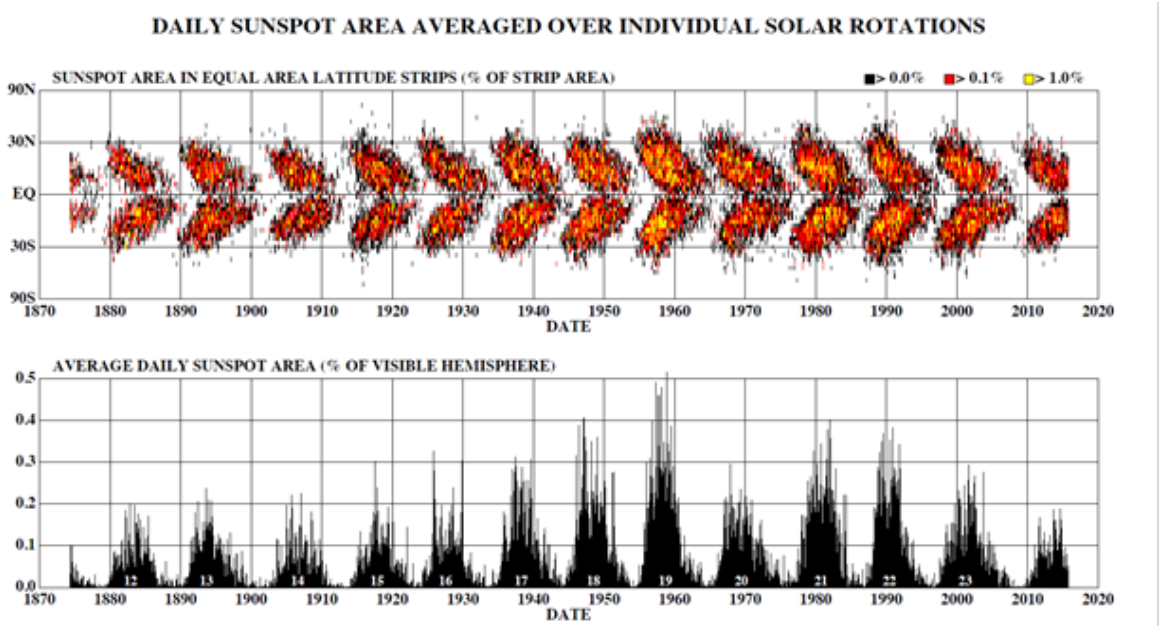

Figure 1.3: Daily sunspot coverage and latitude variation over many solar cycles clearly showing how the location (top image) and area covered (bottom image) of spots varies with the Solar magnetic cycle (Hathaway, 2015), reproduced under Creative Commons license (http://creativecommons.org/licenses/by/4.0/).

In addition to changes in the numbers and sizes of sunspots the location of the sunspots also varies with the solar magnetic cycle period. This is easily visible in the so called 'Butterfly diagram' which shows how the location and number of solar spots evolve during the solar activity cycle, Figure 1.3 (top). At the start of the cycle spots first appear at higher Northern and Southern latitudes, between 30°and 45°and over 11 years as activity levels first increase then decline they migrate towards the equator. During a solar cycle total solar irradiance can vary by as much as 0.1% above the mean at solar maximum to 0.1% below mean at solar minimum (Willson and Hudson, 1991).

Surface spots and activity cycles are not limited to the Sun, star spots are observed on many variable stars with amplitudes up to 0.5 Magnitude. RS Canum Venatiorum (RS CVn) stars exhibit a distortion wave attributed to surface spots on the synchronously rotating primary star that changes in amplitude as the number and/or size of the spots vary.

Cyclic variations in spot numbers, size and latitude means that the effect of stellar activity on exoplanet transit lightcurves varies with the multi-year stellar activity cycle.

1.7.2 Measuring Stellar Rotation

The appearance of star spots on the surface of a star will reduce the flux received which will vary as the spots rotate with the stellar surface allowing the rotation period at the latitude of the star spots to be deduced from time series photometry of the host star, for example

(Vida et al., 2013). The long term continuous monitoring of a single field by the main Kepler mission has allowed statistical comparison of rotation periods between stars hosting and those not hosting transiting planets. One of the largest studies of 12,000 F, G, K and M stars from Kepler confirmed the expected increase in rotation period from B to M spectral type (Nielsen et al., 2013). For the 795 M stars in their sample the authors found a mean rotation period of 15.4 days but with an excess of of rotation periods < 7.5 days which they attribute to the transition to a fully convective interior after spectral type M3. Alternatively the excess of fast rotators could represent a subset of host stars being spun up by closely orbiting (non transiting) exoplanets, see section 1.7.4.

A number of other rotational period studies have focused on M dwarfs which are especially suitable targets for exoplanet searches being much smaller than F, G or K dwarfs meaning transits are deeper and shorter increasing the chances of detection. Planets of a given mass planet will produce a larger Doppler shift in the spectral lines of lower mass stars and along with their more complex spectra with many sharp absorption lines makes them more suitable for radial velocity surveys. These factors, along with their lower luminosity and longer lives, increase the chances detection of low mass planets the habitable zone (HZ). However, this is complicated to some extent by the increased magnetic activity of theses stars resulting in much higher star spot activity than F, G or K dwarfs. Additionally M dwarfs are known to produce strong stellar flares which may render any planet orbiting in the HZ uninhabitable (Yang et al., 2017). Newton et al. (2016) showed that for $0.25 - 0.5 M_{\odot}$ stars the rotation periods coincide with the HZ orbital periods placing significant constraints on the detectability of these planets from RV surveys and thus recommend that searches for planets in HZ focus on $0.1 - 0.25 M_{\odot}$ stars. They also concluded that that searches for planets in the HZ of low mass active stars are more suited to photometric than spectroscopic searches due to the RV noise introduced by stellar activity.

There are some complicating factors that need to be taken into account in the measurement of stellar rotation from starspots. The viewing angle between the observer and the stellar rotation axis, known as the obliquity, will have a significant effect on the visibility of spots and the measured rotation period. For example, if a star is observed nearly pole on then spots at lower latitudes may be invisible alternatively if the spots are at high latitudes we see the spots the whole time so there would be no rotational variation to be measured, instead we would see the variation caused by the waxing and waning of star spot groups (Herrero et al., 2012; Karoff et al., 2009). Stars are not solid bodies and rotate with different periods depending on the stellar latitude. This differential rotation can be seen in the Sun where the solar equator rotates approximately once every 24.47 days while at the poles a single rotation takes 35 days. Thus we measure the rotation period at the latitude of the

spots which is likely different to the equatorial rotation period and which can change as spots migrate in latitude over a stellar cycle.

1.7.3 Effect of Stellar Activity on Transit Measurement

As a transiting planet crosses our line of sight to a surface star spot the amount of starlight occulted by the planet will be reduced due to the lower luminosity of the cooler starspot. This manifests itself as a 'bump' in the transit light curve and the size of this bump can be used to determine the temperature difference and, along with knowledge of the stellar rotation velocity, the size of the occulted spot. The visual impact of a given starspot on a transit lightcurve will be greatest when the spot is in the centre of the disk where limb darkening is minimised and therefore the contrast between the bright photosphere and the cooler starspot is greatest. If an occultation of a starspot occurs away from the centre of the stellar disk, then the brightness contrast will be reduced and the viewing angle will foreshorten the size of the starspot resulting in a reduced impact on the lightcurve. The contrast between the cooler star spot and the photosphere is greater at shorter wavelengths so observations in blue or UV filters will be more affected by spot crossing events than those made in longer red or IR wavebands.

Stars emit a stream of material in the form of a stellar wind through which an orbiting planet has to pass. The wind density is greater closer to the star implying short period planets pass through the densest regions of the stellar wind outflow. The possibility of a planetary magnetospheric bow shock affecting the near UV transit shape was investigated by Llama et al. (2013) following HST observations that appeared to show an early ingress transit asymmetry for HD189733b (Ben-Jaffel and Ballester, 2013). The observation could be explained by a bow shock preceding the planet by $16.7R_P$, increasing the Hydrogen column density within the shock and therefore modifying the near-UV transit shape, Figure 1.4. Changes in the stellar wind density at the planet resulting from stellar rotation will lead to significant variations in the near UV transit asymmetry.

The impact of star spots on transit time measurements has been considered by several authors (Oshagh et al., 2013; Ioannidis et al., 2016). Barros et al. (2013) identified spot transits as the cause of TTVs in WASP-10b previously postulated to be the result of an unseen companion planet. Ioannidis et al. (2016) showed that timing from higher precision lightcurves is more affected by stellar spots and define the transit SNR (TSNR) as the ratio of out of transit noise to the transit depth. They demonstrated that for TSNR $\lesssim 15$ the systematic timimg errors introduced by spot crossing events are indistinguishable from the random noise. They also showed that the magnitude of the effect of spots on timing measurements is determined by the spots longitude on the stellar surface, peaking at $\lambda = \pm 70°$, reducing the

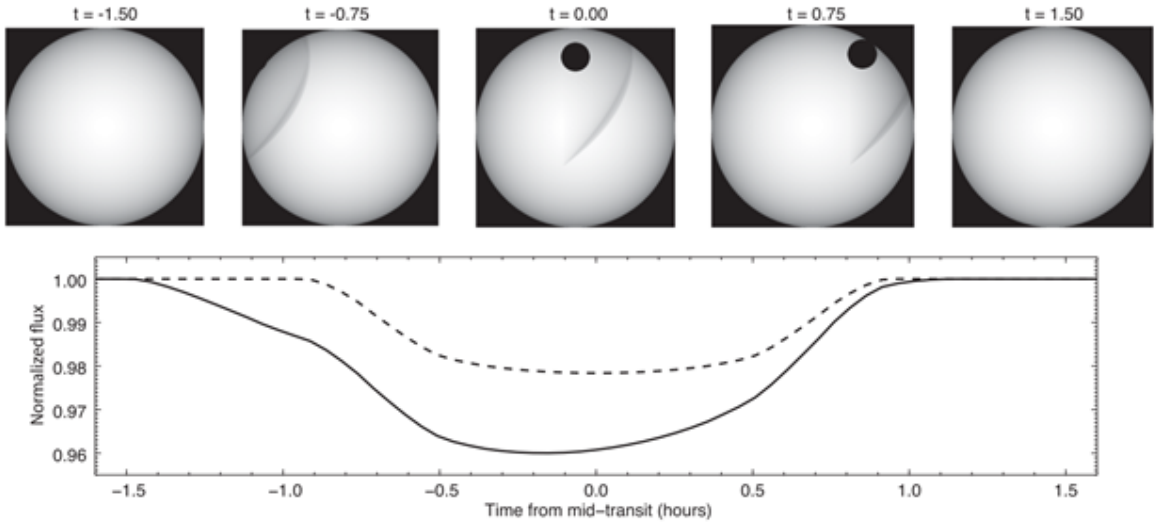

Figure 1.4: From Llama et al. (2013), their Figure 3, showing the predicted early ingress and deeper transits predicted for a bow shock with high enough column density to absorb light from HD189733 at near-UV wavelengths (solid line) versus the transit shape without the bow shock effect (dotted line).

closer a spot is to the stellar limb (as the size of the projected spot is reduced) and becoming zero at the centre of the stellar disk. Therefore a spot crossing will induce a positive time variation where it occurs before the transit mid-time and a negative variation where it occurs after transit mid-time leading to a transit time variation effect than can mimic that caused by a companion planet.

Even where spot crossing events are not observed in transit lightcurves the existence of unocculted surface spots will cause the observed mean integrated stellar flux to decrease. If a transit occurs along a chord that does not cross these spots then it will occult a greater proportion of the stellar flux leading to an increased transit depth as compared to a spot-free surface (Kirk et al., 2016). This effect could be detectable as a correlation between increased measured transit depth with decreasing stellar brightness as measured from the out of transit flux.

In a case of one mans noise is another mans data, spot crossing events can be used to inform us about the obliquity of a system. Stellar obliquity is the alignment (or otherwise) between the stellar spin axis and the planetary orbital plane. The projected stellar obliquity (λ) can be measured via the Rossiter-McLaughlin effect (Triaud, 2018) for fast or moderately rotating star. Successive crossings of the the same star spot as it rotates with the stellar surface implies good alignment between the stellar spin and orbital axes and allows the rotational period, rotational velocity and sky projected obliquity to be determined. Successive crossings of the same spot three or more times allows the true, de-projected, obliquity (Ψ) to be determined (Southworth and Mancini, 2016) if the crossing are sufficiently separated

in longitude.

Other than using photometric monitoring of stars for spot driven variability, spectroscopic methods can also be used to determine magnetic activity through chromosphere activity levels. The most commonly used measures are the Mount-Wilson S-index (Vaughan et al., 1978) and the RHK index (Middelkoop, 1982). The S-index is a measure of the emission-line cores of the Ca II H and K lines in two narrow bands normalised to immediately adjacent continuum bands. The RHK activity index is similar to the S-index but it gives the emission in the same narrow bands normalised to the total bolometric brightness of the star. Chromospheric activity will also be apparent as increased X-ray luminosity where, for example, doppler imaging of chromospheric line profiles above active photospheric regions can be used to map spot locations (E.g. Seward and Charles, 2010).

For transit observations there are several possible routes to mitigating the effects of spot crossing events. Using longer wavelength filters minimises the spot contrast. In transit modelling the affected data can be masked (E.g. Bruno et al. (2018)) or alternativly modelled using code that allows the effect of the spot to be factored into the transit model such as SPOTROD (Beky, 2014) or PyTranSpot (Juvan et al., 2018).

1.7.4 Exoplanet Effects on Host Stars

Until now I have considered the effect of the stellar activity on the exoplanet however for hot Jupiters on short period orbits there exists the potential for the planet to affect its host star in ways that are measurable.

Typically single stars would be expected to show a reducing rate of stellar spin as they age as angular momentum is lost through their stellar winds. The opposite case of stellar spin-up can occur through accretion of mass in to the star or via tidal interaction with a companion planet transferring orbital angular momentum to the star as the orbital separation decreases (Vidotto, 2019). Magnetic activity is linked to the strength of a stars magnetic dynamo which is in turn linked to its rotation velocity, thus stellar spin up through planetary tidal interaction and subsequent orbital decay can lead to increased magnetic activity. The natural end point of this process is planetary engulfment by the host star and studies of fast rotating evolved red giant stars have suggested their fast rotation rates could be the signature of planetary engulfment (Privitera, 2019; Privitera et al., 2016).

1.8 Why Study Transit Times?

The study hot Jupiter transit timing and duration variations can be used to reveal additional information about the systems under study such as orbital period change or the discovery of

additional planetary bodies, which in turn can be used to inform theories of formation and dynamical histories. TTVs and TDV's can also be used to break some of the model parameter degeneracies resulting in more accurate determination of a systems physical characteristics.

Having looked at causes of transit timing variations I now consider the current state of research and opportunities for further research, especially that involving smaller aperture telescopes.

1.8.1 Discovery of additional planetary bodies

As discussed in section 1.2, the presence of another body orbiting in the same system as a hot Jupiter can cause periodic perturbations in the motion of the hot Jupiter or the host star. The detection of these effects is simple in principle, requiring timing measurements of multiple transits spread over a period of time.

Stars that already have 1 transiting planet could reasonably be expected to have a higher probability of hosting additional planets than random field stars thus searches for timing variations can lead to an increased discovery rate (Beatty and Seager, 2010). This detection probability is enhanced as the companion planets do not themselves need to transit to produce detectable TTVs.

It has been shown that TTVs are sensitive to lower mass planets than currently detectable through radial velocity techniques (Steffen, 2016), allowing the detection of Earth mass companions to transiting planets even if they do not transit themselves. The detection of multi planet systems allows the mass of both components to be determined and if both planets transit then their radius and thus bulk density is accessible as well, thus multi transiting systems provide a 'Rosetta Stone' for interpreting results from wider TTV studies (Ragozzine and Holman, 2010).

Planets that are in a low order mean motion resonance will produce the largest amplitude TTVs. For example, a transiting hot Jupiter orbiting with a 3-day period accompanied by a terrestrial mass companion in a 2:1 MMR will exhibit TTVs of approximately 3 minutes over a period of 35 days. This would be easily detectable with ground-based telescopes. Measuring TTVs is also efficient on telescope time given that the calculated times of transit are well known and only the transit needs to be observed rather than monitoring the star for extended periods of time as would be required to search for companion transiting planets.

1.8.1.1 ground-based Observations

Hot Jupiter's have short periods of a few days and large radii allowing many transits to be measured with modest telescopes. In practice achieving precise timing measurements using ground-based telescopes has not proved simple for a number of reasons including poor SNR,

telescope availability and non-continuous coverage. This in turn has led to observations by multiple groups using different equipment and analysis methods being combined, which brings challenges in itself. For these reasons the unambiguous detection of TTVs using ground-based telescopes has not produced a bounty of results and many of those claimed have subsequently been questioned or refuted. Some examples are discussed below.

In HAT-P-13b the presence of a companion planet was first detected in the discovery follow-up RV data showing planet c on a 428 day highly eccentric orbit, but no transits or TTVs were seen in the discovery measurements (Bakos et al., 2009). A third planet on a much longer and unconstrained outer orbit has also been reported from a residual trend in the RV measurements (Winn et al., 2010; Knutson et al., 2014). Searches for transits by planet c have so far been unsuccessful (Szabó et al., 2010). In 2011 a large and sudden 0.015d TTV was reported as could be expected from a companion on a highly eccentric orbit (Pál et al., 2011) however the parameters did not match those for planet c. Further support for the sudden TTV came from additional observations by (Nascimbeni et al., 2011). These claims led to increased studies of HAT-P-13b which greatly refined the planet and host star parameters but found no evidence of TTVs (Fulton et al., 2011; Southworth et al., 2012) even though planet c is known to exist.

WASP-10b is a $3M_J$ planet orbiting a late K star every 3.09 days (Christian et al., 2009). In 2011 Maciejewski et al. (2011a) published 9 transit observations claiming a periodic timing variation with an amplitude of 3.5 minutes which they interpreted as a $0.1M_J$ companion on a 5.23 day orbit, i.e. close to the outer 5:3 mean motion resonance. This claim was challenged when observations showed transit depth variations attributed to star spot crossing events. A further 8 transits and reanalysis of previous results using a model that accounted for the active nature of WASP-10 showed no variations from a linear ephemeris (Barros et al., 2013).

WASP-3b is another well-studied system where TTVs were first reported showing evidence for a $15M_\oplus$ planet in a 2:1 resonant orbit (Maciejewski et al., 2010). Once again though this claim was quickly disputed as more data was gathered showing no evidence of TTVs or RV trends (Maciejewski et al., 2013b; Montalto et al., 2012). Additional observations backed the lack of TTVs but the data showed evidence for a deviation from a linear ephemeris however no period could be determined (Nascimbeni et al., 2012). Further studies have also shown evidence of TDV's with a 3-4 minute amplitude, though again no periodic behaviour could be determined (Eibe et al., 2012). The existence of timing variations for WASP-3b remains an open question.

It has taken until the discovery of WASP-148b (Hebrard et al., 2020) for the first confirmed discovery of an interacting planetary system with TTVs from the ground. The initial discovery was made via large residuals in the single planet fit to the follow up RV monitoring

of a singly transiting planet discovered by the SuperWASP survey. Subsequent follow up photometry revealed transiting timing variation in the first 8.8 day period planet of up to 30 minutes, the second planet with a period of 34.5 days has yet to be detected in transit. Such large TTVs would be easily detectable in timing measurement with small aperture telescopes, indeed some of the follow up lightcurves in the discovery paper were obtained with the 0.4m NITES telescope.

In order to try and address some of the issues associated with long term monitoring of systems for timing variations the Czech Astronomical Society created the Exoplanet Transit Database (ETD) to collate observations from professional and amateurs (Poddaný et al., 2010). This database of almost 10,000 transit observations has been used by a number of authors to look for trends in timing measurements. The planet TrEs-5c was found from timing measurements using predominantly data from the ETD (Sokov et al., 2018).

The main issue with searching for timing variations in transit timing data from multiple ground-based telescopes is its uncontrolled and heterogeneous nature. The data, often sporadic with varying signal to noise ratios, comes from many sources, mostly amateur observers, using a variety of equipment (such as different or no filters). Analysis methods and capabilities vary widely with no governance on the methods used to measure the timestamps of the photometric data used to derive the transit parameters. The wide variety of equipment, methods and atmospheric conditions make detection of periodic trends on the timescales of days, weeks or months difficult. For these reasons only longer-term trends are reliably detected. The recent Exoclock project Kokori et al. (2021) to refine planetary ephemerides ahead of the ARIEL mission are attempting to mitigate as many of these effects as possible through the provision of standard software, processes, observer training and providing feedback to contributors.

Several extensive studies have re-analysed the available data to look for timing variations and, although they have successfully recovered the long term quadratic trend in the ephemeris for WASP-12b and WASP-4b (Section 1.3.1), no further transiting timing variations have been positively detected (Baluev et al., 2015, 2019).

Of course the lack of detection of significant TTVs in hot Jupiter systems studied is in itself a significant result which will be discussed further when I look at how this informs analysis of the formation and dynamical history of these systems (Section 1.8.2). If detecting TTVs from the ground is difficult, detecting transit duration variations will be even more so given that the variation is expected to be around half that of any TTV (Millholland et al., 2016), and that uncertainties in duration measurement are around twice that for transit mid-time.

1.8.1.2 Kepler Observations

Where ground-based observations of TTVs and TDV's have been fraught with difficulty the space based Kepler telescope, with exquisite photometric precision and uninterrupted viewing, has undoubtedly been extremely successful. KOI-142, called "The King of Transit Timing Variations", orbits in 10.95 days and exhibits a nearly 12 hour amplitude TTV with a 630 day period (Nesvorny et al., 2013, and references therein). The authors presented a 'river' chart showing the TTVs over a large number of orbits and they also detected TDV's in phase with the TTVs. The amplitude of TTVs in KOI-142 appears to be changing over time as well (Nesvorny et al., 2013).

K2-19b/c is a system of two Neptune sized planets in a 3:2 MMR orbit discovered during the extended Kepler mission, where both components exhibit measurable TTVs (Armstrong et al., 2015). Both planets are seen to transit the host star and these transits have been observed with the small aperture (0.4m) NITES telescope, highlighting the ability of telescopes in this aperture range to follow up transiting timing variations of systems discovered by orbiting observatories, which generally are only able to follow individual systems for limited periods.

As additional Kepler data sets were released a flood of additional planet discoveries were announced (Steffen et al., 2013; Xie, 2013, 2014). Probably the largest single study, the most recent in a series of papers, provides a catalogue of 2599 KOI's (Holczer et al., 2016) from which 274 objects with detectable TTVs have been catalogued. Some of these systems were previously known and published on a web site run by Eric B Ford (Ford, 2014). Many of these catalogued systems show significant long-term trends with TTVs amplitudes of a few minutes to several hours. Some of these systems are, in principle detectable using ground-based telescopes enabling the baseline of observations to be extended now that the primary Kepler mission is complete. One of the most important results for the K2 mission is the detection of two companion planets through TTVs in the previously known hot Jupiter WASP-47b (Becker et al., 2015). Apart from the fact that all three planets can be seen in transit what makes this system stand out is that it is the first and only discovery of super Earth mass companions on both interior and exterior orbits with a hot Jupiter. The WASP-47 system will be important for studies of planetary formation mechanisms.

1.8.2 Formation Process and Dynamical Histories of Hot Jupiter Systems

Prior to the discovery of the current zoo of exoplanets, planet formation theories were based on the only example we had available, the Solar System. These theories sought to explain the ordered structure of the Solar system with its eight planets moving sedately in near circular,

coplanar and prograde orbits. A theory of formation from the solar nebula explained these facets as well as the four inner rocky planets that formed near the young Sun where the solar nebula was hot allowing only refractory material to condense. The two gas giants formed out near the snow line where much more material was available to form large masses quickly and finally the ice giants formed further out where their slow growth was cut short by the dispersion of the solar nebula (Nesvorný, 2018). The grand tack model later showed how the migration of Jupiter first inwards through the disk and then back outwards explains the planets orbital spacing, the existence of the asteroid belt and why the ice giants orbit at such large distances (Walsh et al., 2011). While this ordered and relatively straight forward model of planet formation has been very successful in explaining the formation of our Solar system it has been unable to explain the widely varied range of exoplanet system architectures discovered to date. These include extremes such as Jupiter mass planets orbiting host stars in only a few days or less (short and ultra-short period hot Jupiters) or systems of tightly packed planets (STIPS) which are mini solar systems with multiple planets all orbiting inside the equivalent orbital distance of Mercury in our own Solar system.

Hot Jupiters and planets on short orbital periods are the easiest to detect having the greatest impact on the radial velocity of their host star and their proximity to the host star increases the likelihood of transiting. Statistical studies have to take this discovery bias into account but as time has progressed and techniques have improved more and more planets have been discovered, many in multi-planet systems a number of real trends becoming visible in hot Jupiter exoplanet systems. Key amongst these are;

1. Hot Jupiters are a relatively rare phenomenon amongst exoplanet systems. While most stars are expect to harbour a planetary system, Wright et al. (2012) finds an occurrence rate for hot Jupiters of just $1.2\% \pm 0.38\%$ around F, G and K stars measured as part of the California Planet Survey.

2. The orbital pile-up at very short periods is unlikely to be real when selection bias is properly accounted for (Winn, 2015).

3. Hot Jupiters have a lack of companion planets on short to medium period orbits (Steffen et al., 2012).

Focussing on hot Jupiters two formation mechanisms have been proposed, formation in situ or formation further out from the host star followed by an inward migration (Ford, 2014). For a long time formation so close to the host star where the disk is hot was thought impossible and thus theoretical efforts focussed on models to explain the inward migration following a rapid planet formation out near the ice line. Again two broad models exist for the

migration mechanism, either a slow inward migration through the remaining disk material or through excitation of eccentricity followed by tidal circularisation at a short period. Both models have their drawbacks but fortunately both make different and testable predictions for the resulting planetary system.

Disk migration is a relatively well understood process which can rapidly reduce the orbital period of a giant planet through angular momentum exchange with a gaseous disk. Stopping the planet's migration rather than it being accreted by the star is the key problem. If the host star creates a magnetospheric cavity then migration can be halted at the edge of the disk (E.g. Rice et al., 2012, and references therein). Thus, in this model, the survival of a hot Jupiter depends on the host star having the time and magnetic field strength to clear a cavity before that planet has formed and migrated. Alternative mechanisms to halt inward migration at short orbital periods include Roche lobe overflow from the planet to the star and tidal dissipation, similar to the Earth moon system (Lin et al., 1996; Trilling et al., 1998). Another mechanism that can be invoked to explain the survival of planets is the co-rotation radius, the orbital radius at which the planet orbits in the same period as the stellar rotation. Inside this radius planets can lose angular momentum to their host star through tidal interactions leading to a reducing semi-major axis. Outside of this radius the opposite occurs and the semi-major axis can increase at the expense of the stellar rotation, similar to the Earth-Moon system. Stars are born with a high rotation rate and as they age and slow down the co-rotation radius moves outwards. Thus planets can initially be pushed away from a fast rotating young star and then pulled inwards later at stellar evolutionary stages, (Vidotto, 2019, and references therein).

Disk migration models predict that the resulting hot Jupiters would be on low eccentricity, co-planar and prograde orbits. Any large mass planet core migrating through a disk will gain more mass from the disk and would disrupt any other forming planets with inner planets being forced into the host star and outer planets being shepherded into MMR orbits (Raymond et al., 2006). The model struggles to explain hot Jupiters at very short orbital periods but the relative rarity of hot Jupiters would be explained if the majority of formed planets were accumulated by the host star with only a few being saved by late migration through the disk being stopped by one of the processes outlined above.

Eccentricity excitation and tidal damping naturally explains the short orbital periods and, in contrast to disk migration models, predicts that the resulting planets would have randomly inclined or even retrograde orbits. The process of eccentricity excitation would be expected to remove other short period companions from the system, either through ejection or collision (Ford, 2014, and references therein).

The key unknown for eccentricity excitation and damping is the method of exciting the

eccentricity. Several mechanisms exist to achieve this excitation such as planet-planet scattering or secular excitation from a long period planetary or stellar companion, possibly through the Kozai-Lidov cycles (Kozai, 1962; Lidov, 1962) where the outer companion with a mutual inclination causes the eccentricity and inclination of the inner planet to oscillate periodically (Fabrycky and Tremaine, 2007; Naoz et al., 2011; Shevchenko, 2017). This oscillation in eccentricity can reduce the pericentre of the inner planets' orbit, bringing it in close to the host star where tidal dissipation can circularise the orbit. It is entirely likely that different methods are at play in different systems.

Thus both models for migration are testable through searches for additional companions of which transit timing variations are a key method along with determining the planetary obliquity via the Rossiter-McLaughlin effect or detection of multiple spot crossing events. Discoveries of long period companions to hot Jupiters have shown that around 50% of hot Jupiters have long period giant companions with masses $1 - 20M_J$ and orbital separations of 5-20AU (Knutson et al., 2014; Bryan et al., 2016). These same studies have not found any statistical evidence of a correlation between hot Jupiter obliquity and the presence of a long period companion. Recent studies have also shown that hot Jupiter host stars have a significant population of long period stellar companions which, for separation between 50-2000AU, is significantly enhanced over the field star population rate (Ngo et al., 2016). In contrast systems with a hot Jupiter show a distinct lack of stellar companions at separation of 1-50AU when compared to the field star population (Ngo et al., 2015). These findings lead to the conclusion that eccentricity excitation via the Kozi-Lidov mechanism may not be the primary cause of hot Jupiter migration and implies that hot Jupiter formation may be preferentially enhanced in systems with high mass or stellar companions (Ngo et al., 2015).

The discovery of super Earth mass planets at short periods and the prevalence of tightly packed short period systems (STIPS) discovered by Kepler (Boley et al., 2016) has led to reconsideration of in-situ giant planet formation close to the host star. These models consider the likelihood of a giant planet core forming close to the star being able to gather enough gas prior to disk dispersion (Batygin et al., 2016). As with the various migration possibilities, in-situ formation makes testable predictions for the final system architecture including a trend towards higher mass hot Jupiter cores, and companion planets with $50 < P < 100$ days that have been scattered to high inclinations and thus are unlikely to transit (Batygin et al., 2016). So far these predictions seem at odds with current observational data though the models can explain short period giants without a gaseous atmosphere as these could not have formed via migration where they would be expected to accumulate a large amount of gas from the disk.

WASP-47b is the only hot Jupiter system discovered to date with two short period companions (Becker et al., 2015). The two companions of with masses $< 22M_\oplus$ and $15.2M_\oplus$ orbit

in 0.79 and 9 days respectively, either side of the $341 M_{\oplus}$ previously known hot Jupiter in its 4-day orbit. All three planets are in non-resonant, near co-planar, circular and prograde orbits indicating that a least some hot Jupiter's can form in a dynamically quiet way providing support for disk migration theories or potentially even in-situ formation. At almost the same time RV evidence was presented for the presence of a long period (572 ± 7 day) Jupiter mass companion in the WASP-47 system (Neveu-VanMalle et al., 2016) making this an important system for the study of hot Jupiter formation and dynamical history. The various models for hot Jupiter formation and dynamical history make testable predictions regarding the likely existence and location of companion planets. Thus the discovery or exclusion of companion planets to known hot Jupiters is key to being able to distinguish between these models. TTVs are a key tool to test for these companions being sensitive to low masses, especially those in MMR, and more suitable than RV techniques for faint stars. The method is able to exclude or at least place limits on the existence of companions, thus for the models of formation, a 'non-discovery' is just as important as a positive discovery.

Looking again at WASP-47b, which orbits a relatively bright magnitude 11.9 host star, the transit depth of 0.011 mag is easily detectable from ground with small telescopes. The TTV amplitude detected in the Kepler data is 0.63 minutes, previous testing of mid transit timing precision has shown that errors of $\pm 30 - 50$ seconds are reasonable (Salisbury, 2015). Thus it is unlikely that the TTVs could have been detected using small ground-based telescopes. WASP-47d has a much larger TTV amplitude of 7.3 minutes, easily detectable but the transit depth is ten times shallower than WASP-47b ruling out detection with ground-based small telescopes.

A number of other known hot Jupiters have been observed by the as part of the extended Kepler mission K2 mission. 19 transits of WASP-157 were observed with as part of the K2 mission in long cadence mode and thus were only able to constrain the existence of TTVs to an upper limit of $\sim$ 1minute over an 80-day period. K2 also observed WASP-85, this time in short cadence mode, obtaining 30 transits over an 82-day period. The TTV analysis showed a possible 7.8s amplitude variation with a 14.7-day period. However, this is suspiciously close to the 13.6-day rotational period of this star which is also shown to be active with recurring starspots. These results seem to reinforce the general finding that hot Jupiters lack companions at short periods (Steffen et al., 2012).

1.8.3 Multi Transiting Systems

The value of using TTVs to characterise systems is significantly enhanced if both (or more) bodies in the system transit the host star. In these systems the period of each planet is well constrained and their radii can be determined from transit model fitting. The TTVs

must also be self-consistent allowing tight constraints on additional perturbing bodies and rejection of false-positive detections (Ragozzine and Holman, 2010). Multiple transits can also be observed even if the mutual inclination is high if the system is observed along the line of nodes. Multi -transiting systems also have the potential for planet-planet transit events.

Where two (or more) planets interact gravitationally to produce TTVs each of the mass ratios can be determined independently and, when combined with the RV semi-amplitude and the stellar density (obtainable from the transit lightcurve alone), the absolute mass and radius of the star can be determined without relying on theoretical stellar models (Agol et al., 2005). Probably the most famous application of this method is for the 7 low mass planets orbiting TRAPPIST-1 in a near resonant chain (Gillion et al., 2017; Luger et al., 2017).

Determining absolute system parameters using TTVs requires that any mutual orbital inclination between the planets is accounted for. For a given stellar radius transit duration is determined by the planets orbital velocity and the impact factor as a proxy for orbital inclination. The transit duration of individual planets transiting the same star can be used as indicator of the mutual inclinations. If the planets are co-planar the duration would be a simple function of semi-major axis with planets on longer orbits having longer transit durations. Any divergence from this trend would indicate differences in impact parameter and thus inclination (Winn, 2015; Fabrycky et al., 2014). With well constrained orbital inclinations, radial velocity measurements can uniquely determine planetary mass allowing their expected gravitationally induced TTV's to be calculated compared with timing measurements. Mutual events (where planets transit each other) when combined with transit durations allow the tightest constraints on mutual inclination (Ragozzine and Holman, 2010; Hirano et al., 2012).

The increasing numbers of detections of TTVs and derivations of planetary parameters has enabled a comparison of mass determined by two separate methods – radial velocity and TTV. Doppler studies of WASP-47b have yielded masses comparable to those from TTVs within the still rather large measurement errors (Dai et al., 2015). Bulk density calculated from RV and TTV masses shows a systematic bias towards lower density for TTV measurements. This is attributed to a sensitivity bias from RV measurements being more sensitive to high mass shorter period planets (Steffen, 2016).

1.8.4 Period Changes Unrelated to Companion Planets

Long term period changes due to apsidal precession or tidally driven orbital decay can be used to infer details regarding the stellar and planetary structures. For apsidal precession the largest contribution to the rate of precession comes from the the tidal deformation of the planet ($\dot{\omega}_P$), Ragozzine and Wolf (2009), see Equation 1.11. Their Equation (14) shows

that the rate of precession for a given planet is dependent on the planetary Love number, κ_2 which is a measure of the central condensation of matter within the planet with small Love numbers corresponding to greater central condensation of mass. Thus measurements of the rate of apsidal precession can provide information on the interior structure of an exoplanet helping inform formation theories such as core accretion and collapse models which make different predictions for the central condensation of matter within the planet.

Similarly Patra et al. (2017) showed in their Equation (14) that in the case of orbital decay through tidal interactions the rate of period change is related to the modified tidal quality factor (Q'_*), a dimensionless ratio encapsulating the stars response to tidal deformation and the stellar Love number κ_2. Thus orbital decay due to constant phase lag tidal interaction can provide information on the central condensation of matter within the star.

1.8.5 System Ages

Determining ages for isolated single stars is a long standing problem in astronomy. For young stars, activity indicators such as Ca H and K or surface Lithium abundances can be used with stellar evolution models. For main sequence exoplanet hosting stars two main methods are commonly used, stellar isochrone fitting and Gyrochronology. Isochrone fitting relies on fitting observable parameters such as metalicity, $T_{\rm eff}$ and absolute magnitude to stellar models in which age is one of a number of free parameters. Gyrochronology relies on the fact that all stars are born with an intrinsic spin and also they lose mass, and therefore angular momentum, through the expulsion of stellar winds which results in a slowing of their spin rates as stars age. Measurement of the stellar rotation, determined either from spectroscopic methods or photometric monitoring where the star exhibits spots that impose a brightness modulation as the star rotates, are compared with models based on initial mass and spectral type to allow an age to be estimated.

Fitting isochrone ages relies on the accuracy of the stellar evolution models adopted. These models make assumptions about factors such as convective mixing processes and metallicity that may not apply precisely to the stars in question. These factors are not easily encompassed in the errors on the gyrochronological ages (Brown, 2014).

One restriction with isochrone fitting has been the requirement to interpolate between either absolute magnitude or stellar surface gravity and $T_{\rm eff}$. Determining absolute magnitudes requires knowledge of distance to the system being studied which has previously introduced large uncertainties, therefore it has been more common for stellar density, which can me measured independently using transit photometry to be used with $T_{\rm eff}$ (Brown, 2014). Accurate distance measurements now available from the Gaia mission (Brown and Gaia Collaboration., 2018) along with detailed dust extinction mapping allow these limitations to be lifted.

Discrepancies in the results from these two methods of determining age can be used to determine if exoplanets are transferring angular momentum to their host stars (Brown, 2014; Maxted et al., 2015). Angular momentum transfer can occur through either mass transfer or via tidal interaction with a binary stellar or short period planetary companion. Both Brown (2014) and Maxted et al. (2015) have found evidence of significant discrepancies between isochrone and gyrochronological ages determined in large samples of exoplanet host stars potentially indicating spin up of exoplanet host stars through angular momentum transfer.

An extreme example is WASP-52b, studied in detail in section 3, which is a $0.4M_J$ planet orbiting a $0.85M_\odot$ star every 1.75d, for which as gyrochronological age of $0.4^{+0.3}_{-0.2}$Gyr was found by Hébrard et al. (2013). Using using stellar isochrone fitting Mancini et al. (2017) find an age of $9.4^{+1.2}_{-1.4}$Gyr, while in section 3, using MIST stellar isochrone fitting constrained with accurate distance priors from Gaia DR2, I find an age of $8.5^{+3.7}_{-4.6}$Gyr. Different methods for determining age were also compared for WASP-135b (Spake et al., 2016) who found a mean isochrone age from fitting three different isochrone models of 4.4 ± 2.5Gyr compared with a Lithium abundance age of $0.60^{+1.40}_{-0.35}$Gyr and an upper limit to the gyrochronological age of $0.82^{+0.41}_{-0.23}$ Gyr.

1.9 Summary

In this section I have looked at the astrophysical scenarios that can lead to the generation of a transit timing signal in transiting exoplanet systems and why these signals are important to our understanding of transiting exoplanets. From the examples of the potential variation amplitude and period, the detection of planets in inner or outer circular orbits with even multiples of Jupiter mass are unlikely to be possible with small ground-based telescopes. However systems in or near a mean motion resonance on the other hand show variations of several to many minutes and should easily be detectable if they exist. This is clearly seen in results from the Kepler space mission which show systems with TTVs from 5 minutes to over 1000 minutes (Mazeh et al., 2013)). The contribution to exoplanet science from the completed Kepler mission continues as the data are still being analysed while on-going dedicated exoplanet missions such as TESS and CHEOPS and planned missions including PLATO and ARIEL are expected to significantly enhance our knowledge of planetary systems, their host stars and interactions. Other missions, not completely focussed on exoplanet research such as JWST and GAIA, will also prove vital to these studies. In the context of the research focus of this thesis, the combination of the exquisite astrometric data from GAIA with new transit observations and radial velocity data will enable significantly tighter constraints to be placed on the properties of exoplanet systems.

Changes in period due to orbital decay accumulate very slowly and require a decade or more of observation to become detectable and to allow differentiation between other causes of longer term periodic variation such as apsidal precession and Rømer effect or from quasi-periodic variations due to stellar activity or the Applegate effect. The timescales of changes to transit timing for many of the scenarios outlined in the preceding sections are very long, much longer than the typical observing program available at large professional observatories. This is where monitoring with small aperture ground-based telescopes that can be dedicated to this sort of long term project can make an important contribution. Such a campaign would require long term stable observations over many years and homogenous data reduction and analysis to minimise systematics. Many results to date have shown that having incomplete data sets missing single or groups of transits (due to poor weather or visibility from a given observatory location) can severely hamper the measurement of transit times leading to the need to combine data from multiple telescopes, ideally in good quality locations spread over a range of longitudes.

Table 1.1 below summarises the amplitude and periods of transit timing variations potentially detectable with small telescope observations from the ground expected from the scenarios discussed above and how they can be distinguished.

Variation cause	Typical amplitude	Typical period	Ways to distinguish between causes
Companions in or close to MMR	From a few to $>$ 1000 minutes	More than 10$\times$ perturbing planets period	Timing variation would be strictly periodic. Supercycle period needs to be consistent with MMR orbit for perturber.
Apsidal precession	Up to several 10's of minutes.	Years to decades	For shorter periods variation will be periodic. Determination of orbital eccentricity via other methods allows amplitude and period of the TTV/TDV's to be calculated. TDV's and variation in the primary and secondary eclipse timing will also occur.
Applegate effect	$\sim$ 0.1 to $>$ 300 seconds.	In line with stellar activity cycle, $>$ 10 years.	Variation will only be quasi-periodic and the host star must be magnetically active. Detection of a stellar cycle from spot measurements commensurate with the TTVs period would be a strong indicator of the effect.
Orbital decay	Up to a few hundredths of a second per year.	Cumulative over time.	The changes would not be periodic and would exhibit a unique shape in the fit to the measured O-C data points.
Rømer delay	From $\ll$ 1 second to several seconds.	Equal to the companion orbital period.	Effect will be strictly periodic. Another body causing significant stellar reflex motion would be expected to show in radial velocity measurements.

Table 1.1: Summary of transit timing effects potentially detectable with small aperture ground-based telescopes.

Previous research using small ground-based telescopes has shown typical measurement uncertainties of ±50 seconds reducing to ±30 seconds for the very highest quality transit measurements (Salisbury, 2015). Therefore the photometric and timing precision achievable with small telescopes means the value of these observations comes from monitoring exoplanet systems over long periods in order to highlight any systems of interest for follow up by professional observatories. Two key areas where small aperture ground-based telescopes are able to contribute to exoplanet science are analysed in this thesis;

1. Decades long periods of monitoring of transit timing.
    - Ephemeris recovery/refinement.
    - Identification of long period large amplitude timing variations due to MMR super-periods, companion planets on long period orbits (via Rømer effect) or apsidal precession.
    - Identification of non-periodic timing changes due to orbital decay
2. Photometric monitoring of exoplanet host stars.
    - To determine rotation rates and activity cycle lengths.
    - To inform professional observatories of optimal times to undertake transmission spectroscopy which can be severely affected by stellar activity.

To be achievable with small aperture ground-based telescopes these types of observations need to be restricted to transits measurable with sufficient SNR with small aperture telescopes such as for the short period hot Jupiters. Fortunately these are also the type of systems where many of these effects are expected to occur.

Chapter 2

Methods

2.1 Introduction

In this chapter I describe the common methods used to obtain and reduce the observational data. First I describe the telescopes used and the approach to planing the observations. Next I detail the methods used to obtain the data with the different telescopes, and I finish with a description of the techniques used to reduce the data and obtain a physical transit model fit.

2.2 Telescopes Used

This project made use of three small aperture ground-based optical telescopes. The primary telescopes were PIRATE and COAST of the OpenScience Observatories, part of the Open University OpenSTEM Labs. Additional observations were made with the POST observatory located in the UK. Each observatory is discussed in turn below.

2.2.1 OSO Telescopes

The OpenScience Observatories (OSO) consist of three robotic telescopes, two optical telescopes located at Observatorio del Teide, part of the Observatorios de Canarias on the island of Tenerife, 28°18′ 00″ N, 16°30′ 35″ W at an altitude of 2390m (Kolb et al., 2018). The third, not used in this project, is ARROW, a remotely controlled radio telescope based in Milton Keynes, UK. The two telescopes owned by the Open University and located in Tenerife are the COmpletely Autonomous Service Telescope (COAST), a 0.35m f11 Schmit-Casegrain optical system, and the Physics Innovations Robotic Telescope Explorer (PIRATE), a 0.45m f6.8 Corrected Dall-Kirkham astrograph. Each telescope is located in its own robotic dome on German equatorial mounts which can be operated completely autonomously via a scheduler or remotely in real time. Both observatories are controlled using the autonomous telescope control software, ABOT (Sybilski et al., 2014), the COAST telescope is also available for public

use as part of telescope.org. PIRATE is equipped with an FLI ProLine 16803 4k × 4k, 9μ pixel CCD camera producing a field of view 42′ square with plate scale of 0.62″/pixel. Prior to 21st May 2018 COAST was equipped with an SBIG STL-1001E CCD camera with 1024×1024 24μ pixels providing a field of view 22′ square with a plate scale of 1.25″/pixel. After 21st May 2018 COAST was equipped with an FLI ProLine 9000 3k × 3k 12μ pixel CCD camera producing a field of view 32′ square with plate scale of 0.63″/pixel. Both FLI CCD cameras were operated at a temperature of -30℃. The FLI cameras can be configured to read the CCD at either 8MHz or 1MHz, the latter providing lower read noise at the expense of a an eight times increase in read time. At 8MHz a PIRATE CCD frame can be read in 4 seconds, a process that takes 32 seconds at 1MHz. Therefore both FLI cameras are set for 8MHz read out to minimise deadtime between exposure and improve the efficiency of the telescopes.

In July 2018 both telescopes were upgraded with the addition of a GPS controlled shutter timing system, see Section 2.2.3. Prior to 21st May 2018 PIRATE was configured with Baader broadband R, G and B filters. After this date Johnson-Cousins B, V and Rc filters were installed and this filter set was extended in July 2018 when U and Ic filters were added. The Baader R, G and B filters on COAST were replaced with Johnson-Cousins B, V and Rc filters in July 2018.

Both telescopes are operated without any form of automated guiding, relying instead on the precise polar alignment of the mounts. ABOT automatically focuses the telescope for each scheduled observation, therefore deliberate defocusing of the telescope to improve photometric precision was not possible in scheduled observation mode. The scheduler will updated in due course to support this functionality.

2.2.2 POST Observatory

The Post Office Small Telescope (POST) is a private observatory owned by the author, located at 51°15′ 51″, 01°14′ 58″E at 20m altitude. POST hosts a 0.4m, f6.8 Optimised Dall-Kirkham (ODK) telescope on a German Equatorial mount. POST has a carbon fibre optical tube to minimise thermal expansion and the resulting changes in focus. It is equipped with an SBIG ST10-XME 2184 × 1472 6.8μ pixel CCD camera providing a field of view 19′ × 13′ with a plate scale of 0.52″/pixel, a full suite of Johnson-Cousins U, B, V, Rc and Ic filters are available. Figure 2.1 shows the filter bandpasses[1] overlaid with the ST-10XME CCD Quantum Efficiency (QE)[2] and the QE for the PIRATE CCD[3]. POST supports closed loop on and off axis guiding options to ensure accurate tracking. Most commonly used is the SBIG

[1] Astrodon, private communication

[2] http://www.company7.com/library/sbig/sbwhtmls/st10.htm

[3] https://www.flicamera.com/proline/

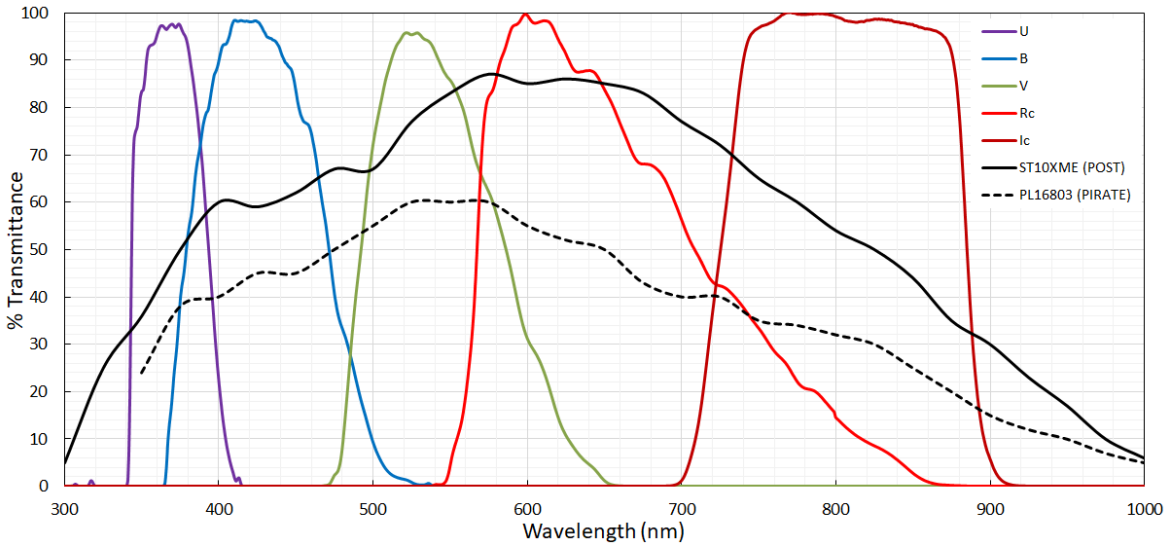

Figure 2.1: Plot showing the POST CCD (ST-10XME) Quantum Efficiency (QE), solid black line, overlaid with the transmission bands of the available Johnson-Cousins filters, based on the Astrodon manufactured filters used in POST. Also shown for comparison is the PIRATE CCD QE, dashed black line. The CCD in the POST observatory has a higher QE than that used on PIRATE at the expense of a significantly smaller field of view.

AO8 fast guiding unit[4] used to provide fast guiding corrections of up to 10Hz depending on the brightness of the guide star available. This guiding mode enables the target star to be maintained on the same CCD pixel throughout the observations without the need to constantly adjust the mount pointing (discussed further in Section 5.2.3). Off-axis guiding is used where no suitable guide star is available for the AO-8 unit. Unlike the OSO telescopes POST is always operated in a real time control mode.

2.2.3 Timing Of Exoplanet Transits

As one of the primary aims of this work is measure transit times and the determine the precision to which they can be measured timing control at the observatory is of paramount importance. In July 2018 both PIRATE and COAST were upgraded with the addition of a GPS controlled shutter timing system, prior to July 2018 the observatory control computers were updated from an Internet time server via the Windows Operating System. During July 2018 a GPS time controller was installed for both telescopes including a camera shutter trigger link to ensure millisecond timing precision for the opening and closing of the camera shutter rather than measuring when the command to open/close the camera shutter is sent. During initial testing the control PC clock was not slaved to the GPS controller so that the FITS header DATE-OBS field recorded the exposure start time in the same way from the before

[4]http://www.company7.com/library/sbig/sbwhtmls/ao8.htm

the GPS upgrade while the GPS trigger start and end times were recorded in separate FITS header fields. This enabled a comparison of the difference in exposure start time between the two timing control methods to be measured and it was found to vary by ±3 seconds. To solve this discrepancy the PC clock was also slaved to the GPS controller and subsequently the only difference in image start time stamps was the time between the exposure being requested and operation of the camera shutter, of the order of milliseconds. The AstroImageJ photometric software uses the DATE-OBS field from the FITS header and adds half the integration time to calculate the exposure mid-time, therefore for science observations made in the period between GPS installation and PC clock time being slaved to the GPS controller the GPS-START time was copied to the DATE-OBS field in the FITS headers using a routine written in Python prior to photometric analysis. ABOT has since been updated to write only the GPS measured start time to the DATE-OBS filed of the FITS headers.

At the time of the observations for this thesis POST was not equipped with a GPS controller and instead used the freeware Dimension4[5] to update the control PC clock from an Internet time server. Although timing updates can be obtained from Internet time servers by the computer operating system the use of a separate application to carry out this function allows direct control over the time server synchronisation and reporting. For POST, which is not left powered all the time unlike COAST and PIRATE, this reporting often showed clock drifts of many tens of seconds between observations which could be separated by several weeks.

2.3 Target selection and planning

2.3.1 Target Selection

Targets for observation had to meet a number of criteria including;

- Being visible from both OSO and POST observatory locations.
- Being brighter than magnitude 14 to keep exposure durations reasonable.
- Having a transit depth minimum of 0.5% to ensure an expected minimum transit SNR (Chapter 5.2.1) of 2.5 - 5 with an assumed expected photometric scatter of 1-2 millmag.
- Being short period to enable multiple transits to be obtained in each observing season.
- Having an outstanding scientific question that could potentially be addressed using small aperture ground-based telescope observations.

[5] http://www.thinkman.com/dimension4/

The first target, WASP-12b, was selected to be observed during all available observing seasons with the first observations being made in January 2016 and the last ones completed in January 2020. Historic observations going back to 2014 were also available from the POST observatory. WASP-12b is an example of a short period hot Jupiter orbiting its F type host star every 1.09 days Hebb et al. (2009) and suspected of losing mass through atmospheric ablation and possibly star-planet interaction (Haswell et al., 2012). Due to this short period and suspected mass loss WASP-12b has been the subject of many transit timing studies over the duration of this thesis to search for non-linear ephemeris variations. In 2016 Maciejewski et al. (2016) presented the first timing analysis indicating a quadratic ephemeris for WASP-12b and orbital decay has subsequently been confirmed for WASP-12b (Yee et al., 2019; Turner et al., 2021). WASP-12 has been shown to have a low rotation rate for its stellar type (Hebb et al., 2009; Nielsen et al., 2013) possibly indicative of a very low, pole-on, inclination Fossati et al. (2010) however no long term monitoring has been undertaken to search for photometric variability in WASP-12, thus monitoring was carried out over three seasons between 2016 and 2019.

A block of observing time occurred in the Summer of 2018 timed to coincide with the period of the upgrades to PIRATE and COAST. The primary aim was to determine the improvement in transit time measurement resulting from the installation of the of the GPS time controllers. Two targets, HAT-P-23b and WASP-52b, both observable over this period, were selected for observation. HAT-P-23b is a short period hot Jupiter orbiting a V = 12.43 magnitude star with a period 1.21 days and a transit depth of 1.4%. At discovery HAT-P-23b was found to have inflated radius and an eccentric orbit Bakos et al. (2011), while subsequent results agreed with the discovery paper (Sada and Ramón-Fox, 2016) others have found a smaller radius or adopted a circular orbit in the analysis (Ciceri et al., 2015; Maciejewski et al., 2018). With an orbital period similar to that of WASP-12b which has been shown to have a decaying orbital period (Yee et al., 2019), hence HAT-P-23b could be expected to show similar behaviour. Published transit times by Ciceri et al. (2015) appear to display a quadratic component while the transits times gathered by amateur observers on ETD appear to show a step change in O-C values between epochs 1900 to 2050, see Figure 3.1. Sada and Ramón-Fox (2016) also report a suspected photometric variation in HAT-P-23 host star so nightly monitoring observations were carried out in addition to the transit observations. The second system selected was WASP-52b, another hot Jupiter with an orbital period of 1.75 days around a small $0.79R_{\odot}$ host star producing very deep 2.7% transits (Hébrard et al., 2013). WASP-52 is known to be active with reported results often showing the effects of spot crossing events on measured lightcurves (Mancini et al., 2017).

2.3.2 Observation Scheduling

Slightly different approaches were taken to the planing and scheduling of observation on the OSO and POST observatories. This was to account for the UK location of the POST observatory which, being weather limited, only allowed observations on a few nights per month. For POST the online ephemeris provided as part of the Exoplanet Transit Database (ETD) [6] was consulted for the visibility of a transit of any of the target systems when weather permitted. Targets above the local horizon for their entire transit duration were observed whenever possible. The observing conditions for PIRATE and COAST are far more predictable, with an estimated 280 clear nights per year at Mt. Teide observatory, allowing observations to be scheduled far in advance using the OpenScience Observatories online Scheduler. The OSO schedulers offers two modes for scheduling of observations, timed requests that need to occur at specific dates/times and filler requests which are undertaken anytime the target is visible and the scheduler determines time is available to make the observations with timed requests always having a higher priority than filler requests. The queuing of the scheduled targets is set by a combination of factors, including how long a request has already been in the queue and when the target is visible, as well as a user-set job priority (which in turn is constrained by the user's access rights). To create the observing schedules a long duration ephemeris was downloaded from an on-line ephemeris calculator[7] and converted to a text file of the correct format for use in the OSO scheduler. The suitability of all transit targets was checked using the object visibility tool provided by Isaac Newton Group of Telescopes.[8] The finalised text file includes the target co-ordinates, observation start and end times as well as exposure, filter and CCD binning parameters.

Scheduling of host star monitoring observations were made as filler requests specifying a number of exposures per image set and number of images sets per night that the system would attempt to schedule. This was generally 6 exposures per image set and one or two image sets per night. A minimum altitude for observation could also be specified and was generally set at 40° depending on the target. Due to the weather limitations and need to operate POST in attended mode, monitoring observation were only carried out with PIRATE.

2.4 Transit Observations

Prior to the Summer of 2018 all observations were made with OSO telescopes and POST in 2×2 on-chip inning mode to improve sensitivity, reduce exposure duration, file size and download times. After 21st July 2018 observations were switched to unbinned mode which

[6] http://var2.astro.cz/ETD/predictions.php

[7] http://astroutils.astronomy.ohio-state.edu/exofast/

[8] http://catserver.ing.iac.es/

also required a commensurate increase in exposure times to maintain signal to noise ratio but was found to offer improved photometric precision with significantly reduced scatter in the photometry, discussed further in Chapter 5.

Exposure times were calculated to ensure the ADU counts remained within the CCD linear response region between 10,000 and 44,000 ADU's. The lower limit was chosen to ensure sufficient counts were recorded while the upper limit was determined from the response graphs of the CCD's. Figure 2.2 shows the response plots for PIRATE in 1×1 and 2×2 binning mode which were obtained using star measurements from the same Landolt standard star field as no stable flat field light source is available at the observatory. The upper limit to the linear response region was set at a the value of 44,000 ADU below which the response of the CCD remains linear. The plots in Figure 2.2 show the linear region is defined is consistent between 1×1 and 2×2 on chip binning. The plots in Figure 2.2 clearly show less scatter about the linear response using the unbinned (1×1) CCD mode compared with the 2×2 binned mode. The RMS scatter in ADU within the linear region is 2649 for the 2×2 binning and 1434 for the 1×1 binning. his may be contributing factor to the improvement seen in the photometric precision after moving from 2×2 to 1×1 on-chip binning. However due to needing to use star fields to obtain this data it may be a systematic effect arising from changing conditions or different airmass at the time the data was obtained. The values used the define the linearity region are conservative, the increase in scatter seen for 2×2 observation would warrant further investigation.

De-focusing of the telescope has been shown to improve the photometric precision achievable as the flat fielding errors decrease according to the square-root of the number of pixels in the stellar point spread function PSF; (Southworth et al., 2009a). The technique also allows very bright stars to be observed which would otherwise saturate the CCD if focused. Spreading the starlight over a larger area however has a significant impact on the exposure duration required to achieve the same SNR. For example increasing the FWHM from $3''$ to $10''$ spreads a given stars flux over 11 times the area on the CCD, requiring an 11 times increase in exposure duration. For 0.4 meter class telescopes typical exposure durations for the targets observed in this project when focused range from $\sim$0.5 to 3 minutes. The increase in exposure time to compensate for de-focusing may not allow a transit lightcurve to be sufficiently sampled. For stars where focused observations require 30 second exposures de-focusing to $6''$ requires just a four fold increase in exposure time to 2 minutes. When employing telescope de-focusing great care has to be taken to avoid overlapping stellar PSFs as this will result in contamination of the photometric aperture leading to errant transit depth determination. Scheduled observations with PIRATE and COAST do not currently support de-focusing (though this can be readily achieved with POST) so an alternative approach to

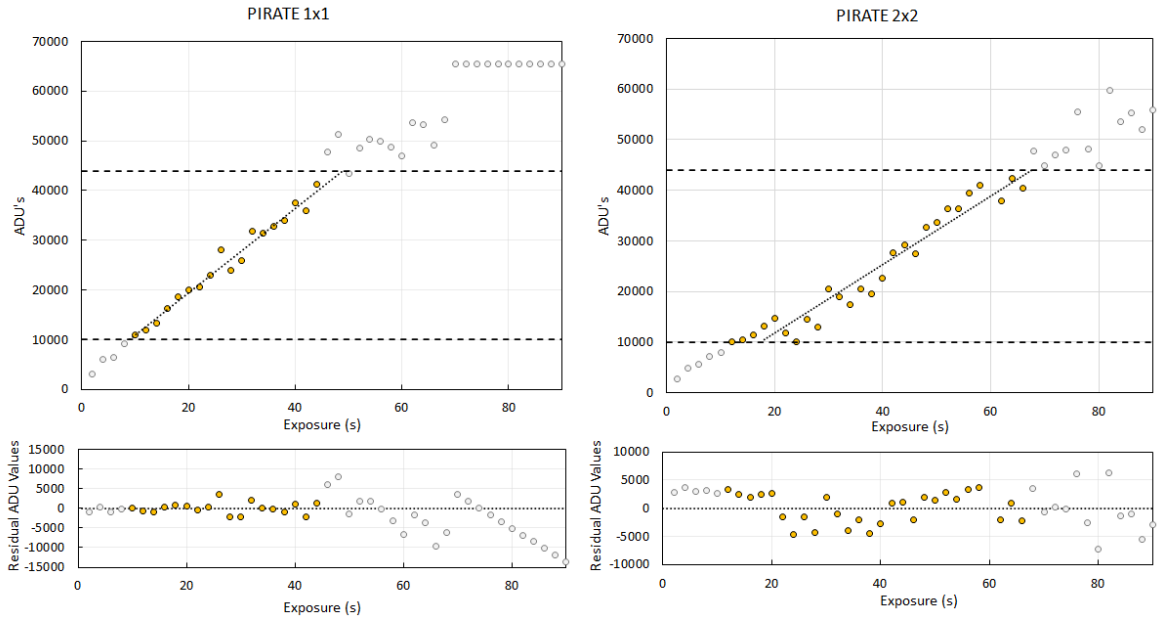

Figure 2.2: Linearity response regions for PIRATE in unbinned (1×1) mode, left, and 2×2 binned mode, right. The horizontal dashed lines indicate the upper and lower bounds used to define the region where the CCD responds linearly to increasing flux. Image exposure times were selected to maintain the ADU count within the linear region. The lower plots show the residual ADU count values after subtraction of the best linear fit to the values in the defined linear response region of the CCD. Uncertainties are smaller than the plot symbols.

de-focusing explored in this thesis (see Chapter 5) is oversampling of the stellar PSF.

Niquist sampling theorem requires that the stellar FWHM is covered by at least 2 CCD pixels[9]. Seeing conditions at Observatorio del Teide are typically of the order of $1''$[10], more often typical FWHM achieved is $2''$ for PIRATE and COAST, likely due to imperfect automated focus or possibly to different seeing conditions at the location of the telescopes being slightly lower than those of the seeing monitors. This requires a plate scale of $\sim 1''$ per pixel while for POST with typical seeing of $3'' - 4''$ this requires $\sim 1.5'' - 2''$ per pixel. With plate scales of $0.63''$, $0.64''$ and $0.52''$ per pixel for COAST, PIRATE and POST respectively, 2x2 on-chip CCD binning for the OSO telescopes with their superior seeing conditions falls slightly short of the Niquist sampling criteria while POST slightly exceeds it. Oversampling the stellar PSF spreads the flux over a greater number of pixels, generating some of the benefits of de-focusing, avoids flux overlap, maintains reasonable exposure times and allows on-axis guiding to be employed on POST.

In order to allow the observations from multiple telescopes to be analysed together all observations were filtered. The Johnson B filter was used for some observations, mainly where both COAST and PIRATE were scheduled to observe the same transit to allow two colour data to be gathered. The Cousins Rc filter was used for the majority of transit observations (broadband Red in earlier observations). A red filter such as the Rc offers a number of benefits including;

- Reducing effects of atmospheric scintillation.

- Of 335 stars listed on the NASA Exoplanet Database as discovered using the transit method with a recorded host star spectral type (accessed 6th Oct 2021), 76% are G,K and M stars with spectral energy distributions that peak in the red. Observing in the red bandpass will collect more photons per second than for shorter wavelength bandpass filters allowing a theoretically higher SNR to be achieved.

- Commercial CCD cameras tend to have a higher quantum efficiency in the red part of the spectrum minimising the impact of flux lost due to the filter transmission characteristics.

- Limb darkening effects are minimised for transits observed at longer wavelengths thus the lightcurves have more sharply defined transition points (E.g. Knutson et al., 2007, Fig. 2). This improves the transit model fit providing increased transit timing precision.

[9] http://www.vikdhillon.staff.shef.ac.uk/teaching/phy217/instruments/phy217_inst_sampling.html
[10] https://www.iac.es/en/observatorios-de-canarias/sky-quality/sky-quality-in-real-time

2.5 Data Reduction

Data reduction is a vital step to correct individual images for the impact on the incoming flux introduced by the optical system and the characteristics of the CCD. Prior to data reduction being carried out all frames are plate solved in AstroImageJ using a link to the Astrometry.net web portal[11] (Lang et al., 2010) and WCS results are added for the individual frames FITS headers. There are three basic types of calibration frame required:

- Bias frames are obtained with a zero duration exposure setting while the CCD shutter is closed. This does not allow any thermal noise to accumulate thus a bias frame is a map of the read out noise from the CCD for each pixel and of the noise accumulated from reading out the CCD, including from the camera electronics and data transfer to the control PC. All bias frames are taken at the same CCD temperature used for the science frames.

- Dark frames are exposures taken with the shutter closed to provide a map of the thermal noise of the CCD at the same temperature as the science frames. For the POST telescope dark frames of the same duration as the science frames were obtained. PIRATE and COAST use a standard 60 second dark frame which is scaled to the science frame exposure duration in AstroImageJ. All data obtained for this thesis was reduced in the standard fashion using dark frames however subsequent testing with PIRATE has shown that, operating at -30°C, insufficient thermal current builds up in 60 seconds resulting in total thermal noise significantly less than the read noise (Jackson et al., 2021). A single PIRATE lightcurve of WASP-12b was analysed both with and without dark frames, the resulting differences in flux measurement were of the order of ten times smaller than the photometric measurement uncertainty, showing either approach would be valid for lightcurves obtained with PIRATE.

- Flat field frames are short exposure frames taken of a uniform light source through the same filter and with the same CCD temperature as the science frames. A flat field provides a map of the effects of the optical path on the data frames such as dust on the optical surfaces or vignetting in the optical system. The flat field also maps any defects in the CCD including pixel to pixel variations in the CCD response.

In the POST observatory the flat fields are obtained using a variable brightness lightbox located immediately in front of the optical tube in the telescopes parked position. The ability to vary the brightness of the lightbox ensures an exposure time of 5-12 seconds for different filter and pixel binning combinations can be used. This range of exposure durations for the

[11] https://nova.astrometry.net/

flat field frames ensures no shutter artefacts remain in the images and at least 27 frames can be obtained with an ADU count of two thirds of the CCD full well count in a reasonable time. With PIRATE and COAST dusk and dawn sky flats are obtained each evening and morning in a sequence controlled by ABOT. This allows a small number of flat field frames to be obtained through each filter each night and therefore frames from multiple nights are used after visually checking for consistency between frames from different nights. The sky flats often contain stars especially as the exposures increase while the sky is getting darker so the telescope pointing is adjusted slightly (dithered) between each exposure so any star images fall on different pixels in each flat field frame.

Data reduction for all observations was carried out using the Data Processing (DP) module within AstroImageJ. DP median combines the individual frames from each group of bias, dark and flat field frames into individual master calibration frames before applying to the science frames. Using a median combine method minimises the impact of any image artifacts such as stars in the flat field frames. The master dark is bias corrected by subtracting the master bias frame. The flat field master is bias and dark corrected by subtracting the bias and exposure duration corrected dark master frames. The final step is to reduce the science frames by subtracting the master bias and dark frames and dividing by the master flat field frame to produce a calibrated science frame. The DP module also allows for modified time stamps to be created and written to the FITS header for each science frame. Based on the observatory location and target co-ordinates the UTC stamp recording the exposure start time in the FITS header is converted to dynamic barycentric, $\mathrm{BJD_{TDB}}$ time and half the exposure time is added to record the frame mid exposure time which is recorded in the FITS header.

2.6 Transit Lightcurve Photometry

AstroImageJ has been specifically created for photometry of transiting exoplanets and includes routines for simultaneous photometry and transit model fitting (Collins et al., 2017b). Below I describe the process used to produce transit lightcurves which follows from the completion of data reduction described in Section 2.5.

Ensemble photometry is used to combine multiple comparison stars, minimising any systematic noise arising from any individual comparison star. For the ensemble photometry up to 24 comparison stars are selected from across the entire field (avoiding stars close to the edges of the frames) with the same sized apertures as the target star. Checks are carried out to ensure that none of the selected comparison stars are known variable stars and that all have ADU counts below the set non-linearity limit. In this approach the most suitable comparison

stars are selected independently for each transit data set, as such the ensemble photometry is optimised for each data set. It was not always practical to use the same comparison stars in the ensemble for every transit data set from a given target due to the differing fields of view between the telescopes used, changes in the FWHM resulting from focus changes between nights and differing on-chip binning and filters used.

The target star is selected and the first photometry aperture applied with an initial aperture radius set to 1.7×FWHM of the target star in the first frame. The inner radius of the sky-background annulus is set to 1.9×FWHM and the outer radius to 2.55×FWHM. These radii provide equal numbers of pixels in the aperture and sky-background annulus which are later refined during the photometry optimisation process (Section 2.6.1) and detrended (Section 2.6.1.1) to minimise photometric scatter. Prior to 7$^{\text{th}}$ June 2019 AIJ counted only whole pixels inside the star aperture and the sky annulus, release 3.3.0 after this date allows exact partial pixel counting, improving photometric precision for smaller apertures.

AIJ calculates the target star flux relative to the sum of the comparison star fluxes, both corrected for the sky background. The use of a large number of comparison stars from across the entire field of view averages out variations due to second order effects arising from colour changes as the airmass changes during the observations.

2.6.1 Photometry Optimisation

Optimising the photometry is an iterative process of modifying the ensemble of comparison stars and photometric apertures to achieve the minimum possible scatter in the resulting residuals to a model of the transit. First the model parameters are defined in AIJ using values from the literature and quadratic limb darkening coefficients for the filter used calculated using an on-line tool [12] (Eastman et al., 2013) which interpolates the limb darkening tables from Claret and Bloemen (2011). AIJ uses a simple stellar model that assumes the host star is on the Zero-Age Main Sequence (ZAMS) and as such does not allow the stellar parameters such as spectral type, effective temperature, mass and radius to be varied independently. For transit photometry the stellar radius is more important than spectral type or T_{eff} in determining the lightcurve parameters so this was set based on the best published value.

Once the ensemble photometry has been calculated for the target star from every frame in the time series data, AIJ fits a transit model based on the formalisation of Mandel and Agol (2002) to the resulting lightcurve. The best fit model is found through minimising the χ^2 of the model residuals. AIJ reports the quality of the model fit to the data providing the residual RMS value, χ^2_ν and the Bayesian Information Criterion (BIC) defined as

[12] http://astroutils.astronomy.ohio-state.edu/exofast/limbdark.shtml

$$\mathrm{BIC} = \chi^2 + \mathrm{p} \times \ln(\mathrm{n}) \tag{2.1}$$

Here p is the number of fitted parameters and n is the number of data points in the lightcurve (Collins et al., 2017b). This process is then repeated for a range of different star aperture and sky annulus radii to determine the values that produce the smallest residual RMS and BIC values. AIJ also provides the option to vary the star aperture based on the target star FWHM from each frame in the time series data which can produce superior results where seeing conditions are changeable through the night or where the focus drifts due to external temperature changes. In this mode AIJ applies a user defined multiplier to the measured FWHM value in each frame to calculate the star aperture radius. Values of the FWHM multiplier are stepped through to find the values that result in the smallest RMS residuals and BIC value. Care is taken to ensure the star aperture radius does not exceed the inner radius of the background annulus.

In both fixed and variable aperture modes the radius of background annulus is selected such that it contains at least the same number of pixels as the star aperture. This will sometimes result in background stars, or hot pixels remaining after reduction, being included in the background annulus. To minimise the effect on the photometry AIJ carries out an iterative 2σ cleaning of the sky background (see Section 5.2.3 for an example). For this reason the sky annuli were set to contain a larger number of pixels than the star aperture to allow for pixels to be removed by this process.

Although AIJ can remove hot pixels from the sky background annulus with the interative 2σ cleaning, this is not possible for the star aperture. This can lead to circumstances where the target star or one or more comparison stars can be affected by transient hot pixels, not corrected for by the data reductions process. Therefore in the final step the lightcurve was visually checked for outlying data points and these were removed from the data where the images revealed artefacts affecting the photometry such as cosmic ray hits or cloud obscuration.

2.6.1.1 Lightcurve Detrending

The above optimisation process for the photometry apertures is undertaken with detrending applied to the lightcurve for airmass and, where required, pier flip offset. The detrending is calculated by including a χ^2 contribution for each detrend parameter in the lightcurve fit following Equation 5 in Collins et al. (2017b). Linear and second order polynomial detrending options are available, the latter being suitable for airmass detrending which uses the airmass values added to the FITS header during the data reduction process. The time of the pier flip is manually set within AIJ before calculating the ensemble photometry. To ensure any

uncertainties associated with the detrending process are properly accounted for in the transit model fitting the final lightcurve is recorded without the detrending applied and the detrend values appended to the AIJ output file to be incorporated in the transit model fitting, see Section 2.7.

2.6.2 Photometric Uncertainties

Correct calculation of the photometric uncertainty is evidently important and directly impacts the model fitting via a weighting of $1/\sigma$ in the χ^2 calculation for each data point, placing a greater emphasis on low noise data in the model fitting process. AIJ employs the standard CCD equation (equation B1 in Collins et al. (2017b)) to calculate the uncertainty on each aperture photometry measurement where the noise N in ADU is given by

$$N = \frac{\sqrt{GF_* + n_{pix}(1 + \frac{n_{pix}}{n_b})(GF_S + F_D + F_R^2 + G^2\sigma_f^2)}}{G} \tag{2.2}$$

Here G is the CCD gain in e/ADU, F_* is the net count in ADU (background subtracted) in the aperture, n_{pix} is the number of pixels in the aperture and n_b is the number of pixels in the background annulus, F_S is the sky background count per pixel in ADU, F_D is the dark count in electrons per pixel, F_R is the read noise in electrons per pixel and $\mathrm{G}\sigma_\mathrm{f}$ is the digitisation noise taken as $0.289 \times \mathrm{G}$. In May 2019 support for exact accounting of partial pixels within an aperture was added in AstroImageJ. Previous to this the pixel accounting method included the contribution of a full pixel if its center fell within the aperture radius, otherwise it was not counted at all. The partial pixel inclusion improves photometric precision for small radius apertures. Calculating the photometric noise correctly requires the parameters for the CCD, these were taken from the manufactures information, Table 2.1. The dark current figures given in Table 2.1 were multiplied by four where 2x2 on-chip binning was employed. In differential ensemble photometry, employed for all transit photometry, AIJ calculates the noise for the target aperture and multiple comparison stars individually and then combines the noise for all comparison stars in quadrature. The uncertainty on the final relative flux measurement for each data point is then calculated as

$$\sigma_\mathrm{relflux} = \frac{\mathrm{F_T}}{\mathrm{F_E}}\sqrt{\frac{\mathrm{N_T^2}}{\mathrm{F_T^2}} + \frac{\mathrm{N_E^2}}{\mathrm{F_E^2}}} \tag{2.3}$$

which is equation B3 in Collins et al. (2017b). Here F is the integrated counts, N is the noise and the subscripts T and E indicate the target and ensemble comparison respectively.

Table 2.1: CCD camera parameters used in AIJ setting for noise calculations. Dark current was interpolated from published temperature values. Read values for PIRATE and COAST are based on the set 8MHz read out rate. The saturation limits were set as shown in Figure 2.2

Parameter	PIRATE	COAST	POST
CCD	PL16803	PL09000	KAF-3200ME
Gain (e^-/ADU)	1.39	1.53	1.34
Read Noise (e^-)	14.0	15.4	14.18
Dark Current (e^-s^{-1})	0.01 @ -30℃	0.02 @ -30℃	0.03 @ -20℃
Full Well (e^-)	89761	98536	87000
Linearity Region (ADU)	10000 to 44000	10000 to 44000	10000 to 44000

2.6.3 Scintillation Noise

There are a number of noise sources that AIJ does not take into consideration when calculating the total photometric noise, the most significant of which is atmospheric scintillation. Atmospheric scintillation is the intensity variation caused when the starlight passes through the turbulent atmosphere which manifests itself as the 'twinkling' of the stars. Scintillation is a strong source of noise for small aperture telescopes on the ground where the aperture of the telescope is of the same scale as the turbulence cells in the atmosphere, typically a few tens of centimeters (Osborn et al., 2015), similar to the aperture of the telescopes used here. For a given telescope aperture scintillation is strongly dependent on airmass and inversely on exposure time so can be minimised by observing targets at low airmass from high altitude locations with longer exposures. Young (1967) proposed an approximate calculation of scintillation noise, a version of which is shown as Equation B4 in Collins et al. (2017b). Kornilov et al. (2012) showed however that this is an underestimate of the scintillation noise by a mean value of 1.5 and present correction values for a number of observatory locations. Osborn et al. (2015) present a revised version of Young's original approximation incorporating this correction:

$$\sigma^2_{\text{scint}} = 10 \times 10^{-6} D^{-\frac{4}{3}} C_Y^2 t^{-1} (cos\gamma)^{-3} exp(-2h/H) \tag{2.4}$$

Here D is the telescope diameter in meters, t is the exposure time in seconds, γ is the zenith angle, h is the observatory altitude and H is the typical height of the turbulent layer causing scintillation, generally assumed to be 8000m. C_Y is the correction factor applied to Young's original equation which Osborn et al. (2015) found was 1.3 for La Palma, used here for the Observatorio del Teide observatory and a mean of 1.5, used for POST. Figure

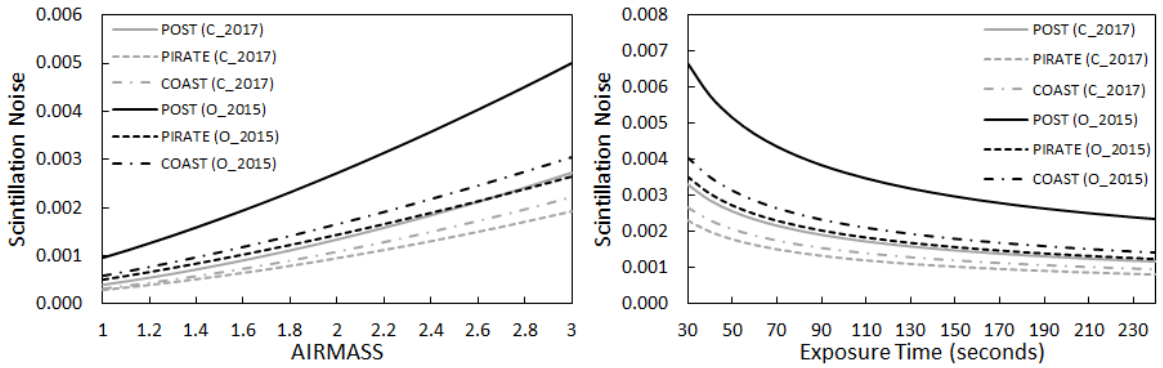

Figure 2.3: Scintillation noise calculated using equation B4 Collins et al. (2017b) (grey lines) and equation 7 of Osborn et al. (2015) (black lines). Left, how changing airmass affects scintillation noise for all three telescopes with an exposure time of 180 seconds and on the right how exposure time affects the scintillation noise with a fixed airmass of 2. The modified Yong approximation shows a stronger effects than the version from Collins et al. (2017b). With a low altitude, POST is more strongly affected than the OSO telescopes.

2.3 compares the scintillation noise calculated using Equation B4 from Collins et al. (2017b) and the modified form given Equation 2.4 for various airmass values and exposure durations. Figure 2.4 shows the effect of adding the scintillation noise as calculated using Equation 2.4 in quadrature with the AIJ calculated photometric noise on two observation of WASP-52b made with PIRATE and with POST. As expected the impact on POST at an altitude of 20 meters above sea level is significantly greater than for PIRATE at 2390 meters altitude. Both observations were made through Rc filters with a 120 second exposure time.

Although AIJ provides a transit model it does not provide uncertainties for the values determined so this model is used solely in optimising the photometric extraction. The completed lightcurves are exported for transit modelling in another specialised and superior transit analysis package.

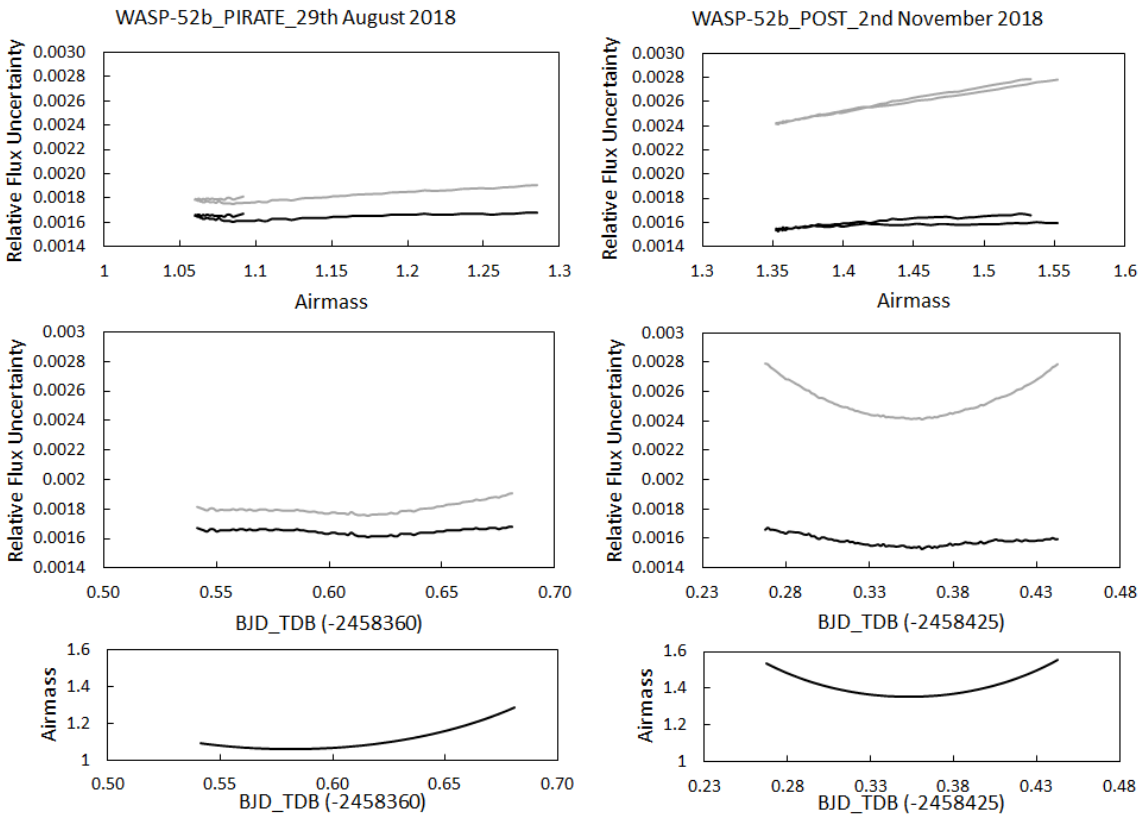

Figure 2.4: Two examples of adding scintillation noise calculated using Equation 2.4 for observations of the same target obtained on different nights with PIRATE (left) and POST (right). Black lines show the values before scintillation noise is added and grey are after the scintillation noise is included. The top row shows how noise varies with airmass, the middle is the noise variation over time and bottom is the airmass of the observations. Relative Flux Uncertainty is the measurement uncertainty as calculated in AIJ(Collins et al., 2017b, Eq. B3). The Y-axis scales have been kept equal to highlight the impact of adding scintillation in quadrature with the standard photometric noise calculated by AIJ. The effect of adding scintillation noise is minimal for the low airmass PIRATE observation but very more significant for the higher airmass POST observation. The dual lines in the top row of plots occurs because the target passed through the Meridian so has two equal airmass values but with slightly different photometric noise.

2.7 Transit model fitting

2.7.1 ExofastV2

All transit analysis was carried out using ExofastV2, a publicly available general exoplanet fitting code released in the Summer 2019 (Eastman et al., 2019). ExofastV2 is written in IDL but is available to run with or without an IDL licence on a Windows PC, with a licence ExofastV2 supports multithreading substantially reducing calculation time. ExofastV2 offers a number of features making it well suited to anayslying the transit lightcurves obtained for this thesis:

- Previous versions of the code have been widely used in peer reviewed publications (E.g. Collins et al., 2017a; Basturk et al., 2019; Zellem et al., 2020).
- Support for simultaneous fitting of multiple transit and radial velocity (RV) data sets from different instruments and with different filters.
- It allows transit timing, depth and duration variations to be modelled.
- Uses a differential evolution Markov chain Monte Carlo DE-MCMC optimisation.
- Provides multiple options for modelling stellar parameters including MESA Isochrones and Stellar Tracks (MIST), Yonsi-Yale isochrone fitting and Torres relationship (see Eastman et al., 2019, and references therein).
- Fits broadband stellar Spectral Energy Distribution (SED) with prior constraints from the Gaia DR2 catalogue (Brown and Gaia Collaboration., 2018) to significantly improve stellar radius determination.
- Allows multi-parameter lightcurve detrending simultaneously with the transit fit to ensure uncertainties arising from detrending are correctly propagated through the model fit.
- ExofastV2 is well documented and provides diagnostic reports to help ensure correct operation.

The one drawback of using ExofastV2 is the time required for the DE-MCMC to converge in a multi-transit and RV fit can take many days running on a Windows PC with a 2.60GHz CPU, the computing platform available for this work. One reason for this is that without an IDL licence ExofastV2 can only use a single CPU core so is limited by the CPU clock speed.

ExofastV2 requires the preparation of a number of input files before being executed. The methods and sources used to create these files are described below.

2.7.2 Transit Lightcurve files

To allow transit timing, duration and depth variations to be modelled ExofastV2 requires each transit lightcurve to be input as a separate text file allowing the baseline flux and its variance to be calculated for each transit lightcurve. The individual lightcurves were output from AIJ as text files containing a single row for each data-point. The data columns included were the BJD_{TDB} mid-time of the observation, the normalised flux measurement without detrending, the photometric uncertainty (including scintillation noise) and then columns for each of the detrending parameters such as airmass and pier flip as required. The transit date, telescope and filter used for each lightcurve are set for ExofastV2 within the lightcurve file name.

2.7.3 RV files

No new radial velocity measurements were obtained as part of this work so catalogue radial velocity data was used with RV data sets obtained from the literature, the NASA Exoplanet Archive [13] or from VizieR[14]. The files contained the date of observation, radial velocity and uncertainty in ms^{-1}. Dates were converted to BJD_{TDB} as required using the on-line date conversion tool provided by the author of ExofastV2[15] . Care was taken to ensure that measurements from different instruments or those widely separated in time were provided as separate input files to allow individual velocity zero points and jitter values to be calculated for each. RV data sets containing predominantly measurements at transit mid-time for Rossiter-McLoughlin analysis were not included.

2.7.4 Photometry files

Photometric input files used to build the broadband SED were created for each target host star using a subroutine in Exofast to query trusted photometry catalogues including TYCHO (Høg et al., 2000), ALLWISE (Cutri, 2013) and 2MASS (Skrutskie et al., 2006). Additional photometry in the Johnson B and V bands and SDSS g', r' and i′ bands was obtained from the AAVSO AllSky Photometric Survey (APASS) Data Release 10[16] (Henden, 2019). It is important that the broadband photometry is not blended with flux from close by stars as this will affect the brightness of the the star leading to a larger radius determination. The literature was checked for reports of close companions to any the systems studied such as lucky imaging studies (E.g. Bergfors et al., 2013). Gaia EDR3 multi-peak flag, a sign a star

[13] https://exoplanetarchive.ipac.caltech.edu/index.html
[14] https://vizier.u-strasbg.fr/viz-bin/VizieR
[15] http://astroutils.astronomy.ohio-state.edu/time/
[16] https://www.aavso.org/apass

Table 2.2: Comparison of the Gaia DR2 parallax results used in the analyses in Chapters 3 and 4 with the Gaia EDR3 values released following completion of the exoplanet system analyses.

	WASP-12b	WASP-52b	HAT-P-23b
DR2 parallax	2.3942414 ± 0.0463423	5.69176 ± 0.043297	2.71288866 ± 0.035138
EDR3 parallax	2.421293 ± 0.0166025	5.7261704 ± 0.013378	2.7358366 ± 0.010759
Change	+1.1%	+0.6%	+0.8%

may be binary, was additionally checked and found to be zero for HAT-P-23 and WASP-52 and 29 for WASP-12, as expected. Deblending of the photometry was required for WASP-12 as described in Chapter 4. The shape of the SED is set by the stellar effective temperature and V band extinction while the normalisation is set by the distance to the star. Therefore when coupled with accurate priors for stellar distance and V band extinction (A_V) the SED model can provide tight constraints on the stellar radius with less dependency being placed on stellar models (Eastman et al., 2019). Accurate distance measurements are now available following the Gaia Data Release 2 (Brown and Gaia Collaboration., 2018) allowing priors on the system parallax to be included in the model prior file. ExofastV2 uses a bolometric corrections grid supplied by the MIST project to fit the SED.

Following completion of the analysis of the exoplanet systems WASP-52b, HAT-P-23b and WASP-12b in Chapters three and four, Gaia Early data Release 3 (EDR3) became available (Gaia_Collaboration, 2021). Table 2.2 compares the updated parallax values from EDR3 with those used in the completed analysis. The changes are small and the analysis has not been repeated though it is noted that future analysis would benefit from using the new EDR3 values, particularly the reduced uncertainty.

2.7.5 Model Priors file

The priors file sets the starting point for the model fit. The starting epoch and period were taken from the literature with the epoch being propagated forwards to the epoch of the transit data sets. Other priors required to start the model fit were taken from the literature including stellar effective temperature and metalicity, orbital inclination and separation ratio. Stellar limb darkening priors were obtained through interpolation of the quadratic limb darkening tables from Claret and Bloemen (2011), obtained from an on-line application created by the author of ExofastV2[17]. Priors for the parallax were obtained from Gaia DR2 (Brown and Gaia Collaboration., 2018) and following the findings of Stassun and Torres (2018), 0.082mas

[17]http://astroutils.astronomy.ohio-state.edu/exofast/limbdark.shtml

is added to the reported parallax and 0.033 mas is added in quadrature to the DR2 reported uncertainty. An upper limit for the V band extinction parameter (A_V) for each system was obtained from the updated dust maps from Schlafly and Finkbeiner (2011) [18] and multiplied by 3.1 to convert to the V band extinction used in ExofastV2 before being applied as a prior to the SED fit. Prior widths were either set as Gaussian values where the prior value is taken as the mean of the Gaussian distribution, as maximum-minimum limits (for dust extinction) or excluded. For Gaussian prior widths ExofastV2 applies a penalty equal to $((\text{value} - \text{prior})/\text{uncertainty})^2$ to the χ^2 at each step of the model fit. Where minimum or maximum limits are set any models exceeding these limits are dropped and if no width is set the prior is used as starting point with no penalty applied for diverging from this value. No transit model parameters were fixed at their starting values (prior width = 0). Poor or uncertain starting priors can result in very long convergence times or convergence failure so initial model fits of a few thousand steps were run and the output from those used as the input prior file for subsequent model runs. This iterative process of refining the prior values enabled model fits with large numbers of steps to converge more quickly, reducing overall run time. The probability function diagnostic plots were checked after each run to ensure consistency.

2.7.6 Arguments files

The arguments file contains the run parameters for the model. For all systems analysed stellar parameter determination was achieved through the combination of the MIST evolutionary models with SED fitting. The arguments file allow flags to be set for a number of other model parameters such as fixing the orbit as circular and including outputs for timing, duration and depth variations. The number of steps for the DE-MCMC chains is set and is a free value, care was taken to ensure the number of steps was sufficient to ensure the chains were fully mixed while managing the model run duration and memory usage which are directly proportional to the number of steps. Because adjacent steps are highly correlated ExofastV2 provides a parameter called NTHIN which allows the code to discard a user configurable number of adjacent steps, significantly reducing the memory required for a model fit while allowing the same parameter space to be explored. Thus a 10,000 step, NTHIN = 6 model run is equivalent to a 60,000 step, NTHIN=1 model run but with a significant reduction in memory required.

[18] https://irsa.ipac.caltech.edu/applications/DUST/

2.8 Monitoring Observations

Snap shot monitoring observations were obtained using PIRATE scheduled to take six frames per group of a given target using the B or Rc filter when the target was higher than 40 degrees altitude. The number of frames obtained each night varied due to weather and telescope commitments. The analysis of the monitoring data photometry was undertaken using a template created in AIJ incorporating stars from the UCAC4 catalogue with known B, V and r′ filter magnitudes. A star with r′ magnitude and B-V colour index close to the target star was selected as a check star (after checking for known variability). The same template was used for all data of the same target. AIJ does not take into account catalogue magnitude uncertainties so I report the uncertainties for the calculated magnitudes based on the standard error in the measurements of the check star. Observations were obtained in both 2x2 and 1x1 on-chip binning mode and was therefore analysed separately before being combined into the overall monitoring data set.

Periodicity analysis for each target and check star was undertaken using a Lomb-Scargle period analysis as implemented in the AstroPy Python 3 library[19].

[19]https://docs.astropy.org/en/stable/timeseries/lombscargle.html

Chapter 3

WASP-52b and HAT-P-23b

3.1 Introduction

As discussed in Chapter 1, timing observations of transiting Exoplanets can provide invaluable insight into exoplanet system properties including the existence of companion bodies (E.g. Sokov et al., 2018) and orbital period evolution (Maciejewski et al., 2016; Patra et al., 2017; Bouma et al., 2019; Chontos et al., 2019). To achieve reliable transit timing results accurate timing of the individual photometric observations is vital.

In the Summer of 2018 a number of upgrades were undertaken at the PIRATE and COAST telescopes as detailed in Chapter 2 The main upgrade at this time was the installation of GPS PCI time synchronisation cards in both observatory control computers to provide external shutter triggering with milli-second control. Two short period hot Jupiter systems (HAT-P-23b and WASP-52b) were selected for observation over the time of the second upgrade, their short periods (1.21 and 1.75 days) allowing multiple transits to be observed. One aim of these observations was to quantify the improvement in the transiting timing measurement accuracy as a result of the GPS timing control. Additional observations were made using POST which remained unchanged over the same period.

3.1.1 HAT-P-23b

HAT-P-23b is a short period (1.21d) hot Jupiter discovered in 2011 by the HATNet transit survey orbiting a V=12.43 magnitude G0 host star (Bakos et al., 2011). The authors found HAT-P-23b is an inflated hot Jupiter with a mass of $2M_J$ and a radius of $1.37R_J$, almost 10% greater than the maximum theoretical radius for a planet of its mass (Fortney et al., 2007). In addition they found HAT-P-23b has a marginally significant orbital eccentricity of 0.106 ± 0.044. Ciceri et al. (2015) subsequently found considerably smaller stellar and planetary radii (Figure 3.4), which we can speculate results from adopting a mass-radius

relationship based on a younger age for HAT-P-23 and using a fixed circular orbit in their transit modelling. Measurement of the Rossiter-McLaughlin effect has shown HAT-P-23b is in an aligned prograde orbit with a projected angle between the orbital plane and the stellar equatorial plane of 15°±22°(Moutou et al., 2011). Previous studies have taken different approaches to the suspected eccentricity with some authors leaving eccentricity as a free parameter, e.g. Bakos et al. (2011); Sada and Ramón-Fox (2016), while others have fixed the orbit as circular in their analyses e.g. Ciceri et al. (2015); Maciejewski et al. (2018). HAT-P-23b has a similar orbital period to that of WASP-12b which has been shown to exhibit a decreasing orbit (Maciejewski et al., 2016; Patra et al., 2017; Maciejewski et al., 2018; Yee et al., 2019) hence HAT-P-23b could be expected to exhibit a similar decreasing orbital period which may require transit measurements over decades to detect. Ciceri et al. (2015) presented O-C results (their Figure 6) that appear to show a quadratic deviation indicative of period change, but this was not commented upon (see section 3.3.2). The transit timing observations available on the Exoplanet Transit Database[1] (ETD) show a change in reported O-C values over the period between transit epochs 1900 and 2050, Figure 3.1. After HAT-P-23b had been selected and the transit observations obtained, Maciejewski et al. (2018) published results of a further 13 new transits and reanalysis of the previously published transit times looking for evidence of orbital decay. They conclude that the best fit ephemeris is linear and that there is no sign of orbital period change which they attributed to inefficient tidal dissipation in the main sequence host star.

3.1.2 WASP-52b

WASP-52b is an inflated hot Jupiter on a 1.75d circular orbit around a K2V star (Hébrard et al., 2013). The $0.79R_{\odot}$ stellar radius and the inflated $1.27R_{J}$ planet radius results in 3% deep transits. Due to the planets large radius and low mass ($0.45M_{J}$), the difference in transit depth of a single scale height equates to 4.4×10^{-4} (Kirk et al., 2016). This makes WASP-52b an excellent target for transit spectroscopy; such studies reveal that WASP-52b has a cloudy atmosphere with no indication of Rayleigh scattering (Kirk et al., 2016; Louden et al., 2017), in which sodium has been detected (Chen et al., 2017).

WASP-52 is an active star with transit photometry often showing spot crossing events complicating the analysis of transit spectroscopy results. Photometrically determined rotational periods between 13.1 ± 0.4d to 17.79 ± 0.05d have been reported, possibly indicative of differential rotation at changing spot latitudes (Hébrard et al., 2013; Mancini et al., 2017; Louden et al., 2017). Measurements of crossings of the same spot has allowed the sky projected and real orbital obliquities to be determined as 3.8°±8.4°and 20°±50°respectively,

[1] http://var2.astro.cz/ETD/.

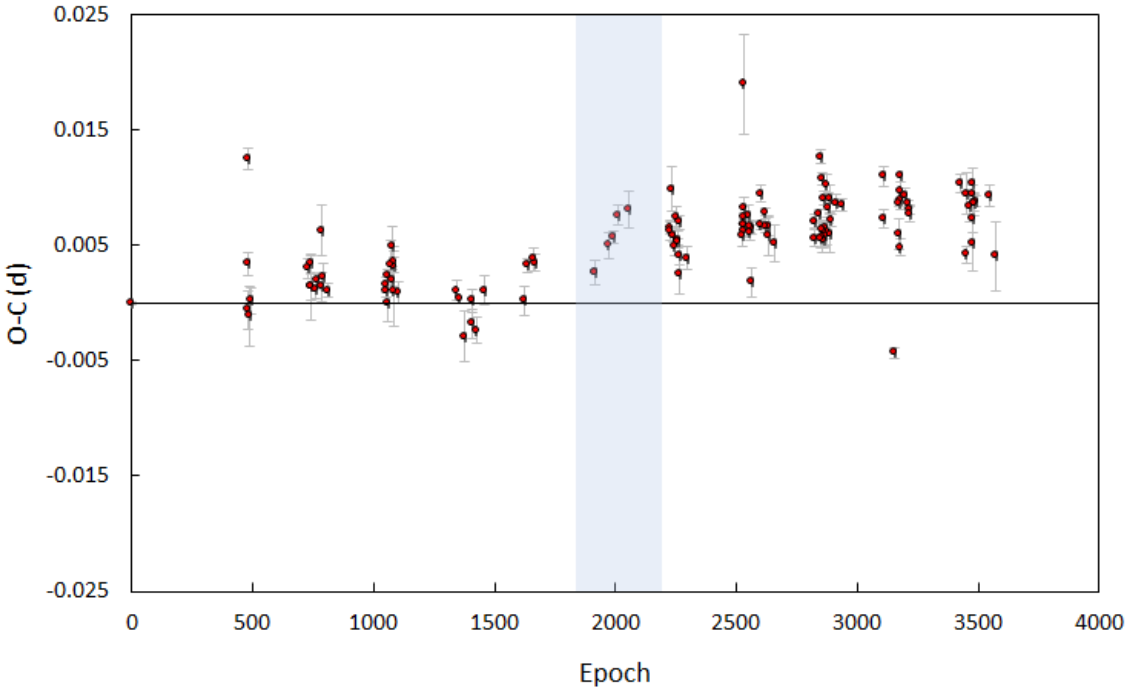

Figure 3.1: Plot of O-C values for HAT-P-23b as recorded on the Exoplanet Transit Database showing the apparent step change in O-C values that occurred between epochs 1900 - 2050.

providing the first measurement of a true orbital obliquity using this method (Mancini et al., 2017).

This chapter is laid out as follows. In section 3.2 I describe the observations, in the section 3.3 I present the results and their analysis. In section 3.4 discusses the results and places them in the context of the published literature. In the final section I briefly summarise the key findings. The published paper included a section discussing the data and performance of small aperture ground-based telescopes which has now been integrated into Chapter 5.

3.2 Methods

3.2.1 Observations

Transit observations of both targets made using PIRATE and COAST were scheduled in advance and obtained in autonomous mode, observations with the POST observatory were made in attended mode with hands-on control of the telescope during each observation. The observations were planned using existing ephemerides and timed to include pre and post transit data where possible. Observations with all telescopes were made with the CCD on-chip binning of 2×2 or 1×1. Exposure times were set to ensure ADU counts remained within the linear response region of the CCD for the target and comparison stars, the same exposure duration was used throughout each individual transit observation. The Cousins Rc filter was

used for all new observations. Three archive observations obtained with the POST telescope were available, one of HAT-P-23b obtained in 2017 using a V filter and two of WASP-52b obtained in 2013 and 2017 using an Rc filter. These archive lightcurves were reanalysed in a way consistent with the new observations. In total the transit observations resulted in 1821 and 695 individual photometric measurements covering 17 and 13 transits of HAT-P-23b and WASP-52b respectively, Table 3.1.

Monitoring observations were obtained of HAT-P-23b using PIRATE scheduled to take up to six 150 second frames per night using the Rc filter with the CCD in 1x1 bin mode when the target was higher than 40 degrees altitude. 218 observations covering 39 nights over a 78 day period were made between 18^{th} August 2018 and 4^{th} November 2018. The number of frames obtained each night varied depending on weather conditions and telescope schedule commitments. Out-of-transit measurements from before and after each transit, where available, were added to the monitoring data to extend the measurement timeline and allow HAT-P-23's magnitude to be measured at the time of each transit recorded with PIRATE.

Dark, bias and sky flat-field calibration frames were obtained for each night of science observation. Due to the limited number of dusk/dawn flat frames obtainable by PIRATE each night frames from multiple nights either side of the observation were combined. For POST a flat field light box is used so an average of 27 flat field frames was obtained on each night of observation. Data reduction was carried out as detailed in Chapter 2.

Table 3.1: Table of observations made. The line between observations 9 and 10 for HAT-P-23b indicates the point at which the GPS upgrade to the PIRATE telescope was undertaken. N_{obs} is the number of observations per transit. Dur is the total duration of the observations in minutes and Exp is the exposure time used in seconds. RMS is the out-of-transit residual RMS scatter in part per thousand. CCD indicates the on-chip binning used. TSNR is the Transit Signal to Noise Ratio (Ioannidis et al., 2016).

Number	Date	Telescope	Dur	Filter	Exp	N_{obs}	Airmass	RMS	CCD	TSNR	Notes
HAT-P-23b											
1	05 October 2017	POST	205	V	150	66	1.27-2.41	2.07	2x2	4.95	
2	20 June 2018	PIRATE	164	Rc	60	158	1.26-1.02	2.04	2x2	6.63	Incomplete ingress coverage.
3	26 June 2018	PIRATE	213	Rc	60	199	1.14-1.02-1.11	2.87	2x2	4.71	
4	30 June 2018	PIRATE	192	Rc	60	178	2.12-1.07	3.29	2x2	4.11	
5	30 June 2018	POST	180	Rc	120	85	1.58-1.21	2.18	2x2	6.19	
6	06 July 2018	PIRATE	216	Rc	60	199	1.33-1.02-1.04	2.73	1x1	4.95	
7	06 July 2018	POST	264	Rc	120	126	1.55-1.21-1.27	2.63	2x2	5.13	
8	12 July 2018	PIRATE	210	Rc	60	196	1.05-1.02-1.25	3.57	2x2	3.78	
9	17 July 2018	POST	200	Rc	120	94	1.55-1.21	2.19	2x2	6.16	
10	03 August 2018	PIRATE	196	Rc	180	63	1.41-1.02	1.49	1x1	9.05	
11	09 August 2018	PIRATE	255	Rc	180	67	1.14-1.02-1.20	0.85	1x1	15.8	Gap in data post egress.
12	26 August 2018	PIRATE	234	Rc	150	92	1.08-1.02-1.24	1.85	1x1	7.3	
13	23 September 2018	PIRATE	195	Rc	180	62	1.06-1.02-1.17	1.06	1x1	12.71	
14	23 September 2018	POST	181	Rc	180	57	1.21-1.49	1.49	2x2	9.08	
15	29 September 2018	PIRATE	156	Rc	180	51	1.02-1.24	1.55	1x1	8.73	Ingress only. No transit mid time.
16	29 September 2018	POST	212	Rc	180	53	1.26-2.38	2.32	2x2	5.82	Gap mid transit.
17	16 October 2018	PIRATE	229	Rc	180	75	1.03-2.12	1.68	1x1	8.02	
WASP-52b											
1	10 November 2013	POST	148	Rc	90	93	1.44 - 1.40	2.06	3x3	12.80	Suspected spot crossing.
2	27 October 2017	POST	214	Rc	180	66	1.4-1.35-1.63	1.60	2x2	16.47	
3	01 August 2018	PIRATE	196	Rc	120	92	1.34-1.06	1.64	1x1	16.13	
4	08 August 2018	PIRATE	197	Rc	180	55	1.25-1.06-1.10	1.80	1x1	14.69	Gap at egress.
5	29 August 2018	PIRATE	201	Rc	120	95	1.09-1.06-1.29	1.62	1x1	16.33	
6	19 September 2018	PIRATE	157	Rc	150	60	1.07-1.58	2.02	1x1	13.10	
7	03 October 2018	PIRATE	139	Rc	150	52	1.19-2.13	2.07	1x1	12.73	
8	05 October 2018	POST	183	Rc	120	77	1.78-1.35	4.02	2x2	6.57	
9	10 October 2018	PIRATE	111	Rc	150	43	1.28-2.15	-	1x1	-	No out of transit coverage.
10	17 October 2018	COAST	133	Rc	240	32	1.21-2.17	1.59	1x1	16.65	Ingress only. No transit mid time.
11	17 October 2018	PIRATE	132	B	240	33	1.21-2.17	2.40	1x1	10.99	Ingress only. No transit mid time.
12	02 November 2018	POST	252	Rc	120	113	1.53-1.35-1.55	2.15	2x2	12.3	
13	07 December 2018	POST	110	Rc	240	25	1.36-1.55	0.90	1x1	29.33	Ingress only. No transit mid time.

Table 3.2: Broadband photometry used in Exofastv2 SED fitting.

Band	HAT-P-23	WASP-52	Catalogue
B(T)	13.362 ± 0.378	-	Tycho
V(T)	12.061 ± 0.195	-	Tycho
B	12.965 ± 0.036	13.116 ± 0.042	APASS R10
V	12.189 ± 0.047	12.231 ± 0.062	APASS R10
gSDSS	12.586 ± 0.043	12.617 ± 0.025	APASS R10
rSDSS	11.969 ± 0.089	11.901 ± 0.095	APASS R10
iSDSS	11.774 ± 0.143	11.698 ± 0.047	APASS R10
J	11.103 ± 0.020	10.588 ± 0.020	2MASS(via UCAC4)
H	10.846 ± 0.020	10.186 ± 0.030	2MASS(via UCAC4)
K	10.791 ± 0.020	10.086 ± 0.030	2MASS(via UCAC4)
WISE1	$10.748^{+0.030}_{-0.023}$	$10.011^{+0.030}_{-0.023}$	AllWISE
WISE2	$10.793^{+0.030}_{-0.020}$	$10.094^{+0.030}_{-0.021}$	AllWISE
WISE3	10.816 ± 0.122	9.983 ± 0.061	AllWISE
Gaia	$12.174^{+0.020}_{-0.001}$	$11.954^{+0.020}_{-0.001}$	Gaia DR2
GaiaBP	$12.518^{+0.020}_{-0.002}$	$12.444^{+0.020}_{-0.004}$	Gaia DR2
GaiaRP	$11.679^{+0.020}_{-0.002}$	$11.331^{+0.020}_{-0.003}$	Gaia DR2

3.2.2 Analysis

Combined transit and radial velocity model fitting was carried out with the most recent version of ExofastV2 (Eastman et al., 2019) using the new transit data and previously published radial velocity (RV) measurements. For HAT-P-23b 13 radial velocity measurements obtained using the HIRES instrument on the Keck telescope (Bakos et al., 2011) were used. For WASP-52b 16 measurements obtained with CORALIE instrument on the ESO Euler telescope and 29 measurements obtained with the SOPHIE instrument on the 1.93m OHP telescope (Hébrard et al., 2013) were used. The RV data from SOPHIE was divided into separate inputs for the High-Efficiency mode (HE1, HE2) and High-Resolution mode (HR) measurements allowing different zero-points to be set for each. The data set obtained in HE mode covering the Rossiter-McLaughlin effect measurements (HE-RM) over a short period during transit was not used in the analysis. Broadband photometry was taken from known trusted catalogues, see Table 3.2. Priors and argument files were created for ExofastV2 input as described in Section 2.7.1.

All transit lightcurves, including those with partial coverage but excluding the 2013 transit of WASP-52b which showed a significant suspected spot crossing event, were included to produce a single global model fit in ExofastV2 for each system. The transit mid-time for each lightcurve was allowed to vary within the global model fit and the transit mid-times were output from ExofastV2 and combined with previously published transit times to calculate a refined ephemeris for each system. Only transits with full coverage of all transition points t_1 to t_4 were used in the ephemeris analysis. All transit lightcurves with their best fit Exofast models can be found in Figure 3.2 for HAT-P-23b and in Figure 3.3 for WASP-52b.

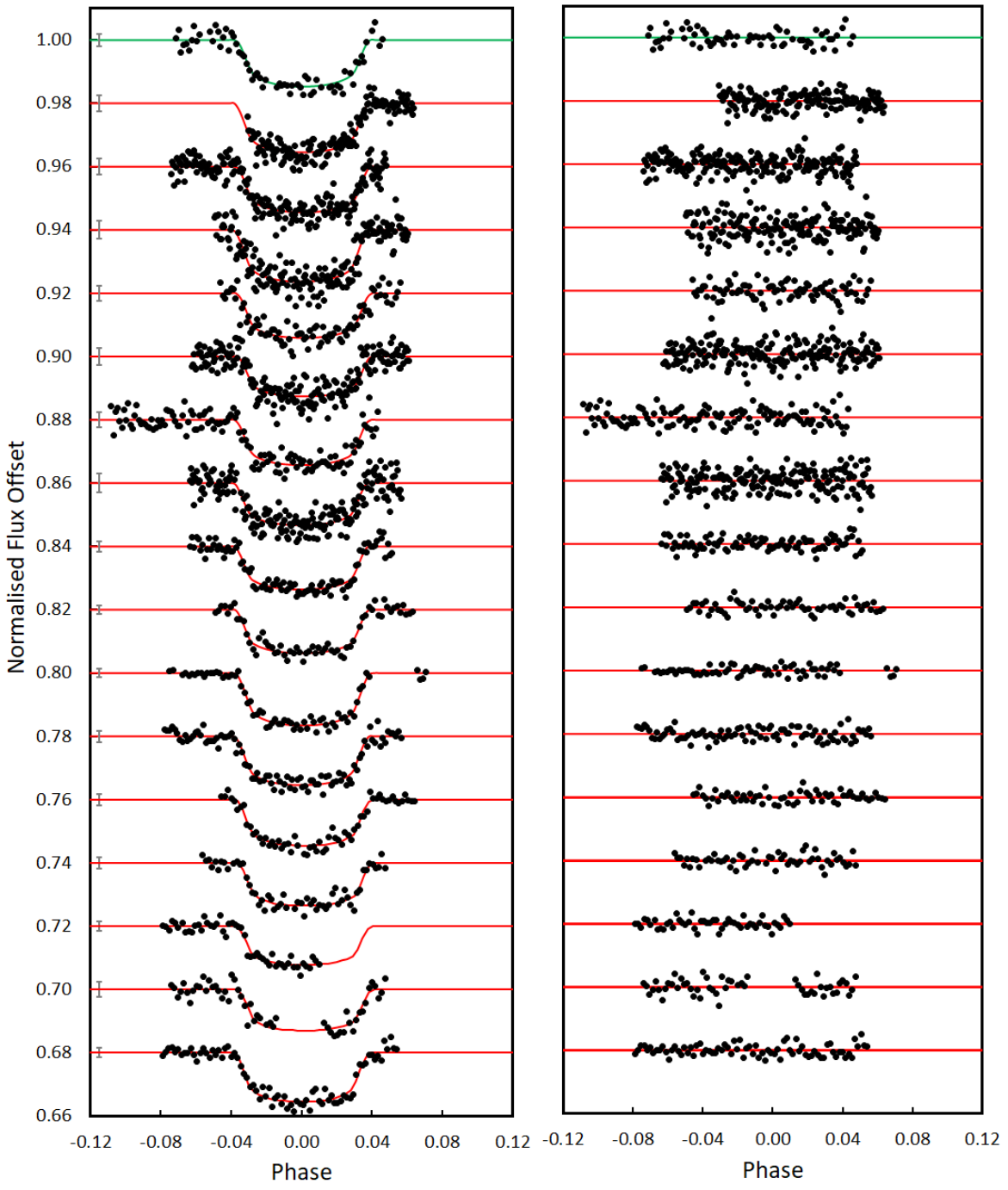

Figure 3.2: 17 new HAT-P-23b Transit lightcurves obtained as part of this study where the transit numbering refers to the observations detailed in Table 3.1. Black dots are individual data points. On the left is the lightcurve where the solid lines are the best fit ExofastV2 model for each transit. On the right are the residuals after subtraction of the transit model fit. The numbers are the observations detailed in Table 3.1. Green lines represent fits to V filter observations and red lines represent fits to Rc observations. On the left of each transit model is a indicator of the mean photometric uncertainty from each nights observation.

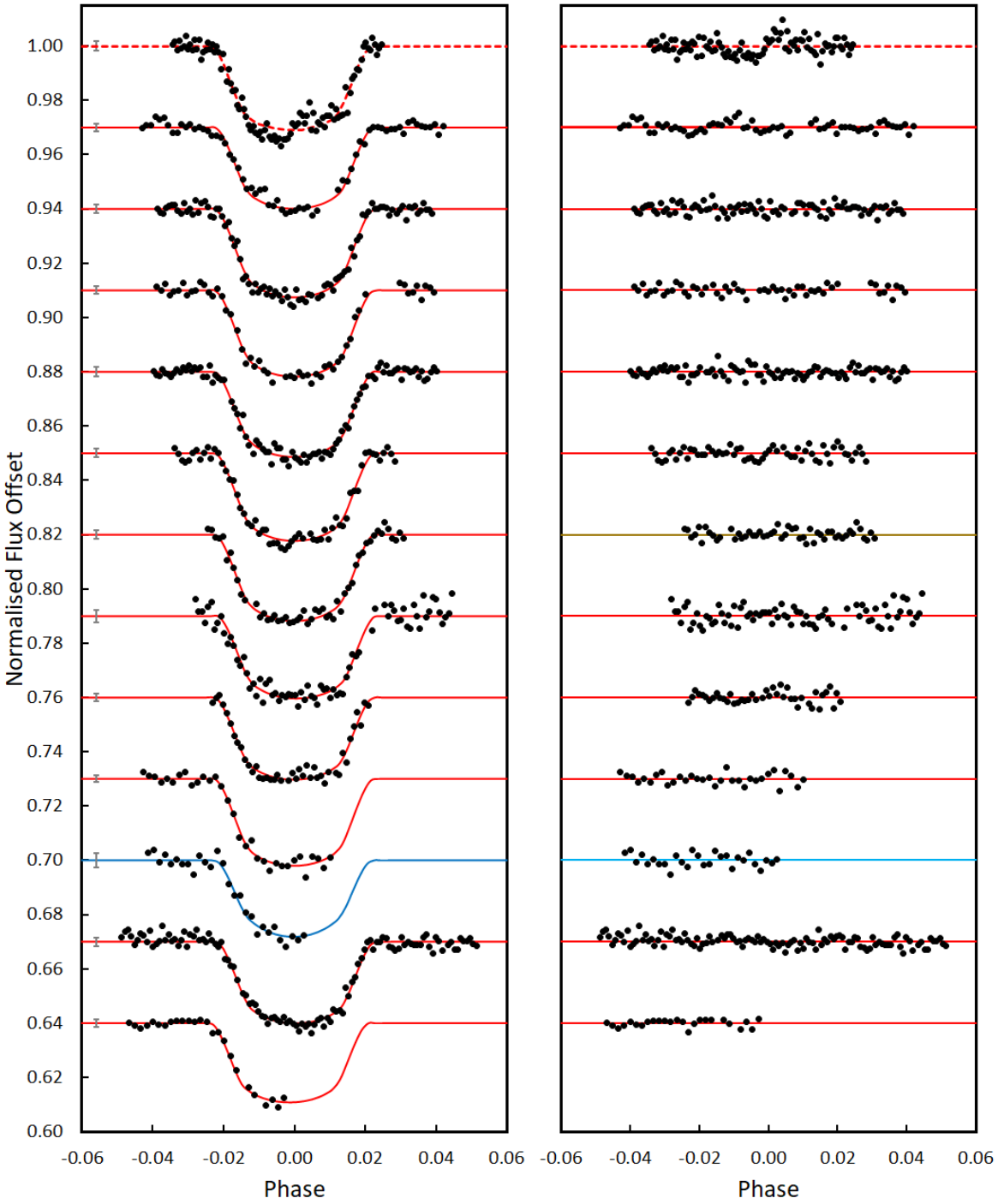

Figure 3.3: 13 new WASP-52b transit lightcurves and ExofastV2 model fits obtained as part of this project. Black dots are individual data points. On the left is the lightcurve where the solid lines are the best fit ExofastV2 model for each transit. On the right are the residuals after subtraction of the transit model fit. Red lines represent fits to Rc observations and blue lines represent fits to B filter observations. The numbers refer to the transits detailed in Table 3.1. On the left of each transit models the mean photometric uncertainty for each observation is indicated. Only complete transits with full coverage were used in the updated ephemeris calculation, transit 1 (shown with a dotted model fit) was excluded from the global model fit in ExofastV2 due to the significant spot crossing event.

For the HAT-P-23 monitoring data a photometry template was created in AIJ incorporating stars from the UCAC4 catalogue (Zacharias et al., 2013) with known B, V and r′ filter magnitudes. Six suitable comparison stars were selected and a seventh, with B-V=1.375 similar to HAT-P-23 (B-V=1.301), was used as a check star. AIJ does not take into account catalogue magnitude uncertainties so the uncertainties for the calculated magnitudes are based on the standard error in the measurements of the check star.

3.3 Results

3.3.1 HAT-P-23b System Parameters

At discovery Bakos et al. (2011) found a marginally significant orbital eccentricity of 0.106 ± 0.044. The subsequent study by Sada and Ramón-Fox (2016) also found an orbital eccentricity of 0.096 ± 0.024, however using secondary occulatation measurements O'Rourke et al. (2014) determined that the orbit was probably circular, a result supported by subsequent RV studies (Bonomo et al., 2017). Subsequent studies of HAT-P-23b made by Ciceri et al. (2015) and Maciejewski et al. (2018) therefore assumed a circular orbit. Maciejewski et al. (2018) reported that the increased value they found for the scaled system parameter a/R_*, over that seen by Bakos et al. (2011) and Sada and Ramón-Fox (2016) is due to the adoption of a non zero eccentricity in those studies.

To ensure the results were not biased by a prior determination of eccentricity the orbital eccentricity was left as a free parameter. This resulted in $e = 0.027^{+0.029}_{-0.019}$, consistent with a circular orbit within 1.4σ. The same model was also calculated with eccentricity forced to zero resulting in the same value for the scaled a/R_* parameter as found when the eccentricity left as a free parameter. This would be expected given the near zero eccentricity determined when it is left as a free parameter and the argument of periastron (ω_*) is close to 180°, resulting in $e \sin \omega_* = 0.000$(to 3 dp.). The result found for a/R_* is consistent with that determined by Bakos et al. (2011) and Sada and Ramón-Fox (2016), Figure 3.4, indicating free eccentricity alone may not the cause of the differences in a/R_* seen by Maciejewski et al. (2018).

From the global model fit the stellar radius and mass of HAT-P-23 were found to be $1.157^{+0.023}_{-0.022}\mathrm{R}_\odot$ and $1.063^{+0.063}_{-0.060}\mathrm{M}_\odot$, which is 3.8% and 5.9% smaller respectively than found by Bakos et al. (2011). The results are also 6.2% larger and 3.7% smaller respectively than the only other published stellar mass and radius values by Ciceri et al. (2015). The revised radius found for HAT-P-23b is $1.308^{+0.044}_{-0.043}\mathrm{R_J}$. It is notable that the radius determined by Ciceri et al. (2015) of 1.224 ± 0.036 is 2σ smaller than the newly determined value and 4σ smaller than that found by Bakos et al. (2011), a fact commented on by the independent reviewer of the published version of this chapter. The planetary radius found by Ciceri

et al. (2015) moved HAT-P-23b out of the region of the mass-radius diagram occupied by inflated hot Jupiter systems. The transits obtained by Ciceri et al. (2015) were modelled using JKTEBOP[2] (Southworth, 2013), with the authors assuming circular orbits and a fixed mass ratio. The fits of the light curves were performed using theoretical values of the limb darkening coefficients. Although not explicitly stated in their published paper, there is no discussion of the use of RV data so it is unlikely a joint fit of transit and RV data was applied. In the same paper the authors also analysed transit data for WASP-48b and similarly report lower stellar and planetary radii compared with the discovery paper, $R_* = 1.519 \pm 0.051 \mathrm{R}_\odot$ vs $1.75 \pm 0.09 \mathrm{R}_\odot$ and $\mathrm{R_p} = 1.396 \pm 0.051 \mathrm{R_J}$ vs $1.67 \pm 0.1 \mathrm{R_J}$.

The transit lightcurves obtained by Ciceri et al. (2015) are available online via the VizieR database[3]. This includes six transits with full coverage obtained with the Calar Alto 1.23m telescope using the same Rc filter as used for the PIRATE and POST observations. These six transits were modelled using Exofastv2 in the same way as for the new lightcurves, using the same priors, RV and photometric values to see whether the result obtained by Ciceri et al. (2015) could be replicated. The transit fits were computed twice, once with eccentricity left as free parameter and again with a forced circular orbit as used by Ciceri et al. (2015).

The results for the ExofastV2 model computed with eccentricity left free resulted in planetary radius $\mathrm{R_p} = 1.312^{+0.031}_{-0.003} \mathrm{R_J}$, within 1% of the result obtained from the analysis of the new PIRATE and POST lightcurves but 7% larger than found by Ciceri et al. (2015). Similarly the stellar radius $\mathrm{R_*} = 1.146 \pm 0.024 \mathrm{R}_\odot$, is within 1% of the value determined from the PIRATE and POST lightcurves. The forced circular ExofastV2 model fit resulted $R_* = 1.133^{+0.019}_{-0.020} \mathrm{R}_\odot$ and $\mathrm{R_p} = 1.303 \pm 0.028 \mathrm{R_J}$. Thus the results for $\mathrm{R_*}$ and $\mathrm{R_p}$ from the forced circular analysis of the Ciceri et al. (2015) lightcurves gave values within approximately 1% of the free eccentricity model.

It cannot be stated with certainty but seems likely the combination of the radius derived from the theoretical models using the mass/age relationship possibly along with the fixed circular orbit for HAT-P-23b have led to the smaller radius determination. The other significant difference in the two approaches was that Ciceri et al. (2015) fit the lightcurves only.

The value for $\mathrm{a/R_*} = 4.22^{+0.11}_{-0.10}$ is consistent with the previous studies which assumed a non zero eccentricity (Bakos et al., 2011; Sada and Ramón-Fox, 2016) and approximately 6% smaller than that found by studies which fixed orbital eccentricity to zero (Ciceri et al., 2015; Maciejewski et al., 2018). Key stellar and planetary parameters are compared with the previously published values in Figure 3.4 and all newly derived parameters can be found in Table 3.6.

[2]https://www.astro.keele.ac.uk/jkt/codes/jktebop.html

[3]https://vizier.u-strasbg.fr/viz-bin/VizieR

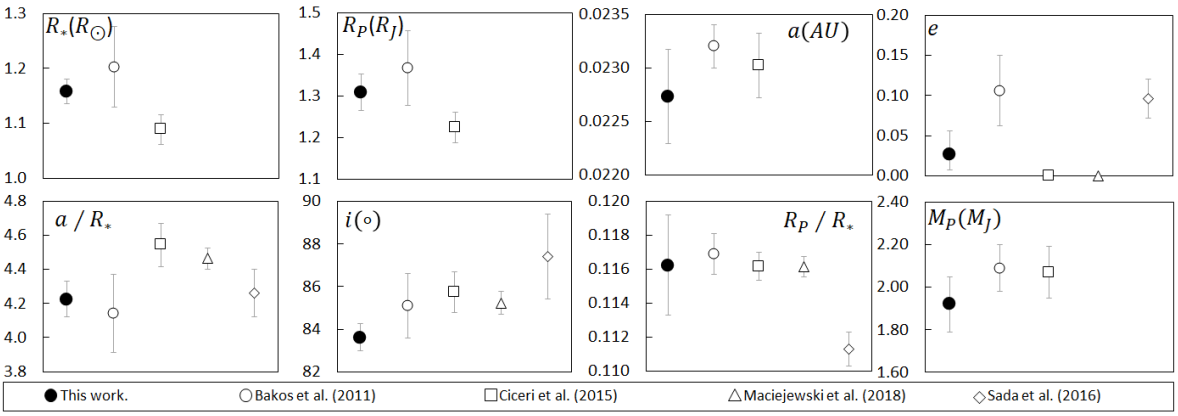

Figure 3.4: HAT-P-23b results from the analysis of the new transits (filled circles) compared with results from published works where values are available (open symbols).

3.3.2 HAT-P-23b Ephemeris Calculation

To calculate the updated ephemeris for HAT-P-23b the transit mid times for all complete transits were combined with those from the literature. Only transits with full coverage of the ingress and egress transition points, $t_1 - t_4$ were included in the timing analysis. Full transit lightcurves published by Ciceri et al. (2015) and Maciejewski et al. (2018) which were available on-line were reanalysed in ExofastV2 in exactly the same way as for the new transit data. The recalculation of transit mid-time for the five lightcurves obtained from Ciceri et al. (2015) resulted in transit mid-times on average 6 minutes later than the values calculated by those authors. The same transit lightcurves were also recalculated by Maciejewski et al. (2018) who also found later transit times. The new recalculated transit times found here agree with those from Maciejewski et al. (2018) to within the uncertainties (mean difference is 10s). The recalculated transit times also have reduced uncertainties. As discussed in Section 3.3.1 the likely improvement seen in the timing results both here and by Maciejewski et al. (2018) likely arise from undertaking a joint transit and RV fit whereas Ciceri et al. (2015) undertook transit only fits. All but two transit times recalculated from transit lightcurves obtained by Maciejewski et al. (2018) agreed within the published measurement uncertainty, the other two being within 1.4σ. Using the BUSCA instrument Ciceri et al. (2015) obtained simultaneous transit measurements through multiple filters, only the transit time resulting from the R filter data was included in the timing analysis. Where the lightcurve data was not available, transit mid times from other publications were taken from the literature and converted to $\mathrm{BJD_{TDB}}$ as required. The resulting transit mid-time data set contained a number of simultaneous observations, in these cases the mean value for the transit mid-time was used. The transit mid-times from the newly obtained lightcurves can be found in Table 3.3, and a full list of the transit times used in the ephemeris calculation is available at the end of this chapter.

Table 3.3: HAT-P-23b transit times for complete new transits used in the transit timing analysis. Transit numbers follow Table 3.1. All transit times used in the ephemeris calculations can be found at the end of this chapter.

Transit No.	Epoch	Tc (BJD_{TDB})	Tc Uncertainty	Linear O-C	Telescope
1	2622	2458032.45353	0.00076	0.000075	POST
3	2839	2458295.65089	0.00057	0.001074	PIRATE
4	2843	2458300.50097	0.00075	-0.000392	PIRATE
5	2843	2458300.50190	0.00120	0.000538	POST
6	2848	2458306.56787	0.00071	0.002075	PIRATE
7	2848	2458306.56574	0.00070	-0.000055	POST
8	2853	2458312.62941	0.00078	-0.000817	PIRATE
9	2857	2458317.48136	0.00054	-0.000413	POST
10	2871	2458334.46187	0.00066	-0.000313	PIRATE
11	2876	2458340.5272	0.00045	0.000585	PIRATE
12	2890	2458357.50703	0.00060	0.000004	PIRATE
13	2913	2458385.40434	0.00068	0.000926	PIRATE
14	2913	2458385.40582	0.00075	0.002406	POST
16	2918	2458391.47024	0.00093	0.002393	POST
17	2932	2458408.44838	0.0006	0.000123	PIRATE

The new linear ephemeris found using this data set is

$$\mathrm{T_c(BJD_{TDB})} = 2454852.265165(120) + 1.212886457(54) \times \mathrm{E} \tag{3.1}$$

where the first value on the right-hand side is the reference epoch ($\mathrm{T_0}$), the second value is the orbital period in days and E is the epoch of observation. Values in brackets are the uncertainties relative to the last digits. The χ^2_ν of the linear fit is 2.08 and the Bayesian Information Criterion (BIC) is 33.01. A quadratic ephemeris of the form in Equation 3.2 was also calculated

$$\mathrm{T_c(BJD_{TDB})} = \mathrm{T_0} + \mathrm{P_{orb}} \times \mathrm{E} + 0.5(\delta \mathrm{P_{orb}}/\delta \mathrm{E}) \times \mathrm{E}^2 \tag{3.2}$$

where $(\delta P_{orb}/\delta E)$ is the period change per orbit. This model resulted in $\chi^2_\nu = 2.20$ and BIC = 37.75. Therefore I find no departure from a linear ephemeris for HAT-P-23b, in agreement with the results from Maciejewski et al. (2018). The timing residuals to the linear ephemeris are shown in Figure 3.5.

3.3.3 HAT-P-23 Variability

The monitoring data obtained for HAT-P-23 was analysed to look for periodic variations arising from star spots on the rotating stellar surface in order to identify a roation period for HAT-P-23. A Lomb-Scargle periodogram analysis over the period range of 0.1d to 100d reveals a 7.015d period with an amplitude of 0.011 magnitude, substantially less than the 0.03 magnitude seen by Sada and Ramón-Fox (2016), see Figure 3.6. Moutou et al. (2011) mea-

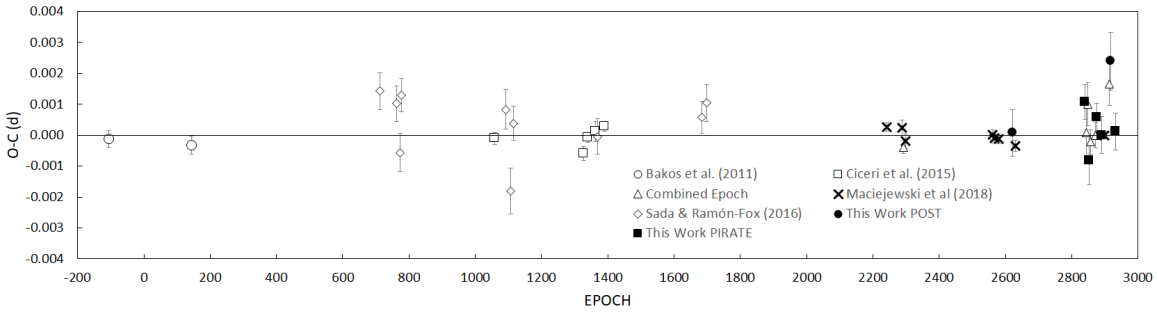

Figure 3.5: Transit O-C)times for HAT-P-23b from the literature and this work calculated using the new linear ephemeris. Transit times for complete transits where lightcurve data was available were recalulated (Bakos et al., 2011; Ciceri et al., 2015; Maciejewski et al., 2018). Other transit times were taken from the literature and converted to BJD_{TDB} as required. The mean value derived for simultaneous observations of the same transit are shown as open triangles.

sured HAT-P-23's rotational velocity as $7.8 \pm 1.6 \mathrm{kms}^{-1}$ which, given the newly determined stellar radius, results in an equatorial rotation period of 7.50 ± 1.55 days, consistent with the measured period of variation. The same Lomb-Scargle period analysis was carried out for the field check star and the result did not exhibit any periodicity of the same frequency as found for HAT-P-23. The only periodicity found in the check star occurred at the 1 day observing cadence. The variability seen in the HAT-P-23 monitoring lightcurve is therefore attributed to the rotation period of HAT-P-23 at the (unknown) latitude of the surface spots.

3.3.4 WASP-52b System Parameters

As with HAT-P-23b a joint transit and RV fit was undertaken using all new full and partial transit data sets, except transit number 1 which exhibits a large suspected spot crossing event. Again to avoid bias through fixing model parameters the orbital eccentricity was left as a free parameter in the ExofastV2 fits, resulting in $e = 0.05^{+0.033}_{-0.03}$, within 1.6σ of a circular orbit, thus the eccentricity found is consistent with zero.

The determined stellar radius of $0.834 \pm 0.013 R_{\odot}$ is 5.6% larger than that found by Hébrard et al. (2013) and 6.1% larger than found by Mancini et al. (2017). This larger stellar radius value results in a planetary radius of $1.319^{+0.026}_{-0.027} R_J$, 3.9% and 5.3% larger respectively than found in the previous studies. The larger value found for the stellar radius likely results from the use of an extinction corrected SED model with Gaia parallax to constrain the system distance. The distance to WASP-52b was found to be 173 ± 1.6pc, 24% greater than the 140 ± 20pc found by Hébrard et al. (2013). The result for the semi-major axis remained within 2% of the results from previous studies so the derived scaled system parameter a/R_* is smaller than

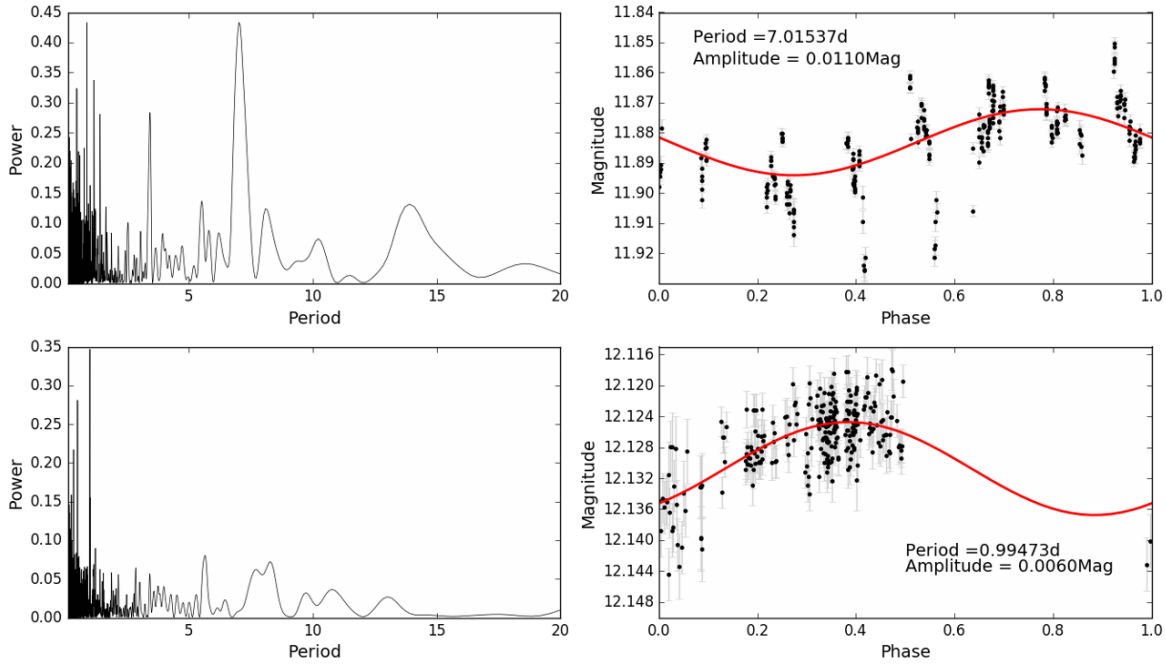

Figure 3.6: Lomb Scargle periodograms and phase folded results showing the detected rotation period for HAT-P-23 (top) and for the check star (bottom). The period region shown is between 0.1d and 20d, no periods were detected outside of this range. The periodograms for HAT-P-23 also shows lower power alias' at half and twice the detected period (3.5d and 14d). The periods detected in the check star is the one day observing cadence and its aliases.

previous results by 5.8% and 3.8% respectively. Other parameters determined are consistent with previously published results. The results for key parameters are presented in Figure 3.7 along with previously published values. The newly derived effective temperature of 5039^{+40}_{-39}K is consistent with $T_{\rm eff}$= 5000 ± 100K from Hébrard et al. (2013), though with improved uncertainties. The age reported for WASP-52 varies widely in the literature from $0.4^{+0.3}_{-0.2}$Gyr (Hébrard et al., 2013) to $9.4^{+4.7}_{-4.3}$Gyr in Mancini et al. (2017). The newly determined age for WASP-52 of $8.5^{+3.7}_{-4.6}$Gyr agrees within 1σ with that found by Mancini et al. (2017).

3.3.5 WASP-52b Ephemeris Calculation

The transit mid times for all 9 new transits with complete coverage (excluding archive transit number 1) were combined with those from the literature from Hébrard et al. (2013), Swift et al. (2015), Bruno et al. (2018), Mancini et al. (2017), Öztürk and Erdem (2019) and Baluev et al. (2019). The transit times calculated by Baluev et al. (2019) make extensive use of observations recorded on the Exoplanet Transit Database; only those results classified as being from "high quality" lightcurves by those authors were included in the new analysis. Table 3.5 lists the new transit times determined from the observations, the full table of transit times used in the ephemeris calculations can be found at the end of this chapter.

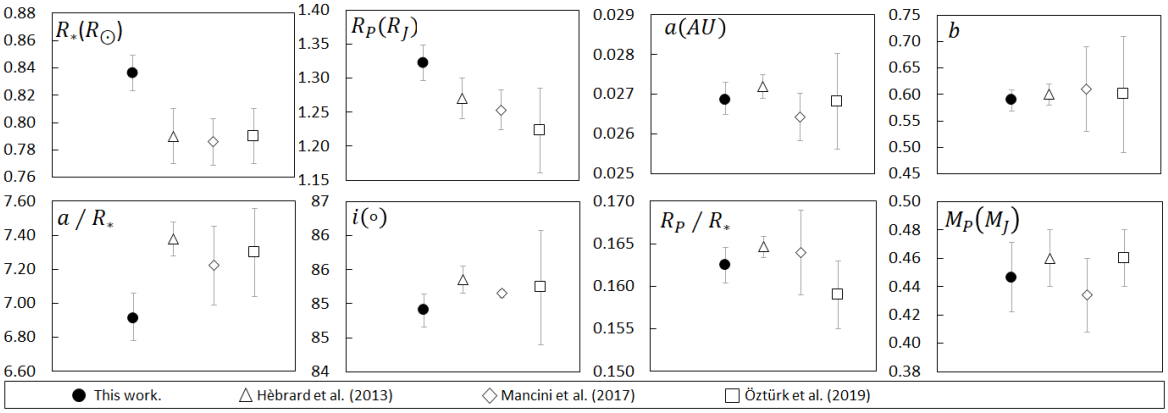

Figure 3.7: WASP-52b key system parameters from both this work (filled circles) compared with those from published works discussed in this chapter. Semi-major axis and impact parameter shown for the Öztürk and Erdem (2019) results were calculated from published parameters as was the scaled R_P/R_* and impact parameter for Mancini et al. (2017). Values calculated in this way typically show larger uncertainties than values calculated with the model analysis.

The transit times published by Mancini et al. (2017) have extremely small uncertainties and including these transit times and uncertainties in the ephemeris model was found to increase the χ^2_ν of the ephemeris. The uncertainties of the full transit lightcurves used from those obtained by Mancini et al. (2017) range from 0.00006d (5 seconds) to 0.0002d (17 seconds) with a mean value of 0.00013d (11 seconds). The mean uncertainty of all the other transit times used to calculate the ephemeris is 0.00065d (56 seconds).

Initial analysis of all the transit mid times from the published results resulted in an ephemeris with χ^2_ν of 2.5. Adding the newly obtained data had the effect of slightly reducing the χ^2_ν and residual RMS by approximately 6% and 3% respectively. To understand the impact of including each of the existing published transit mid-times datasets and to determine whether any individual dataset was adversely affecting the ephemeris calculation, both the linear and quadratic ephemeris models were calculated adding each published transit time data set in turn. The Hébrard et al. (2013) observations were not fit on their own as the data set (as recalculated by Mancini et al. (2017)) contains only three closely spaced observations. The effect on χ^2_ν, the RMS residual to the ephemeris, the starting epoch and period and their uncertainties were measured and the results for χ^2_ν and the RMS values are shown in Figure 3.8. It can be seen in the left panel of this Figure that when the transit time results published by Mancini et al. (2017) are added they almost double the χ^2_ν of both the linear and quadratic ephemeris fits. Mancini et al. (2017) noted that their linear ephemeris had a high χ^2_ν of 8.98 and they subsequently multiplied the uncertainties on their final linear ephemeris by this value. Following Mancini et al. (2017) the individual transit time uncertainties were

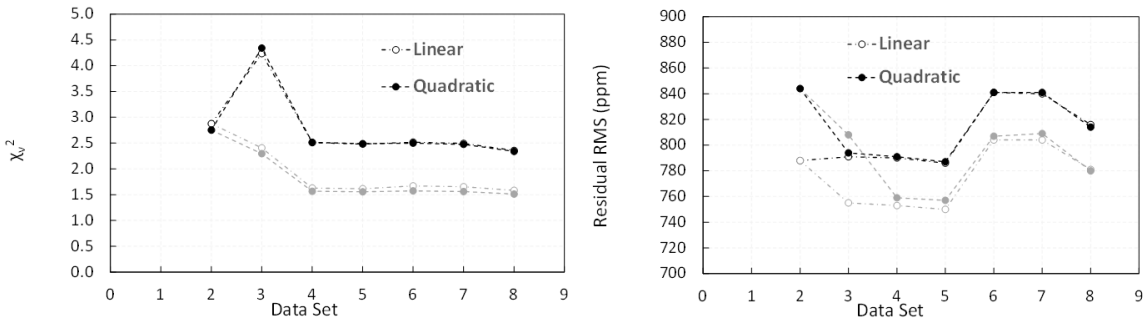

Figure 3.8: Resulting χ^2_ν (left) and residual RMS (right) for ephemerides calculated when each published dataset was added in turn. See Table 3.4 for data set detail. The ephemeris calculations using original transit mid-time uncertainties from Mancini et al. (2017) are shown in black while the ephemerides calculated with the uncertainties on the Mancini et al. (2017) times increased by 8.98 are shown in grey.

Table 3.4: Transit time data sets used in WASP-52b ephemeris calculations.

Data Set	**Data Source**
1	Hébrard et al. (2013)
2	Data Set 1 + Baluev et al. (2019)
3	Data Set 2 + Mancini et al. (2017)
4	Data Set 3 + Öztürk and Erdem (2019)(ETD)
5	Data Set 4 + Swift et al. (2015)
6	Data Set 5 + Öztürk and Erdem (2019)
7	Data Set 6 + Bruno et al. (2016)
8	Data Set 7 + New data PIRATE and POST

multiplied by 8.98 prior to re-calculating both ephemerides again as each individual dataset was added (see Figure 3.8). The result produced both linear and quadratic ephemerides with smaller χ^2_ν by a third and an increased preference for the quadratic ephemeris.

The final recalculated linear ephemeris (Eq. 3.3) achieved $\chi^2_\nu = 1.58$ and BIC = 59.41.

$$\mathrm{T_c(BJD_{TDB})} = 2455793.681914(141) + 1.749781099(126) \times \mathrm{E} \tag{3.3}$$

The final recalculated quadratic ephemeris (Eq. 3.4) of the form from Equation 3.2 resulted in a slightly lower $\chi^2_\nu = 1.51$ and BIC = 57.88.

$$\begin{aligned}\mathrm{T_c(BJD_{TDB})} = 2455793.680977(141) + 1.749783241(177) \times \mathrm{E} \\ + (-2.14 \pm 0.24) \times 10^{-9} \times \mathrm{E}^2\end{aligned} \tag{3.4}$$

Using Mancini et al. (2017)'s originally published uncertainties results in the same χ^2_ν for the linear and quadratic ephemeris models. It is possible the small published uncertainties on these results have masked previous detection of a non-linear ephemeris for WASP-52b. Excluding the transit times reported by Mancini et al. (2017), while retaining the recalculation of the three transit times from Hébrard et al. (2013), produces increased χ^2_ν for both

Table 3.5: WASP-52b transit times for complete new transits. Results for both the linear and quadratic ephemerides are shown along with the difference between the two results. Transit numbers follow table 3. All transit times used in the ephemeris calculations can be found at the end of this chapter.

Transit	Epoch	Tc (BJD_{TDB})	Tc Uncertainty	Linear O-C	Quad O-C	Δ O-C
2	1292	2458054.39890	0.00039	-0.000194	-0.000238	0.000044
3	1451	2458332.61424	0.00026	-0.000049	0.000033	-0.000082
4	1455	2458339.61298	0.00031	-0.000433	-0.000347	-0.000086
5	1467	2458360.61083	0.00031	0.000044	0.000141	-0.000097
6	1479	2458381.60813	0.00036	-0.000029	0.00008	-0.00011
7	1487	2458395.60619	0.00035	-0.000218	-0.0001	-0.000118
8	1488	2458397.35716	0.00054	0.000971	0.00109	-0.000119
9	1491	2458402.60516	0.00076	-0.000373	-0.000251	-0.000122
12	1504	2458425.35296	0.00029	0.000273	0.000409	-0.000136

ephemerides but retains a preference for the quadratic model. As a final test the newly obtained transit times obtained from the PIRATE and POST observations were removed from the ephemeris analysis and the quadratic model was still preferred, though again with a slightly increased χ^2_ν. In the quadratic ephemeris the values found for the quadratic term between 1.90×10^{-9} and 2.38×10^{-9} resulted in the same χ^2_ν values (measured to 2 decimal places), therefore the formal uncertainty on the period derivative was increased to reflect this range of possible values.

The quadratic term $\frac{\delta P}{\delta E} = (-2.14 \pm 0.24) \times 10^{-9}$ can be used to calculate the period derivative of

$$\frac{\delta P}{\delta t} = \frac{1}{P}\frac{\delta P}{\delta E} = (-1.22 \pm 0.14) \times 10^{-9} = -38.6 \pm 4\text{ms yr}^{-1} \tag{3.5}$$

where $^{\delta P}/_{\delta t}$ is the period change per day and P is the orbital period. This is 34% larger than seen for the largest secure period change detected for WASP-12b (Yee et al., 2019). This result is discussed further in Section 3.4.2. Figure 3.9 shows the O-C values with both the linear and quadratic ephemerides projected forwards.

WASP-52 is an active star with many spot crossing events previously recorded, e.g. Mancini et al. (2017); Kirk et al. (2016). No spot crossing events are visible in the transits observed during the 2018 season however transit number 1 obtained in 2013 shows a large brightening during the transit. This was the same season as the observations made by Mancini et al. (2017) who detected spot crossing events at 5 of their 8 observation epochs, thus this brightening is likely a significant spot crossing. Figure 3.3 shows how ExofastV2 can significantly underestimate the transit depth, where a large spot crossing occurs therefore this transit was excluded from the ExofastV2 model fit and ephemeris calculation for WASP-52b. The final derived system parameters and uncertainties are detailed in Table 3.6.

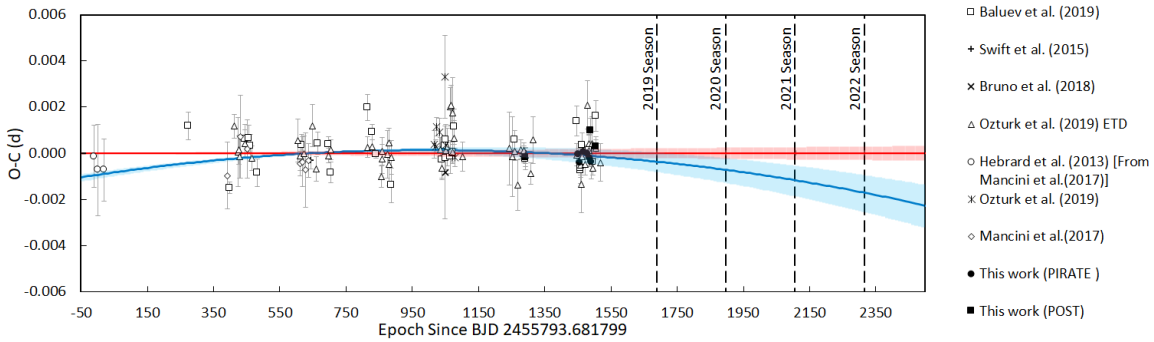

Figure 3.9: Predicted transit times for WASP-52b based on both the linear and quadratic ephemerides shows that it should be possible to clearly differentiate between the two models with data from the 2021 observing season.

3.3.6 WASP-52 Variability

Unfortunately concurrent photometric monitoring of WASP-52 over the 2018 season is not available; instead the stellar magnitude was measured using out of transit data from four transits observed using PIRATE with sufficient unbroken data available on both sides of the transit (transits 3 to 6 in Table 3.1). As for HAT-P-23, a photometry template was generated using comparison stars from the UCAC4 catalogue. Eight stars were used in the range $r' = 13.00$ to 14.90 magnitude. WASP-52 itself has no B, V or r' photometry in the UCAC4 catalogue so $B - V = 0.9$ was taken from Hébrard et al. (2013) and a check star of similar $B - V = 0.86$ was selected from UCAC4. Although this data set contained data from only 4 observations a variation of $\Delta Rc = 0.03$ mag, similar to the WASP-52b transit depth is clearly visible. The standard deviation between the mean nightly values (red squares in Figure 3.10) is 0.0143 for WASP-52 but 10 times smaller at 0.0014 for the check star indicating the magnitude variations seen in WASP-52 are real, Figure 3.10.

3.3.6.1 Transit depth correlation with magnitude.

If stellar spots at a latitude different to the transit chord are reducing the stellar flux this would result in the transit chord crossing a brighter part of the star, blocking a greater proportion of the flux and a greater transit depth would be recorded when spots are present compared to when they not. As a result we would expect to see a correlation between transit depth and stellar brightness with the transit depth being greater when the star is fainter. A Kendall Rank Correlation was used due to the small number of data points giving $\tau_b = 0.66$ and p-value = 0.17 indicating a strong positive, but not statistically significant, correlation is seen for the four data points available, see Figure 3.12. Due to the small number of data points and large uncertainties, particularly in transit depth, further observations would be required to determine if this effect is real.

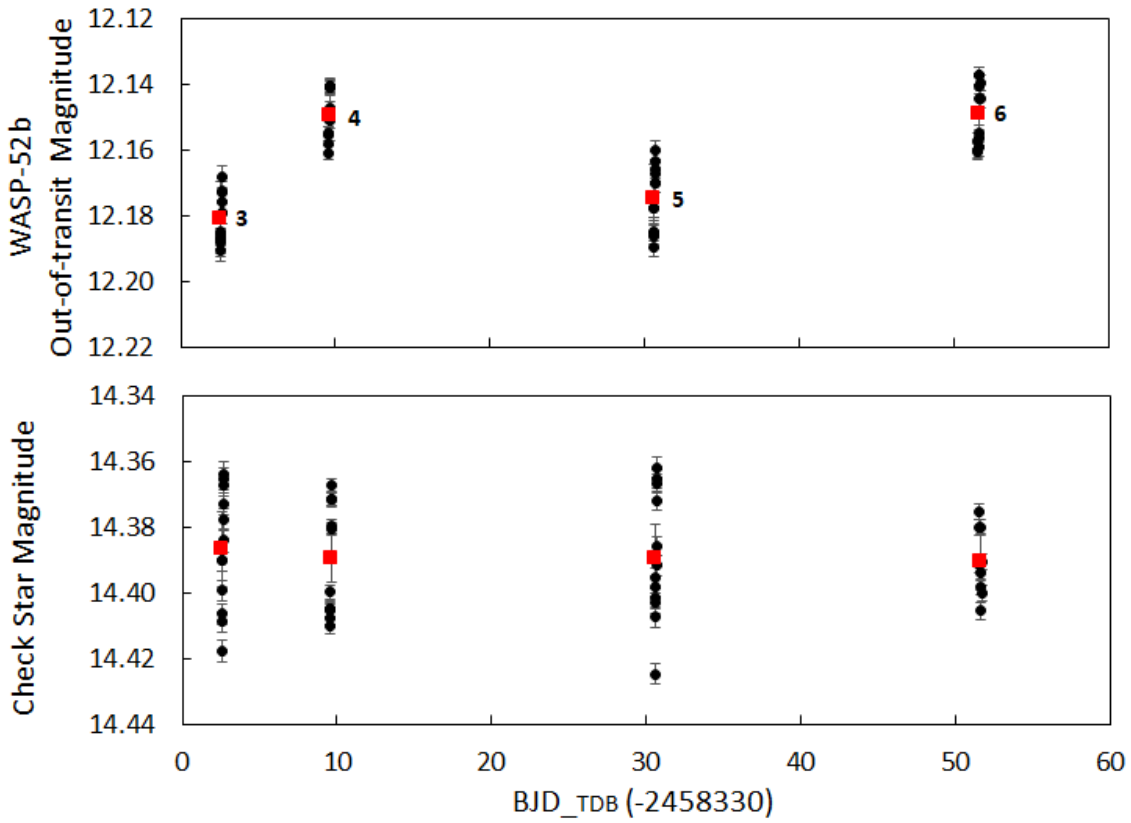

Figure 3.10: Top; magnitude variation measured by PIRATE for WASP-52 from out of transit lightcurve photometry. The numbers indicate the transit from Table 3.1. Bottom is the same plot for the check star. The black dots are the individual measurements from pre and post transit data and the red squares the mean values for each nights observation. The magnitude axis shows the same 0.1 magnitude range for both stars, the fainter check star has a greater nightly spread in measurement values resulting from lower SNR. The standard deviation in the mean values is 10 times smaller for the check star than for WASP-52 indicating the variation seen is real despite the small number of data points.

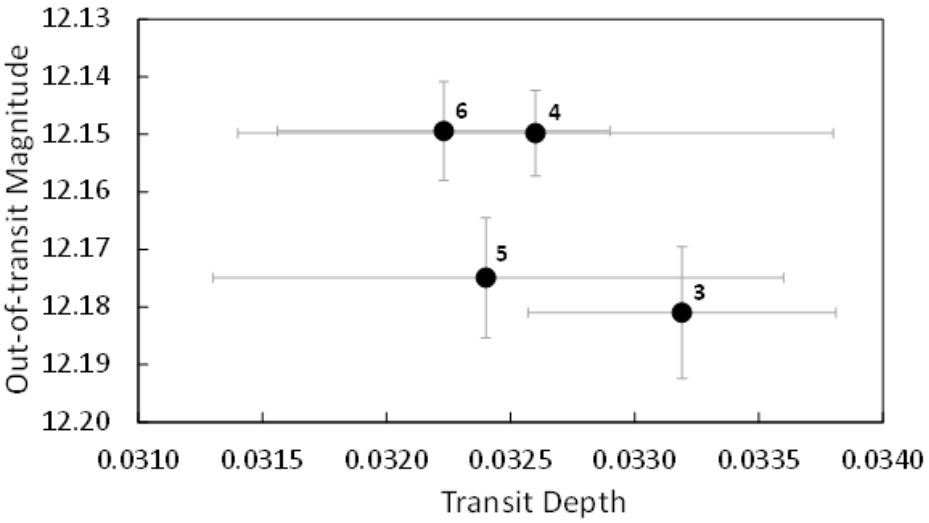

Figure 3.11: Variation in transit depth with host star magnitude. The numbers indicate the transits listed in Table 3.1. The plot shows tentative evidence for greater transit depth when the star is fainter, though the large uncertainties and small number of data points do not allow a firm conclusion to be drawn.

3.3.6.2 Photometric Noise During Transit.

With the photometric precision achievable with small aperture ground-based telescopes it is possible that spot crossing events may not be individually obvious in the transit photometry. If the surface spots are of low contrast or small size such that they are not resolved at the cadence of the imaging, the impact may be below the noise floor. A possibility is that, while surface spots may not be individually detectable, their existence may be inferred through an increase in in the photometric noise seen during transit when compared to the noise level out of transit. We can consider this most likely where the surface is covered in a number of small dark spots or bright plages.

To test for this effect the pre, during and post transit RMS values in the residuals from the model fits for the same four transits of WASP-52b used to look for stellar brightness vs transit depth correlations were measured. Two data points either side of the ingress/egress transition points were excluded from the RMS calculations to ensure any uncertainty associated with the transition point did not influence the RMS values for the out of transit or in transit regions. The mean was taken of the pre and post out of transit regions and the ratio of out of transit to in transit RMS noise was calculated. The results are shown in Figure 3.12. In three of the four transits measured we see an increase in RMS noise during transit.

Taken at face value this could be indicative of stellar activity below the level individually

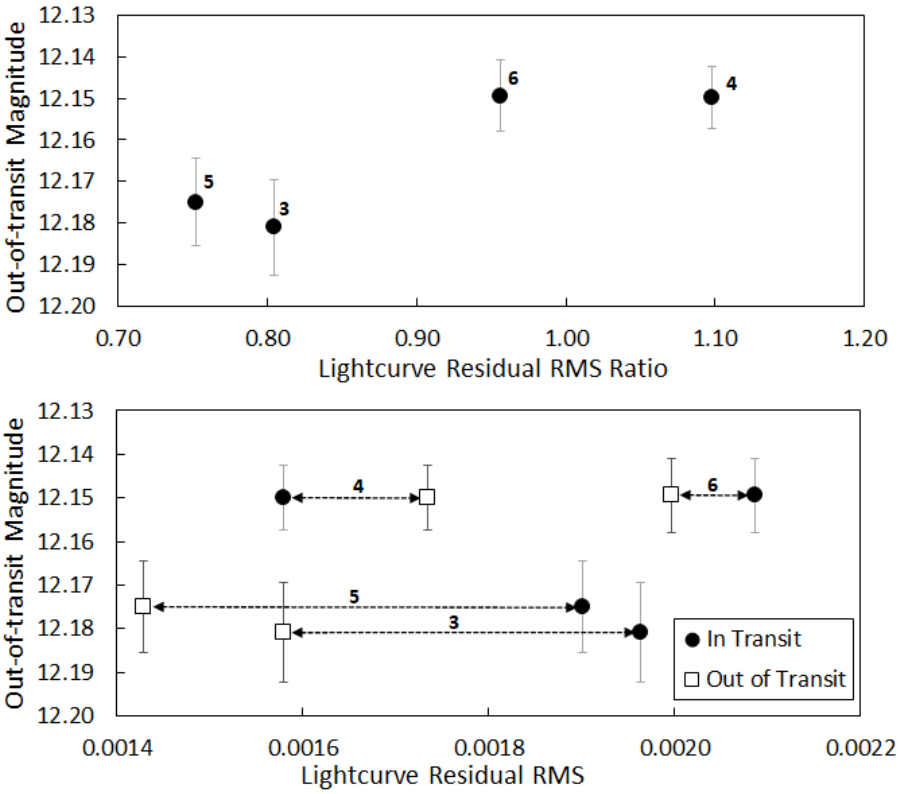

Figure 3.12: Top, ratio of out of transit RMS to in transit RMS of the model fit residuals. Values less than unity indicate a greater RMS noise during transit compared to the mean pre and post transit region. The numbers indicate the transits as detailed in Table 3.1. Bottom, the extent of the variation in RMS noise between the in and out of transit regions.

resolvable by the photometry, a conclusion supported by the fact the two transits with the smallest RMS ratio occur when the host star brightness is at its lowest. However the result is entirely dependent on the precision of the transit model as the out of transit residual are determined from the single baseline flux value while the during transit residuals are measured from the continuously changing transit model.

Other factors that can affect this measurement are the corrections applied to the photometry to detrend the lightcurve for pier flips and changing airmass. Of the four lightcurves measured no pier flip was required for transit number 6 and for transit number 4 the pier flip occurred during the transition point excluded from the RMS calculations. These two transit exhibit the smallest RMS ratio as seen in Figure 3.12. For the two remaining transits with the greatest RMS ratio, the pier flip for number 3 occurred during the out of transit region and during the transit for number 5. So although the number data points is small this would appear to indicate the pier flip correction is not the cause of the RMS ratio values seen.

Changing airmass will also change the RMS value as scatter in the photometric measurements increase with airmass. For example if observations start at low altitude before transit ingress, increases through the zenith during transit then decreases post transit this will result in lower RMS scatter during transit compared to out of transit. Figure 3.12 shows how the RMS scatter and the mean photometric noise change before, during and after transit along with the changing airmass value for each observation. We can see that the transit (number 4) which exhibits the opposite RMS scatter profile to the others, decreasing during transit is also the transit with the lowest mean photometric noise and the two transits which exhibit the greatest RMS increase during transit are also those with the greatest overall photometric noise (transits 3 and 5). Looking at the impact of changing airmass for each transit:

- Transit 3. Airmass decreases through the transit with a very slight increase towards the end of the observation. Mean photometric noise is lower during transit, higher before and after. Pier flip occurred during post transit observation. RMS scatter is significantly greater during transit than either before or after, being lowest after transit.

- Transit 4. Airmass follows almost exactly the same profile as in transit 3 but slightly lower value at the start and greater at the end of observation. Mean photometric noise is lowest of all observations, being at a minimum during transit when airmass is a minimum. Pier flip occurred in ingress transition region excluded from RMS and photometric noise calculation. RMS scatter decreases during observation following the airmass and mean photometric noise profiles.

- Transit 5. Airmass is low at the start of observation, reaches a minimum early during transit and then increases. The profile is the opposite of that seen for transits 3 and 4.

Photometric noise is very similar to observation 3 but overall highest of all observations. The value changes minimally given the larger airmass change through the observation. Pier flip occurs early during transit at the same time as airmass is at a minimum. RMS scatter shows the greatest increase during transit. The value post transit is greater than pre transit as expected from airmass change profile.

- Transit 6. Airmass is low at the start of observation, reaches a minimum early during transit and then increases to the highest value of all observations. Photometric noise is minimum during transit and greatest after transit when airmass is greatest. No pier flip was required during the observation. RMS scatter is greater during transit and lower before and after despite the significantly greater airmass at the end of observation.

Overall there is no common trend between the RMS scatter and observational parameters of mean photometric noise, airmass and pier flip. Therefore it remains a possibility that the in-transit increase in RMS scatter from the model residuals has a physical origin in the activity of the host star with the transit chord crossing regions where spots exist on the stellar surface which are individually undetectable in the photometry. The possibility of the effect seen being due to the imperfect transit model fitting, especially in lightcurves with higher noise, also remains a strong likelihood.

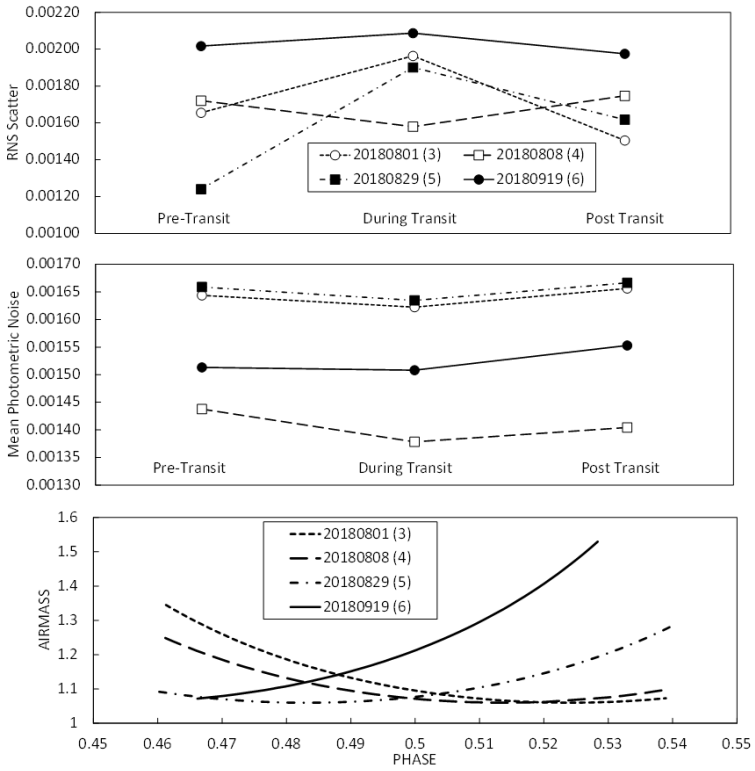

Figure 3.13: Top. RMS scatter before, during and after transit for four complete PIRATE lightcurves, showing three with increased scatter during transit. Middle, mean photometric noise, showing all lightcurves have a lower mean photometric noise during transit. Bottom, airmass during all four observations, transit of WASP-52b occurs from phase 0.48 to 0.52.

Table 3.6: Median parameter values and 68% confidence interval for WASP-52b and HAT-P-23b obtained from ExofastV2 analysis.

Parameter	Description	WASP-52b	HAT-P-23b
M_*	Mass ($M_\odot$)	$0.844^{+0.042}_{-0.034}$	$1.063^{+0.063}_{-0.060}$
R_*	Radius ($R_\odot$)	0.836 ± 0.013	$1.157^{+0.023}_{-0.022}$
L_*	Luminosity ($L_\odot$)	0.399 ± 0.013	$1.460^{+0.087}_{-0.079}$
ρ_*	Density (cgs)	$2.04^{+0.14}_{-0.12}$	$0.967^{+0.075}_{-0.069}$
$\log g$	Surface gravity (cgs)	$4.52^{+0.024}_{-0.021}$	4.338 ± 0.028
$T_{\rm eff}$	Effective Temperature (K)	5017 ± 41	5899^{+71}_{-68}
[Fe/H]	Metallicity (dex)	$0.13^{+0.11}_{-0.11}$	0.150 ± 0.015
Age	Age (Gyr)	$8.5^{+3.7}_{-4.6}$	$5.5^{+3.0}_{-2.5}$
$A_{\rm V}$	V-band extinction (mag)	$0.060^{+0.034}_{-0.039}$	$0.132^{+0.079}_{-0.072}$
d	Distance (pc)	173.1 ± 1.6	$360.0^{+6.0}_{-5.8}$
$R_{\rm P}$	Planetary Radius ($R_{\rm J}$)	1.322 ± 0.026	$1.308^{+0.044}_{-0.043}$
$M_{\rm P}$	Planetary Mass ($M_{\rm J}$)	$0.446^{+0.025}_{-0.024}$	1.92 ± 0.13
a	Semi-major axis (AU)	$0.02686^{+0.00044}_{-0.00037}$	0.02273 ± 0.00044
i	Inclination (Degrees)	84.90 ± 0.24	$83.60^{+0.67}_{-0.61}$
e	Eccentricity	$0.048^{+0.026}_{-0.027}$	$0.027^{+0.029}_{-0.019}$
ω_*	Argument of Periastron (Degrees)	85^{+33}_{-34}	178^{+93}_{-91}
T_{eq}	Equilibrium temperature (K)	1349^{+13}_{-14}	2029^{+29}_{-28}
$\tau_{\rm circ}$	Tidal circularisation timescale (Gyr)	$0.00402^{+0.00052}_{-0.000546}$	$0.00435^{+0.00090}_{-0.00074}$
K	RV semi-amplitude (m/s)	$83.8^{+4.0}_{-3.9}$	349^{+19}_{-20}
$R_{\rm P}/R_*$	Radius of planet in stellar radii	0.1625 ± 0.0021	$0.1162^{+0.0030}_{-0.0029}$
a/R_*	Semi-major axis in stellar radii	$6.91^{+0.15}_{-0.13}$	$4.22^{+0.11}_{-0.10}$
δ	Transit depth (fraction)	0.02640 ± 0.00069	$0.01350^{+0.00069}_{-0.00067}$
τ	Ingress/egress transit duration (days)	$0.01589^{+0.00073}_{-0.00071}$	$0.01243^{+0.00081}_{-0.00078}$
T_{14}	Total transit duration (days)	$0.07795^{+0.00069}_{-0.00066}$	$0.09406^{+0.00089}_{-0.00088}$
$T_{\rm FWHM}$	FWHM transit duration (days)	0.06206 ± 0.00039	$0.08161^{+0.00042}_{-0.00041}$
b	Transit Impact parameter	$0.590^{+0.019}_{-0.021}$	$0.472^{+0.039}_{-0.046}$
ρ_P	Density (cgs)	$0.239^{+0.020}_{-0.019}$	$1.06^{+0.13}_{-0.12}$
$\log g_{\rm P}$	Surface gravity	2.801 ± 0.029	3.445 ± 0.040
$\langle F \rangle$	Incident Flux (cgs)	0.75 ± 0.029	$3.85^{+0.23}_{-0.21}$
$e \cos \omega_*$		$0.002^{+0.023}_{-0.021}$	$-0.008^{+0.017}_{-0.030}$
$e \sin \omega_*$		$0.042^{+0.027}_{-0.029}$	$-0.000^{+0.023}_{-0.024}$
u_1(B)	linear limb-darkening coeff (B)	$0.882^{+0.050}_{-0.051}$	–
u_1(V)	linear limb-darkening coeff (V)	–	0.425 ± 0.048
u_1(R)	linear limb-darkening coeff (R)	0.532 ± 0.018	0.351 ± 0.016
u_2(B)	quadratic limb-darkening coeff (B)	-0.026 ± 0.051	–
u_2(V)	quadratic limb-darkening coeff (V)	–	0.252 ± 0.049
u_2(R)	quadratic limb-darkening coeff (R)	0.180 ± 0.017	0.288 ± 0.014

3.4 Discussion

3.4.1 HAT-P-23b

Previous results for the radius of HAT-P-23b have varied from an inflated $1.368 \pm 0.09 R_J$ Bakos et al. (2011) to the 4σ smaller radius of $1.224^{+0.036}_{-0.007} R_J$ (Ciceri et al., 2015). The newly derived radius of $1.308^{+0.044}_{-0.043} R_J$ is between these two values with a slightly smaller mass. This places HAT-P-23b very close to two other inflated hot Jupiters, TrEs-3b (O'Donovan et al., 2007) and WASP-135b (Spake et al., 2016) in terms of of planetary radius, mass and semi major axis, though with very different ages and an equilibrium temperature that is 300-400K greater than for the other two planets, Table 3.7 and Figure 3.14. A strong dependency on planetary radius with incident flux was found by Weiss et al. (2013) who derived an empirical relationship for planetary radius dependent on mass and incident flux. The authors noted that for planets with $M_P > 150 M_\oplus$ the radius depends only very weakly on mass, thus the incident flux is the most important factor affecting planetary radius in this mass range. Using this empirical relation and the new planetary mass and incident flux, the theoretical radius for HAT-P-23b is $1.355 \pm 0.008 R_J$. This is 4% larger than the radius measured, closer to that determined by Bakos et al. (2011), though the newly measured and the theoretical radii are close to agreement at 1σ. It is likely that factors other than just incident flux such as core mass fraction, atmospheric composition or age play an important role in determining the radius of HAT-P-23b. The determination of precise planetary and host star parameters for known hot Jupiters along with the discovery of new examples will allow comparative planetology to tease out the relative importance of the factors affecting the radii of hot Jupiters.

Because the eccentricity value cannot be smaller than zero, ExofastV2 model values can only scatter upwards resulting in a Lucy-Sweeney type bias (Lucy and Sweeney, 1971). As a result eccentricity should not be considered significant if it is less than 2.3σ from zero (Eastman et al., 2019). The value found HAT-P-23b's eccentricity of $e = 0.027^{+0.029}_{-0.019}$ is therefore considered consistent with zero and in agreement with the findings from secondary eclipse measurements and RV analysis from (O'Rourke et al., 2014; Moutou et al., 2011). Figure 3.4 shows previous studies treating eccentricity as a free parameter yielded a smaller scaled system parameter a/R_* (Bakos et al., 2011; Sada and Ramón-Fox, 2016) than studies where the eccentricity is fixed to zero (Ciceri et al., 2015; Maciejewski et al., 2018). This suggests fixing the orbit as circular biases results towards larger values of a/R_*. In this new analysis no difference in a/R_* was found between between the new ExofastV2 free eccentricity and circular model results.

The ephemeris for HAT-P-23b has been updated using the newly obtained observations and remodelling of those published observations where the lightcurve data was available.

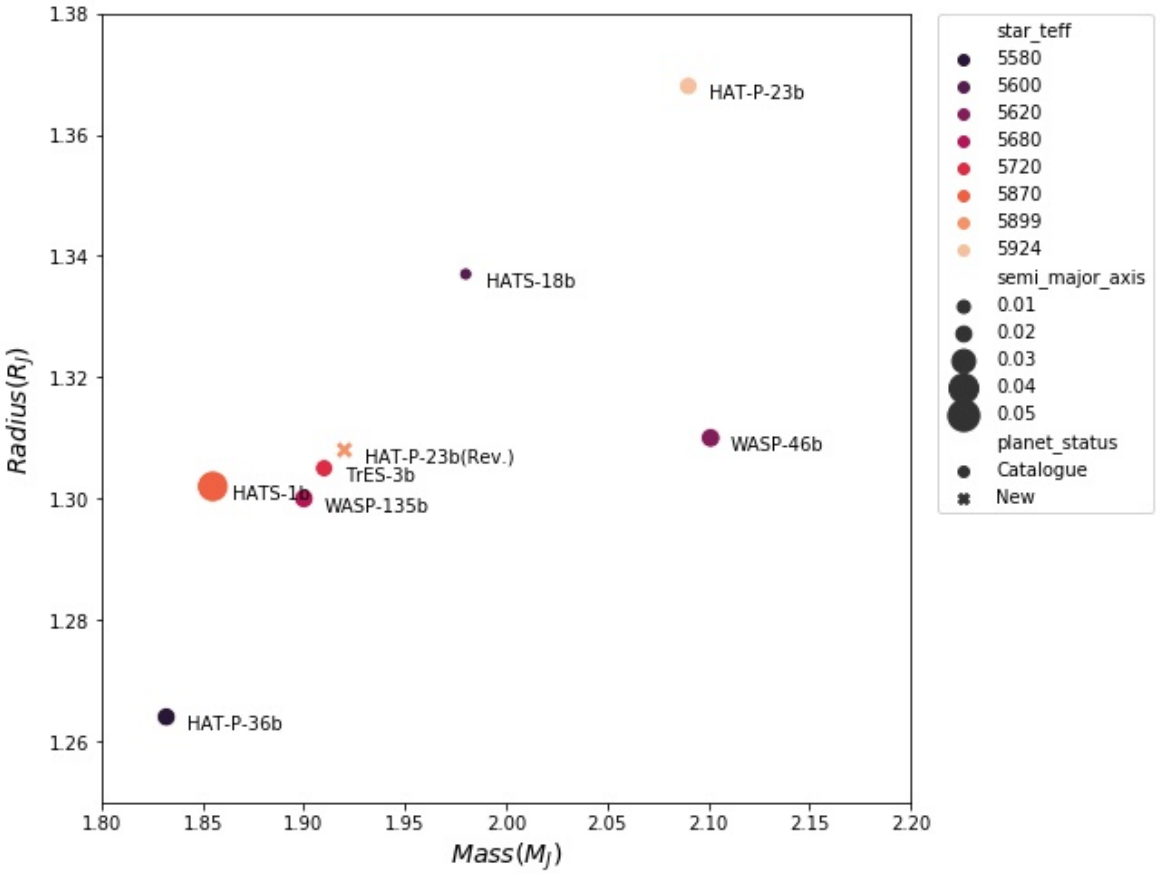

Figure 3.14: Plot showing the revised values of HAT-P-23b resulting from this work compared with other similar systems and how the newly determined parameters change its location in a plot of radius, mass, semi-major axis and host star effective temperature. See also Table 3.7

Table 3.7: Parameter comparison for HAT-P-23b with TrEs-3b and WASP-135b which occupy the same location on a graph of planetary mass vs. radius vs. semi-major axis. Values for HAT-P-23b from this work and TrEs-3b are taken from NASA Exoplanet Archive (accessed 2020-01-02). WASP-135b values are from (Spake et al., 2016), except for T_{eq} which was calculated from their published parameters using (Southworth, 2010, Eq.5). See HAT-P-23b discussion.

Planet Parameter	**HAT-P-23b**	**TrEs-3b**	**WASP-135b**
M_P (M_J)	1.92 ± 0.13	$1.910^{+0.075}_{-0.080}$	1.90 ± 0.08
R_P (R_J)	$1.308^{+0.044}_{-0.043}$	$1.336^{+0.031}_{-0.037}$	1.30 ± 0.09
a (AU)	0.02273 ± 0.00044	$0.02282^{+0.00023}_{-0.00040}$	0.0243 ± 0.0005
Age (Gyr)	$5.5^{+3.0}_{-2.5}$	$0.90^{+2.80}_{-0.80}$	$0.60^{+1.40}_{-0.35}$
T_{eq} (K)	2029^{+29}_{-28}	1638 ± 22	1720 ± 51
$\langle F \rangle$ (10^9erg s^{-1}cm^{-2})	$3.85^{+0.23}_{-0.21}$	1.650 ± 0.079	1.98 ± 0.24

Only transits with full coverage of both the ingress and egress phases were included in the ephemeris calculation and mean combined simultaneous transit times for six epochs where the same transit was observed by multiple observers were used. A linear ephemeris was found to be the best fit to the available data with a $\chi^2_\nu = 2.02$. Though greater than unity, such χ^2_ν values are not uncommon in exoplanet ephemeris results that combine data sets from multiple observers, for example Southworth et al. (2019).

Motivated by the unconfirmed detection of a 0.03 magnitude brightness variation by Sada and Ramón-Fox (2016) during their observing campaign between 2012 and 2014, photometric monitoring of HAT-P-23 was obtained over a 78-day period in 2018. The resulting lightcurve shows a periodic variation of 7.015 days (see Figure 3.6) which is attributed to spots in the rotating photosphere of HAT-P-23b. The amplitude of the variation seen was 0.011 magnitude, significantly less than that seen by Sada and Ramón-Fox (2016), suggesting that the activity cycle of HAT-P-23 has declined since their observations were made. HAT-P-23 is a G0 dwarf star (Bakos et al., 2011) similar to the Sun ($M_* = 1.063 M_\odot$, Table 3.6) but with a significantly shorter period of rotation. The solar cycle is 22 years with activity maximums/minimums every 11 years. The relationship between P_{rot} and P_{cycle} found by Bohm-Vitense (2007) implies an activity cycle period closer to 4 years. Further photometric monitoring observations would be required to accurately determine the activity cycle period for HAT-P-23.

3.4.2 WASP-52b

Long term monitoring of known transiting hot Jupiters has revealed several systems suspected of exhibiting a non-linear ephemeris such as WASP-12b (Maciejewski et al., 2016), WASP-4b (Bouma et al., 2019) and Kepler-1658 (Chontos et al., 2019). Orbital decay is postulated as the cause of the declining orbits while apsidal precession is an alternative explanation and it is difficult to distinguish between these explanations with the available timeline of observations. This is one motivation for extending the timeline of precise transit mid-time observations for short period hot Jupiter systems using readily available small aperture ground-based telescopes.

The new transit timing results obtained with multiple small aperture ground-based telescopes combined with previously published data finds a quadratic ephemeris provides the best fit to the available data. The $\Delta\chi^2_\nu = 0.07$ and $\Delta BIC = 1.53$ between the linear and quadratic ephemerides are small and have not been reported in previous analysis of transit times for WASP-52b, (Mancini et al., 2017; Öztürk and Erdem, 2019; Baluev et al., 2019). The BIC is used to determine whether adding additional free parameters to a model provides a better fit to the data with a smaller BIC indicating a preference for the inclusion of the additional parameters. A BIC decrease of 2.0 is typically the threshold for clearly indicating the inclusion of the additional parameter is preferred. The ΔBIC of 1.53 found for the quadratic over the linear ephemeris is slightly below this threshold. Extrapolating both ephemerides shows that with timing measurements from the 2021 observing season it should be possible to determine if the linear or quadratic model is correct, see Figure 3.9.

Below I consider some possible causes for the period change implied by the quadratic ephemeris model result.

3.4.2.1 Orbital Decay

The result for the period change (Equation 3.5) implies a decay time (based on linear decay to $a = 0$) of 4.1 ± 0.4 Myr, approximately $0.05 \pm 0.03\%$ of the derived age for WASP-52. Following equation 14 from Patra et al. (2017) and using $\delta P/\delta t = -1.22 \pm 0.14 \times 10^{-9}$ the modified tidal quality factor is found to be $Q'_* = 1.1 \pm 0.2 \times 10^3$. This is at least 2-3 orders of magnitude smaller than typically expected (Patra et al., 2017, and references therein), ruling out tidal decay as a potential cause of the observed period change.

3.4.2.2 Apsidal Precession

Apsidal precession requires the planet has an eccentric orbit and the new results presented indicate an eccentricity consistent with zero. If a small eccentricity exists, with a short

1.75d period, a method of maintaining that eccentricity is not clear. Due to the mass ratio, circularisation timescales are dominated by tides raised on the planet (Goldreich and Soter, 1966; Adams and Laughlin, 2006). Aassuming a value for $Q_{\rm P}$ of 10^6 the tidal circularisation timescale ($\tau_{\rm circ}$) is just 4Myr, significantly less than the $8.5^{+3.7}_{-4.6}$Gyr age of the system. The ExofastV2 analysis finds no significant evidence for a departure from a circular orbit, however it is noted that a small eccentricity is possible and additional radial velocity monitoring or secondary occultation observations would be required to confirm the existence, or otherwise, of a small orbital eccentricity.

3.4.2.3 Applegate Effect

In the Applegate effect (Applegate, 1992), changes in the stellar quadrupole moment drive angular momentum transfer within the star over the magnetic cycle period of the star. If angular momentum is transferred from the core to the stellar envelope the star will become more oblate. An orbiting planet period change due to the Applegate effect has been considered by Watson and Marsh (2010). To maintain a constant angular momentum in the changing gravitation potential as the star becomes more oblate the orbital speed must increase and therefore the period decrease. The opposite is true if the oblateness of the star decreases, the period will increase, giving rise to a sinusoidal change in the orbiting planets transit times. Following Equation 13 from Watson and Marsh (2010), setting the time-scale over which the quadrupole changes occur to either the approximate 7.5 years duration of WASP-52b observations, or twice this value, the amplitude of period change is 0.244 or 0.59 seconds respectively. This equates to a maximum period change of 37 ± 10ms yr^{-1} for the 7.5 year quadrupole change or 53 ± 14ms yr^{-1} if the cycle is 15 years. This is consistent with the detected period change value of -38.6 ± 4ms yr^{-1} so orbital period changes due to the Applegate effects cannot be ruled out. For a given set of stellar parameters the magnitude of the O-C value arising from the Applegate effect is sensitive to both the stellar rotation period and the assumed modulation period, with longer a rotation period reducing the O-C value and longer modulation periods increasing it. The stellar rotation period from Hébrard et al. (2013) is dependent on the poorly constrained inclination of the system. Based on spot crossing events Mancini et al. (2017) derived a rotation period of 15.3 ± 1.96d which yields period change values of 28 ± 5ms yr^{-1} for an assumed 7.5 year modulation period. The modulation period is therefore the main unknown parameter and will require further observations to determine.

3.4.2.4 Distant Perturber

Hébrard et al. (2013) identified a possible long term RV trend of $+40\text{ms}^{-1}$ over a period of 15 months which they concluded could be due to a distant companion or a systematic effect resulting from combining multiple data sets. A companion in the range of $10 - 15\text{M}_\text{J}$ out to 6AU was ruled out by a lack of transit timing variation signal (Swift et al., 2015). In their re-analysis of publicly available data from the ETD Baluev et al. (2019) also find no periodic variation attributable to TTVs. A Lomb-Scargle period analysis was undertaken of the combined data set with the new observations finding no evidence of periodicity resulting from TTVs. The acceleration away from Earth of $+40\text{ms}^{-1}$ over 15 months would produce a radial velocity acceleration $\dot{\nu}_r \approx 0.09\text{ms}^{-1}\text{d}^{-1}$ resulting in a positive period derivative of approximately $\dot{P} \approx \dot{\nu}_r P/c \approx 5 \times 10^{-10}$, of opposite sign and an order of magnitude smaller than seen. The measured $\dot{P}$ of -39ms yr^{-1} would require a $\dot{\nu}_r \approx 0.2\text{ms}^{-1}\text{d}^{-1}$, which would be readily detectable in the available radial velocity measurements.

3.4.2.5 Star Spots

The impact of star spots on transit time measurements has been considered by previous authors (E.g. Oshagh et al., 2013; Ioannidis et al., 2016). Barros et al. (2013) identified spot transits as the cause of TTVs in WASP-10b. Ioannidis et al. (2016) showed that timing measurements from higher precision lightcurves are more affected by stellar spots, and they define the transit SNR (TSNR) as the transit depth divided by the out of transit light curve noise level. They demonstrated that for TSNR $\lesssim 15$ systematic timing errors introduced by spot crossing events are not distinguishable from the random noise. They also showed that the magnitude of the effect of spots on timing measurements is determined by the spot longitude on the stellar surface, peaking at $\lambda = \pm 70°$, reducing the closer a spot is to the stellar limb (as the size of the projected spot is reduced) and becoming zero at the centre of the stellar disk. Therefore a spot crossing will induce a positive time variation where it occurs before the transit mid-time and a negative variation where it occurs after transit mid-time, leading to a transit time variation effect than can mimic that caused by a companion planet. For a well aligned and prograde planetary orbit such as that for WASP-52b (Hébrard et al., 2013; Mancini et al., 2017) this TTV mimicking effect would result in detectable variations, or at least an increase in the spread of O-C measurements if the sampling is poor, rather than the declining period seen in the ephemeris of WASP-52b.

The approximately 2.7% deep transits of WASP-52b means that an out of transit noise level of 0.0018 or less is required to achieve $TSNR > 15$, a level of photometric precision marginally achieved in only a small number of the new WASP-52b transits used in the

ephemeris calculation. Therefore it would not expected that the transit mid-time measurements be systematically affected by spot crossing events. While no spot crossing events were positively identified in the new photometry obtained in the 2017-18 season the 2013 archive observation from the UK shows a clear brightening during transit. This observation was obtained during the same period as those by Mancini et al. (2017) who positively detected spot crossing events at 5 of their 7 epochs with full transit coverage. The absence of spot crossing events in the 2017-18 transits could indicate that the photometric precision achieved is insufficient to resolve the spot crossings or that since the 2012-2014 seasons WASP-52's stellar cycle has either quieted or the spot latitude has migrated away from the transit chord. If the spots have ceased or migrated to a different latitude from the transit chord this would be apparent in photometric monitoring of WASP-52. Stellar spots occurring at a latitude different to the transit chord would be visible as stellar variability and potentially detectable as a correlation between stellar flux and transit depth (E.g. Kirk et al., 2016). If WASP-52 is in a reduced activity phase of its stellar cycle it would not be expected to see either effect.

Taken together the lack of transit spot crossing events in the 2017-18 season, along with the brightness variation seen in WASP-52 and the tentative indication that transit depth is greater when stellar brightness is lower, indicate WASP-52 is still active but that the activity latitude has likely migrated away from the transit chord. Observations in future seasons, ideally with a B filter to increase spot contrast, would be required to follow the stellar activity cycle and determine its periodicity. This result shows how observations obtained using small aperture ground-based telescopes can provide monitoring of transiting systems to identify activity cycles. This information can help advise the planning of transmission spectroscopy observations which are complicated by activity on the host star. Identifying the stellar cycle period will also enable any timing variation due to the Applegate effect to be better characterised (see Section 3.4.2.3.

Long term out of transit photometric monitoring is required to gain a better understanding of the activity levels and stellar cycles of exoplanet host stars. The results presented here show that monitoring can be achieved with small aperture ground-based telescopes as part of ongoing transit monitoring campaigns of specific systems. General photometric monitoring could be obtained from long term all sky surveys such as the All Sky Automated Survey [4] with decadal photometric archives. Future exoplanet host monitoring photometry will become available from the Vera C.Rubin Observatory [5] which will measure the entire visible night sky every few nights.

[4] http://www.astrouw.edu.pl/asas/

[5] https://www.lsst.org/

Table 3.8: Ephemeris values for WASP-52b and HAT-P-23b. Epoch is shown as 2450000+.

Planet	Ephemeris	Epoch	Period	Quadratic	χ^2_ν	BIC
WASP-52b	Linear	5793.681914(141)	1.749781099(126)	–	1.58	59.41
WASP-52b	Quadratic	5793.680977(141)	1.749783241(177)	−2.14(24)	1.51	57.88
HAT-P-23b	Linear	4852.265165(120)	1.212886457(54)	–	2.08	33.01

3.5 Summary

17 new transits for HAT-P-23b and 13 new transits of WASP-52b are presented along with contemporaneous photometric monitoring for HAT-P-23, all made with 0.4m class telescopes. For HAT-P-23b the combined radial velocity and new transit analysis results in an orbital eccentricity consistent with zero, in contrast the some previous studies (Bakos et al., 2011; Sada and Ramón-Fox, 2016), but consistent with the assumption of circular orbit by other authors (Maciejewski et al., 2018; Ciceri et al., 2015). The new radius found for HAT-P-23b between previously published values. The planet should still be considered inflated, though the mechanism driving the inflation is not clear as the radius is smaller than that indicated by the empirical mass/incident flux relation for planetary radius derived by Weiss et al. (2013). The monitoring observations of HAT-P-23 have revealed a photometric modulation of 0.011 mag with a period of 7.015 days which is interpreted as the rotation period of HAT-P-23 due to stellar surface spots.

The WASP-52b observations show no evidence for the large spot crossing events seen in previous works. The detection of continuing brightness variations indicates that the spot latitude has migrated away from the transit chord. The analysis of the new and previously published transit times slightly prefers a quadratic ephemeris but only with a $\Delta\chi^2_\nu = 0.07$ and $\Delta\mathrm{BIC} = 1.53$. The effects of removing different new and published transit timing data sets have been investigated and find the quadratic model is preferred in all scenarios except where the very small uncertainties in the timing from Mancini et al. (2017) are taken at face value. Predicting the ephemerides forwards shows that transit observations in the 2021 season will likely be able to reveal if the quadratic ephemeris is real.

The results for HAT-P-23b and WASP-52b presented here have demonstrated that small aperture ground-based telescopes can be used to make valuable contributions to transiting exoplanet studies when deployed for long term monitoring campaigns. In this chapter I have presented results from observations of HAT-P-23b and WASP-52b obtained in a single season. In the next chapter I extend this work to multi-season observations of WASP-12b, a system showing the best evidence yet for orbital decay amongst the hot Jupiter population.

Table 3.9: All transit times used in the ephemeris calculation for HAT-P-23b. Ramon-Fox and Sada (2013) times taken from Sada and Ramón-Fox (2016)

BJD_{TDB}	Error	Source	Epoch	Linear Calc	Linear O-C
2454723.69908	0.00027	Bakos et al. (2011)	-106	2454723.699201	-0.000121
2455026.92049	0.0003	Bakos et al. (2011)	144	2455026.920815	-0.000325
2455715.84175	0.0006	Ramon-Fox et al. (2013)	712	2455715.840322	0.001428
2455777.69855	0.00058	Ramon-Fox et al. (2013)	763	2455777.697532	0.001018
2455789.82583	0.00062	Ramon-Fox et al. (2013)	773	2455789.826396	-0.000566
2455794.67924	0.00054	Ramon-Fox et al. (2013)	777	2455794.677942	0.001298
2456135.49893	0.0002	Ciceri et al. (2015)	1058	2456135.499037	-0.000107
2456176.73801	0.00064	Sada et al. (2016)	1092	2456176.737176	0.000834
2456193.71578	0.00075	Sada et al. (2016)	1106	2456193.717586	-0.001806
2456204.63395	0.00056	Sada et al. (2016)	1115	2456204.633565	0.000385
2456460.55201	0.00022	Ciceri et al. (2015)	1326	2456460.552607	-0.000597
2456477.53294	0.00015	Ciceri et al. (2015)	1340	2456477.533017	-0.000077
2456505.42953	0.00033	Ciceri et al. (2015)	1363	2456505.429406	0.000124
2456512.70668	0.00058	Sada et al. (2016)	1369	2456512.706725	-0.000045
2456539.39052	0.00016	Ciceri et al. (2015)	1391	2456539.390227	0.000293
2456894.76653	0.00052	Sada et al. (2016)	1684	2456894.765959	0.000571
2456911.74741	0.0006	Sada et al. (2016)	1698	2456911.746369	0.001041
2457571.55687	0.00014	Maciejewski et al (2018)	2242	2457571.556602	0.000268
2457627.34962	0.00025	Maciejewski et al (2018)	2288	2457627.349379	0.000241
2457633.41347	0.00018	Maciejewski et al (2018)	2293	2457633.413811	-0.000341
2457633.41302	0.00029	Maciejewski et al (2018)	2293	2457633.413811	-0.000791
2457633.41381	0.00014	Maciejewski et al (2018)	2293	2457633.413811	-0.000001
2457639.47805	0.00024	Maciejewski et al (2018)	2298	2457639.478243	-0.000193
2457958.46740	0.00015	Maciejewski et al (2018)	2561	2457958.467381	0.000019
2457964.53171	0.00015	Maciejewski et al (2018)	2566	2457964.531814	-0.000104
2457981.51210	0.00016	Maciejewski et al (2018)	2580	2457981.512224	-0.000124
2458032.45353	0.00076	This work.	2622	2458032.453455	0.000075
2458043.36908	0.00018	Maciejewski et al (2018)	2631	2458043.369433	-0.000353
2458295.65089	0.00057	This work.	2839	2458295.649816	0.001074
2458300.50097	0.00075	This work.	2843	2458300.501362	-0.000392
2458300.50190	0.0012	This work.	2843	2458300.501362	0.000538
2458306.56787	0.00071	This work.	2848	2458306.565795	0.002075
2458306.56574	0.0007	This work.	2848	2458306.565795	-0.000055
2458312.62941	0.00078	This work.	2853	2458312.630227	-0.000817
2458317.48136	0.00054	This work.	2857	2458317.481773	-0.000413
2458317.48176	0.00025	Maciejewski et al (2018)	2857	2458317.481773	-0.000013
2458334.46187	0.00066	This work.	2871	2458334.462183	-0.000313
2458334.46250	0.00018	Maciejewski et al (2018)	2871	2458334.462183	0.000317
2458340.52720	0.00045	This work.	2876	2458340.526615	0.000585
2458357.50703	0.0006	This work.	2890	2458357.507026	0.000004
2458368.42299	0.00011	Maciejewski et al (2018)	2899	2458368.423004	-0.000014
2458385.40434	0.00068	PIRATE	2913	2458385.403414	0.000926
2458385.40582	0.00075	This work.	2913	2458385.403414	0.002406
2458391.47024	0.00093	This work.	2918	2458391.467847	0.002393
2458408.44838	0.0006	This work.	2932	2458408.448257	0.000123

Table 3.10: All transit times used in the ephemeris calculation for WASP-52b. Delta is the difference between the linear and quadratic ephemeris times. Hébrard et al. (2013) transits times as recalculated by Mancini et al. (2017)

BJD_{TDB}	Error	Source	Epoch	Linear Calc	Linear O-C	Quad Calc	Quad O-C	Delta
2455776.183950	0.001347	Hebrard et al. (2013)	-10	2455776.184103	-0.000153	2455776.183144	0.000806	-0.000959
2455793.681180	0.001976	Hebrard et al. (2013)	0	2455793.681914	-0.000734	2455793.680977	0.000203	-0.000937
2455828.676800	0.001347	Hebrard et al. (2013)	20	2455828.677536	-0.000736	2455828.676641	0.000159	-0.000895
2456271.373314	0.000599	Baluev et al. (2019)	273	2456271.372154	0.00116	2456271.371722	0.001592	-0.000432
2456479.595130	0.001437	Mancini et al.(2017)	392	2456479.596105	-0.000975	2456479.595843	-0.000713	-0.000262
2456491.843065	0.000259	Baluev et al. (2019)	399	2456491.844573	-0.001508	2456491.844320	-0.001255	-0.000253
2456514.592890	0.00052	Ozturk et al. (2019) ETD	412	2456514.591727	0.001163	2456514.591491	0.001399	-0.000236
2456537.338920	0.0015	Ozturk et al. (2019) ETD	425	2456537.338881	0.000039	2456537.338661	0.000259	-0.00022
2456540.838580	0.00061	Ozturk et al. (2019) ETD	427	2456540.838443	0.000137	2456540.838226	0.000354	-0.000217
2456542.588060	0.00093	Ozturk et al. (2019) ETD	428	2456542.588224	-0.000164	2456542.588008	0.000052	-0.000216
2456549.588050	0.001796	Mancini et al.(2017)	432	2456549.587349	0.000701	2456549.587137	0.000913	-0.000211
2456570.585339	0.000625	Baluev et al. (2019)	444	2456570.584722	0.000617	2456570.584525	0.000814	-0.000197
2456572.334910	0.00059	Ozturk et al. (2019) ETD	445	2456572.334503	0.000407	2456572.334307	0.000603	-0.000196
2456586.332920	0.001257	Mancini et al.(2017)	453	2456586.332752	0.000168	2456586.332566	0.000354	-0.000186
2456593.332516	0.000584	Baluev et al. (2019)	457	2456593.331876	0.000639	2456593.331695	0.000821	-0.000182
2456600.331300	0.000517	Baluev et al. (2019)	461	2456600.331001	0.0003	2456600.330824	0.000477	-0.000177
2456607.329890	0.00053	Ozturk et al. (2019) ETD	465	2456607.330125	-0.000235	2456607.329953	-0.000063	-0.000172
2456635.325779	0.000593	Baluev et al. (2019)	481	2456635.326623	-0.000843	2456635.326468	-0.000689	-0.000154
2456850.550250	0.00093	Ozturk et al. (2019) ETD	604	2456850.549698	0.000552	2456850.549664	0.000586	-0.000034
2456862.797710	0.000539	Mancini et al.(2017)	611	2456862.798165	-0.000455	2456862.798138	-0.000428	-0.000028
2456864.547830	0.00065	Ozturk et al. (2019) ETD	612	2456864.547947	-0.000117	2456864.547920	-0.00009	-0.000027
2456869.797637	0.000477	Baluev et al. (2019)	615	2456869.797290	0.000347	2456869.797266	0.000372	-0.000024
2456876.796040	0.001078	Mancini et al.(2017)	619	2456876.796414	-0.000374	2456876.796393	-0.000353	-0.000021
2456883.795520	0.00075	Ozturk et al. (2019) ETD	623	2456883.795539	-0.000019	2456883.795521	-0.000001	-0.000018
2456890.793930	0.001616	Mancini et al.(2017)	627	2456890.794663	-0.000733	2456890.794648	-0.000718	-0.000015
2456906.542370	0.000718	Mancini et al.(2017)	636	2456906.542693	-0.000323	2456906.542685	-0.000315	-0.000007
2456918.790850	0.00036	Swift et al. (2015)	643	2456918.791161	-0.000311	2456918.791159	-0.000309	-0.000002
2456927.541250	0.00091	Ozturk et al. (2019) ETD	648	2456927.540066	0.001184	2456927.540068	0.001182	0.000002

Continued from Table 3.10

BJD_{TDB}	Error	Source	Epoch	Linear Calc	Linear O-C	Quad Calc	Quad O-C	Delta
2456950.286530	0.00052	Ozturk et al. (2019) ETD	661	2456950.287220	-0.00069	2456950.287232	-0.000702	0.000011
2456957.286765	0.000481	Baluev et al. (2019)	665	2456957.286345	0.00042	2456957.286359	0.000406	0.000014
2457013.279716	0.000323	Baluev et al. (2019)	697	2457013.279340	0.000376	2457013.279376	0.00034	0.000036
2457013.279230	0.00032	Ozturk et al. (2019) ETD	697	2457013.279340	-0.00011	2457013.279376	-0.000146	0.000036
2457027.276752	0.000453	Baluev et al. (2019)	705	2457027.277589	-0.000837	2457027.277630	-0.000878	0.000041
2457027.277730	0.00042	Ozturk et al. (2019) ETD	705	2457027.277589	0.000141	2457027.277630	0.0001	0.000041
2457221.505274	0.000565	Baluev et al. (2019)	816	2457221.503291	0.001983	2457221.503389	0.001885	0.000098
2457221.503550	0.00045	Ozturk et al. (2019) ETD	816	2457221.503291	0.000259	2457221.503389	0.000161	0.000098
2457242.501562	0.000334	Baluev et al. (2019)	828	2457242.500664	0.000898	2457242.500767	0.000795	0.000103
2457242.500930	0.00031	Ozturk et al. (2019) ETD	828	2457242.500664	0.000266	2457242.500767	0.000163	0.000103
2457263.497977	0.000155	Baluev et al. (2019)	840	2457263.498037	-0.00006	2457263.498144	-0.000167	0.000107
2457291.493510	0.00047	Ozturk et al. (2019) ETD	856	2457291.494535	-0.001025	2457291.494647	-0.001137	0.000113
2457296.743950	0.0006	Ozturk et al. (2019) ETD	859	2457296.743878	0.000072	2457296.743991	-0.000041	0.000113
2457298.493400	0.00063	Ozturk et al. (2019) ETD	860	2457298.493659	-0.000259	2457298.493773	-0.000373	0.000114
2457326.490090	0.00103	Ozturk et al. (2019) ETD	876	2457326.490157	-0.000067	2457326.490275	-0.000185	0.000118
2457333.488790	0.00092	Ozturk et al. (2019) ETD	880	2457333.489281	-0.000491	2457333.489400	-0.00061	0.000119
2457335.239520	0.00062	Ozturk et al. (2019) ETD	881	2457335.239062	0.000458	2457335.239182	0.000338	0.00012
2457347.486139	0.000753	Baluev et al. (2019)	888	2457347.487530	-0.001391	2457347.487651	-0.001512	0.000121
2457347.487350	0.00073	Ozturk et al. (2019) ETD	888	2457347.487530	-0.00018	2457347.487651	-0.000301	0.000121
2457571.459900	0.0006	Ozturk et al. (2019)	1016	2457571.459511	0.000389	2457571.459645	0.000255	0.000135
2457578.458900	0.0003	Ozturk et al. (2019)	1020	2457578.458635	0.000265	2457578.458770	0.00013	0.000135
2457585.458900	0.0004	Ozturk et al. (2019)	1024	2457585.457759	0.001141	2457585.457894	0.001006	0.000134
2457599.456900	0.0006	Ozturk et al. (2019)	1032	2457599.456008	0.000892	2457599.456142	0.000758	0.000134
2457606.455290	0.00053	Ozturk et al. (2019) ETD	1036	2457606.455133	0.000157	2457606.455266	0.000024	0.000134
2457613.453985	0.000894	Baluev et al. (2019)	1040	2457613.454257	-0.000272	2457613.454390	-0.000405	0.000133
2457613.453610	0.00043	Ozturk et al. (2019) ETD	1040	2457613.454257	-0.000647	2457613.454390	-0.00078	0.000133
2457627.452821	0.000413	Baluev et al. (2019)	1048	2457627.452506	0.000315	2457627.452638	0.000182	0.000133
2457627.455800	0.0018	Ozturk et al. (2019)	1048	2457627.452506	0.003294	2457627.452638	0.003162	0.000133

Continued from Table 3.10

BJD_{TDB}	Error	Source	Epoch	Linear Calc	Linear O-C	Quad Calc	Quad O-C	Delta
2457629.201450	0.002	Bruno et al. (2018)	1049	2457629.202287	-0.000837	2457629.202419	-0.000969	0.000133
2457632.702422	0.000671	Baluev et al. (2019)	1051	2457632.701849	0.000573	2457632.701981	0.000441	0.000132
2457632.701960	0.00025	Ozturk et al. (2019) ETD	1051	2457632.701849	0.000111	2457632.701981	-0.000021	0.000132
2457634.451410	0.000514	Baluev et al. (2019)	1052	2457634.451630	-0.00022	2457634.451762	-0.000352	0.000132
2457634.451970	0.00033	Ozturk et al. (2019)	1052	2457634.451630	0.00034	2457634.451762	0.000208	0.000132
2457641.451020	0.00082	Ozturk et al. (2019) ETD	1056	2457641.450755	0.000265	2457641.450886	0.000134	0.000132
2457655.448840	0.000721	Baluev et al. (2019)	1064	2457655.449003	-0.000163	2457655.449134	-0.000294	0.000131
2457655.451010	0.00083	Ozturk et al. (2019) ETD	1064	2457655.449003	0.002007	2457655.449134	0.001876	0.000131
2457662.450210	0.00087	Ozturk et al. (2019) ETD	1068	2457662.448128	0.002082	2457662.448258	0.001952	0.00013
2457667.697440	0.000414	Baluev et al. (2019)	1071	2457667.697471	-0.000032	2457667.697601	-0.000161	0.00013
2457667.697518	0.000507	Baluev et al. (2019)	1071	2457667.697471	0.000047	2457667.697601	-0.000083	0.00013
2457667.697510	0.00043	Ozturk et al. (2019) ETD	1071	2457667.697471	0.000039	2457667.697601	-0.000091	0.00013
2457669.448980	0.00153	Ozturk et al. (2019) ETD	1072	2457669.447252	0.001728	2457669.447382	0.001598	0.00013
2457676.447507	0.000765	Baluev et al. (2019)	1076	2457676.446377	0.00113	2457676.446506	0.001001	0.000129
2457676.447010	0.00076	Ozturk et al. (2019) ETD	1076	2457676.446377	0.000633	2457676.446506	0.000505	0.000129
2457683.445300	0.0004	Ozturk et al. (2019)	1080	2457683.445501	-0.000201	2457683.445629	-0.000329	0.000128
2457723.690310	0.00062	Ozturk et al. (2019) ETD	1103	2457723.690466	-0.000156	2457723.690590	-0.00028	0.000124
2457970.409800	0.00157	Ozturk et al. (2019) ETD	1244	2457970.409601	0.000199	2457970.409673	0.000127	0.000072
2457984.407700	0.00172	Ozturk et al. (2019) ETD	1252	2457984.407850	-0.00015	2457984.407918	-0.000218	0.000068
2457998.406666	0.000406	Baluev et al. (2019)	1260	2457998.406099	0.000567	2457998.406162	0.000504	0.000063
2457998.406190	0.00041	Ozturk et al. (2019) ETD	1260	2457998.406099	0.000091	2457998.406162	0.000028	0.000063
2458012.402970	0.0011	Ozturk et al. (2019) ETD	1268	2458012.404348	-0.001378	2458012.404406	-0.001436	0.000059
2458031.652100	0.00043	Ozturk et al. (2019) ETD	1279	2458031.651940	0.00016	2458031.651992	0.000108	0.000052
2458045.650141	0.000368	Baluev et al. (2019)	1287	2458045.650188	-0.000047	2458045.650236	-0.000095	0.000047
2458045.650300	0.00032	Ozturk et al. (2019) ETD	1287	2458045.650188	0.000112	2458045.650236	0.000064	0.000047
2458054.398849	0.000479	Baluev et al. (2019)	1292	2458054.399094	-0.000245	2458054.399138	-0.000289	0.000044
2458054.398990	0.00035	Ozturk et al. (2019) ETD	1292	2458054.399094	-0.000104	2458054.399138	-0.000148	0.000044
2458054.398900	0.00039	This work	1292	2458054.399094	-0.000194	2458054.399138	-0.000238	0.000044

Continued from Table 3.10

BJD_{TDB}	Error	Source	Epoch	Linear Calc	Linear O-C	Quad Calc	Quad O-C	Delta
2458080.644920	0.00047	Ozturk et al. (2019) ETD	1307	2458080.645810	-0.00089	2458080.645845	-0.000925	0.000035
2458096.394400	0.001	Ozturk et al. (2019) ETD	1316	2458096.393840	0.00056	2458096.393869	0.000531	0.000029
2458325.616547	0.00064	Baluev et al. (2019)	1447	2458325.615164	0.001383	2458325.615086	0.001461	-0.000078
2458325.615090	0.00047	Ozturk et al. (2019) ETD	1447	2458325.615164	-0.000074	2458325.615086	0.000004	-0.000078
2458332.614240	0.00026	This work	1451	2458332.614289	-0.000049	2458332.614207	0.000033	-0.000082
2458339.612980	0.00031	This work	1455	2458339.613413	-0.000433	2458339.613327	-0.000347	-0.000086
2458346.611794	0.0003	Baluev et al. (2019)	1459	2458346.612537	-0.000743	2458346.612448	-0.000654	-0.00009
2458346.611877	0.000653	Baluev et al. (2019)	1459	2458346.612537	-0.000661	2458346.612448	-0.000571	-0.00009
2458346.612000	0.00041	Ozturk et al. (2019) ETD	1459	2458346.612537	-0.000537	2458346.612448	-0.000448	-0.00009
2458348.360960	0.00123	Ozturk et al. (2019) ETD	1460	2458348.362319	-0.001359	2458348.362228	-0.001268	-0.00009
2458353.612008	0.000538	Baluev et al. (2019)	1463	2458353.611662	0.000346	2458353.611568	0.000439	-0.000093
2458353.611500	0.00033	Ozturk et al. (2019) ETD	1463	2458353.611662	-0.000162	2458353.611568	-0.000068	-0.000093
2458360.610830	0.00031	This work	1467	2458360.610786	0.000044	2458360.610689	0.000141	-0.000097
2458369.359200	0.00045	Ozturk et al. (2019) ETD	1472	2458369.359692	-0.000492	2458369.359589	-0.000389	-0.000102
2458381.608130	0.00036	This work	1479	2458381.608159	-0.000029	2458381.608050	0.00008	-0.00011
2458383.360020	0.00105	Ozturk et al. (2019) ETD	1480	2458383.357941	0.002079	2458383.357830	0.00219	-0.000111
2458388.607390	0.00071	Ozturk et al. (2019) ETD	1483	2458388.607284	0.000106	2458388.607170	0.00022	-0.000114
2458390.357176	0.000658	Baluev et al. (2019)	1484	2458390.357065	0.000111	2458390.356950	0.000225	-0.000115
2458390.357490	0.00053	Ozturk et al. (2019) ETD	1484	2458390.357065	0.000425	2458390.356950	0.00054	-0.000115
2458395.606190	0.00035	This work	1487	2458395.606408	-0.000218	2458395.606290	-0.0001	-0.000118
2458397.357160	0.00054	This work	1488	2458397.356189	0.000971	2458397.356070	0.00109	-0.000119
2458402.605160	0.00076	This work	1491	2458402.605533	-0.000373	2458402.605411	-0.000251	-0.000122
2458404.355710	0.00117	Ozturk et al. (2019) ETD	1492	2458404.355314	0.000396	2458404.355191	0.000519	-0.000123
2458411.354044	0.00039	Baluev et al. (2019)	1496	2458411.354438	-0.000394	2458411.354311	-0.000267	-0.000127
2458411.353790	0.0003	Ozturk et al. (2019) ETD	1496	2458411.354438	-0.000648	2458411.354311	-0.000521	-0.000127
2458425.354291	0.000676	Baluev et al. (2019)	1504	2458425.352687	0.001604	2458425.352551	0.001739	-0.000136
2458425.352900	0.00048	Ozturk et al. (2019) ETD	1504	2458425.352687	0.000213	2458425.352551	0.000349	-0.000136
2458425.352960	0.00029	This work	1504	2458425.352687	0.000273	2458425.352551	0.000409	-0.000136
2458451.598990	0.00081	Ozturk et al. (2019) ETD	1519	2458451.599403	-0.000413	2458451.599251	-0.000261	-0.000152

Chapter 4

WASP-12b

4.1 Introduction

In the previous chapter I considered observations made of two systems over a single season. I now move on to consider observations made of a single target, WASP-12b, using the same small aperture ground-based telescopes over multiple observing seasons. This enables a longer term, and therefore more in depth, study but introduces additional complexities of combining data obtained in different seasons with different observing modes.

Its relatively bright host star (V=11.57), deep transits (1.4%) and very short period (1.09d) make WASP-12b an excellent candidate for follow up with small aperture telescopes on the ground over long, multi season, observing campaigns. Host star monitoring was carried out between 2016 and 2019 and transit observations were made from 2016 to 2020 using the PIRATE, COAST and POST telescopes as described in Chapter 2 with the aim of:

- To monitor WASP-12 over multiple seasons for photometric variations that may result from stellar activity or rotation.
- To determine the precision and accuracy (in comparison with the literature) of the planetary and stellar parameters determined from transit observations made with multiple small aperture ground-based telescopes.
- To measure transit times obtained over multiple observing seasons in the search for periodic and secular timing variations.
- To analyse of the ability of the small aperture ground-based telescope observations to detect transit timing changes over multiple seasons.

This chapter is laid out as follows. First I discuss the current state of knowledge for the WASP-12 system. I then detail the observations made, followed by the data reduction

and analysis. Next I report results for the host star monitoring, transit analysis and transit timing. Finally I consider the results from the small aperture ground-based telescopes in the context of the current understanding of WASP-12 system.

4.2 WASP-12b Background

WASP-12b is a highly irradiated hot Jupiter orbiting a late F-type star in just 1.09 days (Hebb et al., 2009) and has become one of the most heavily studied exoplanets, thought to be highly bloated and losing mass (Li et al., 2010; Fossati et al., 2010; Haswell et al., 2012). In 2014 WASP-12 was discovered to be part of a hierarchical triple system when the previously known companion was resolved, through lucky imaging techniques, to be composed of two M0V stars (Bechter et al., 2014).

Observations in the near-UV made with the Hubble Space Telescope showed that WASP-12b is surrounded by an extended and diffuse exosphere of near-UV absorbing gas that extends beyond WASP-12b's Roche lobe (Haswell et al., 2012). Further observations with Hubble supported these findings and confirmed that the near-UV gas surrounding WASP-12b is patchy in nature suggesting variable mass loss from the planet (Fossati et al., 2010; Haswell et al., 2012). Swain et al. (2013) found an IR brightness temperature for WASP-12b of 3000K, similar to that of an M class dwarf star.

In their near UV measurements made with HST Fossati et al. (2010) detected an early transit ingress, the UV transit ingress occurring before the optical ingress implying the existence of UV absorbing material ahead of WASP-12b. Llama et al. (2011) considered the possibility of a bow shock as the cause, where the planet moves supersonically through the local stellar outflow. If bow shocks exist they provide a unique way to measure the planetary and stellar magnetic fields and their interaction. Subsequent ground-based searches have not detected this early ingress (Turner et al., 2016). A variation in the homogeneity of the gas surrounding WASP-12 is not unexpected, two near UV transits observed with HST 184 days apart showed differences in the transit depth indicating changes in the distribution of the surrounding gas (Haswell et al., 2012). Stellar activity could lead to such variation in the gas surrounding WASP-12 through which the planet orbits, highlighting the importance of long term monitoring to characterise hot Jupiter host stars.

Due to its extremely short period, several studies have focused on measuring transit timings to detect variations indicative of companion planets in exterior orbits. A search of the SuperWASP data by Smith et al. (2009) looking for additional transit events with a period between 5-25 days found no evidence of an additional transiting planet. The first claim of timing variations came from two transit timing observations that suggested a TTV

at the 3.4σ level, which the authors suggested could be caused by a terrestrial type planet in a close resonance orbit (Maciejewski et al., 2011b). A further study of 61 light curves from 13 different observatories, including from amateur observers and including RV studies, indicated "marginal support" for an additional $0.1M_J$ planet on an eccentric 3.6d orbit (Maciejewski et al., 2013a).

Collins et al. (2017a) published a further 23 complete WASP-12b lightcurves obtained with a 0.6m telescope and analysed in a homogenous fashion. They found no evidence of sinusoidal TTVs at the ±35 second level. However, as the authors concede, the coverage was sparse and they could not rule out short term or non-sinusoidal variation. Reviewing the coverage, the 23 transits were observed over a 64-month period. With WASP-12b's 1.09d orbit this project therefore sampled only 1.3% of the total number of transits occurring during this period, highlighting the difficulties of measuring TTVs with ground-based telescopes.

The small but non zero eccentricity of 0.049±0.015 reported by Hebb et al. (2009) raises the possibility of detecting apsidal precession for WASP-12b. Ragozzine and Wolf (2009) investigated using apsidal precession in hot Jupiters to probe the planetary interior, concluding that the quadrupole of the planetary tidal bulge is the dominant source of apsidal precession for hot Jupiters. They found that, out of planets known at the time, WASP-12b represented the best opportunity for detecting apsidal precession with a predicted total apsidal motion of $19.9^{\circ}\mathrm{yr}^{-1}$ resulting in a periodic timing variation amplitude of 25 minutes occurring over an 18.09 year period, assuming the eccentricity reported by Hebb et al. (2009) is real. This rapid precession period led to a number of studies of occultations of WASP-12b as a way to determine the reality of the eccentricity indicated by the radial velocity measurements. The results of these analyses preferred an eccentricity consistent with zero (Croll et al., 2011; Campo et al., 2011).

In an attempt to detect angular momentum transfer and orbital precession in WASP-12b Maciejewski et al. (2016) presented 29 transit observations made over 4 observing seasons with multiple medium class (0.6m to 2.56m) telescopes. While their results do not show evidence for periodic variations they do show that, when combined with previous data and the observations binned into observing seasons, the transit times do not follow a linear ephemeris, indicating the orbital period is declining at a rate of $-25.6 \pm 4\mathrm{msyr}^{-1}$. The authors were unable to conclusively distinguish between orbital decay or apsidal precession. Interestingly this study covers a similar number of transits over a similar and slightly overlapping time span as that carried out by Collins et al. (2017a) who made no claim of variation from a linear ephemeris. This initial finding triggered a rapid succession of studies into the non-linear ephemeris for WASP-12b with new observations incrementing the baseline with additional transit and/or eclipse measurements (Patra et al., 2017; Maciejewski et al., 2018; Baluev

et al., 2019; Öztürk and Erdem, 2019). Observations of occultations of WASP-12b are key to determining between the orbital and apsidal precession models. In the case of a precessing orbit the occurrence of the transits and occultations will be 180° out of phase, while in the case of orbital decay they will occur in phase (Patra et al., 2017). Yee et al. (2019) published new transit times and a further 9 previously unpublished occultation times showing the transits and occultations are occurring in phase and therefore confirming the orbital decay model for WASP-12b. The same authors also presented additional RV data, extending the baseline of measurements and improving the precision of the line of sight acceleration of WASP-12 ($|\dot{v}| < 0.005\text{m s}^{-1}\text{ day}^{-1}$), ruling out the Rømer effect as a significant contribution to the changing period. Observations of 21 transits with TESS in 2020 support the orbital decay model (Turner et al., 2021).

One of the largest studies of transits of WASP-12b was carried out by Baluev et al. (2019) who homogeneously analysed 280 transit light curves obtained over an 11 year period comprised mostly of amateur observations recorded on the Exoplanet Transit Database. They were able to successfully recover the quadratic ephemeris for orbital decay (they did not fit for apsidal precession), though with an approximately 10% smaller rate of decay.

The existence of orbital decay in WASP-12b requires a mechanism to dissipate the orbital energy. The commonly invoked mechanism for this is raising of tides and their subsequent dissipation within the host star. Main sequence F type stars have small convective cores with largely radiative envelopes surrounded by a thin outer convective envelope. Studies have determined tidal dissipation within this stellar structure is insufficient to explain the orbital rate decay seen (Chernov et al., 2017; Weinberg et al., 2017). However once an F star evolves onto the sub-giant branch its core becomes radiative allowing the tidal wave breaking at much smaller radii and making tidal dissipation in a sub-giant host star a better fit to the observed decay rate (Weinberg et al., 2017). This explanation also provides an answer to how WASP-12b has survived for the 1-2 Gyr life of the host star, tidal decay would only have commenced as the star evolved on to the sub-giant branch. Furthermore this finding would be consistent with the measured slow rotation for WASP-12 as tidal spin up would only affect the very small core of a sub-giant which would be insufficient to spin up the outer envelope (Weinberg et al., 2017). Further analysis by Bailey and Goodman (2019) finds that while neither main sequence or sub giant models fit all the observational data, specifically a disagreement between spectroscopically derived T_{eff} and metalicity with the Gaia derived luminosity (an issue the authors note would exist regardless of orbital decay), the main sequence models are less discrepant leaving the question of the source of the tidal damping open.

Using a combination of published and new RV data Maciejewski et al. (2020) confirmed

the existence of a tidal bulge on the surface of WASP-12 through measurement of an RV period of half that of the orbital period with an amplitude of just a few meters per second. This signal mimics a non zero eccentricity with a longitude of periastron of 270°. The authors find e $= 0.035 \pm 0.006$ and $\omega = 270.7 \pm 0.6°$, a 5.8σ detection of eccentricity indicating a tidal bulge height of approximately 150km is being raised on WASP-12 by the orbiting hot Jupiter. The authors predict the tidal bulge should cause a photometric variation of 80ppm, potentially detectable with space based telescopes. This result also neatly explains why eccentricity has been found from RV studies but occultation timing studies have indicated a circular orbit.

When discovered, WASP-12 was determined to have a low rotation speed for a late F type star with a projected stellar $v\sin i = 2.2 \pm 1.5$ km s^{-1} (Hebb et al., 2009). The same authors were also unable to detect any signs of a Rossiter-McLaughlin (RM) effect, consistent with a low projected rotational velocity. A study of 12,000 stars observed by the Kepler telescope finds a mean equatorial velocity of $10 - 40$ km s^{-1} and rotation periods of 2 to 4 days for F7 stellar types (Nielsen et al., 2013). The implication being that either WASP-12 is an abnormally slow rotator or is viewed at a very low inclination, i.e. near pole on. Fossati et al. (2010) determined that the stellar macro-turbulence is greater than the measured rotation velocity, leaving the RM effect as the only spectroscopic approach to determining rotational velocity. Husnoo et al. (2012) obtained 16 spectroscopic measurements during a single transit and found a weak RM signal but their analysis of the sky projected spin-orbit angle (λ) was inconclusive. Albrecht et al. (2012) obtained 38 radial velocity measurement before, during and after transit. In their analysis they find an orbital misalignment of $\lambda = 59^{+15}_{-20}{}^{\circ}$ and $v\sin i = 1.6^{+0.8}_{-0.4}$ k ms^{-1}. Their conclusion is that we observe WASP-12 at low stellar rotational inclination and therefore the orbit of WASP-12b the planet must be significantly misaligned. No long term photometric monitoring of WASP-12 has been found in the literature.

The existence of secular period changes has important implications for theories of planetary formation and dynamical history, whether the cause is apsidal precession, orbital decay or due to a long period companion . Despite the intense scrutiny WASP-12b has received in recent years, especially since the discovery of the non linear ephemeris, long term monitoring of this (and similar systems) is required to follow the detected period change over multiple observing seasons.

4.3 The Observations

4.3.1 Monitoring Observations

Monitoring observations were obtained during the 2016-17, 2017-18 and 2018-19 seasons as detailed in Table 4.1. All the observation were made with PIRATE using either Baader Red, Rc or Blue filters. Blue filter observation of WASP-12 obtained during the 2016-17 observing season could not be analysed due to saturation of the CCD.

Table 4.1: Photometric monitoring observations obtained of WASP-12 over three seasons The first two seasons were obtained using Baader broadband Red and Blue filters and in the final season using Johnson-Cousins Rc and B filters. Bin is the CCD on chip binning mode used, N indicates the number of observations made. Dur(d) is the number of days the observations span and density indicates the number of available nights during this period observations were made.

Season	Start	End	Filter	Exp.(s)	Bin	N	Dur(d)	Density
2016-17	06/10/2016	27/03/2017	Red	45	2×2	2487	173	40%
2016-17	25/11/2016	29/01/2017	Blue	90	2×2	568	66	44%
2017-18	18/01/2018	28/04/2018	Red	45	2×2	167	100	26%
2017-18	18/01/2018	28/04/2018	Blue	45-60	2×2	156	100	23%
2018-19	29/08/2018	02/03/2019	Rc	90-120	1×1	216	186	41%
2018-19	30/08/2018	02/03/2019	B	180	1×1	233	185	42%

4.3.2 Transit Observations

In total 65 transit observations were obtained between 2013 and 2020, including three archive transits observed with POST between 2013 and 2016. Of these transits 47 have full coverage of the primary transit and 18 have only partial coverage as summarised in Tables 4.2 and 4.3. The observations were made with the three telescopes, PIRATE, COAST and POST as described in Chapter 2. As the transit and monitoring observations were obtained over a much longer duration than those for HAT-P-23b and WASP-52b in the previous chapter a number of equipment changes and upgrades were made at the observatories resulting in observations being made with a variety of cameras and filters which needed to be accounted for.

Table 4.2: Transit observations made of WASP-12b between 2013 and Summer of 2018 before PIRATE and COAST were upgraded. Obs is the observation number corresponding to the transit plots in Figures 4.3 to 4.5. Exp. is the exposure duration in seconds, N_{obs} is the number of frames obtained over the duration (in hours) of each observation. Flip indicates whether a pier flip was carried out to cross the Meridian and RMS is the RMS scatter in the out of transit data. Coverage indicates whether the transit has full coverage or is partial.

Obs	Date	Telescope	Filter	Binning	Exp(s)	N_{obs}f	Flip	Duration	Airmass Range	RMS	Coverage	Notes
1	19/11/2013	POST	Rc	3×3	60	218	N	3.63	1.62-1.08	0.005377	Full	
2	24/11/2014	POST	Rc	2×2	90	144	N	3.6	1.55-1.08	0.002127	Full	Gap during transit
3	10/03/2015	POST	Rc	2×2	120	104	N	3.47	1.08-1.39	0.001941	Full	
4	15/01/2016	POST	Rc	2×2	120	131	N	4.37	1.44-1.08-1.10	0.002496	Full	
5	04/12/2016	PIRATE	Red	2×2	45	123	Y	1.54	1.31-1.02-1.04	-	Partial	Several large gaps.
6	06/12/2016	PIRATE	Red	2×2	45	265	Y	3.31	1.00-1.39	0.00235	Full	
7	15/12/2016	COAST	Rc	1×1	60	225	N	3.75	1.85-1.00	0.003503	Full	STL1001 CCD
8	15/12/2016	PIRATE	Red	2×2	45	342	N	4.28	1.88-1.00	0.002921	Full	
9	27/12/2016	POST	Rc	2×2	120	132	Y	4.4	1.23-1.07-1.18	0.001722	Full	
10	28/12/2016	POST	Rc	2×2	120	122	N	4.07	1.07-1.59	0.001891	Full	
11	09/01/2017	PIRATE	Red	2×2	45	297	Y	3.71	1.00-1.56	0.002922	Full	CCD temp -20
12	19/01/2017	PIRATE	Red	2×2	45	320	Y	4	1.42-1.00-1.02	0.002162	Full	
13	20/01/2017	POST	Rc	2×2	120	122	N	4.07	1.06-1.00-1.23	0.00142	Full	
14	31/01/2017	PIRATE	Red	2×2	45	241	Y	3.01	1.19-1.00-1.06	0.002618	Full	Several gaps during transit
15	13/02/2017	COAST	Rc	1×1	60	201	N	3.35	1.00-1.80	0.001655	Full	STL1001 CCD
16	13/02/2017	POST	Rc	2×2	120	136	N	4.53	1.01-2.37	0.002748	Full	
17	24/02/2017	POST	Rc	2×2	150	77	N	3.21	1.07-1.35	-	Partial	Data ends prior to t3. Defocused.
18	08/12/2017	POST	Rc	2×2	75	198	N	4.13	1.58-1.08	0.001868	Full	
19	21/12/2017	PIRATE	Red	2×2	45	350	Y	4.38	1.14-1.00-1.20	0.002347	Full	
20	23/12/2017	PIRATE	Red	2×2	45	336	N	4.2	1.00-2.13	0.004197	Full	
21	13/01/2018	PIRATE	Red	2×2	45	193	N	2.41	1.21-1.00-1.19	-	Partial	First half of transit only.
22	14/01/2018	PIRATE	Red	2×2	45	218	Y	2.73	1.00-1.20	-	Partial	First half of transit only.
23	25/01/2018	COAST	Rc	1×1	60	233	Y	3.88	1.08-1.00-1.26	0.002567	Full	STL1001 CCD
24	25/01/2018	PIRATE	Red	2×2	45	350	Y	4.38	1.07-1.00-1.31	0.003078	Full	
25	25/01/2018	POST	Rc	2×2	90	76	N	1.9	1.08-1.35	-	Partial	No OOT data, large gap.
26	17/02/2018	POST	Rc	2×2	90	180	Y	4.5	1.13-1.08-1.42	0.002417	Full	
27	13/03/2018	COAST	Rc	1×1	60	220	N	3.67	1.01-1.96	0.003643	Full	STL1001 CCD. Defocussed (38″).

Table 4.3: Transit observations made of WASP-12b after PIRATE and COAST were upgraded. Column headings are as described for Table 4.2

Obs.	Date	Telescope	Filter	Binning	Exp(s)	N_{obs}	Flip	Duration	Airmass Range	oot RMS	Coverage	Notes
28	16/10/2018	PIRATE	Rc	1×1	120	107	N	3.57	2.25-1.04	0.003047	Full	
29	08/11/2018	COAST	Rc	1×1	180	72	N	3.6	2.27-1.03	-	Partial	missing t_1 and pre ingress data
30	08/11/2018	PIRATE	Rc	1×1	120	43	N	1.43	1.23-1.04	-	Partial	Second half and post egress only.
31	09/11/2018	COAST	Rc	1×1	180	77	Y	3.85	1.29-1.00-1.05	0.001464	Full	
32	09/11/2018	PIRATE	Rc	1×1	120	120	Y	4	1.34-1.00-1.03	0.001333	Full	
33	10/11/2018	COAST	Rc	1×1	180	60	Y	3	1.28-1.00-1.25	-	Partial	Missing t_4 and post egress data.
34	03/12/2018	PIRATE	Rc	1×1	90	133	Y	3.33	1.03-1.00-1.29	0.001655	Full	Gap between Tc and t_3.
35	14/12/2018	COAST	Rc	1×1	180	69	Y	3.45	1.24-1.00-1.10	-	Partial	Large gap during transit
36	14/12/2018	PIRATE	Rc	1×1	90	158	Y	3.95	1.19-1.00-1.08	0.002055	Full	
37	15/12/2018	COAST	Rc	1×1	180	81	Y	4.05	1.00-1.63	0.001466	Full	
38	15/12/2018	PIRATE	Rc	1×1	90	154	Y	3.85	1.00-1.59	0.001697	Full	
39	26/12/2018	PIRATE	Rc	1×1	90	80	N	2	1.00-1.20	-	Partial	Second half and post egress only.
40	27/12/2018	COAST	Rc	1×1	150	93	N	3.88	1.01-2.25	0.001269	Full	
41	27/12/2018	PIRATE	Rc	1×1	90	146	N	3.65	1.02-2.30	0.002118	Full	Coverage starts at t_1
42	07/01/2019	COAST	Rc	1×1	120	64	N	2.13	1.03-1.35	-	Partial	Second half and post egress only.
43	07/01/2019	PIRATE	B	1×1	180	47	N	2.35	1.03-1.42	-	Partial	Second half and post egress only.
44	17/01/2019	POST	Rc	1×1	240	63	N	4.2	1.43-1.09	0.001486	Full	
45	28/01/2019	POST	Rc	1×1	180	74	N	3.7	1.56-1.08	0.000995	Full	
46	29/01/2019	COAST	Rc	1×1	150	76	Y	3.17	1.22-1.00-1.02	-	Partial	t_1 and pre-ingress missing
47	29/01/2019	PIRATE	Rc	1×1	90	147	Y	3.68	1.28-1.00-1.02	-	Partial	t_1 missing
48	30/01/2019	PIRATE	B	1×1	180	84	Y	4.2	1.03-1.00-1.33	0.001625	Full	
49	30/01/2019	COAST	Rc	1×1	150	97	Y	4.04	1.05-1.00-1.36	0.001824	Full	
50	31/01/2019	PIRATE	B	1×1	180	67	N	3.35	1.06-2.22	0.002273	Full	Little pre ingress data
51	31/01/2019	COAST	Rc	1×1	150	80	N	3.33	1.04-2.29	0.002079	Full	
52	10/02/2019	COAST	Rc	1×1	150	87	Y	3.63	1.13-1.00-1.15	-	Partial	t_1 and pre-ingress missing
53	11/02/2019	COAST	Rc	1×1	150	80	Y	3.33	1.02-1.00-1.43	-	Partial	Flip at t_1. Data gaps.
54	11/02/2019	PIRATE	B	1×1	180	52	Y	2.6	1.00-1.42	-	Partial	Mid transit missing, clouds.
55	21/02/2019	POST	Rc	1×1	180	76	N	3.8	1.20-1.08-1.15	0.001378	Full	
56	22/02/2019	PIRATE	B	1×1	180	80	Y	4	1.05-1.00-1.25	0.001454	Full	Coverage starts at t_1
57	22/02/2019	COAST	Rc	1×1	150	96	Y	4	1.05-1.00-1.32	0.001406	Full	Coverage starts at t_1
58	23/02/2019	COAST	Rc	1×1	150	100	N	4.17	1.00-2.04	0.001865	Full	
59	23/02/2019	PIRATE	B	1×1	180	72	Y	3.6	1.00-2.04	-	Partial	Ingress missing
60	30/12/2019	POST	Ic	1×1	180	99	N	4.95	1.65-1.07-1.09	0.001899	Full	
61	31/12/2019	PIRATE	Rc	1×1	90	171	Y	4.28	1.13-1.00-1.22	0.001677	Full	
62	01/01/2020	PIRATE	Rc	1×1	90	161	N	4.03	1.00-2.08	0.003349	Full	
63	10/01/2020	POST	Rc	1×1	180	85	N	4.25	1.72-1.07	0.003581	Full	
64	12/01/2020	PIRATE	Rc	1×1	90	168	Y	4.2	1.04-1.00-1.39	0.001759	Full	
65	22/03/2020	POST	Rc	1×1	180	81	N	4.05	1.10-2.22	0.001631	Full	

4.4 Data Analysis

Data reduction was undertaken as documented in Chapter 2.

4.4.1 Monitoring Data Analysis

Ensemble photometry was carried out for each season and filter in AstroImageJ using the comparison and check stars shown in Tables 4.4, 4.5 and 4.6. Scintillation noise was calculated and added to the photometric uncertainties generated by AstroImageJ as detailed in Chapter 3.2. As the formal uncertainties on the UCAC4 catalogue magnitudes dominate the measurement uncertainties by at least an order of magnitude and contribute a constant value to every uncertainty value only the photometric uncertainties were used.

After photometric extraction the seasonal data sets were corrected as follows before period analysis was carried out;

1. A linear trend for each individual data group (filter, exposure and mount direction) was identified separately and corrected for.

2. As with the transit data an offset is seen between observations made when the optical tube was on the East or the West side of the mount. The difference in measured magnitude (offset) was identified between each different mount direction data set and corrected for by adding or subtracting half the offset value as appropriate.

An example of before and after correction for the 2016-17 season observations obtained through the Red filter is shown in Figure 4.1. The final detrended monitoring data sets for each season and filter were analysed both individually and together as a whole using a Lomb-Scargle period analysis to allow any variation in any detected periodicities between seasons to be identified.

A suitable check star was selected based on having a similar magnitude and B-V colour index to WASP-12. The check star was analysed as a target in the same way as for WASP-12.

4.4.2 Transit Analysis in ExofastV2

The large number of transit lightcurves to be analysed simultaneously using Exofastv2 places limits on the number of MCMC steps that could be completed in a reasonable run time and within the computer memory available. Therefore a stepwise iterative approach was adopted starting with an initial priors file, 1000 steps and *nthin* set at 1. The parameter *nthin* sets the number of adjacent (and therefore highly correlated) steps to be discarded thereby reducing memory requirement (Eastman et al., 2019). Once complete the output from this short run was used to create the starting priors file for a longer 4000 step run with $nthin = 1$. This was

Table 4.4: WASP-12b 16-17 and 17-18 seasons Blue filter photometry template stars. The aperture column indicates whether the star was a target (T_n) or a member of the comparison ensemble (C_n).

Aperture	UCAC4 Ref.	B Mag	σ B	B-V	Target
T1	599-033155	12.883	0.03	0.693	J0630+2942
C2	599-033108	13.631	0.04	0.624	
C3	599-033103	14.124	0.05	0.274	
C4	599-033109	14.6	0.05	1.203	
C5	599-033158	14.412	0.02	1.043	
C6	599-033061	14.374	0.03	0.561	
C7	599-033048	14.236	0.06	0.512	
C8	599-033166	14.86	0.04	1.411	
C9	599-033225	14.089	0.03	0.592	
C10	599-033239	14.253	0.03	1.02	
C11	599-033258	13.826	0.02	1.082	
C12	599-033264	13.997	0.03	0.648	
C13	600-034092	13.571	0.03	0.661	
T14	600-034149	13.363	0.04	0.605	Check Star
T15	599-033160	12.138	0.02	0.578	WASP-12 (2017-18 only)

Table 4.5: WASP-12b 16-17 and 17-18 seasons Red filter photometry template stars.

Aperture	UCAC4 Ref.	r′ Mag	σr′	B-V	Target
T1	599-033160	11.427	0.06	0.578	WASP-12
T2	599-033155	11.993	0.07	0.693	J0630+2940
C3	599-033126	11.565	0.07	0.515	
C4	598-033148	11.779	0.06	0.451	
C5	599-033054	11.906	0.07	1.1	
C6	598-033283	11.921	0.05	0.609	
C7	600-033816	11.88	0.08	0.716	
C8	599-033368	11.862	0.03	0.646	
C9	599-033206	11.393	0.05	0.266	
C10	600-033847	12.586	0.06	0.172	
T11	599-032930	11.519	0.08	0.658	Check Star

Table 4.6: WASP-12b 18-19 season Red and Blue filter photometry template stars.

Aperture	UCAC4 Ref.	B Mag	σ B	r′ Mag	σ r′	B-V	Target
T1	599-033160	12.138	0.02	11.427	0.06	0.578	WASP-12
T2	599-033155	12.883	0.03	11.993	0.07	0.693	J0630+2942
C3	599-033126	12.187	0.04	11.565	0.07	0.515	
C4	598-033148	12.32	0.03	11.779	0.06	0.451	
C5	599-033054	13.359	0.03	11.906	0.07	1.1	
C6	598-033283	12.67	0.02	11.921	0.05	0.609	
C7	600-033816	12.79	0.05	11.88	0.08	0.716	
C8	599-033368	12.622	0.03	11.826	0.03	0.646	
C9	599-033206	11.647	0.04	11.393	0.05	0.266	
C10	600-033847	12.692	0.05	12.586	0.06	0.172	
T11	599-032930	12.345	0.05	11.519	0.08	0.658	Check Star

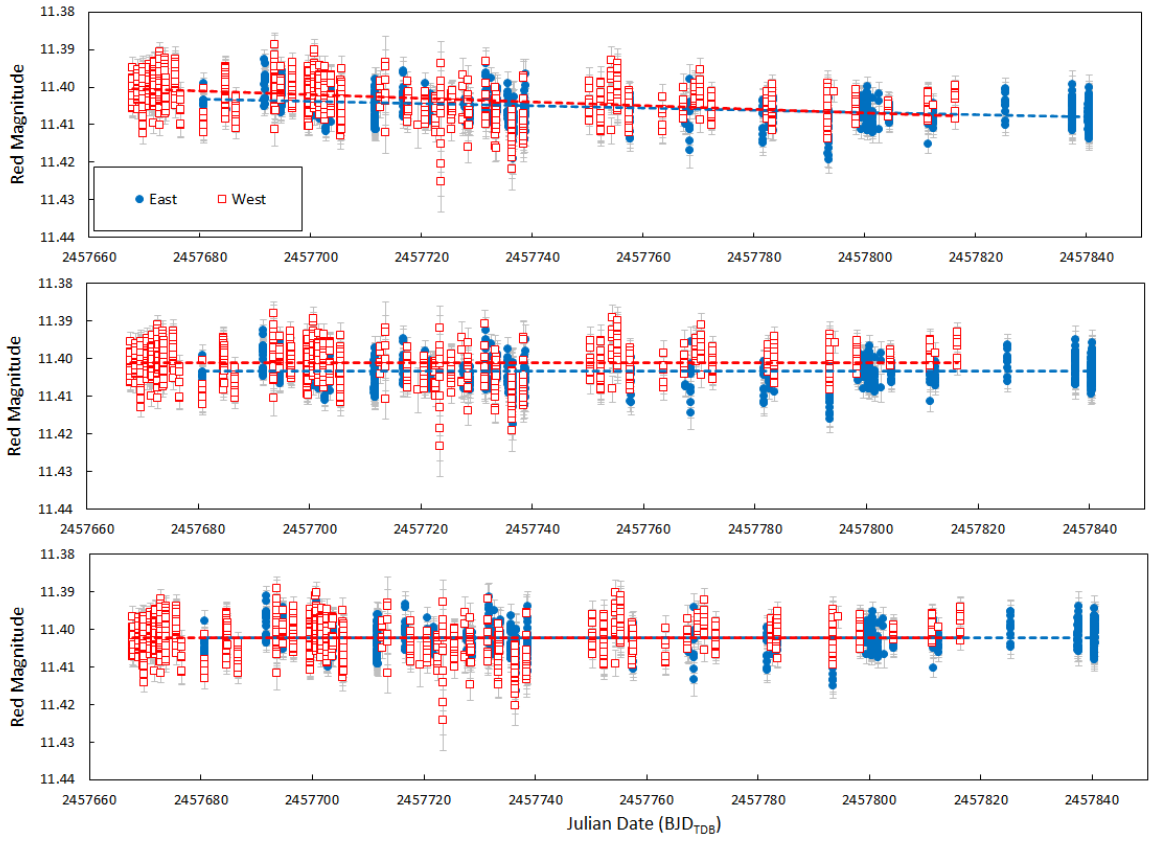

Figure 4.1: Example of the monitoring data correction process covering the WASP-12 observations for the 2016-17 season in the Red filter. Top, original photometry. Middle, after correction for linear correction for linear trend separately to East and West data showing offset. Bottom, correction for offset between East and West mount direction magnitude values.

followed by a 4000 step run with nthin = 3 giving 12,000 steps, updating the starting priors with the previous output each time. A final run was carried with 4000 steps and *nthin* = 50, giving 200,000 steps. At each stage the output was checked for consistency before being used to create the priors file for the next stage. The initial starting priors values and sources are shown in Table 4.7. Detrending of the transit lightcurves was carried out in Exofastv2 using airmass values and where applicable pier flip offsets.

Table 4.7: Priors and sources used in the starting Exofastv2 fit. As recommended by Eastman et al. (2019) the starting epoch was forward projected closer to the time of the first observation from 2013. A Gaussian prior width was not used for the dust extinction value, instead the prior width was set with a minimum of zero and a maximum equal to value determined from the dust maps.

Prior	Description	Value	σ	Source
rstar	Star Radius ($R_\odot$)	1.619	0.076	Bonomo et al. (2017)
mstar	Star Mass ($M_\odot$)	1.38	0.19	Knutson et al. (2014)
teff	Star Temp.(K)	6360	140	Chakrabarty and Sengupta (2019)
feh	Star Metalicity	0.32	0.12	Fossati et al. (2010).
A_V	Extinction	0.3238	0 to 0.5528	https://irsa.ipac.caltech.edu /applications/DUST/
parallax	Parallax (mas)	2.3942413534	0.04634231	https://gea.esac.esa.int/archive/
period	Orbital Period (d)	1.09142245		Stassun 2017
tc	Start Epoch	2456615.36		Fist transit minus 1 × period.
ideg	Inclination (°)	83.3	1.1	Southworth et al. (2012)
dr	Ratio d to rstar	3.039	0.034	Collins et al. (2017a)
u1(B)	Linear LD B filter	0.5223791473		Limb darkening from
u2(B)	Quad LD B filter	0.1901998266		http://astroutils.astronomy.
u1(I)	Linear LD I filter	0.2429178297		ohio-state.edu
u2(I)	Quad LD I filter	0.0807106464		/exofast/limbdark.shtml.
u1(R)	Linear LD R filter	0.2955668909		
u2(R)	Quad LD R filter	0.3082340871		

Two different red filters were used to obtain the transit data, broadband red and Cousins Rc which could potentially lead to differing transit depth measurements. The filter transmission and CCD quantum efficiency are plotted in Figure 4.2 showing the overlap between the two filters. Also shown are the prominent absorption line locations for NaI and, Hα which could affect the transit depth measurement (Jensen et al., 2018). Both absorption lines fall within the bandpass of both filters confirming that absorption in these bands will not cause a depth variation between the filters and that the lightcurves obtained can be treated as the same Red band input for the ExofastV2 models.

4.4.2.1 RV Data

RV data files used for the joint fit in Exofastv2 were obtained from the sources detailed over. Separate Exofastv2 input RV files created for each to allow each RV data set to be individually fitted with its own zero point and jitter values.

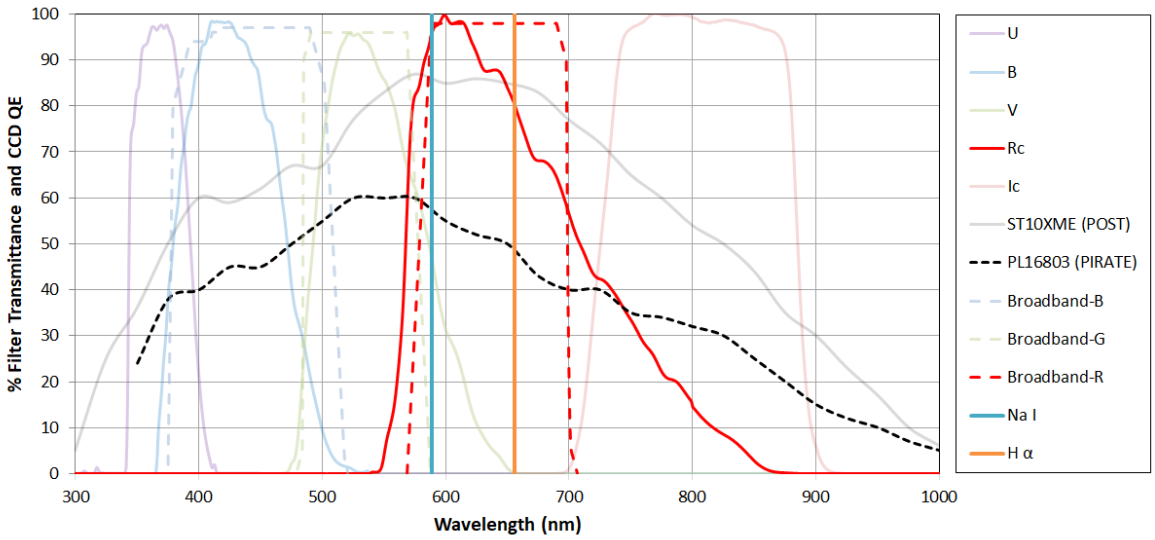

Figure 4.2: Plot of the broadband and John-Cousins filters used for transit measurements, focusing on the overlap between the two red band filters employed. Also shown are the CCD QE and the prominent absorption lines for NaI and, Hα, both of which fall within the bandpass for both filters.

- Hebb et al. (2009) provides 21 measurements made with SOPHIE in high efficiency (HE) mode on the 1.93m OHP telescope between 12/2/2008 and 22/02/2008. The data was downloaded from NASA Exoplanet Archive. The $\mathrm{BJD_{UTC}}$ timestamp was converted to $\mathrm{BJD_{TDB}}$ in line with Eastman et al. (2013). The number of leap seconds to apply is 33 for all dates, no leap second increments occurred during observation period. The $\mathrm{BJD_{UTC}}$ to $\mathrm{BJD_{TDB}}$ correction is therefore 32.184s+33s = 65.184s. It is noted this correction is significantly less than 15 to 18 minute SOPHIE exposures used but ensures all rv data uses the same time standard.

- Husnoo et al. (2011) made 29 radial velocity measurements for WASP-12 (16 during a single night, and 13 at various values of orbital phase) also obtained with SOPHIE in high efficiency (HE) mode on the 1.93m OHP telescope. The 16 data points obtained during transit to measure the Rossiter-McLaughlin effect were excluded, the remaining data was obtained between 26/2/2009 and 27/03/2010. Again the $\mathrm{BJD_{UTC}}$ timestamp was converted to $\mathrm{BJD_{TDB}}$, the number of leap seconds to apply is 34 for all dates, again no leap second increment occurred during observation period. The $\mathrm{BJD_{UTC}}$ to $\mathrm{BJD_{TDB}}$ correction is therefore 32.184s+34s = 66.184s. The authors note the velocity zero point determined with SOPHIE can drift by up several dozen m $\mathrm{s^{-1}}$ over a time span of several months. The authors correct for this drift "as far as possible" however to allow for any remaining differences in the zero point the RV measurements were split into two input files, one covering measurements obtained over a 46 day period and the

other over a 14 day period, separated by almost a year.

- Bonomo et al. (2017) made 15 measurements with HARPS-N which were downloaded from the catalogue published on VIZIER (`https://vizier.u-strasbg.fr/viz-bin/VizieR`). The table as downloaded stated the RV measurements are m s^{-1} but are actually km s^{-1} so were multiplied by 1000 to convert to m s^{-1} as required by Exofastv2. The time stamps states the observation are in BJD_{UTC}. The first observation above was made on 13/11/2012 and the last was made on 07/01/2015. Leap seconds were added on 30/6/2012 and 30/06/2015. The number of leap seconds to apply is 35 for all dates, again no leap second increment occurred during the observation period. The BJD_{UTC} to BJD_{TDB} correction is therefore 32.184s+35s = 67.184s.

- Yee et al. (2019) published the Knutson et al. (2014) data set with three new measurements to extend the coverage baseline to six years. The new and existing data were uniformly analysed using the standard California Planet Search pipeline in mid-2019 resulting in RV values updated by an average of -6m s^{-1} so this data set was used in place of the original RV observations published by Knutson et al. (2014)[1]. Observations obtained to measure the Rossiter-McLaughlin effect were excluded leaving 31 measurements covering just over 9 years.

- Seventeen measurements published by Maciejewski et al. (2020) with the HARPS-N instrument between 02/01/2013 and 16/11/2017.

The full transit lightcurves along with the best fitting ExofastV2 transit models can be found in Figures 4.3, 4.4 and 4.5. The best fit RV model is shown in Figure 4.6.

[1]Confirmed by private communication with the author

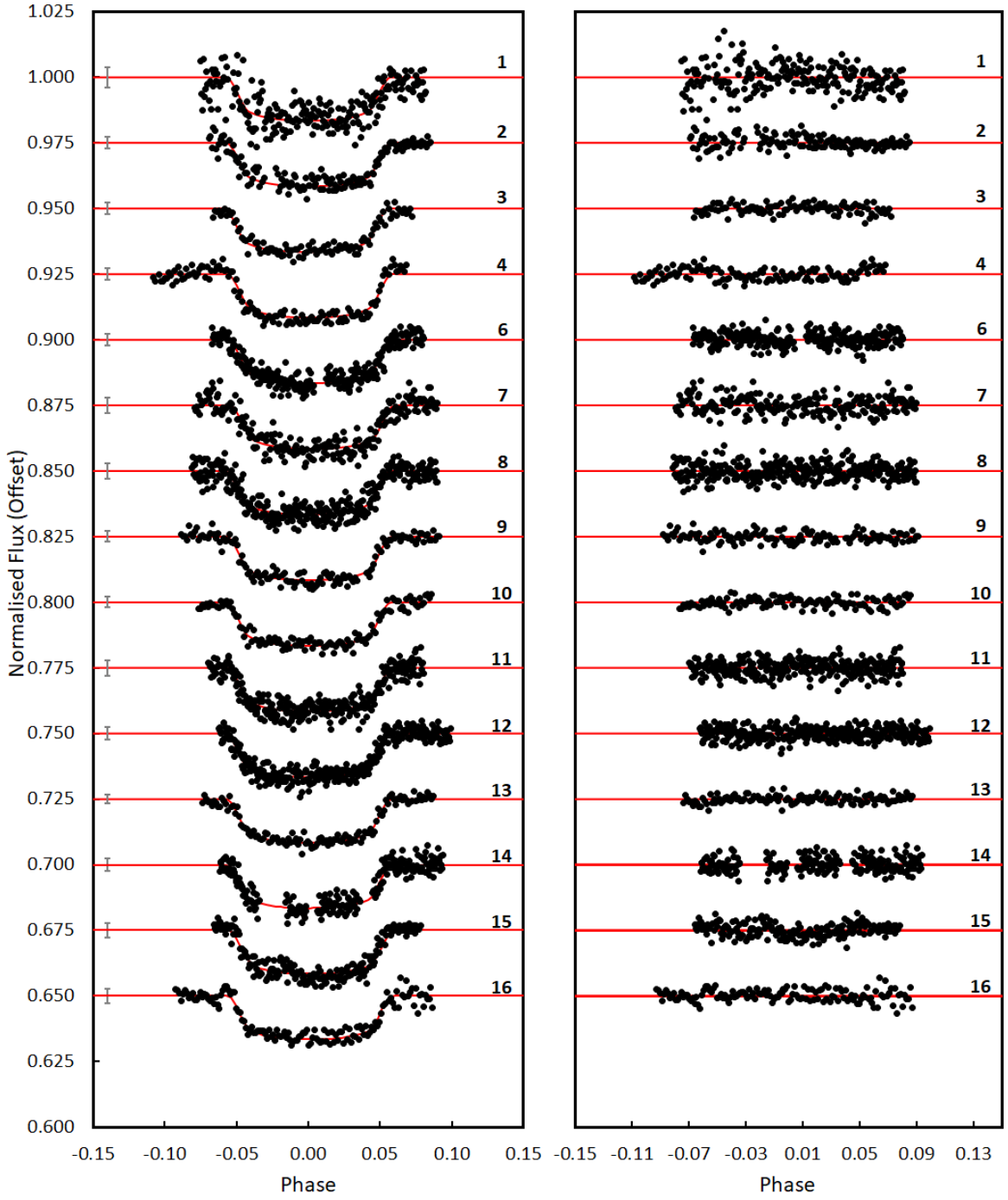

Figure 4.3: WASP-12b lightcurves with full transit coverage used for transit timing and system parameter determination. Black dots are individual data points. On the left is the lightcurve where the solid lines are the best fit ExofastV2 model for each transit. On the right are the residuals after subtraction of the transit model fit. Mean photometric uncertainty is shown for each transit with a grey bar at phase 0.36. The colour used for the transit model represents the filter used for each observation. Transit numbers are as given in Tables 4.2 and 4.3. Plot 1 of 3.

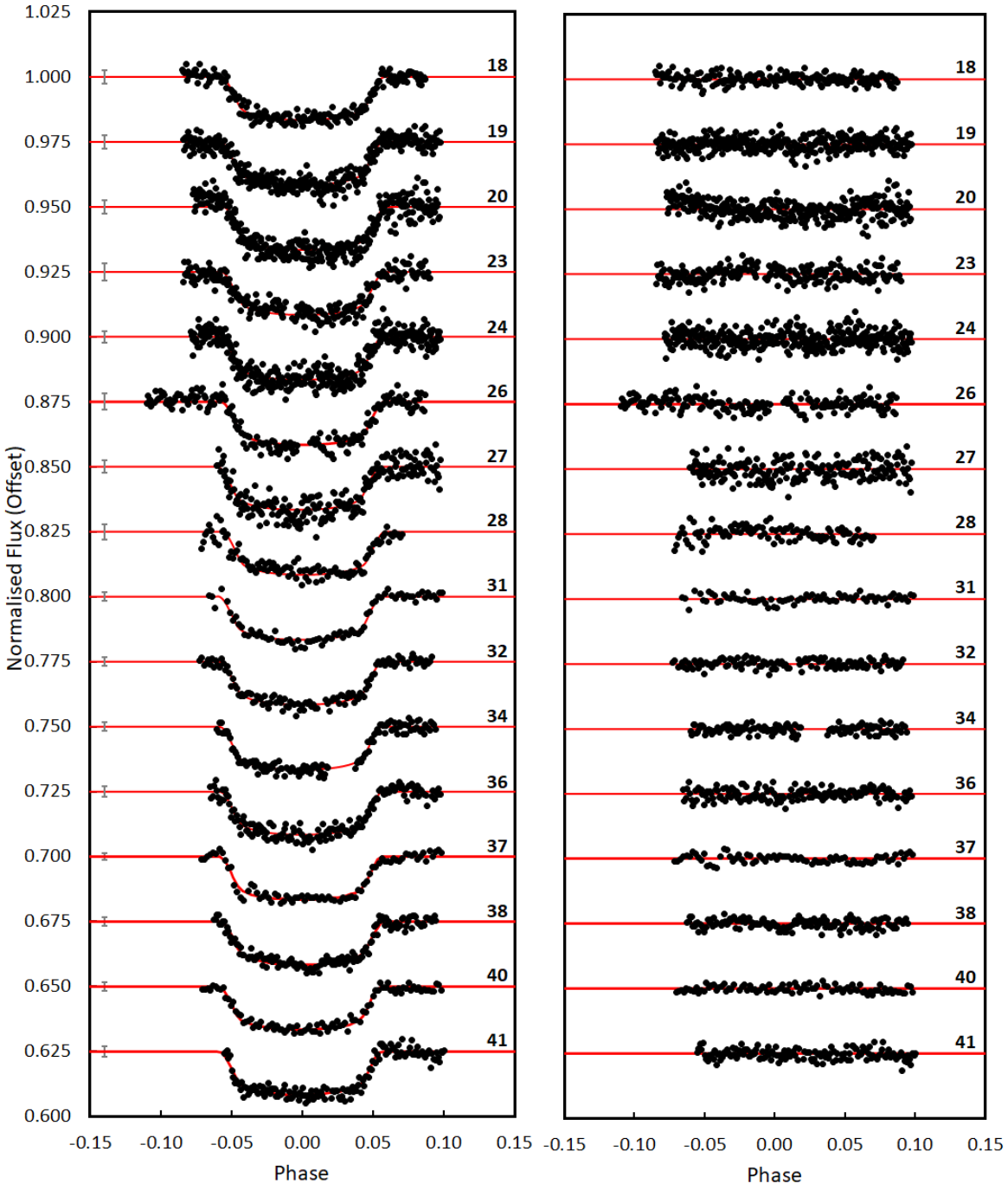

Figure 4.4: WASP-12b lightcurves, plot 2 of 3. Description as given for Figure 4.3.

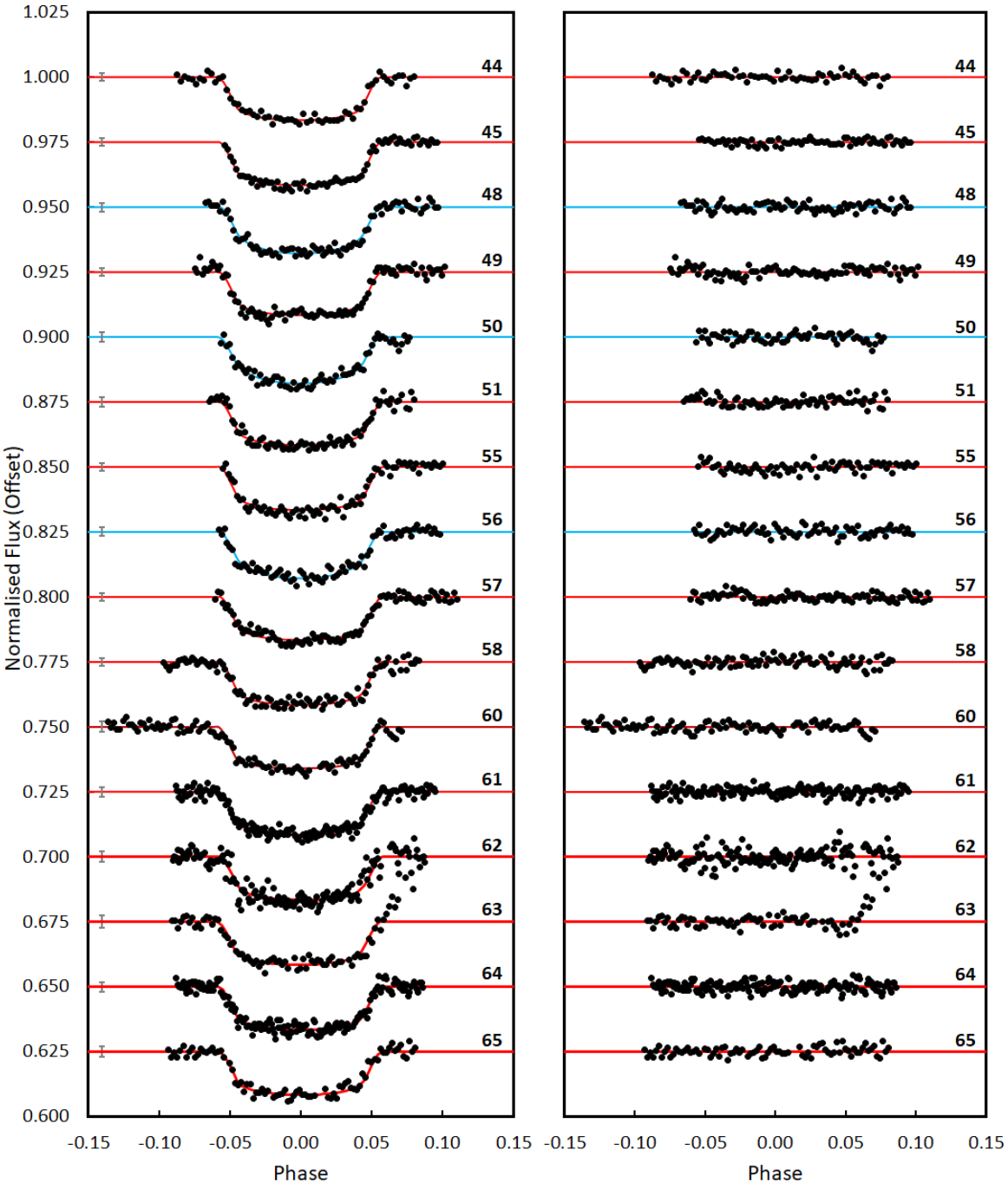

Figure 4.5: WASP-12b lightcurves, plot 3 of 3. Description as given for Figure 4.3.

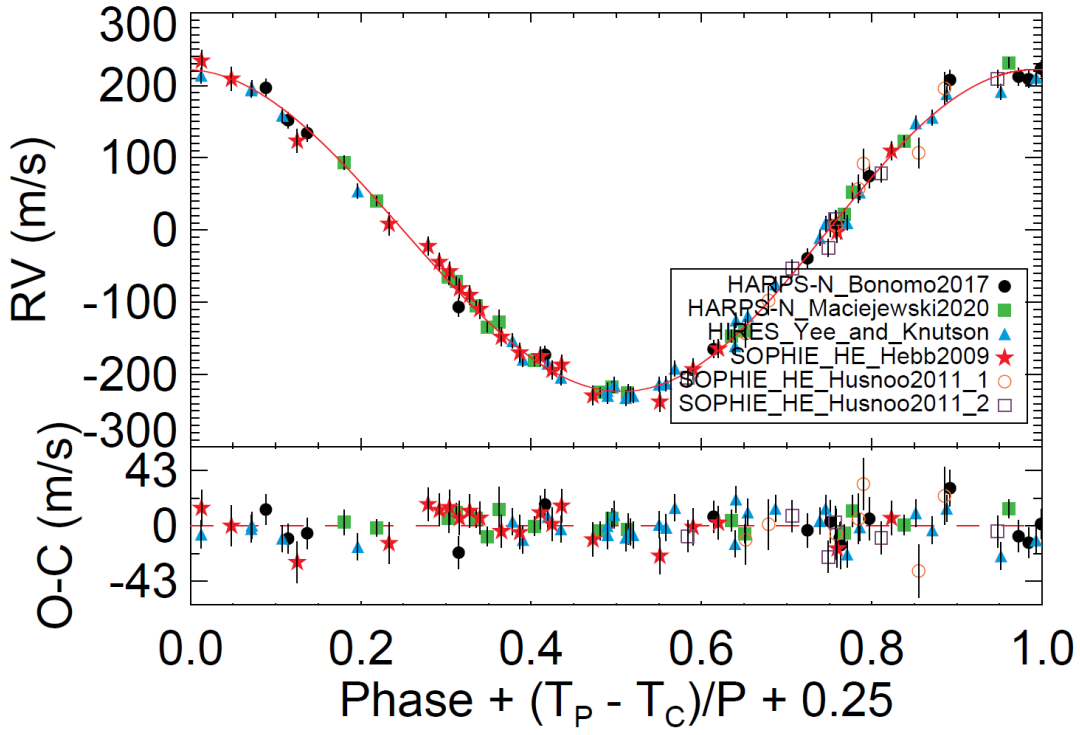

Figure 4.6: Plot of WASP-12 radial velocity fit from Exofastv2.

4.4.2.2 Host Star Photometry De-blending

ExofastV2 provides the ability to use a stellar spectral energy distribution (SED) model combined with a bolometric correction grid provided by the MESA Isochrones and stellar tracks (MIST) project (see Chapter 2.7) in order to determine the stellar parameters. The normalisation of the SED model with an understanding of the distance to WASP-12b taken from the Gaia DR2 catalogue (Brown and Gaia Collaboration., 2016) provides a strong constraint on $(R_*/d)^2$ (Eastman et al., 2019). Using this method ExofastV2 can provide a much stronger constraint on the stellar radius than other approaches using the empirical Torres relation (Torres et al., 2010). As the stellar radius uncertainty is generally the largest source of uncertainty in determining the planetary radius, this approach allows a more accurate planetary radius to be determined. The SED model is constructed from trusted broadband photometric catalogues along with priors on the stellar distance from Gaia DR2 and V band extinction (A_V) from https://irsa.ipac.caltech.edu/applications/DUST/. It is important however that only the flux from the star is incorporated into the SED model, flux contribution from photometric blending of nearby stars will result in an anomalous radius determination.

Lucky imaging of WASP-12 by Bergfors et al. (2013) discovered a companion 1″ from WASP-12A and from their photometry they determined a spectral type between K0V to M0V. They also noted the companion appears elongated suggesting it is itself a double star. Follow up observations by Bechter et al. (2014) confirmed the binary nature of the companion and

determined spectral type of M0V for each component from their J and K band photometry. Due to the close proximity of the two companion stars all the photometric measurements obtained from the catalogues used in the WASP-12 SED model will include the contribution from these companions and will therefore require correction for the contribution from the B and C components prior to fitting in ExofastV2. The WASP-12B and C components are significantly cooler than WASP-12A and will provide a greater fractional contribution to the overall flux as wavelength increases. Photometric de-blending was undertaken as described below and tested in Exofastv2 to prove the validity of the approach.

ExofastV2 provides a routine to automatically extract broadband photometry from trusted catalogues. WASP-12 photometry was available from the following sources;

- Tycho catalog (BT and VT) (Høg et al., 2000)
  `http://adsabs.harvard.edu/abs/2000A%26A...355L..27H`
- 2MASS, via UCAC4, (J, H and K) (Skrutskie et al., 2006)
  `http://adsabs.harvard.edu/abs/2003yCat.2246....0C`
- AllWISE, (3.35, 4.6 and 11.6μm) (Cutri, 2013)
  `http://adsabs.harvard.edu/abs/2013yCat.2328....0C`
- Gaia DR2, (Gaia G, BP and RP) (Brown and Gaia Collaboration., 2018)
  `http://adsabs.harvard.edu/abs/2016A%26A...595A...2G`

Additionally Johnson B, V and SLOAN g', r' and i' band photometry was obtained from the AAVSO Photometric All Sky Survey (APASS) DR10 (Henden, 2019), `https://www.aavso.org/cgi-bin/apass_dr10_download.pl`.

The SEDs provided by Kraus and Hillenbrand (2007) were used by Bechter et al. (2014) to determine the spectral types based on the apparent magnitudes of the two companion stars. The M0V spectral type for the two companions was first confirmed by calculating the absolute magnitudes

$$M_\lambda = m_\lambda + 5 \times log_{10}(d) - A_\lambda \tag{4.1}$$

before comparing with the Kraus and Hillenbrand (2007) SED values. Here A_λ is the wavelength dependent extinction and d is the distance in parsecs, calculated from the corrected Gaia DR2 parallax

$$d(pc) = \pi^{-1} = \frac{1}{(2.3942 \pm 0.0463) \times 10^{-3}} = 417.67 \pm 8.08 \tag{4.2}$$

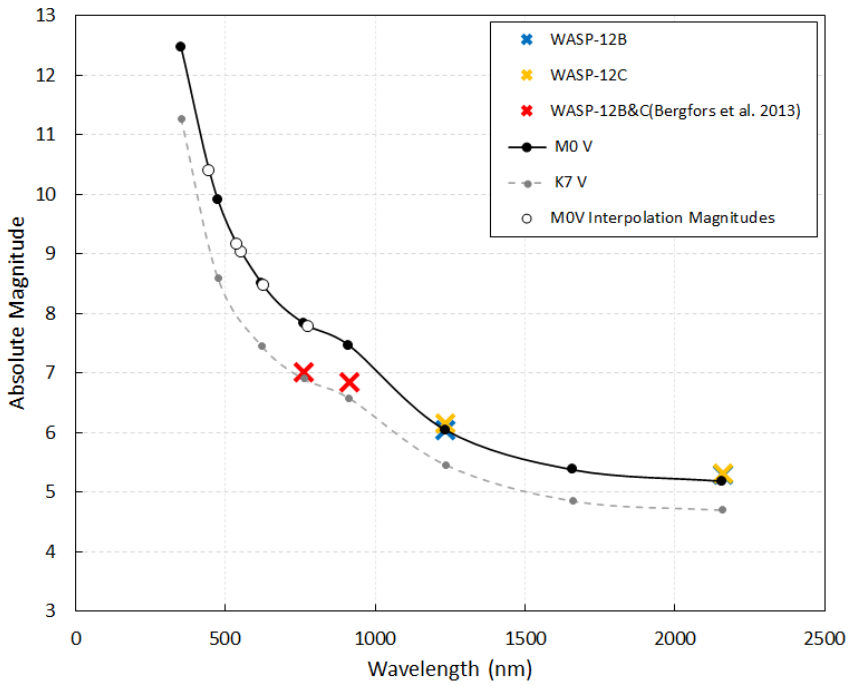

Figure 4.7: Calculated absolute J and K magnitudes for WASP-12B (Blue) and WASP-12C (Amber) from the aparent magnitudes reported in Bechter et al. (2014), showing the close match of each star to the SED for a M0V star. The red crosses indicate the combined SLOAN $i'and z'$ observations of the B and C components from Bergfors et al. (2013) who estimated a spectral type between M0V and K0V, K7V SED is shown for reference. Filled circles are the magnitudes from Kraus and Hillenbrand (2007) and the open cirlces are the interpolated values for filter bands used in the SED for WASP-12 not specified by Kraus and Hillenbrand (2007).

where π is the parallax obtained from Gaia DR2 (Brown and Gaia Collaboration., 2018) corrected by adding $82\mu as$ to the reported value and adding $33\mu as$ in quadrature to the uncertainty following the results of Stassun and Torres (2018).

The extinction value (A_λ) in the same bandpass as the apparent magnitude measurement were obtained from the tables at `https://irsa.ipac.caltech.edu/workspace/TMP_8OTzpo_5751/DUST/WASP-12.v0002/extinction.html`. The resulting absolute magnitudes in J and K_S are shown in Figure 4.7 along with the SED for a M0V star (Kraus and Hillenbrand, 2007).

The SEDs provided by Kraus and Hillenbrand (2007) include discrete magnitude values in the u', g', r', i', z', J, H and K_S bands. To obtain values for the B, V GaiaG, GaiaBP and GaiaRP bands the SEDs were interpolated using the published mid filter wavelength. For the very broad Gaia bandpasses this was taken as the FWHM mid point for each of the

three filters. It was not possible to extend the corrections to the WISE IR bandpasses as the Kraus and Hillenbrand (2007) SEDs do not extend beyond K band. No other suitable published SEDs extending into this region are available.

This provided absolute magnitudes for an M0V star in the same filter bandpasses available for the WASP-12 SED. The apparent magnitudes were calculated in each filter by reversing Equation 4.2. The final de-blending step was to subtract the contribution of the two M0V companion stars from the WASP-12 flux for each filter,

$$m_{A_{corr\lambda}} = -2.512 \times \log_{10}(10^{-0.4\mathrm{m_{A\lambda}}} - 10^{-0.4\mathrm{m_{B\lambda}}} - 10^{-0.4\mathrm{m_{C\lambda}}}) \tag{4.3}$$

where $m_{A_{corr\lambda}}$ is the de-blended apparent magnitude for each filter. The original catalogue and resulting de-blended photometry are shown in Table 4.8.

Table 4.8: De-blended photometry results. The catalogue values shown for WASP-12A are the values taken from the on-line catalogues listed. The de-blended values are the apparent magnitudes after correction.

Band	WASP-12A Catalogue	WASP-12A De-blended	Source Catalogue
B(T)	12.259 ± 0.207	12.32 ± 0.21	Tycho
V(T)	11.635 ± 0.160	11.70 ± 0.16	Tycho
B	12.192 ± 0.043	12.25 ± 0.04	APASS R10
V	11.607 ± 0.049	11.67 ± 0.05	APASS R10
gSDSS	11.878 ± 0.053	11.94 ± 0.05	APASS R10
rSDSS	11.427 ± 0.04	11.49 ± 0.04	APASS R10
iSDSS	11.332 ± 0.06	11.41 ± 0.06	APASS R10
J	10.477 ± 0.02	10.595 ± 0.02	2MASS(via UCAC4)
H	10.228 ± 0.02	10.383 ± 0.02	2MASS(via UCAC4)
K	10.188 ± 0.02	10.363 ± 0.02	2MASS(via UCAC4)
WISE1	$10.111^{+0.03}_{-0.022}$	-	AllWISE
WISE2	$10.109^{+0.03}_{-0.021}$	-	AllWISE
WISE3	10.121 ± 0.073	-	AllWISE
GaiaG	$11.500^{+0.02}_{-0.001}$	11.58 ± 0.020	Gaia DR2
GaiaBP	$11.804^{+0.02}_{-0.003}$	11.88 ± 0.020	Gaia DR2
GaiaRP	$11.036^{+0.02}_{-0.003}$	11.12 ± 0.020	Gaia DR2

4.4.2.3 Testing the De-blended Photometry

To test the effect of using the de-blended photometry to calculate a SED in ExofastV2 models for the WASP-12 system a number of tests were run. The tests used all the RV data obtained from the literature as detailed in Section 4.4.2.1 along with three full transit light curves, one from each telescope, all obtained using an Rc filter. Three lightcurves were used to provide a test between the different models without needing the multi-day time to run as is required when modelling with all 47 transits. The ExofastV2 tests made were;

1. Using the original catalogue photometry as shown in Table 4.8.
2. Using the original catalogue photometry as shown in Table 4.8, but excluding the WISE photometry.
3. Using the de-blended photometry which excludes the WISE photometry.
4. Using the empirical Torres relationship which does not use the broadband photometry SED or priors on extinction and parallax.

The aim of the second test was to determine whether there was any effect on the results from removing the WISE photometry. The fourth test, using a different method to determine the system parameters, was run as a control test. The results from the tests for key system parameters are plotted in Figure 4.8.

In all cases the transit depth is deeper than the values recorded in the NASA Exoplanet Archive, the difference being 5σ or greater. This results in a larger scaled system parameter R_P/R_* than seen in the archive. It is noted that there is a 25-fold spread for the uncertainty values reported in the NASA Exoplanet Archive for R_P/R_*. Öztürk and Erdem (2019) report the largest value of 0.119 ± 0.004 while the smallest value reported is 0.1119 ± 0.0002, (Albrecht et al., 2012). The first two tests using the catalogue photometric values with and without the mid-IR photometry from WISE agree with each other within the calculated uncertainties. Without the WISE photometry ExofastV2 calculates a stellar radius 2% smaller than when the WISE photometry is included.

The de-blended photometry results in R_* smaller than both the original photometry and the archive values, by 3% in the latter case. R_P is in close agreement with the mean literature value. The results from the de-blended photometry and the model test just using the Torres relationship are in closer agreement than the results using the original photometry. Results using the Torres relationship generally show larger uncertainties. Distance determined using the de-blended photometry matches that calculated from the Gaia DR2 parallax. σ SED is the amount the photometric uncertainties have to be multiplied by to remain consistent with

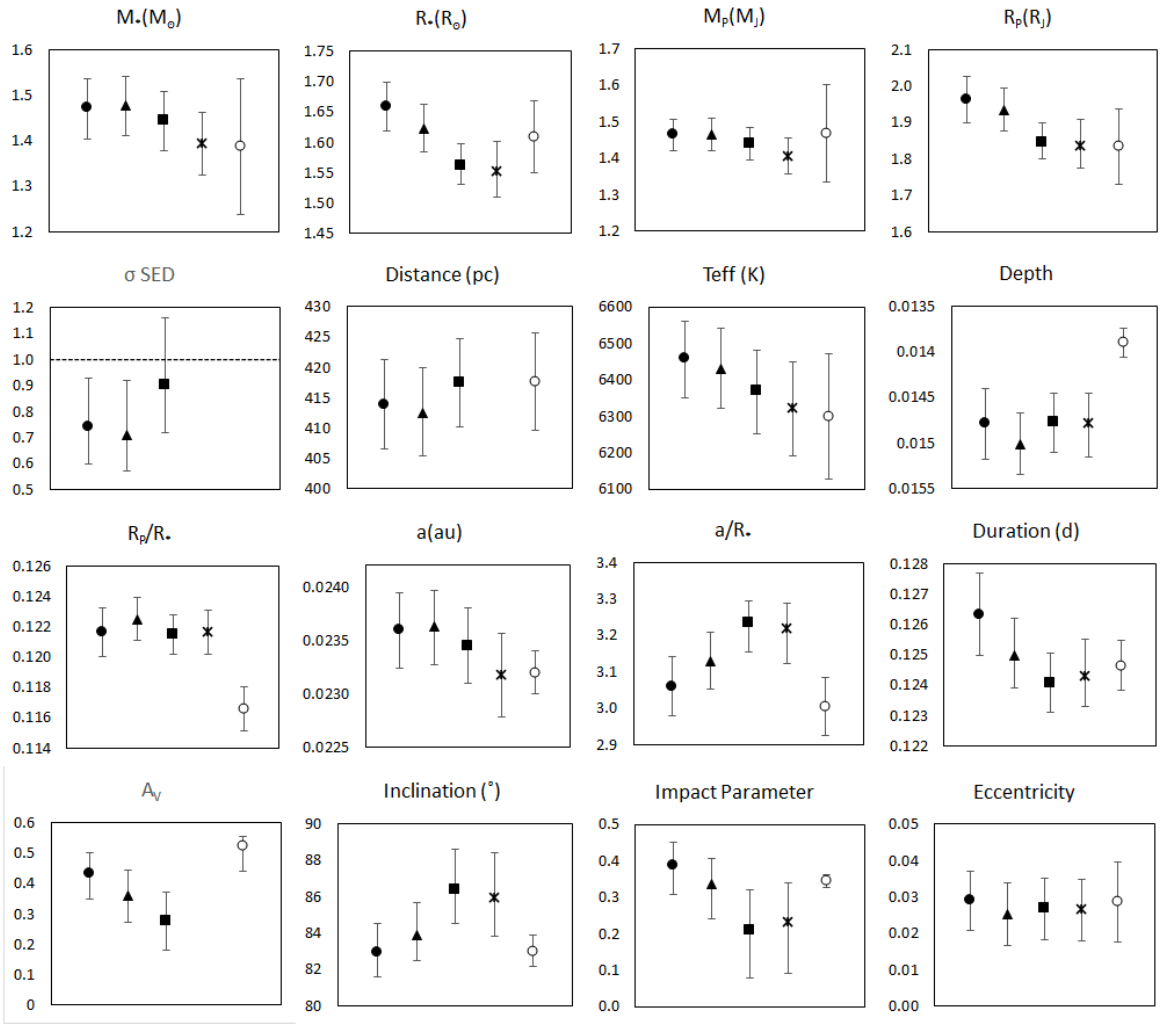

Figure 4.8: Results of ExofastV2 model tests with original and de-blended photometry. Circles are the results using the unaltered photometry, triangles are the original photometry minus the WISE photometry, squares are the de-blended photometry and crosses are the results using the empirical Torres relationship. Open symbols represent the mean parameter values and uncertainties reported on the NASA Exoplanet Archive. σSED, described in the text, is a diagnostic parameter reported by ExofastV2 and is not a value reported in the archive. The open symbol value for distance was taken from Equation 4.2 and the value for extinction was calculated from the tables at https://irsa.ipac.caltech.edu/applications/DUST/).

the model. σSED is closer to unity for the de-blended photometry. Distance and σSED are not computed for the Torres relationship.

Based on these test results the de-blended photometry without the WISE photometric values was used in the full ExofastV2 model calculations for the WASP-12 system using all 47 transits, the results for which are detailed in Section 4.5.4.

4.5 Results

4.5.1 J0630+2942

The WASP-12 field was monitored over 3 observing seasons, 2016 to 2019, using PIRATE with the aim of detecting any photometric variation, specifically periodic variation that could be attributed to a stellar rotation period. Within each observing season the density of observations, as a percentage of the possible nights J0630+2942 could be observed, was between 23% and 44% (Table 4.1) determined by telescope availability, weather, telescope maintenance and the target field airmass. In total the WASP-12 field was observed on 170 nights between October 2016 and March 2019, coverage during the 2017-18 season was low due to periods of poor weather and storm damage to the observatory weather mast.

Early during the 2016-17 observing season monitoring observations it became clear that the near neighbour to WASP-12, J0630+2942 was varying in brightness. This star was removed from the comparison ensemble (for both monitoring and transit analysis) and measured as a target star. Being located just 2 arcmin from WASP-12, J0630+2942 is listed by the AAVSO as the closest photometric comparison star to WASP-12 with a V mag of 12.244 and B-V of 0.699 (compared with V mag of 11.69 and B-V of 0.578 for WASP-12). As a result J0630+2942 is often used as a photometric comparison and may, for large telescopes with correspondingly small fields of view, be the only suitable comparison star available, see Figure 4.9.

The variability of J0630+2942 is immediately obvious in the photometry obtained for the 2016-17 season in both Red and Blue filters. It is also clear the amplitude of the variability has decreased over the three seasons of monitoring (Figure 4.10). This can also be seen in the reducing standard deviation in the magnitudes measurements detailed in Table 4.9 which reduces from 0.01 magnitudes to 0.004 magnitudes in the red filter between 2016-17 and 2018-19. A similar reduction is seen in the standard deviation of the blue filter observations.

A Lomb-Scargle period analysis implemented in Python using the AstroPy library[2] was carried out for each season and filter combination, Figure 4.11. Each period range was divided into 100,000 bins providing a high resolution periodogram. False alarm probabilities were

[2](`https://www.astropy.org/`)

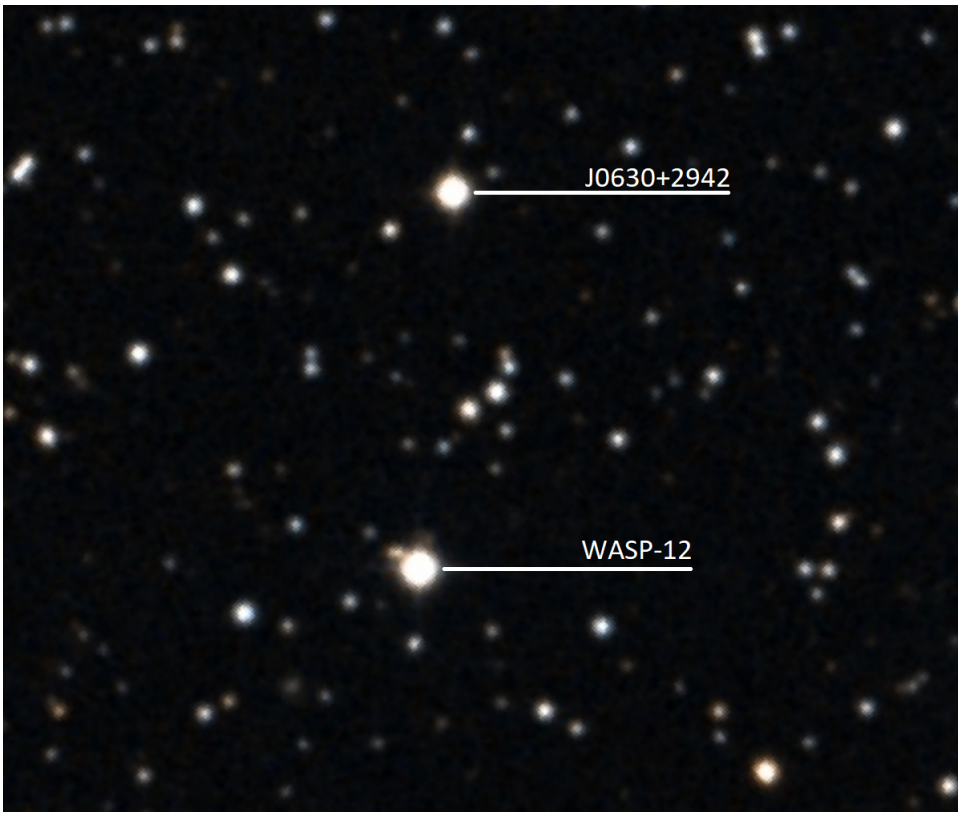

Figure 4.9: J06303188+2942273 is located just 2 arcmin from WASP-12 (adapted from DSS2 image).

calculated using the bootstrap method, again with 100,000 simulations. False alarm levels were measured at the 0.05%, 0.1% and 0.5% levels. For the 2016-17 season the variability clearly seen in the red filter lightcurve shows a periodicity of 6.830 days with an amplitude of 0.009 mag surrounded by a large number of significant peaks. The Blue filter data from the same season but obtained over a different duration shows a strong peak at 9.043 days. The proximity to an integer value and data grouping seen in the phase folded lightcurve suggest this is an observing cadence artifact. The second most significant peak occurs at 6.925 days with an amplitude of 0.006 mag, close to the 6.830 days seen in the red data.

The data for the 2017-18 season is more scarce than for the other seasons with a significant gap in the observations and the Lomb-Scargle periodogram shows many significant peaks in the approximately 5 to 10 day range. For the red data the strongest of these peaks occurs at 10.377 days but with a false alarm probability of 16%. The strongest peak in the blue data is 6.605 days, close to that seen in the previous seasons. The forest of peaks visible in the 5-10 day period region of the periodogram occur at a separation of 0.011 cycles per day which is attributed to a frequency associated with the observing duration of 89 days (0.011c/d = 90.9d).

The final 2018-19 season shows a strong peak at 6.342 days in the Rc filter with an

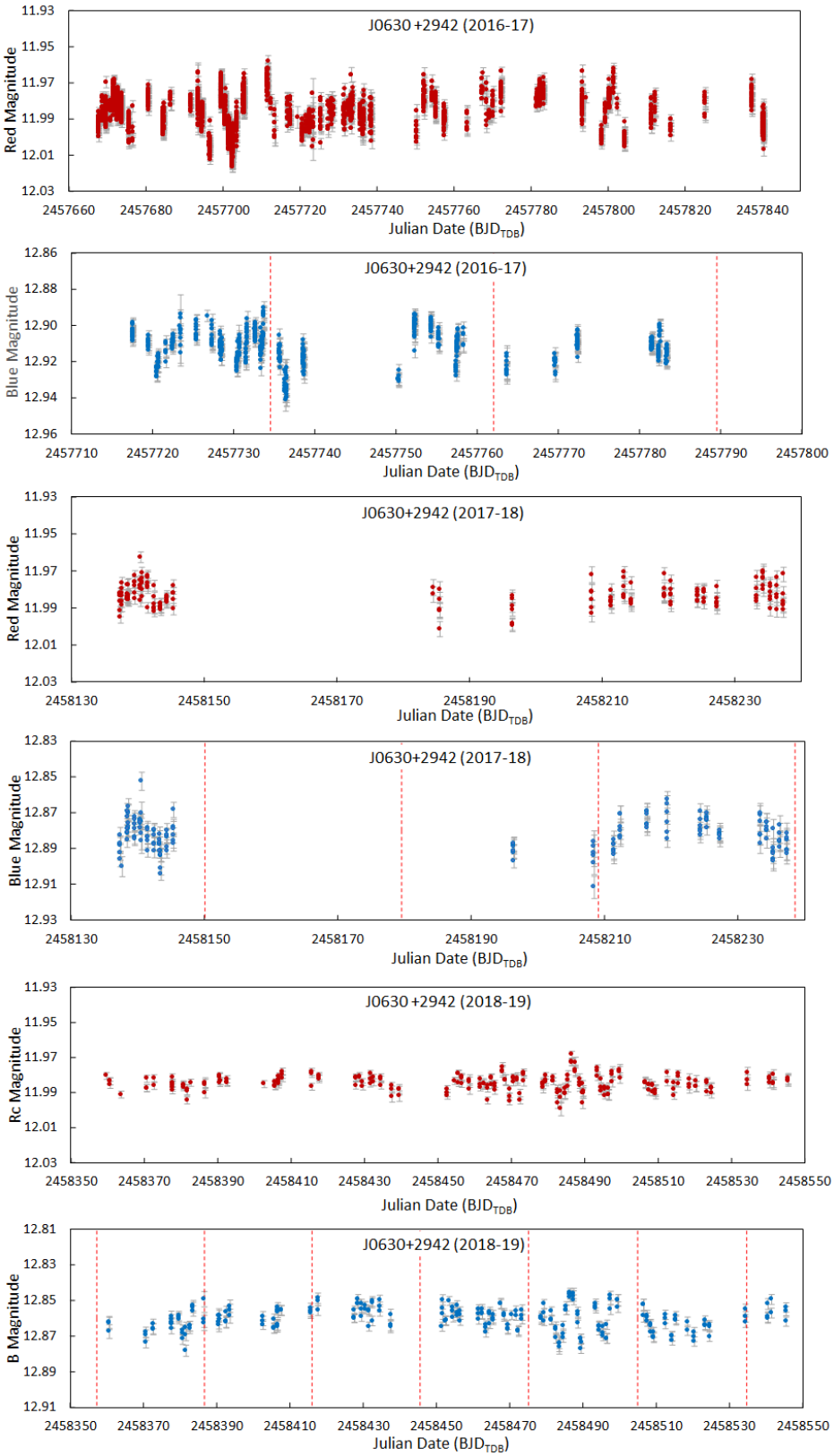

Figure 4.10: Red and Blue filter photometry of the suspected variable J0630+2942. For the 2016-17 season the Red data was gathered over a longer timescale than the Blue filter data.

amplitude of 0.002 magnitudes and 6.316 days for the B filter data with an amplitude of 0.004 magnitudes. This period shows a double peak in both the Rc and B observations with the second, lower power peak occurring at an integer period of 6.0 days.

Lastly all three seasons were analysed as a single data set. The mean magnitude for each season and filter was subtracted and then a Lomb-Scargle period analysis was undertaken, this time covering a range from 2 to 200 days to search for longer duration periods. For both the Red and Blue filters the strongest peaks in the periodogram occur at 6.79d and 7.04d respectively. The blue filter shows a second peak at 9.16d.

4.5.2 WASP-12 Monitoring

The photometry for WASP-12 was analysed in the same way as described above for J0630+2942. Blue filter observations of WASP-12 for the 2016-17 season were not usable due to saturation of the CCD pixels resulting from an exposure duration that was too long for the brightness of WASP-12. The full detrended photometry from each season and filter, for WASP-12 and the photometric check star selected with a similar B-V and brightness to WASP-12, is shown in Figures 4.12, 4.13 and 4.14.

The magnitudes determined are shown in Table 4.9 where the measurement uncertainty is taken as the standard deviation of the nightly mean magnitude measurement. The 2016-17 and 2017-18 seasons photometry was obtained using the same filters allowing a direct comparison between the magnitudes measured over the two seasons. The determined magnitudes for the check star agree with each other between seasons to within 1.5σ in the Red band while the Blue filter magnitudes agree to better than 1σ. In general the uncertainty on the Blue filter observations is greater than that of the Red data. The standard deviation for WASP-12 magnitude in both filters over both seasons is less than or equal to that of the selected check star, indicating no detectable variability in WASP-12 over the measurement period. Absolute comparison of the measured magnitudes with catalogue values is not possible due to the non-photometric standard filters used. The Red filter observations for both WASP-12 and the check star agree with the UCAC4 catalogue values to within the rather large catalogue uncertainties. The blue filter UCAC4 catalogue values have smaller uncertainties and the observed magnitudes agree within 2σ of the catalogue uncertainty indicating a greater bandpass difference between the catalogue B and the Baader Blue filter used here.

For the 2018-19 observations where Johnson-Cousins photometric filters were used and the CCD on-chip binning changed to 1×1 the agreements to the UCAC4 catalogue values for both Rc and B filters are within 1σ of the catalogue uncertainty for both WASP-12 and the check star used, despite the slightly different filter bands measured.

A Lomb-Scargle period analysis was undertaken in the same was undertaken in the same

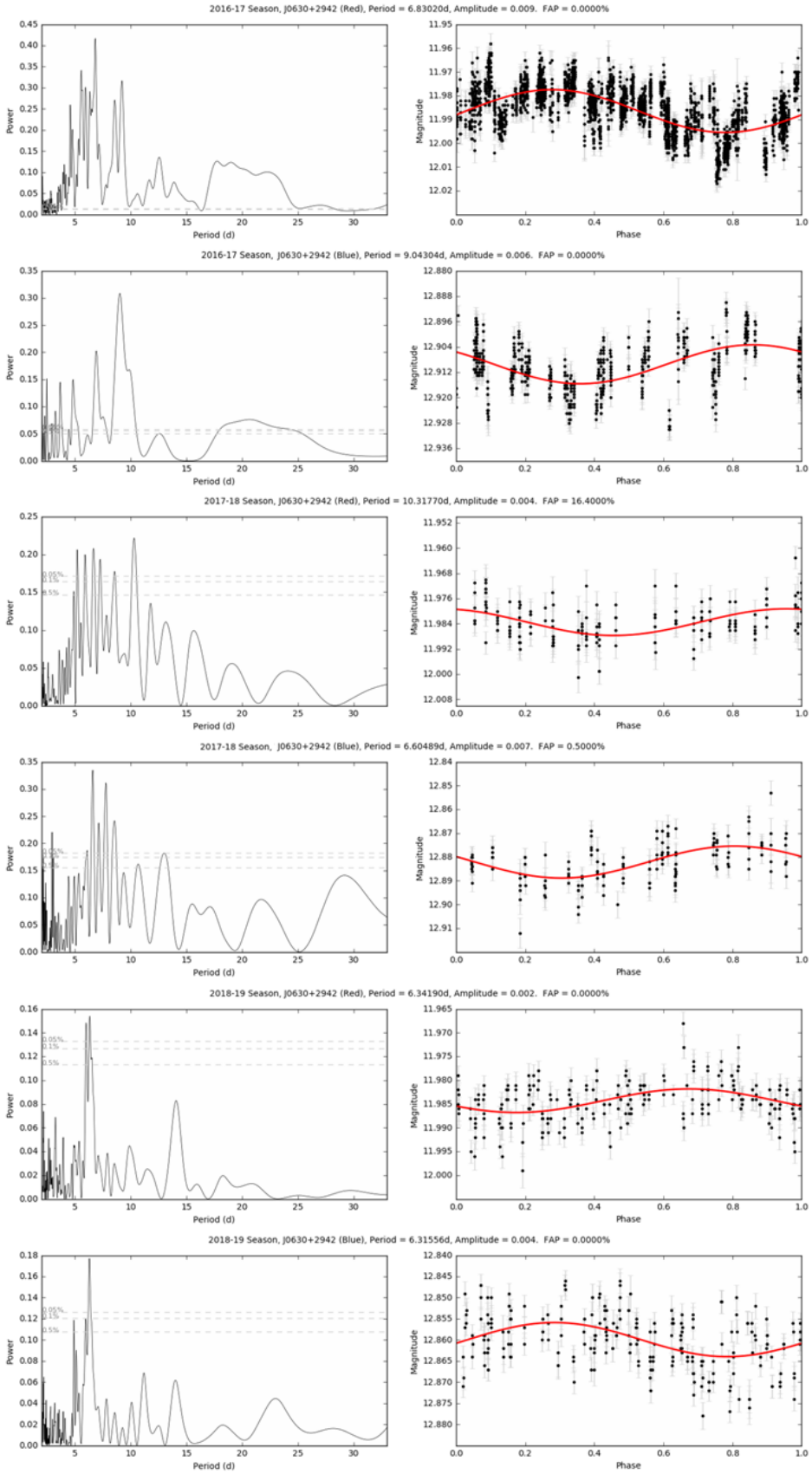

Figure 4.11: Left column, Lomb-Scargle periodograms for J0630+2942 covering the period range from 2 to 33 days. Right column, data phase folded over most significant period detected. Plots show results for each season in each colour separately.

Table 4.9: Instrumental magnitudes measured from detrended monitoring photometry for each season and filter to allow comparison between each seasons results. The magnitudes and their uncertainties are calculated from the nightly mean observation and its standard deviation over the season. The uncertainties quoted exclude the catalogue uncertainty which is typically an order of magnitude greater. The blue filter check star used for the 2018-19 season is different to that used in 2016-18. Variability in J0630+2942 is clear in the larger standard deviation in the data which reduces in later seasons.

Season	Filter	WASP-12	J0630+2942	Check Star
16-17	Red	11.402 ± 0.003	11.986 ± 0.008	11.496 ± 0.004
16-17	Blue	N/A	12.912 ± 0.008	13.420 ± 0.003
17-18	Red	11.407 ± 0.002	11.983 ± 0.004	11.490 ± 0.004
17-18	Blue	12.174 ± 0.006	12.882 ± 0.007	13.424 ± 0.005
18-19	Rc	11.395 ± 0.003	11.985 ± 0.004	11.504 ± 0.004
18-19	B	12.119 ± 0.004	12.860 ± 0.006	12.331 ± 0.004

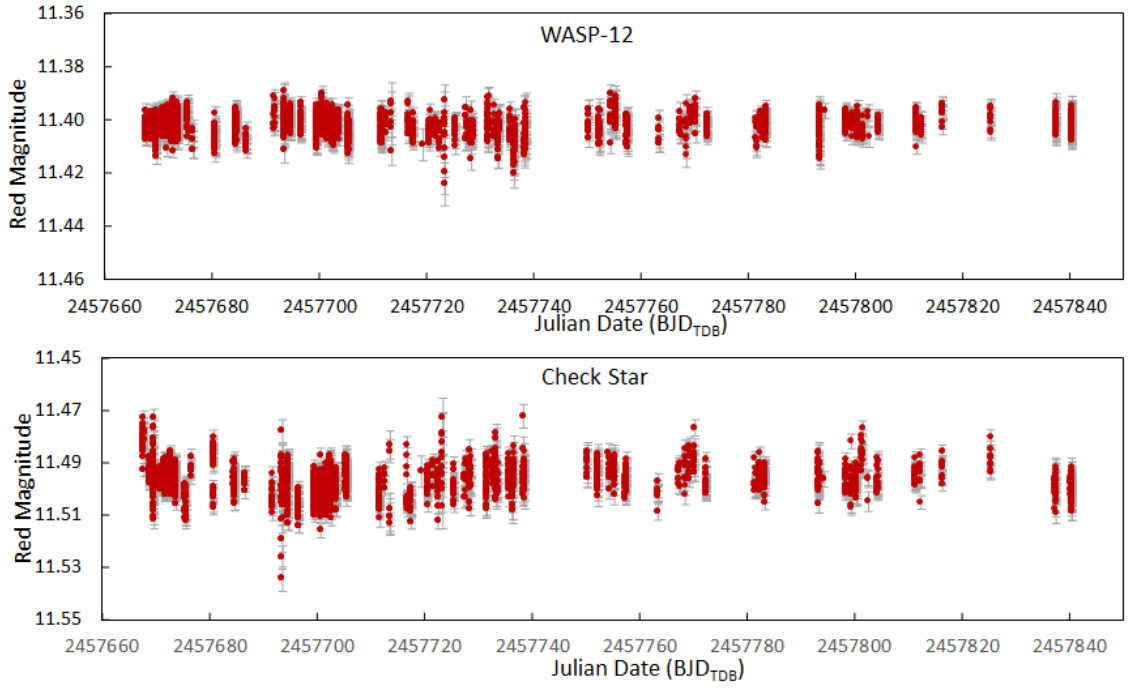

Figure 4.12: Detrended photometry obtained with PIRATE for WASP-12 (top) and check star(bottom) for the 2016-2017 observing season. No Blue filter photometry is available for this season. All photometry plots are scaled to 0.1 Magnitudes on the Y axis to allow easy comparison of the photometry between filters and seasons.

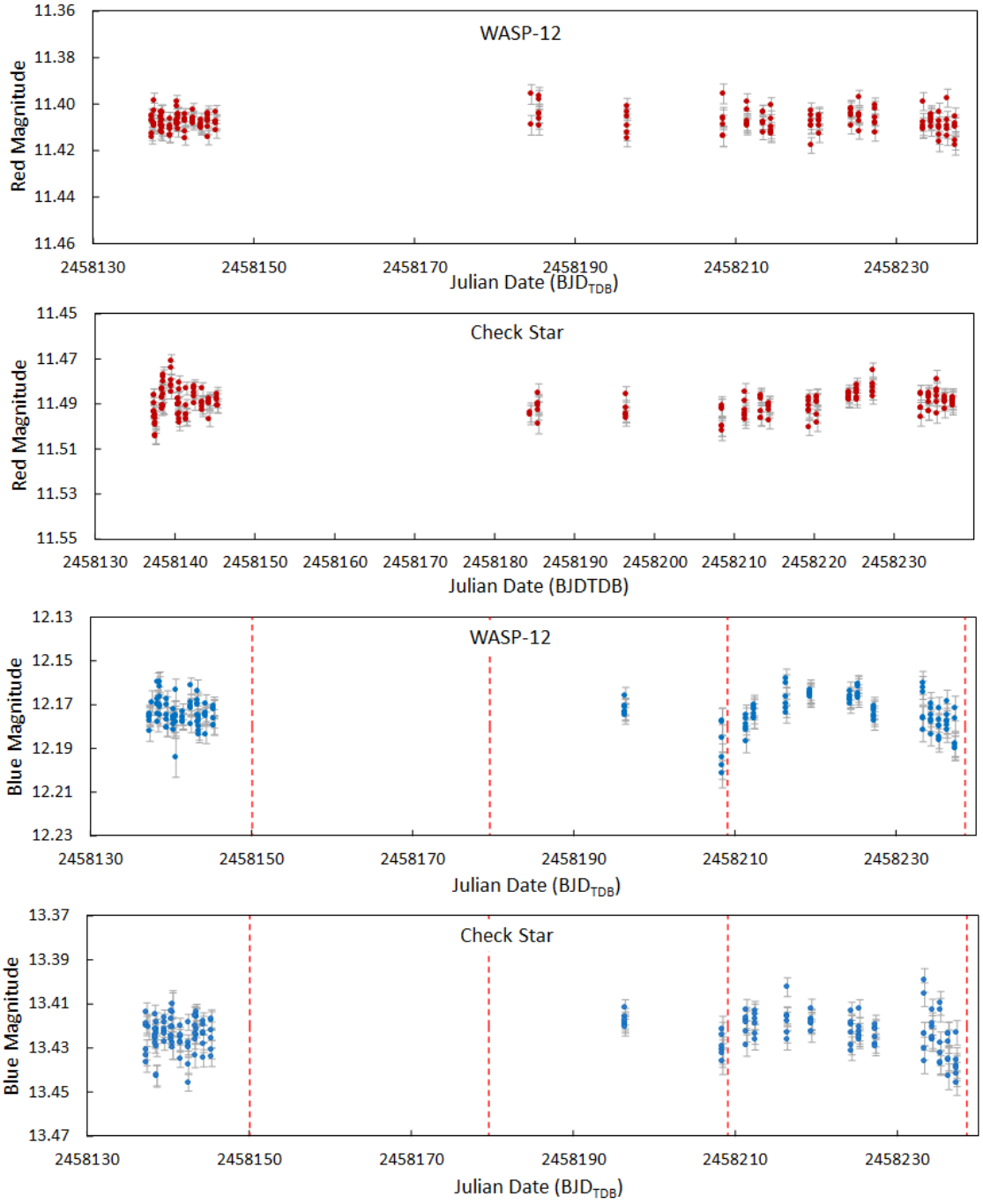

Figure 4.13: Detrended photometry obtain with PIRATE for WASP-12 and check star for the 2017-2018 observing season. The red dashed lines on the Blue filter plots indicate the date of each full moon. All plots are scaled with 0.1 Magnitudes on the Y axis to allow easy comparison of magnitude variations.

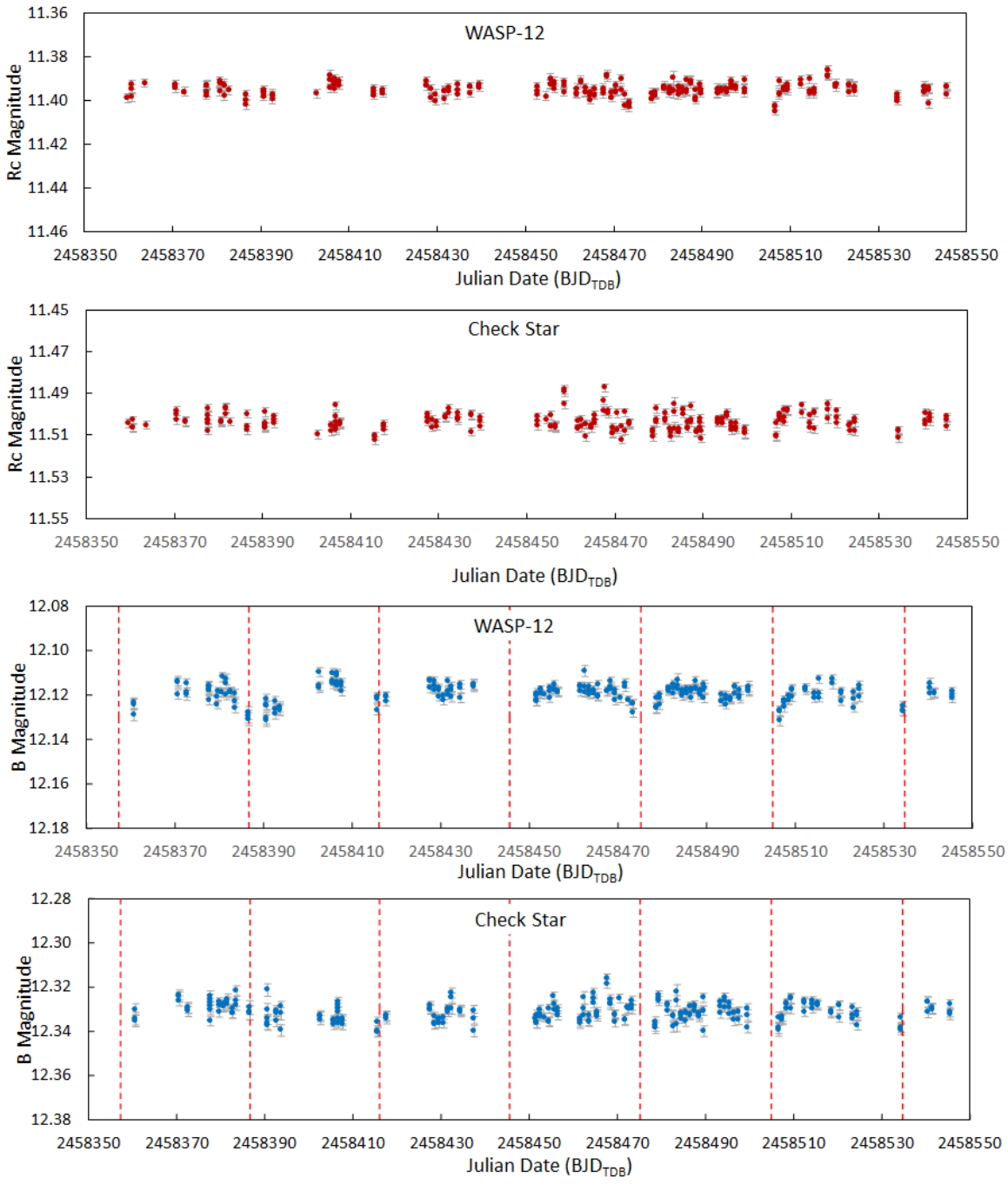

Figure 4.14: Detrended photometry obtained with PIRATE for WASP-12 and check star for the 2018-2019 observing season.

way as described above for J0630+2942. An initial period analysis was carried out covering periodicities between 0.5 days up to half the duration of the observations. As expected these periodograms are dominated by the 1 day observing cadence and/or alias of detected periods. The periodograms, shown in Figures 4.15 and 4.16 for WASP-12 and the check stars respectively, cover periods between 2 and 33 days. This range was chosen to cover periods expected from rotation of an F type star out to periods for G type stars similar to the Sun (Nielsen et al., 2013) while excluding the observing cadence and its alias often seen around 1 and 0.5 days respectively.

The WASP-12 observations for the 2016-17 season though the red filter show only a low significance peak at 3.05 days. The proximity to an integer value makes it likely this is an alias of the nightly observing cadence. The check star for the same period shows a peak at 19.94 days, though the data in the phase folded lightcurve at this period is highly grouped, making it likely this is an artifact from the observation cadence. No other significant periodicities are seen.

For the 2017-18 season the red filter observations show no significant periods, the strongest peak occurring at 2.28 days. The Blue filter observations show a strong period at 30.36 days. It is likely this period is a systematic effect resulting from the lunar period. This is clearly seen in the Blue filter lightcurve data where the vertical dashed red lines indicate the full moons occurring on the 31st March 2018 and 30th April 2018 (Figure 4.13). This effect is greatest when the angle of observation between the target and full moon is less than approximately 50°. This effect should be investigated further as an observing constraint. The check star of the 2017-18 season observations in the red filter show a non-significant peak at 2.93 days, very close to the 2.28 day peak also seen in the red filter observation of WASP-12. The strongest peaks seen arise for 0.588 days and 4.74 days, the former being an alias of the latter.

For the 2018-19 season the only significant period seen in the WASP-12 monitoring photometry occurs at 28.43 days in the red filter observations and at 28.32 days in the blue. During the period of the observations the mean Luna cycle duration was 29.6 days. No significant peaks are seen in either the red or blue periodograms for the check star.

Lastly all three seasons were analysed as a single data set as described for J0630+2942. The strongest period seen in the red filter data occurs at 3.05d, as seen in the 2016-17 season with a second peak at 27.37d. This longer period is the first in a range of periods seen between 27 and 31 days with decreasing powers as period increases. In the blue filter a strong peak is seen at 29.60d with a secondary peak at 27d. The check star exhibits several peaks at period below 15d in the blue filter, the strongest occurring at 11.87d. In the red filter the strongest check star peak seen occurs at 70.87d.

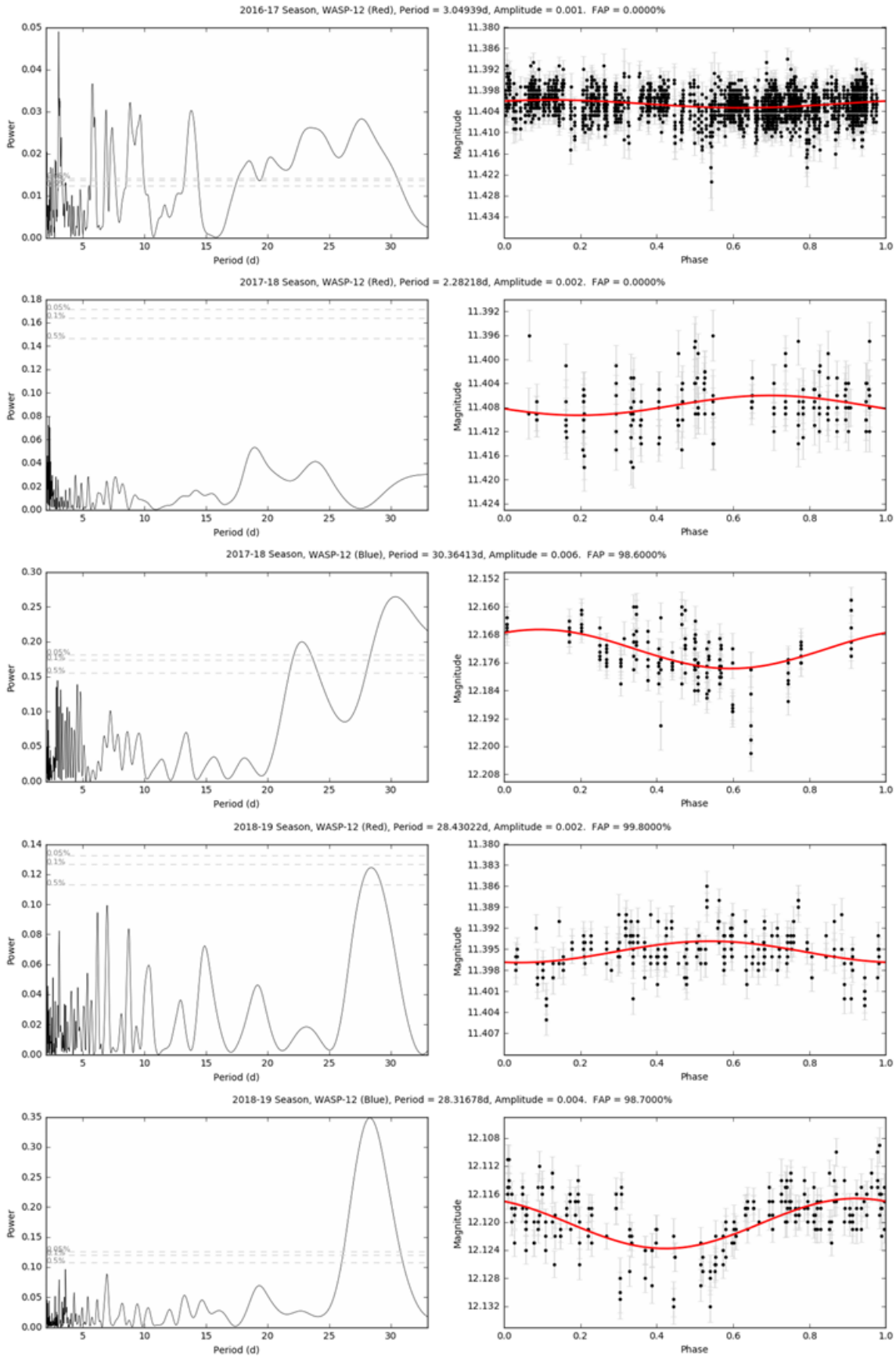

Figure 4.15: Left column, Lomb-Scargle periodograms for WASP-12 covering the period range from 2 to 33 days. Right column, data phase folded over most significant period detected. Plots show results for each season in each colour separately.

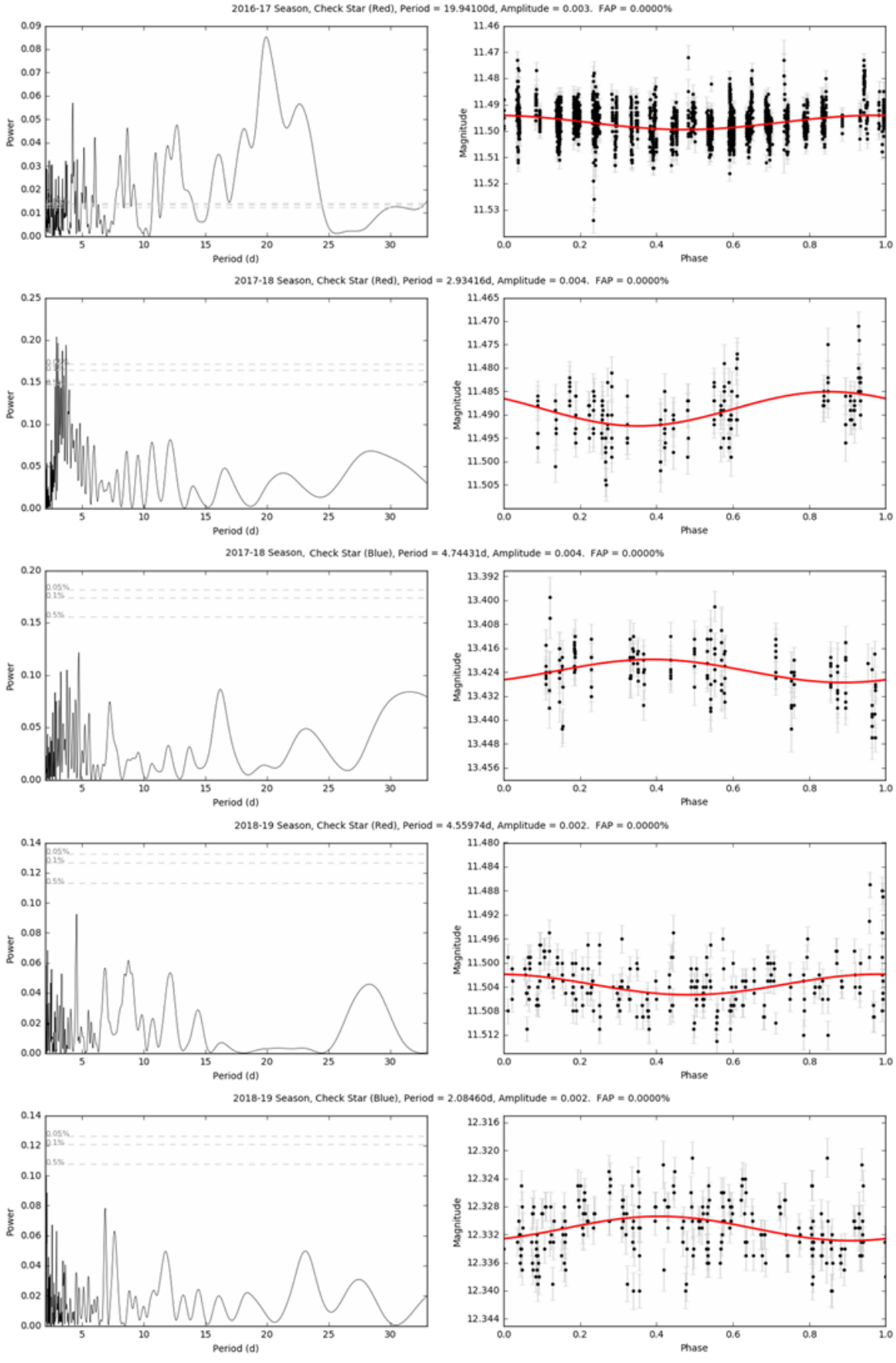

Figure 4.16: As for 4.15 but showing results for the check stars used.

4.5.3 WASP-12b Transit Timing

Before undertaking an ephemeris fit to the newly obtained transit times a test fit was carried out using the transit times published by Yee et al. (2019) to ensure the published results could be reproduced. All 139 published primary transit times were used with the linear ephemeris value published by Yee et al. (2019) as the starting value. The fit converged to values that are in excellent agreement, well within the uncertainties on both the new and published ephemerides, Table 4.10. The newly calculated ephemeris has slightly larger uncertainties than those published by Yee et al. (2019).

The following data sets were modeled independently to understand the impact of various data inputs on the derived ephemeris and to inform the optimum approach to integrating the new observations with those within Yee et al. (2019), hereafter Y19. The results of the ephemeris calculations are summarised in Table 4.10 and Figure 4.18.

4.5.3.1 All 47 new transit time observations only.

The new data set consists of 47 transit observations covering seven seasons from 2013 to 2020. Coverage was greatest in the 2016-17, 2017-18 and 2018-19 seasons with only 10 observations available for the other four seasons. The four data points covering the first three seasons were exclusively from the POST observatory. The starting epoch, period and $\dot{P}$ for the quadratic ephemeris obtained are compared with the results from Y19 in Figure 4.18, left. The calculated epoch agrees with Y19 within 42 seconds but the quadratic period found is 1.15×10^{-6}d greater and the value found for $\dot{P}$ is almost twice the value determined by Y19. Using this data set it is not possible differentiate between a linear or quadratic ephemeris with $\chi^2_\nu = 3.1$ for the linear and $\chi^2_\nu = 3.2$ for the quadratic ephemerides. The uncertainties on the determined quadratic epoch and period are approximately 25 times greater than found from modelling just the Y19 data set while the $\dot{P}$ uncertainty is 10 times greater.

4.5.3.2 All 47 new transit times integrated with those from Y19.

The two data sets of 139 measurement from Y19 and the 47 new measurements were combined to a single data set. The new data overlaps with seasonal observations in the Y19 data set except for the 2019-20 season not covered in the Y19 data. The result confirms a strong preference for a quadratic ephemeris ($\chi^2_\nu = 1.60$, BIC = 99.93) over a linear ephemeris ($\chi^2_\nu = 3.10$, BIC = 217.84). The result confirm the findings of Y19 with the same or improved uncertainties. Although the uncertainties on the ephemeris are reduced the newly determined χ^2_ν values are approximately 60% greater than found by Y19. For seasons with more than a single measurement, the mean seasonal scatter in timing measurements divided by the mean

transit mid-time uncertainty in each season averages 0.8 for the 11 seasons in the Y19 data set and 1.6 for the 9 seasons of the new observations. This shows that, on average, the scatter in the transit mid times combined from multiple observers in the Y19 data set was smaller than the mean mid-time uncertainty for individual measurements in each season. For the new observations the seasonal scatter is on average 60% greater than the mean mid-time uncertainty. This result and its implications for transit timing precision achievable by small aperture ground-based telescopes is discussed further in Chapter 5.

Despite the greater measurement scatter in some seasons, adding the new data to the published data shows an improvement in the derived ephemeris parameters.

4.5.3.3 Transit times obtained using OSO telescopes after the GPS installation and integrated with the times from Y19.

As the new data set contains transit times obtained from multiple telescopes using different timing methods another model was created incorporating just the observations made with PIRATE and COAST after the GPS upgrade. This left thirteen transit times from the 2018-19 season and three from the 2019-20 season all made through the Rc filter. This smaller data set was combined with the transit times from Y19. The resulting values for the starting epoch and period are closer to those from Y19. The χ^2_ν values are much closer to those from Y19 with $\chi^2_\nu = 2.8$ for the linear ephemeris and $\chi^2_\nu = 1.17$ for the quadratic ephemeris.

4.5.3.4 All new observations with simultaneous transits binned to a single data point added to the Y19 data set.

There are a number of simultaneous transit time observations which occur in the combined transit timing data set including nine pairs of simultaneous observations within the 47 newly obtained transit times. These simultaneous observations, including those that occur in the previously published data and those that occur between new and published observations are discussed fully in Section 5.6 of Chapter 5. The difference in measured transit mid-times ranges from 0.8σ to 5.1σ with the only pair of observations agreeing within 1σ being between COAST and POST obtained in February 2017. The remaining six pairs of transit times agree to within 2σ. Six of the nine time differences are smaller than the exposure time used which varied between 45 to 180 seconds depending on telescope, filter and CCD binning.

As these simultaneous observations comprise nearly 40% of the new transit time data set the possibility exists that combining the two transit times to a single data point will impact the ephemeris calculation. To consider this the mean transit mid time value for each pair of transit times was calculated along with their uncertainties. This was only done for the newly obtained data, simultaneous observations within the Y19 data set were not averaged. This

Table 4.10: WASP-12b quadratic ephemeris model results using different data sets as described in the text. DS1 is the result published by (Yee et al., 2019), DS2 is the Y19 data recalculated to check consistency with the original. DS3 is all 47 new transit times alone and DS4 is the combined Y19 and new transit times. DS5 is Y19 + new OSO telescope observations only after GPS install (Rc filter). DS6 is Y19 + new data with mean simultaneous observation times and DS7 is as DS6 but just for OSO telescope data after GPS install.

DS	Epoch - 2456305	Period (d)	$\dot{P}$	χ^2_ν	RMS
1	0.455809(32)	1.091420107(42)	$-10.04(69) \times 10^{-10}$	1.08	-
2	0.455812(32)	1.091420121(43)	$-10.25(71) \times 10^{-10}$	1.10	0.000342
3	0.455323(320)	1.091421257(1100)	$-18.49(670) \times 10^{-10}$	3.11	0.001002
4	0.455815(31)	1.091420132(42)	$-10.15(61) \times 10^{-10}$	1.60	0.000592
5	0.455811(32)	1.091420119(43)	$-10.21(64) \times 10^{-10}$	1.17	0.000396
6	0.455814(31)	1.091420129(42)	$-10.17(62) \times 10^{-10}$	1.40	0.000519
7	0.455813(32)	1.09142012(43)	$-10.28(65) \times 10^{-10}$	1.08	0.000362

left 38 transit mid time measurements which were combined with the Y19 data set. This approach did not substantially change the resulting ephemeris calculation and the χ^2_ν and residual RMS values increased.

4.5.3.5 Only OSO observations made after the GPS install with simultaneous transits binned to a single data point and added to the Y19 data set.

The same procedure was carried out as detailed above but this time only including the transit times from the OSO telescopes obtained after the installation of GPS time control. Six pairs of transit times were averaged, three pairs through Rc and B filters. This approach provided the lowest overall χ^2_ν and residual RMS values where new observations were included and is therefore the selected data set used to calculate the updated orbital ephemeris for WASP-12b

$$\begin{aligned} \mathrm{T_c(BJD_{TDB})} = 2456305.455813(32) + 1.09142012(43) \times \mathrm{E} \\ + (-10.28(65) \times 10^{-10} \times \mathrm{E}^2) \end{aligned} \tag{4.4}$$

where the first value on the right-hand side is the reference epoch ($\mathrm{T_0}$), the second value is the orbital period in days and E is the epoch of observation. Values in brackets are the uncertainty on the last two digits. The quadratic term $\frac{\delta P}{\delta E} = (-10.28 \pm 0.65) \times 10^{-10}$ can be used to calculate the period derivative of

$$\frac{\delta P}{\delta t} = \frac{1}{P}\frac{\delta P}{\delta E} = (-9.419 \pm 0.596) \times 10^{-10} = -29.7 \pm 1.9 \text{ ms yr}^{-1} \tag{4.5}$$

where $^{\delta P}/_{\delta t}$ is the period change per day and P is the orbital period. This result is in agreement with the value of $(-10.04 \pm 0.69) \times 10^{-10}$ found by (Yee et al., 2019). The transit data plotted against the new quadratic ephemeris is shown in Figure 4.17.

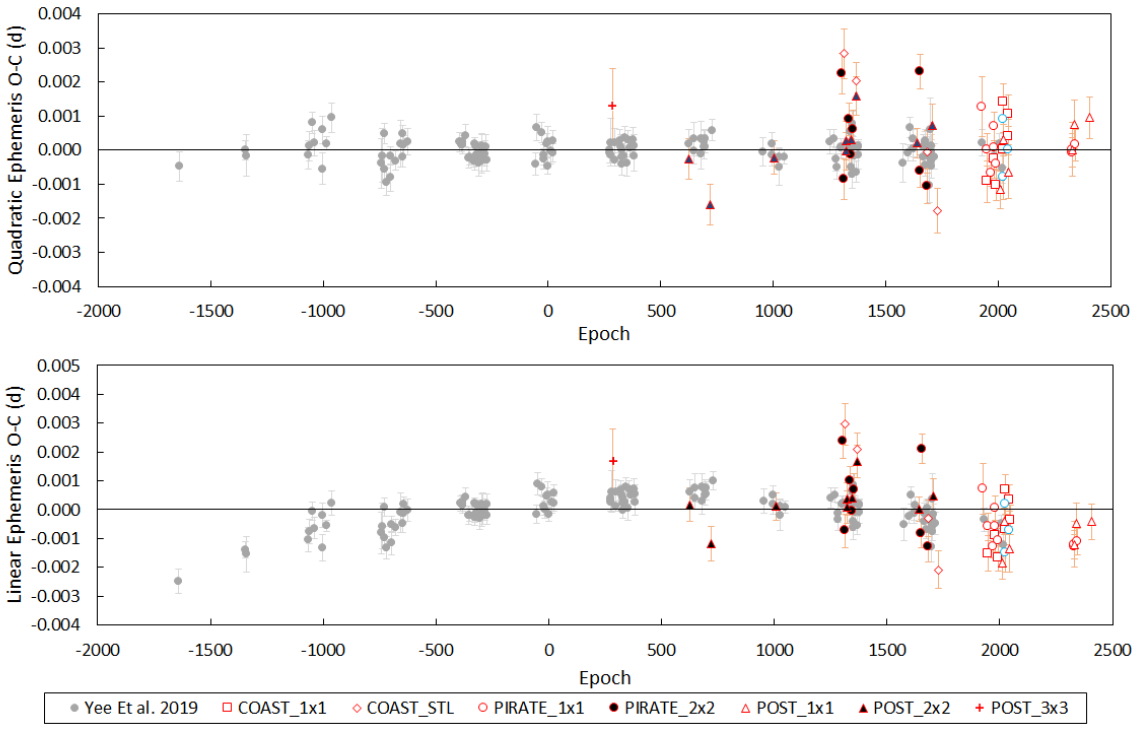

Figure 4.17: Top, WASP-12b transit time results plotted against the newly calculated ephemeris. Bottom, same data plotted against the the best fit linear ephemeris.

4.5.4 WASP-12b System Parameters

The combined analysis using new transit observations, catalogue RV data, de-blended host star photometry and precises distance information from Gaia DR2 allows ExofastV2 to provide precise system parameters.

The new results provide the tightest constraints yet on the values for R_*, R_P, a, M_* and M_P for the WASP-12b system. The results of the ExofastV2 analysis are given in Table 4.11 and compared with previously published results in Figure 4.19.

The newly determined value for R_* is 1% smaller and for R_P is 0.5% larger than the mean value from previous publications, the new value for R_P is 5% smaller than the most recently published results by Chakrabarty and Sengupta (2019) who used a larger stellar radius published previously by Collins et al. (2017a). I find a stellar mass 5% larger than the mean published value. If the low value of $1.2M_*$ found by Stassun et al. (2017) is excluded from the published mean, the new stellar mass determined agrees with the mean within 2%. As can be seen from Figure 4.19 the value for planetary mass from Turner et al. (2016) is $2.01M_P$, 4.3σ discrepant from both the new results presented here and the previous mean value from published works. These authors analysis was based on near-UV lightcurve data and determined a low stellar mass value of $1.28M_\odot$. Excluding this result for M_P from the published mean value brings the new mass for WASP-12b determined here and the published

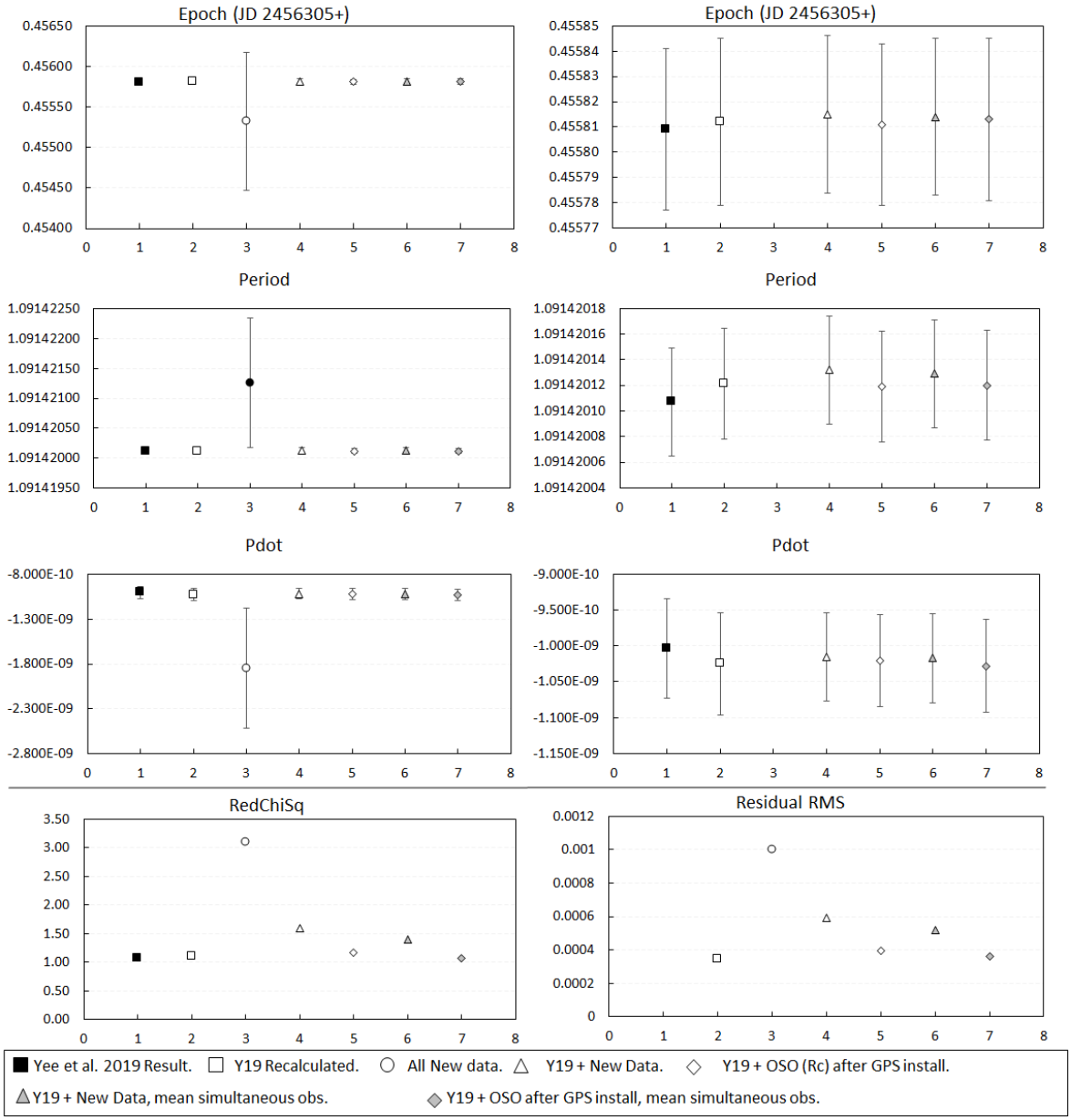

Figure 4.18: Graphical representation of the data in Table 4.10. On the left the plots include the results for all data sets for Epoch, Period and $\dot{P}$. On the right the same plots are shown without the result from the 47 new transit times times alone to better show the overlap in the derived parameters. The two plots at the bottom show the χ^2_ν and residual RMS for each data set. X axis numbers indicate the data set number as detailed in Table 4.10

mean value into almost perfect agreement.

Although the new results are in excellent general agreement with the range of values previously found the precise measurements mean that the differences are significant. This is apparent in the new value for the scaled system parameter a/R_* which is found to be 3.2σ greater than the mean value of the previously published results. Orbital inclination is 2.7σ larger and transit depth is 6.0σ greater. The results provide a smaller value for orbital eccentricity of $0.028^{+0.008}_{-0.009}$, a 3σ detection which is smaller than the most recently published value of 0.035 ± 0.006 (Maciejewski et al., 2020) while the determined argument of periastron, $\omega = 265^\circ \pm 9^\circ$ is in excellent agreement with their result ($270.7^\circ \pm 0.6^\circ$). The tidal circularistion timescale of 0.36Myr is significantly less than the derived age of 1.76Gyr. The distance to WASP-12b was calculated as $419.3^{+7.3}_{-7.1}$pc in agreement with the value calculated in Eq. 4.2 but with slightly smaller uncertainty.

4.6 Discussion

4.6.1 J0630+2942

The close companion star to WASP-12, J6030+2942, is variable. The period was seen to change from 6.83 days in 2016/17 to 6.34 days in 2018/19, at the same time the amplitude of the photometric variation decreased from 0.01 mag to 0.004 mag. If the photometric variation is due to spots and therefore following the (differential) stellar surface rotation then the changing period would be due to spots at different latitudes while the change in amplitude would indicate smaller or less dark spots. It is therefore possible that J0630+2942 is in a phase of its stellar cycle declining towards minimum activity. This would also provide an explanation to why the star is listed as a photometric standard by the AAVSO if it were catalogued during a period of quiescence.

Due to its similarity and proximity to WASP-12, J0630+2942 makes an ideal photometric comparison star, the variability detected could lead to variations in the flux measured for WASP-12b transits. As a precaution this star was excluded from the photometry comparison ensemble used for all new transit and monitoring measurements. The maximum amplitude variation observed was 0.01 mag in the Red filter during the 2016-17 season with a periodicity of 6.83 d meaning that J0630+2942 changes brightness by a maximum of 0.02 mag in half this period, a brightness change greater than the transit depth of WASP-12b. The transit duration for WASP-12b is 3 hours so an optimal observing session would cover 50% of the duration either side of the transit for a total observing time of 6 hours. The mean maximum to minimum rate of change for J0630+2942 in the 2016-17 data is 244 ppm hr^{-1} giving total magnitude change of 1.5 milli-mag over the optimal 6 hour observation. The maximum rate

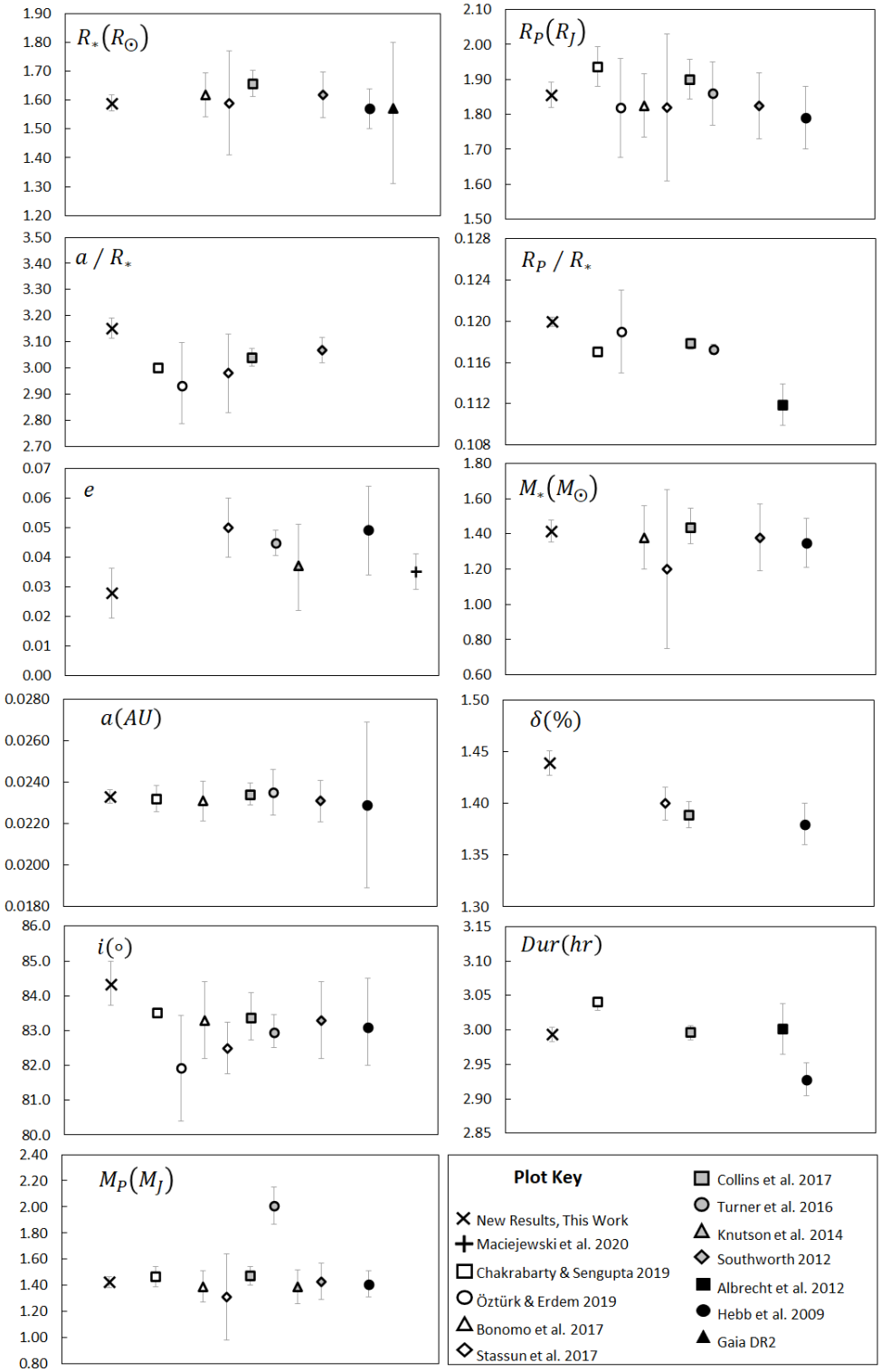

Figure 4.19: Results from ExofastV2 for new transit data compared with published values as taken from the NASA Exoplanet Archive (accessed 13/10/2020). Missing values were not reported by authors or the authors used values previously published by another author.

Table 4.11: Median parameter values and 68% confidence interval for WASP-12b obtained from ExofastV2.

Parameter	Description	WASP-12b
M_*	Mass ($M_\odot$)	$1.416^{+0.062}_{-0.061}$
R_*	Radius ($R_\odot$)	1.590 ± 0.028
L_*	Luminosity ($L_\odot$)	$3.61^{+0.28}_{-0.26}$
ρ_*	Density (cgs)	0.596 ± 0.019
$\log g$	Surface gravity (cgs)	4.186 ± 0.013
$T_{\rm eff}$	Effective Temperature (K)	6311^{+93}_{-92}
[Fe/H]	Metallicity (dex)	$0.366^{+0.068}_{-0.088}$
Age	Age (Gyr)	$1.76^{+0.78}_{-0.63}$
A_V	V-band extinction (mag)	0.261 ± 0.087
d	Distance (pc)	$419.3^{+7.3}_{-7.1}$
R_P	Planetary Radius (R_J)	1.856 ± 0.036
M_P	Planetary Mass (M_J)	1.426 ± 0.043
a	Semi-major axis (AU)	0.02330 ± 0.00033
i	Inclination (Degrees)	$84.33^{+0.67}_{-0.60}$
e	Eccentricity	$0.028^{+0.008}_{-0.009}$
ω_*	Argument of Periastron (Degrees)	-95.4 ± 9
T_{eq}	Equilibrium temperature (K)	2514 ± 40
$\tau_{\rm circ}$	Tidal circularisation timescale (Myr)	$0.360^{+0.027}_{-0.025}$
K	RV semi-amplitude (m/s)	222 ± 2
R_P/R_*	Radius of planet in stellar radii	$0.11995^{+0.00048}_{-0.00049}$
a/R_*	Semi-major axis in stellar radii	$3.151^{+0.038}_{-0.039}$
δ	Transit depth (fraction)	0.01439 ± 0.00012
τ	Ingress/egress transit duration (days)	0.01514 ± 0.00040
T_{14}	Total transit duration (days)	0.12473 ± 0.00042
$T_{\rm FWHM}$	FWHM transit duration (days)	0.10959 ± 0.00023
b	Transit Impact parameter	$0.32^{+0.03}_{-0.04}$
ρ_P	Density (cgs)	0.277 ± 0.013
$\log g_P$	Surface gravity	3.011 ± 0.013
$\langle F \rangle$	Incident Flux (cgs)	$9.05^{+0.59}_{-0.56}$
$e \cos \omega_*$		$-0.0026^{+0.0038}_{-0.0039}$
$e \sin \omega_*$		$-0.0274^{+0.0087}_{-0.0084}$
u_1(B)	linear limb-darkening coeff (B)	0.549 ± 0.030
u_2(B)	quadratic limb-darkening coeff (B)	0.212 ± 0.031
u_1(I)	linear limb-darkening coeff (V)	0.225 ± 0.042
u_2(I)	quadratic limb-darkening coeff (V)	0.302 ± 0.046
u_1(R)	linear limb-darkening coeff (R)	0.301 ± 0.014
u_2(R)	quadratic limb-darkening coeff (R)	0.324 ± 0.010

of change is greater at 382 ppm hr^{-1} giving total magnitude change of 2.3 milli-mag over a 6 hour observation. Thus the variation over a 6 hour period is comparable to the photometric uncertainty in the transit data, typically between 1.3 - 3.5 milli-mag depending on the quality of the observation, and is equal to approximately 15% of the transit depth for WASP-12b. If J0630+2942 is used as part of a large number of comparison stars in a photometric ensemble the effect would be significantly reduced but if J0630+2942 is used as the sole comparison star this effect will require correcting for, in turn requiring knowledge of the amplitude of the variation over time. The amplitude of the variation was significantly reduced in the 2018-19 season at 0.004 mag, giving a mean and maximum rate of change over 6 hours of 0.6 milli-mag and 0.9 milli-mag respectively, less than the typical photometric uncertainties.

Variability in J0630+2942 was not searched for in individual time series transit data. In the 2016-17 season, when the variability amplitude in J0630+2942 was was at its greatest, the mean variation in J0630+2942 was less than 1 milli-mag over the mean observing duration of 3.9 hr. Thus the mean change in flux from J0630+2942 was only 40% of the mean transit lightcurve RMS scatter in the transit data for this seasons. Higher precision photometry was obtained in the 2018-19 season but the reduction in amplitude of variations seen in J0630+2942 means the expected mean magnitude change over the typical transit observation duration was even less, just 25% of the mean RMS scatter.

4.6.2 WASP-12 Monitoring

No periodic variability attributable to rotation was unambiguously detected in the photometry of WASP-12 obtained over three observing season between 2016 and 2019. The detection of photometric variability in field star J0630+2942 provides a variability detection threshold of 2 millimags for the data collected, any variability in WASP-12 at this level or greater should be detected. The 29.6d periodicity seen strongly in the blue filter and similar periods seen less strongly in the red filter suggest a systematic effect of lunar illumination variation affecting the photometry rather than a physical attribute of WASP-12. This is seen especially clearly seen in the blue filter photometry from the 2017-18 season. The same strong periodicity is not seen in the check star and J0630+2942 measurements which remains unexplained. It is worth noting that given the newly calculated radius of WASP-12, a 29.6d period implies a rotation velocity of 2.7 km s^{-1}, in general agreement with the values of $v\sin i = 2.2 \pm 1.5$ km s^{-1} reported by (Hebb et al., 2009) and $v\sin i = 1.6^{+0.8}_{-0.4}$ km s^{-1} (Albrecht et al., 2012)). While it remains possible that the true rotation period for WASP-12 is close to the lunar month duration, the matching phase (see Figure 4.14 for example) makes a systematic effect the more likely explanation.

The lack of conclusively detected variability in WASP-12 over all three seasons of moni-

toring implies that the system is (1) being viewed at a high inclination with respect to the stellar rotation pole, (2) it was at a quiet stage of its stellar cycle when observed, (3) the photometric modulations are below the PIRATE detection threshold, or that (4) WASP-12 is anomalously quiescent. Each of these have implications for our understanding of the system.

Schlaufman (2010) used a Monte Carlo simulation to determine the range of observable νsini expected for a control sample of almost 900 field stars. The same simulation was performed for known exoplanet host stars under assumption of spin-orbit alignment. Comparison of the host stars with a random sample allowed systems with significantly slower than expected νsini to be identified as misaligned. 10 out of 75 systems were identified, including WASP-12, as being either anomalously slow rotators or aligned close to pole on to our line of sight.

Using the method of Schlaufman (2010), Albrecht et al. (2012) calculated the expected equatorial rotation velocity for WASP-12 as 13.7 ± 2.5 kms^{-1}. Their measured rotation velocity of νsini $= 1.6^{+0.8}_{-0.4}$ kms^{-1} implies we are viewing WASP-12 just 6.7° from pole on. Using the newly calculated value for the radius of WASP-12 the projected rotation period would be 5.8 days for the estimated νsini and 50 days for the measured νsini. No matching period is seen in the monitoring photometry.

Both anomalously slow rotation or spin-orbit misalignment are consistent with the non-detection of the Rossiter-McLaughlin effect in spectroscopic observations of WASP-12b (Albrecht et al., 2012; Husnoo et al., 2011).

The Sun shows a repeatable pattern of sunspots (the butterfly diagram seen in Figure 1.3) appearing at latitudes as high as 60° at the start of each solar cycle and migrating towards the equator as the cycle progresses. If WASP-12 is viewed at a high stellar inclination only surface spots at high latitudes early in the stellar cycle would be visible to produce photometric variations. Spots at high latitudes may be visible for complete stellar rotations and would not produce the expected periodic photometric variations. Instead any photometric variation would occur at the timescales of the spot lifetimes and would therefore only produce irregular variations as spots are formed and dissipate at the visible latitudes. Surface spots would become less visible as they migrate to lower latitudes implying the stellar cycle could be detected in the level of variation of stellar brightness between observing seasons. The difference seen in the mean red magnitude of WASP-12 between the 16-17 and 17-18 seasons was 0.005 Mag, comparable to the measured 1σ uncertainty of 0.004 Mag, so not significant. Blue filter data is not available for the 16-17 season and the change in filters for the 18-19 season means direct comparison is not possible.

There is no a-priori reason to suspect WASP-12 is an anomalously slow rotator, the detection of the orbital decay for WASP-12b Yee et al. (2019) shows that angular momentum

is being transferred from the planetary orbit to the host star which would be expected to result in a faster rotation for WASP-12. Weinberg et al. (2017) showed that this would not be inconsistent with observations of slow rotation if WASP-12 is on the sub-giant branch as the transfer of angular momentum would occur very close to the stellar core, resulting in spin up of the core while leaving the extended stellar envelope unaffected. This result was not supported by subsequent analysis preferring the conclusion that WASP-12 is a main sequence star (Bailey and Goodman, 2019).

The extremely short orbital period of WASP-12b, well below any likely stellar rotational period, can result in star-planet interactions through either the raising of tidal bulges on the stellar surface or through magnetic interaction. The orbit of WASP-12b will raise tidal bulges on the surface of WASP-12 at both the sub-planetary point and its antipode, resulting in two bulges thus any signal arising from this equilibrium tidal approximation would occur at half the orbital period. A signal consistent with the predictions from this equilibrium tide approximation have been observed in RV measurements(Maciejewski et al., 2020). The authors predict tides would be raised with a height of 150km and they predict the photometric variation resulting from this departure from the spherical would cause a photometric variation of 80ppm, well below the detection threshold from ground-based observations. Another potential source of photometric variation arises from magnetic interaction between the planet and the star which could be expected to create a hot or cool spot on the stellar surface where the magnetic field interact (Vidotto, 2019). Unlike tidal bulges, this effect would at occur only at (or close to) the sub-planetary point, causing any variation to occur at the orbital period.

Apart from their small amplitude the difficulty in detecting any photometric variation caused by star-planet interaction is compounded in WASP-12 by two other effects. Firstly the orbital period of 1.09-day being so close to the ground-based observational cadence. The second issue results from the simple fact that WASP-12b transits and this signal has been removed from the monitoring photometry. It would therefore not be expected that any variation due to magnetic interaction occurring at P_{orb} would be detectable it this data set. A period search around both P_{orb} and $P_{orb}/2$ do not reveal any signal other than the alias created by the observing cadence.

There is the possibility that the surface spots exist but that they are below the detection threshold of the small aperture ground-based telescope photometric precision, either due to small size, low contrast or geometric effects arising from a near pole-on stellar orientation of WASP-12. To investigate this the Spot Oscillation And Planet (SOAP)[3] (Boisse et al., 2011) software was used to model the effects of different size spots at varying latitudes for

[3]http://www.astro.up.pt/soap/

stellar inclinations of 6.7°and 90°, the latter as a control. A single spot with a projected size of 3% of the visible stellar radius and a brightness 0.8 × stellar flux, was modelled at latitudes of 0° (equatorial), 15°, 30°, 45°, 60°, 75°and 90° (pole) for both values of stellar inclination. A second set of models was run for a single spot with a fixed latitude of 60° but with varying sizes of 1%, 2% and 3%, again with a fixed brightness of 0.8 × stellar flux. It is noted that for small spot sizes the size and brightness are degenerate, a small dark spot being indistinguishable from a larger brighter spot (Boisse et al., 2011).

Several key points can be seen looking at the results plotted in Figure 4.20. Firstly it is clear that at low stellar rotational inclination, i.e. close to pole, on the magnitude of any photometric variation for given spot parameters and latitude is significantly smaller than if the star is viewed at high inclination, i.e. on the equator, greater than four times smaller when the spot latitude is 30° and twice as small when the latitude is 60°. The continuous variability caused by a portion of the spot area always being visible is clearly seen in the high inclination results, in both cases a spot on the pole creates no photometric variation as expected. Another effect that can be seen in the top plot in Figure 4.20 is the reversal in the magnitude of the photometric variation as the spot latitude moves from the pole towards the equator. As expected the magnitude of the variation increases when the spot moves to lower latitudes as more of the spot becomes hidden during each stellar revolution until at 45° and 30° the amplitude of the variation is the same. As the latitude reduces further to 15° and then 0° the amplitude of the variation reduces as the projected spot area visible diminishes. Taking the minimum detectable photometric variation as 0.002 magnitude, these results for a stellar inclination of 6.7° show that spot sizes of 3% with an 80% flux level would only be detectable in the latitude range 15° to 60°. Smaller or lower contrast spots are unlikely to be detectable in the monitoring photometry obtained with PIRATE. For single main sequence stars the spot filling factors decline as we move through the spectral sequence towards hotter stars with fully radiative envelopes. The Sun (G2) has a filling factor peaking at 0.5% of the visible hemisphere (Hathaway, 2015), thus we would not expect a filling factor of 3% on a lone F type star. However the existence of the extremely close hot Jupiter companion however could be expected the drive additional activity (through tidal or magnetic interactions) to a level greater than that expected for a lone star of the same spectral type (Poppenhaeger and Wolk, 2014; Poppenhaeger, 2016; Vidotto, 2019).

The SOAP models only considered a single surface spot. The existence of a large number of surface spots at similar latitudes but well distributed in longitude, which would not produce any detectable photometric variation, cannot be ruled out.

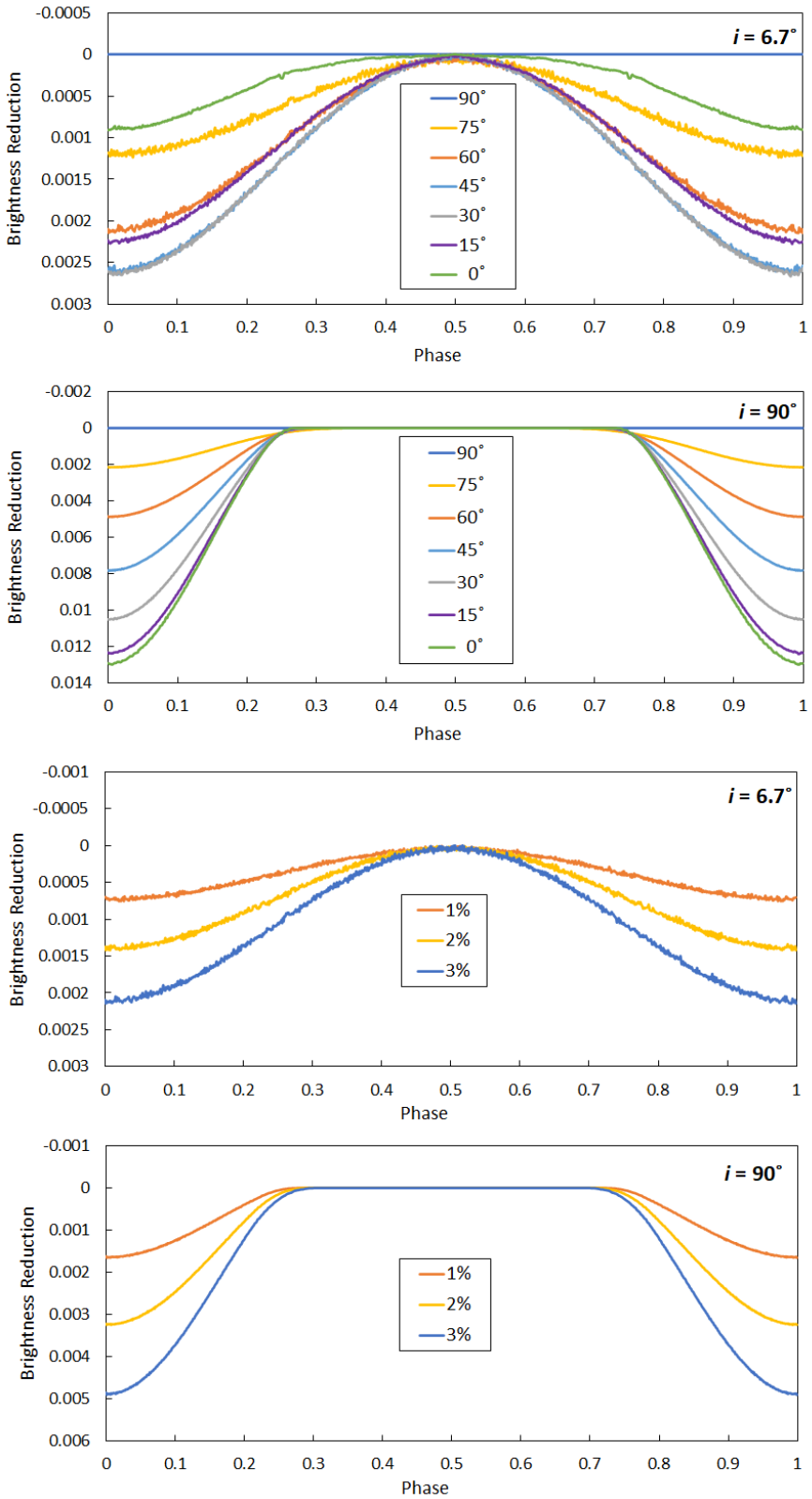

Figure 4.20: SOAP model results. Top, single surface spot of 3% with 80% brightness at a range of latitudes for stellar inclination of 6.7°. Second from top, as per the plot above but for stellar inclination of 90°, i.e. seen equator on. Third from top, a range of spot sizes with fixed brightness of 80% and fixed 60°latitude. Bottom, as for the plot above but for stellar inclination of 90°.

4.6.3 WASP-12b Transit Timing

It was not possible to determine between a linear and quadratic ephemeris using only the 47 newly obtained transit times. This is likely a result of the shorter coverage duration and greater scatter in transit mid-time measurement than seen in the Y19 data set. The first three seasons of the new data set (2013/14, 2014/15 and 2015/16) have only four data points available. Over the four seasons (3.5 years) from 2016/17 to 2019/20 with greater coverage the visible change in transit mid-time resulting from the quadratic component of the ephemeris in 4.5 (page 143) when compared to a linear ephemeris is -61 seconds. This is slightly greater than the mean transit mid-time uncertainty of ± 50 seconds seen over the same period for the new transit measurements. The spread in transit mid-time determination was greater than the mid-time uncertainty, ranging from a minimum of 76 seconds in the 2019/20 season to a maximum 361 seconds in the 2017/18 season. The typical spread in seasonal mid-time measurement in the data set published by Yee et al. (2019) was $\sim 62s$. It was this large spread in seasonal transit mid-time measurement, particularly during the three seasons 2016/17 to 2018/19, that resulted in the quadratic ephemeris not being positively detected on the new data set. The causes of this large spread in transit mid-time measurements are discussed further in Chapter 5 where I analyse further the performance of the small aperture telescope observations.

Combining the new data with existing published results provided results in close agreement to those from Yee et al. (2019), Figure 4.18. Combining all 47 new transit times with the 139 times from Y19 provided an ephemeris result with smaller uncertainties than just the Y19 data on its own. A smaller data set based on the Y19 transit times combined with those obtained from COAST and PIRATE observations made after the installation of the GPS time control and using a mean Tc for simultaneous observations provided an ephemeris model with the smallest χ^2_ν and residual RMS values, so this was selected as the updated ephemeris.

The typical per-season standard deviation in transit mid-time measurements in the Y19 data set is 2 to 3 times smaller than that seen for the newly obtained data. This level of spread in transit time measurements obtained for WASP-12b is greater than seen in the HAT-P-23b or WASP-52b measurements, a periodicity search does not reveal any intrinsic periodicity that may explain this. It is noted that for the 2019/20 season of data, not covered by the Y19 data, the standard deviation in mid-times is closer to that seen in the Y19 data. Three observations obtained by PIRATE over a 12 day period in 2020 show an extremely low transit mid-time scatter of just 0.00009d, 16% of the mean mid-time uncertainty for the three observations (0.00056d).

The analysis includes a number of simultaneous transit times where the same transit was observed by two different telescopes or observers. Two observations made as part of this project were simultaneous with observations in the Y19 data set and show a mid-time difference of 0.8σ. A further nine simultaneous transit mid-time obtained with different telescopes used in this project varied between 0.8σ and 5.1σ with a mean of 1.72σ. Both the greatest and smallest difference was seen prior to the installation of the GPS system. After the GPS upgrade the transit mid-time between pairs observed ranged from 1.5σ to 3.27σ. This is not greatly at odds with results seen for the same transit observations in the data compiled by Yee et al. (2019) where the the transit mid-time differences for simultaneous observations varied between 0.8σ and 3.4σ. The simultaneous transit measurements for WASP-12b and for HAT-P-23b are discussed further in Chapter 5.

The existence of tidal decay implies ongoing tidal dissipation between the planetary orbit and the host star, parameterised by the tidal quality factor Q'_*, (Yee et al., 2019).

$$\dot{P} = -\frac{27\pi}{2Q'_*}\left(\frac{M_P}{M_*}\right)\left(\frac{R_*}{a}\right)^5 \tag{4.6}$$

$$Q'_* = -\frac{27\pi}{2}\dot{P}^{-1}\left(\frac{M_P}{M_*}\right)\left(\frac{R_*}{a}\right)^5. \tag{4.7}$$

Using the newly determined value for the period change of $-9.419\pm0.596\times10^{-10}d$ and other parameters taken from Table 4.11, the tidal quality factor is $Q'_* = 1.35 \pm 0.15 \times 10^5$ which compares with $Q'_* = 1.75^{+0.13}_{-0.11}\times10^5$ reported by Yee et al. (2019). This is a continuation of the downward trend in values calculated for Q'_* as more data have become available. Maciejewski et al. (2016) reported a value for Q'_* of 2.5×10^5, a year later Patra et al. (2017) reported a value of 2×10^5 and in 2019, Yee et al. (2019) reported a value of 1.75×10^5.

As can be seen from Equation 4.7 the value of Q'_* is extremely sensitive to R*/a, a small R*/a value will increase Q'_* while a large value of R*/a value will decrease Q'_*. Keeping all other values fixed but using the smallest value reported for R*/a, Öztürk and Erdem (2019), results in a determination for Q'_* that is $\approx 30\%$ larger. Thus variations in the distance ratios used to calculate Q'_* can easily account for the range of values seen in the literature.

Equation 4.7 assumes a constant mass ratio and thus neglects any mass loss from the planet. We know that WASP-12b is losing mass (Haswell et al., 2012) but it is unknown how much mass is being lost and whether this is conservative, non-conservative or a combination of both (Haswell, 2018). In the extreme case of fully conservative mass transfer the amount of mass required to produce the orbital decay seen would be in the region of 2.5×10^{25} kg yr^{-1}. This is significantly in excess of the extreme mass loss scenario calculated by Lai et al. (2010) of $\approx 10^{-7}$ M$_\mathrm{J}$ yr^{-1}. Although we can rule out conservative mass transfer as the cause of the

period change, the impact of mass loss from WASP-12b is still an open question (Haswell, 2018).

4.6.4 WASP-12b System Parameters

The new results provide the tightest constraints yet on the values for R_*, R_P, a, M_* and M_P for the WASP-12b system showing that large number of filtered observations obtained with small aperture ground-based telescopes, primarily for the purposes of transit timing, can be combined with published RV and photometric data to retrieve precise system parameters.

The age determined for WASP-12b of 1.76 Gyr and the tidal circularisation time scale of 0.36Myr imply that, unless we consider we seeing WASP-12b at a special time, the orbit of WASP-12b should not be eccentric. Maciejewski et al. (2020) reported a 5.8σ detection of orbital eccentricity in WASP-12b of $e = 0.035 \pm 0.006$ and $\omega = 270.7 \pm 0.6°$. This result was interpreted resulting from a combination of the RV signal arising from a circular orbit combined with the signal arising from tides being raised on the surface host star by the closely orbiting planet which the authors determine will mimic an apparent non-zero eccentricity with an argument of periastron at 270°. My finding from the combined RV and transit analysis for WASP-12b orbital eccentricity and argument of periastron of $e = 0.028^{+0.008}_{-0.009}$ and $\omega = 265 \pm 9°$ are in agreement with the values found by Maciejewski et al. (2020) within the quoted uncertainties and which is consistent with the calculated age and tidal circularisation timescale for the system.

Comparison with the results for parameter determination from other authors is not always straightforwards for a number of reasons. As can be seen from Figure 4.19 many authors do not publish a standard set of values for systems under study. It is trivial to calculate some specific values such as semi major axis given R_* and a/R_*, however simple combination of uncertainties in standard fashion often results in greater uncertainties for values calculated in this way rather than being modelled by the transit analysis software used. Authors do not publish the values used for scaling their results to Solar System values, potentially introducing a source of systematic error if different transit analysis software makes use of different values. For example IAU 2015 resolution B3 provides values for the polar and equatorial radii of Jupiter, if the analysis reports the results using units of mean Jupiter radius the planetary radius will be over reported. ExofastV2 publishes the constants used in calculating and reporting results with the equatorial radius of Jupiter being used for reporting planetary radii. Some authors use previously published values as fixed parameters in their model fits. Chakrabarty and Sengupta (2019) used R_* and M_* from Collins et al. (2017a) while Öztürk and Erdem (2019) use values for R_* and M_* and M_P published by Hebb et al. (2009). These duplicate values were not presented in the comparison of the new results with existing

published data in Figure 4.19. The updated WASP-12 system parameter values reported in Table 4.11 used ExofastV2 to provide a homogeneous set of results.

4.7 Summary of findings

1. No periodicity was detected in the photometry of WASP-12. The balance of evidence favours a scenario where we see WASP-12 almost pole on significantly reducing the magnitude of any photometric variation resulting from rotation of stellar spots. Models using SOAP indicate any spots will need to be larger than 3% of the stellar surface (with an 80% flux level) and residing between latitudes 15° to 60° to generate a photometric variation detectable with PIRATE.

2. A periodic variation was detected on J0630+2942 just 2′ from WASP-12 which is attributed to rotational modulation caused by surface spots. The period and amplitude were seen to vary over the 3 seasons of observations. Further photometric monitoring will be required to measure the long term variation and thus the stellar cycle period.

3. The analysis of transit mid-times combined with the existing published data highlights the requirement for very long term (decade+) accurate transit mid-time monitoring to detect orbital period changes. In conclusion the new observations complement the Y19 data set and extend it by a further season allowing a revision of the ephemeris which is in excellent agreement with that published by Y19.

4. The new results provide the tightest constraints yet on many key values for the WASP-12b system and clearly demonstrate the use of large numbers of transit lightcurves, obtained using small aperture ground-based telescopes for transit timing purposes can be used to provide precise system parameters.

In this and the previous chapter I have considered the results of transit observations made with multiple small aperture ground-based telescopes measuring transit timing, system parameters and host star variability. In the final chapter I look at the performance of the small aperture ground-based telescope observations and consider the suitability of and role for these observations to contribute to exoplanet science.

Chapter 5

Small Aperture Telescope Performance

5.1 Introduction

In this chapter I take a closer look at the performance of the small aperture ground-based telescopes used to make the observations of HAT-P-23b, WASP-12b and WASP-52b discussed in the preceding chapters. The aim is to quantify the capabilities of small aperture ground-based telescopes for making observations of transiting exoplanets and to identify best best practice methods.

In the first section I look at the data quality in general achieved with each telescope in the different observing modes, considering the effect of different CCD binning, photometric SNR and systematic noise. In the second and third sections I look at the ability to define precise systems parameters from single and multiple observations and the quality of the long term photometric monitoring of exoplanet host stars. In the fourth section I look at how the data quality and observing modes affect the transiting timing measurements. In the final section I consider results from simultaneous observations of the same transit with multiple telescopes.

5.1.1 There is 'binning' and there is 'binning'

Before continuing it is worth just briefly covering the two contexts where the wording "binning" is used in the following discussions. The first relates to on chip binning of the CCD cameras used to gather the photometric data. This is referred to as "CCD" or "on chip" binning and refers to the settings used in the camera control where the camera is operated in un-binned or 1×1 mode, or where individual CCD pixels are binned into groups of 4 (2×2 binning) or even 9 (3x3) and read out from the CCD camera as single larger pixels.

The second use of the word binning is where individual measurements are combined usually into time related groups of data. An example is where photometric data points in phase folded lightcurves are combined into 5-minute bins. The use is stated where the context of the surrounding discussion does not make it clear which use of the term applies.

5.2 Data Quality

5.2.1 Signal to Noise Ratio

There are a number of measures for the quality of a transit lightcurve, one such measure is the Transit SNR (TSNR) (Ioannidis et al., 2016) which is the ratio of transit depth (δ) to out-of-transit (oot) measurement scatter, measured as the RMS of the detrended data points before and after ingress and egress. Figure 5.1 shows the mean TSNR and mean oot RMS broken down by system observed and telescope/CCD mode used. The observations made with the CCD camera in 1×1 on chip binning mode show a lower mean oot RMS and therefore a greater mean TSNR. For the WASP-12b observations both the smaller aperture COAST and POST telescopes, operating in 1×1 binning mode, show a greater mean TSNR/lower oot RMS than the PIRATE 1×1 observations.

To understand how the photometric SNR impacts the RMS scatter and thus TSNR, mean oot RMS and mean photometric SNR were plotted by telescope and binning mode. Figure 5.2 shows clear correlation between increasing SNR and decreasing oot RMS scatter in the measurements which in turn leads to an increased TSNR with photometric SNR. The observations binned 1×1 dominate the higher SNR/lower oot RMS end of the curve, but there is considerable scatter. The data in Figure 5.2 is fit with two power law curves for SNR^{-1}, grey line and $\mathrm{SNR}^{-0.95}$, black line. The results show that mean oot RMS is not quite a perfect inverse proportionality, the best fit power is -0.95, indicating a slightly greater SNR requirement to achieve a given oot RMS value. SNR values above 1000 show little improvement in reducing scatter.

As TSNR $= \delta /$oot RMS, we can can substitute the relation found between oot RMS and photometric SNR to calculate the expected TSNR for a given photometric SNR or, alternatively, to estimate the photometric SNR required to achieve a given TSNR

$$\mathrm{TSNR} = \delta \times \mathrm{SNR}^{0.95}. \tag{5.1}$$

Figure 5.3 plots the TSNR against mean photometric SNR for each of the three systems along with the result of Equation 5.1. The plots show that Eq.5.1 is a good fit for the results for WASP-12b, HAT-P-23b achieved a greater TSNR for a given mean photometric SNR, though the plot is dominated by two high TSNR measurements. WASP-52b has the

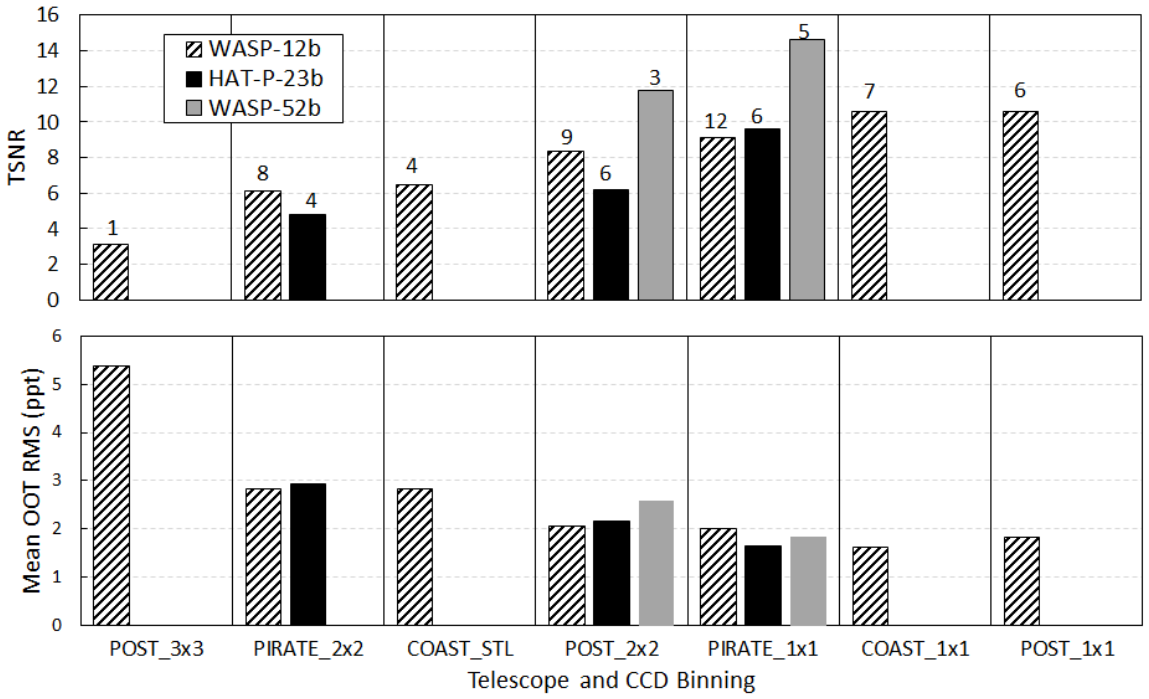

Figure 5.1: Top, plot of the mean TSNR for each of the three systems broken down by telescope and CCD binning. The number above each bar indicate the quantity of lightcurves in each calculated mean, except for POST 3×3 which shows the values derived from that single lightcurve. Plot is ordered from left to right in increasing TSNR for WASP-12b. Bottom, plot of mean out-of-transit RMS value, in parts per thousand (ppt), again by system and telescope as RMS value is independent of transit depth.

deepest transits of the three targets with a single outlying low TSNR observation (transit number 8) made with POST. The simple relation in Equation 5.1 can be used to estimate the photometric SNR required to achieve a given TSNR and therefore provides a starting estimate the exposure time required.

Returning to consider the RMS scatter and lower TSNR of the WASP-12b lightcurves obtained with PIRATE in 1×1 binning mode, a plot of photometric SNR against exposure time for all observations is shown in Figure 5.4. The photometric SNR achieved in the PIRATE 90 second and 120 second exposures is lower than that achieved with COAST or POST (except the 3×3 observations). This suggests the lower TSNR seen stems from slight under exposure of these observations. There are several other possible reasons for the strong TSNR results obtained with POST, which is counter intuitive given the sub-optimal location of this observatory, including:

- Observations made with POST are manually controlled and only made when conditions are ideal, whereas the automated observations made with PIRATE allow many more transits to be obtained but could be made in sub-optimal conditions.

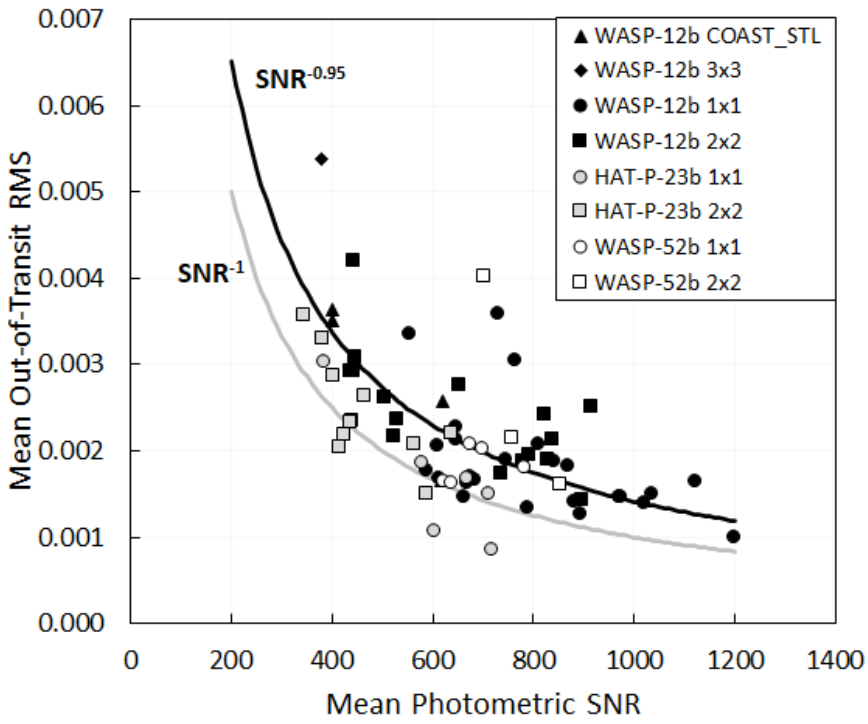

Figure 5.2: The relationship between mean photometric SNR and mean oot transit RMS plotted for exoplanet system and CCD binning mode. The grey line is SNR^{-1} the black line is $\mathrm{SNR}^{-0.95}$

- The limited horizon at POST prevents observations at higher airmass. The highest airmass observation obtained with POST is 1.65, while with PIRATE it is 2.30. Higher airmass observations will be at start or end of observation (or both), systematically affecting oot RMS measurements and therefore TSNR for the whole lightcurve.

- POST uses a higher sensitivity CCD camera (at the expense of a much smaller field of view) allowing higher photometric SNR to be achieved in similar exposure times.

- Flat field calibration frames are obtained on the same night as the observations removing the need to combine frames from multiple different nights.

- The POST images were autoguided, maintaining the target star on the same pixel, see Section 5.2.3.

- During the 2018-19 and 2019-20 season PIRATE exhibited trailing in a number of WASP-12b lightcurves caused by an oscillation in the RA axis. This is thought to be caused by the RA balance of the OTA being too perfect making the OTA susceptible to wind driven vibration. This will be rectified by offsetting the counter balance weights slightly to ensure better RA gear meshing. As a result a number of science frames from some observations had to be discarded while those retained in order to 'save the

lightcurve' may also explain a lower SNR.

- The highly peaked PSF seen in PIRATE star images records the stellar flux in a very small number of pixels increasing the impact of pixel response variations not perfectly corrected by flat fielding as the stars drift across the CCD during observations.

5.2.2 Systematic Noise

The quality of the transit lightcurves can be affected by correlated (red) noise, sources of which can include airmass changes, changes in seeing conditions, variable comparison stars, imperfect transit model fitting or pier flip correction, essentially any noise source which is not stochastic. The existence of correlated noise can be determined by comparing the lightcurve residual RMS noise for increasing data bin sizes with the theoretical expectation for white noise. White noise is expected to follow $\sigma_1/\sqrt{N}$ where σ_1 is the un-binned residual RMS and N is the number of data points in each bin. Departures from this theoretical expectation would be indicative of the existence of correlated noise. All 47 full transit lightcurves obtained for WASP-12b, which was observed with a wide range of telescope and camera mode combinations, were binned up to a maximum of 50 data bins. The number of bins calculated for each lightcurve was set so a minimum of 3 data points was included in each bin to minimise the impact of statistical fluctuations at high bin/low data numbers. The results along with the theoretical white noise expectation are shown in Figures 5.5, 5.6 and 5.7. Generally the data follows the theoretical white noise expectation, though there are some notable departures. A number points can be seen in these plots, which are ordered by decreasing full transit RMS residuals for each telescope;

- As noted in the preceding discussion the 1×1 CCD binned data has consistently smaller un-binned full transit RMS noise than the 2×2 CCD binned data.

- The scatter around the white noise prediction increases, generally starting after bin sizes covering 10-20 minutes. This is likely due to the relatively low number of data points in the larger bin sizes.

- A few lightcurves exhibit a significant departure from the white noise expectation, including PIRATE 20171223 and COAST-STL 13022017, indicative of red noise. For all 47 lightcurves there is no correlation seen between instrumental factors including CCD binning, filter and pier flip. All the data sets that show some form of deviation from the white noise expectation were observations made where the airmass change during the observation was large. However many observations with similar large airmass

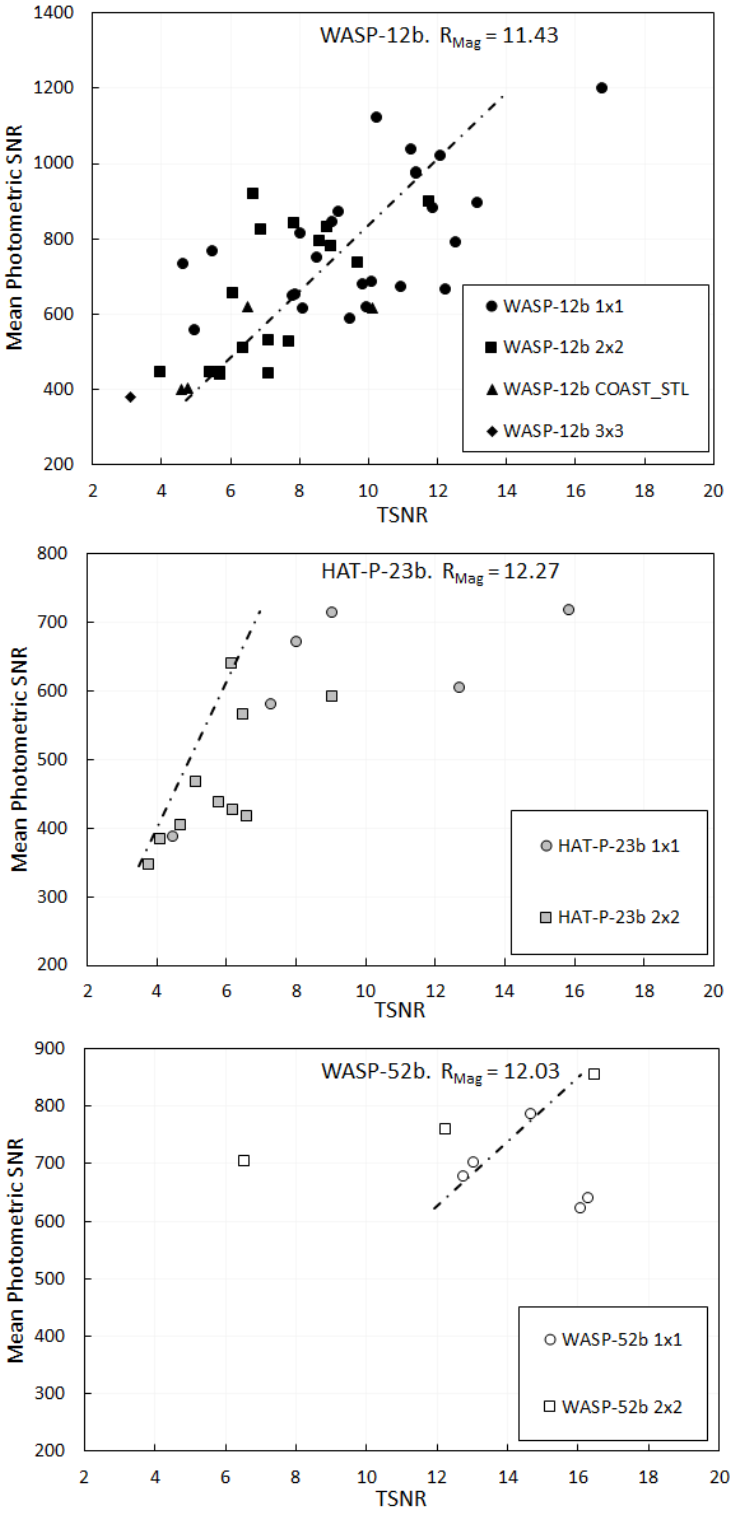

Figure 5.3: A plot showing the relationship between TSNR and mean photometric SNR by CCD binning mode. Each system is shown separately as TSNR is dependent on transit depth which is different for each system. The dash-dot line is from Equation 5.1

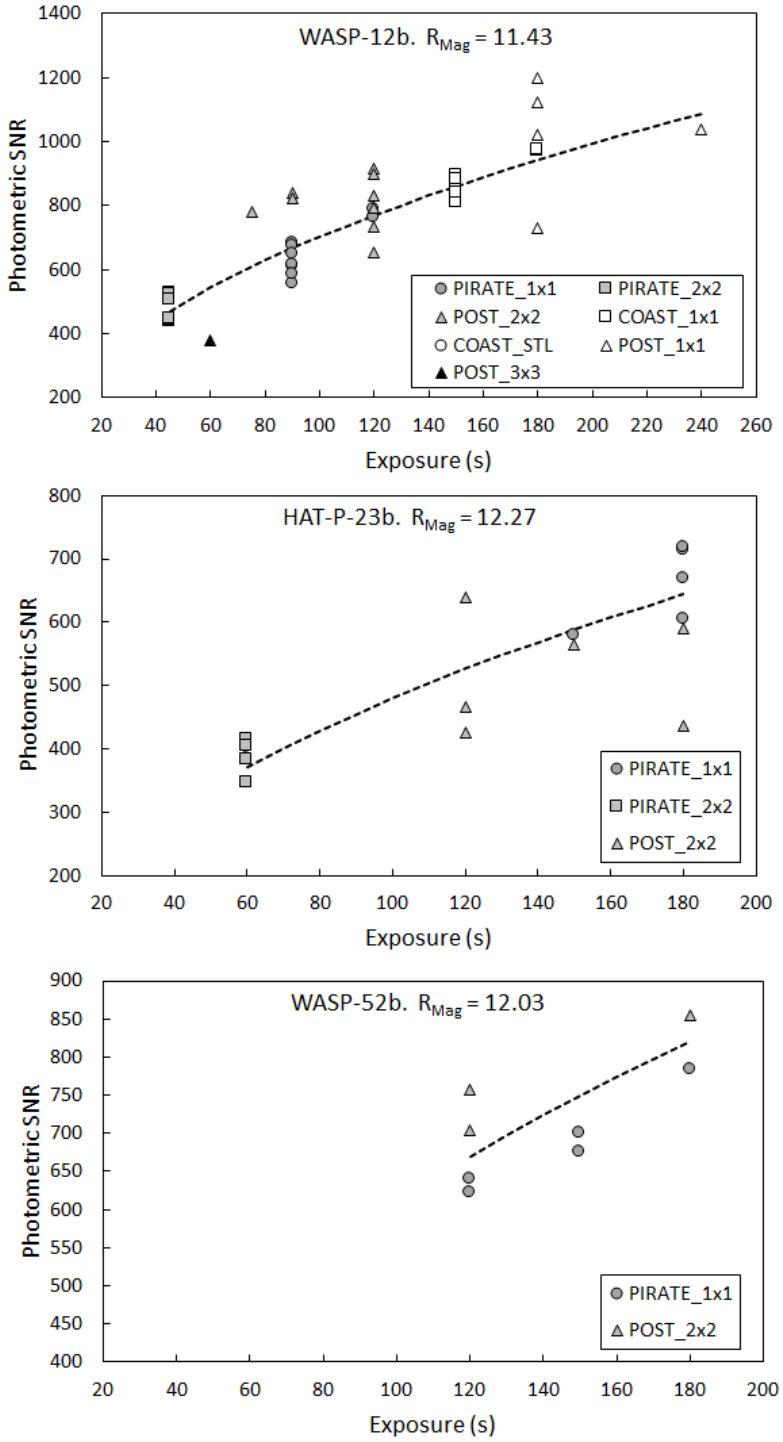

Figure 5.4: A plot showing how mean photometric SNR varied with exposure duration for each telescope and CCD binning mode for each exoplanet system. Plots show only full transits obtained through R filters. As expected SNR increases as $\sqrt{\text{Exposure}}$ with the long exposure/high SNR region dominated by the 1×1 binning observation despite the four fold increase in pixels for the 1×1 vs 2×2 binned observations. The plot for WASP-12b also indicates the apparent under-exposure for the PIRATE 1×1 observations where the 90 second exposures only average SNR values of 600 versus 800 for the 150 second exposures with COAST.

changes do not show any deviation from the white noise expectation, indicating airmass detrending is unlikely the only cause in these cases.

The WASP-12b data set contains nine simultaneous observations made with different telescopes. Eight of these pairs were made with PIRATE and COAST and seven of those lightcurves show excellent agreement with each other in the red noise plots (see Figure 5.8). This indicates the cause of any variation from the white noise expectation is likely to be of either environmental or astrophysical origin, rather than instrumental, specific to each telescope. Red noise between a pair of simultaneous lightcurves caused either by astrophysical effects or arising from environmental changes, where the telescopes are co-located, will be highly correlated. Astrophysical effects include spot crossings or intrinsic stellar variability, while changing seeing conditions at the Mt Teide observatory are a likely environmental cause. Correlation of red noise seen in lightcurves obtained by widely separated telescopes is more likely to be of astrophysical origin. The only pair of lightcurves obtained by the widely separated POST and COAST telescopes on 20170213 do not exhibit a correlation so it is possible to conclude the red noise seen in the COAST lightcurve is not of astrophysical origin. Artifacts introduced in the data analysis can also lead to a correlation in red noise between two lightcurves. These artifacts can arise from factors such as the inclusion of variable stars in the comparison star ensemble or from errors in the transit model fit, which has been subtracted from the lightcurve prior to red noise analysis. Effects arising from variable ensemble stars have been mitigated through careful analysis and selection of the stars used. The mean full transit RMS residuals are smaller than the mean out of transit RMS residuals indicating the subtraction of the lightcurve model does not introduce measurable noise. Observations made with PIRATE and COAST on 20190222 were made with different filters and the COAST observation exhibits correlated noise structure not seen in the PIRATE lightcurve. This could be indicative of an astrophysical origin though effects such as spot activity on the host star would be expected to affect the B lightcurve more than the Rc. This difference is not seen in the other two Rc and B filter pairs from 20190130 and 20190131 so it is not possible to draw definitive conclusions from this single simultaneous observation.

To understand if correlated noise has an effect on the transit timing a metric was created to characterise the level of departure from the white noise expectation, with increasing values indicating increasing departure from the white noise value

$$\text{Red Noise Metric} = \sum_{\mathrm{N}=1}^{\mathrm{N}=50} \left| \frac{\sigma_1}{\sqrt{\mathrm{N}}} \; - \; \sigma(\mathrm{N}) \right| \tag{5.2}$$

where N is the bin size and σ_1 is the residual RMS measured at N=1 and $\sigma(N)$ is the residual RMS measured at bin N.

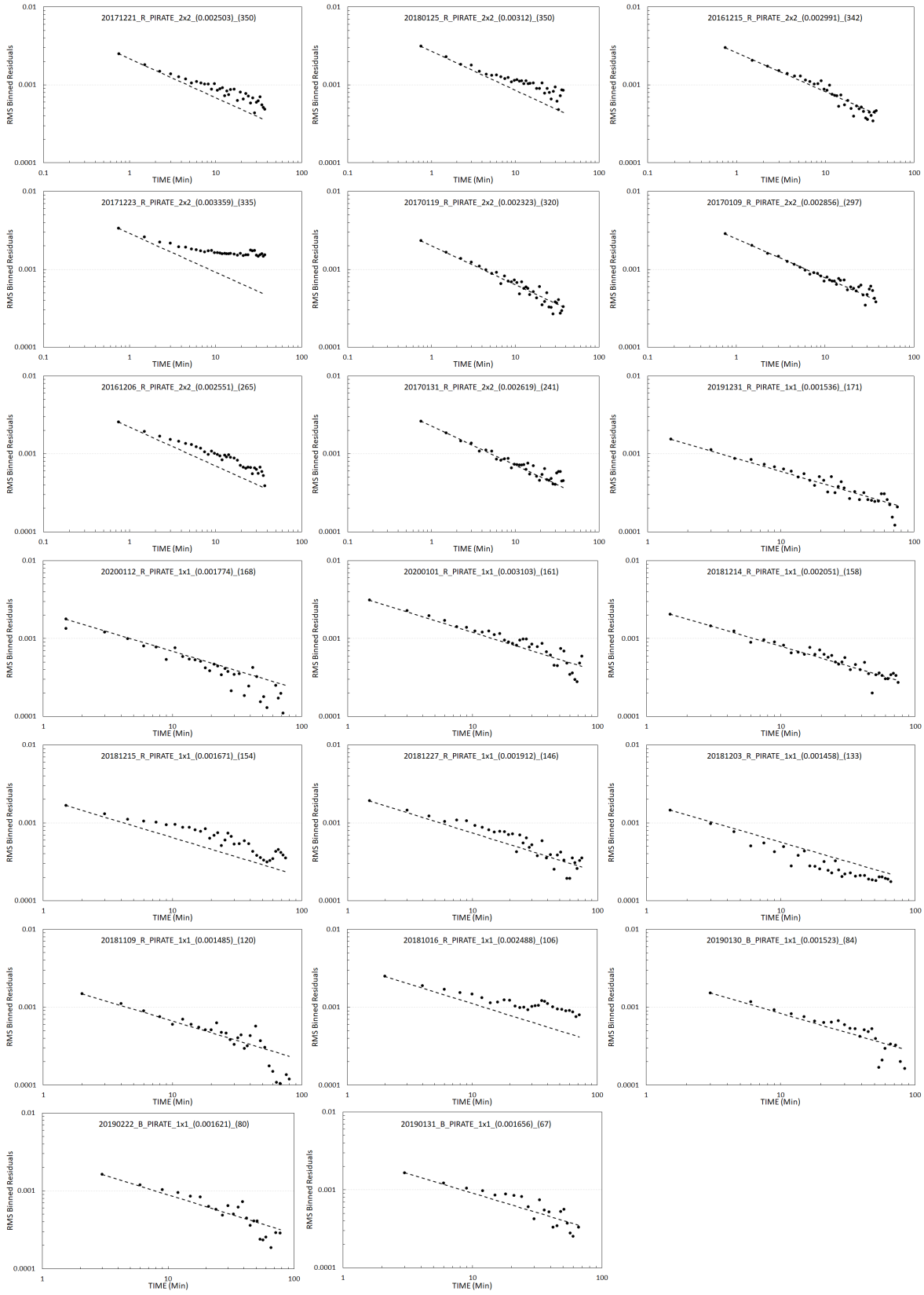

Figure 5.5: A plot showing the full transit lightcurve residuals obtained with PIRATE. Th bins are plotted from 1-20 in steps of 1 bin and from 22-50 in steps of two bins. Bins with less than 3 data points are excluded. The dashed line shows the white noise expectation ($\sigma_1/\sqrt{N}$).

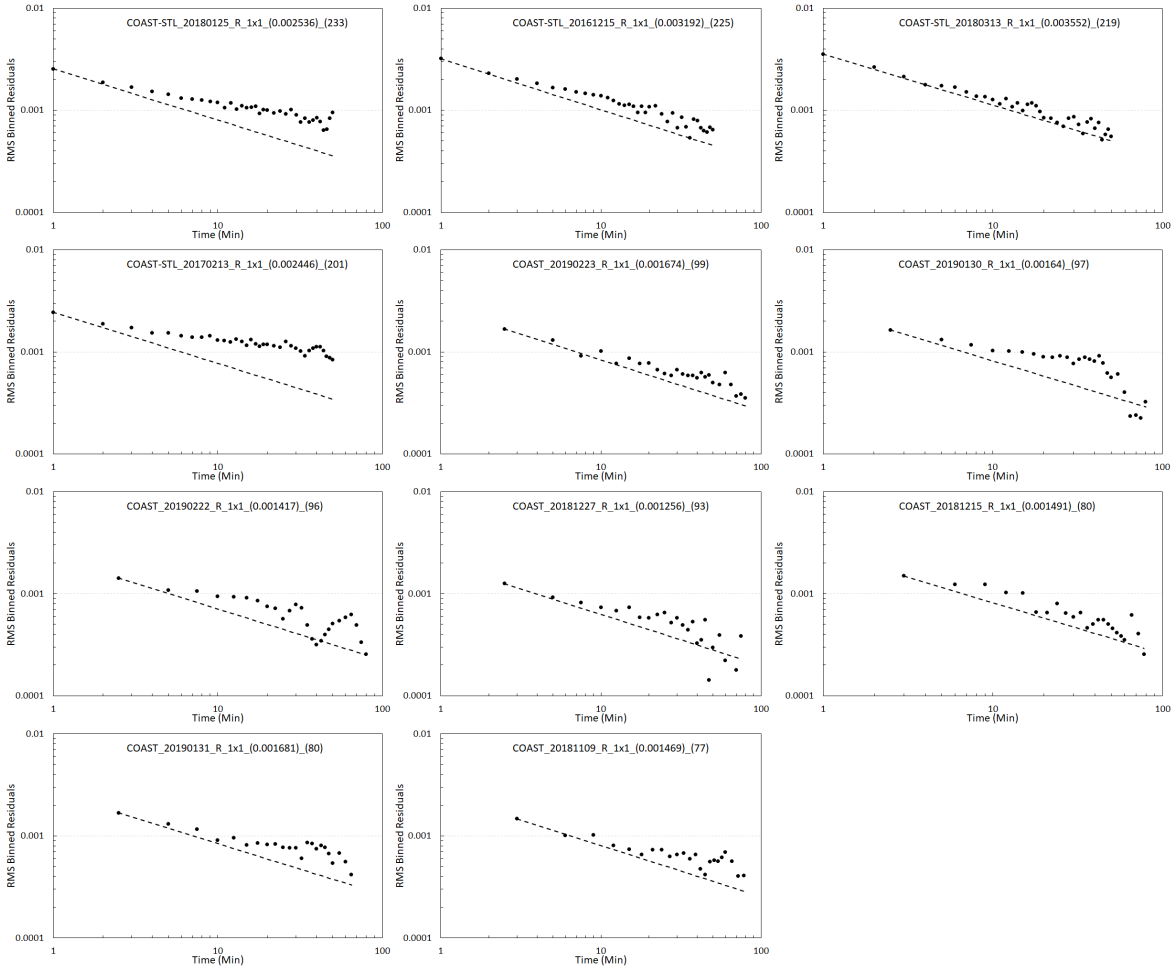

Figure 5.6: As for Figure 5.5 but for the lightcurve residuals obtained with the COAST telescope.

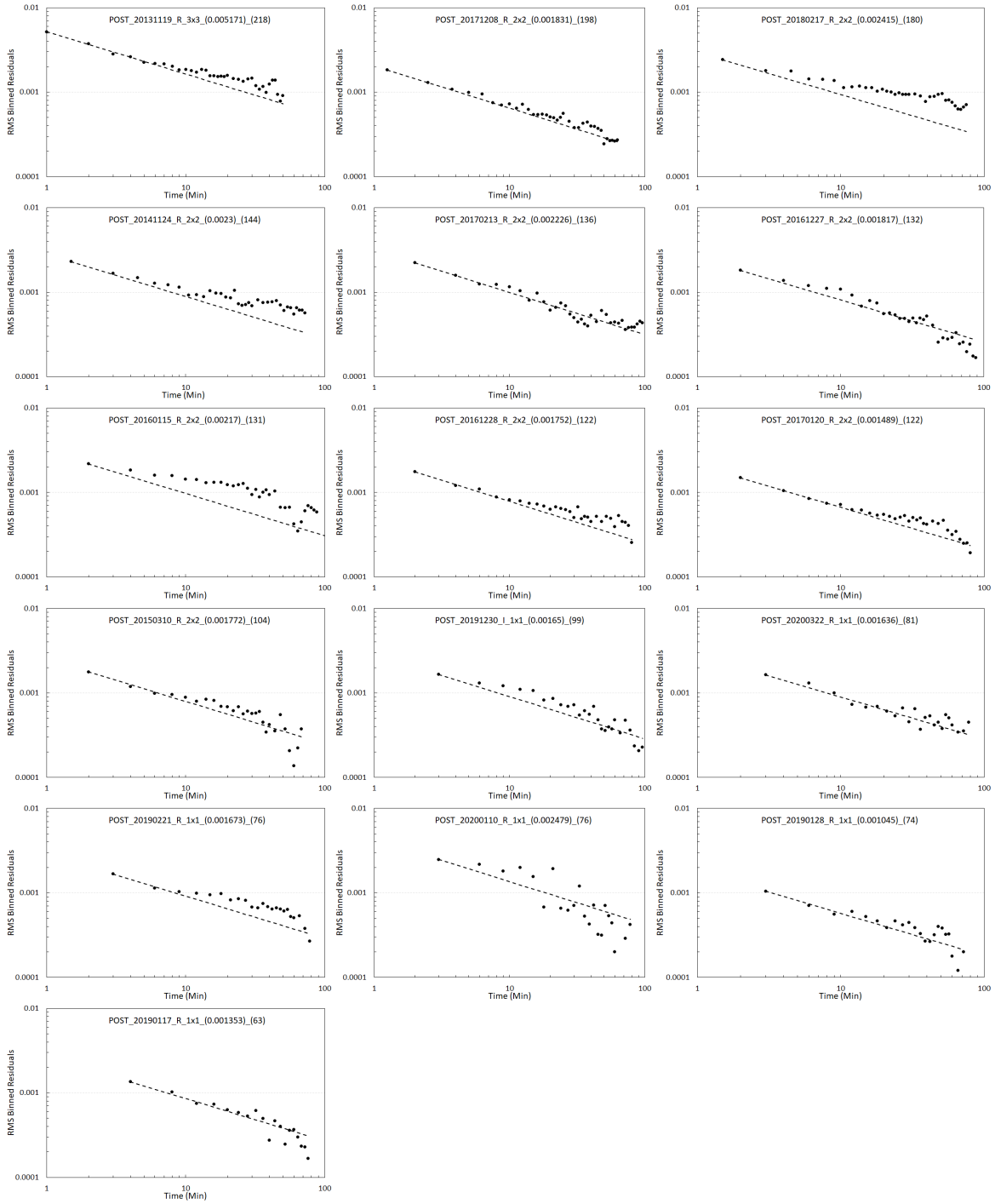

Figure 5.7: As for Figure 5.5 but for the lightcurve residuals obtained with the POST telescope.

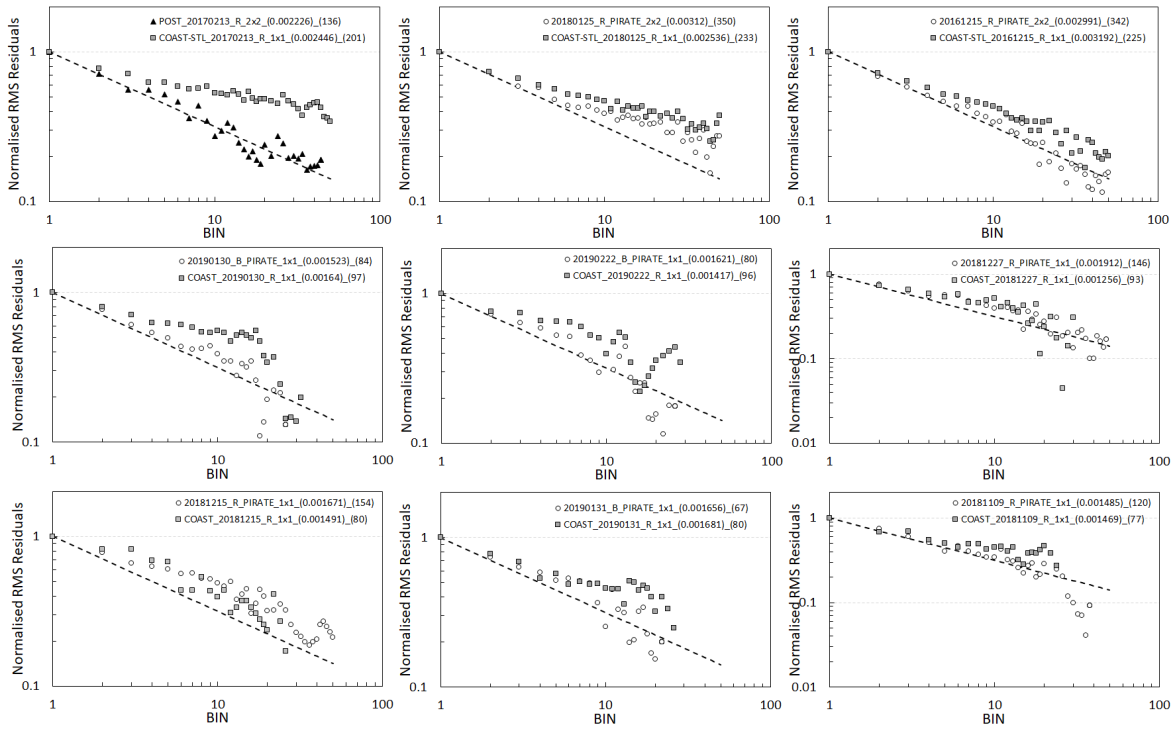

Figure 5.8: Red noise results for nine simultaneous transit observations of WASP-12b. The RMS values have been normalised to unity, the data is displayed by bin size on the X axis.

This metric was then plotted against both the transit mid-time uncertainty and the O-C of the new quadratic ephemeris (Eq. 4.4) as well as the out of transit and full transit mean photometric RMS values, Figure 5.9. The two transits previously identified as showing a large correlated noise component (PIRATE 20171223 and COAST-STL 20170213) are clearly seen as the only two lightcurves with a red noise metric around 8.0. No statistically significant correlation is seen between the red noise metric and the fours parameters plotted. There are two transits with O-C values similar to the high red noise lightcurves (> 0.002d) but with much lower red noise metrics themselves (lightcurve numbers 6 and 7). Overall the scatter in the O-C measurements is greater for the 2×2 binned observations than the 1×1 binned data. Both the 1×1 and 2×2 binned data exhibit very similar mean transit mid-time uncertainties despite the lower cadence of the 1×1 binned lightcurves. The mean FTRMS values are very slightly lower than for the OOTRMS data so we have good confidence that the models are a good fit to the data and do not introduce any additional red noise. The single 3×3 binned lightcurve from POST stands out has having low red noise but high RMS photometric noise and transit mid-time uncertainty.

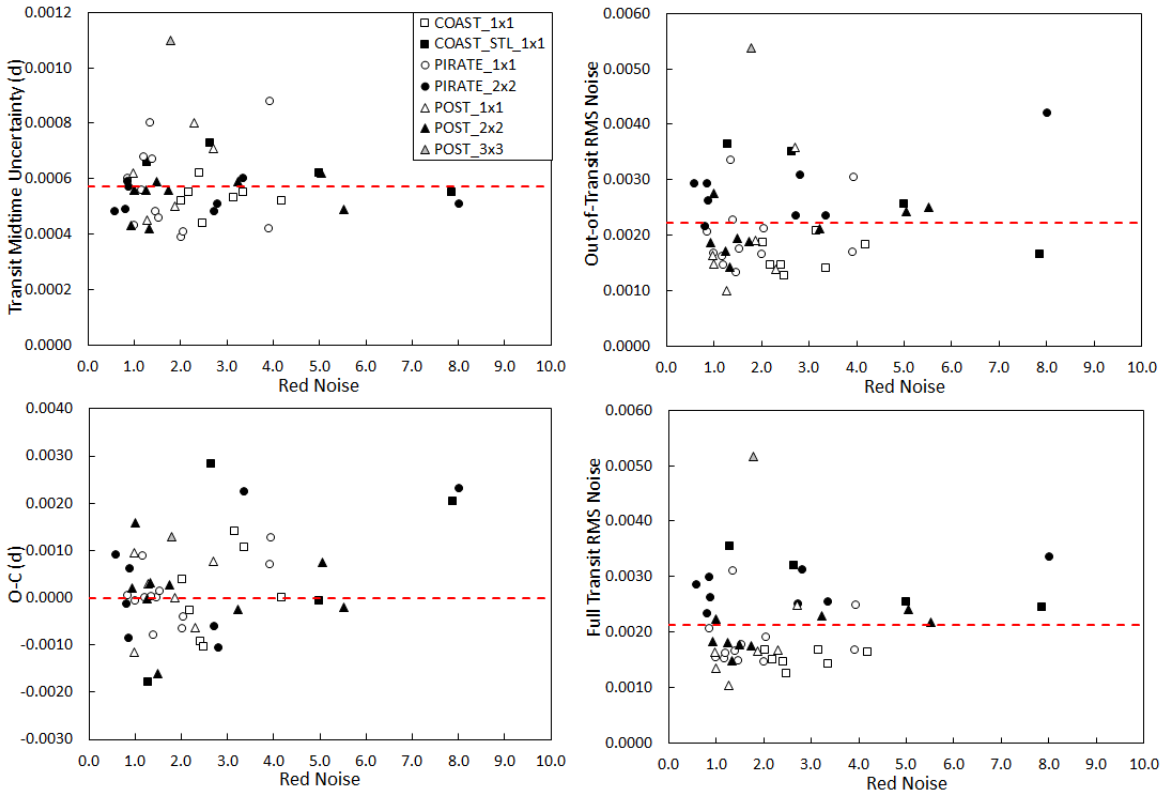

Figure 5.9: Transit parameters plotted against calculated red noise metric. Top left, transit mid time measurement uncertainty, bottom left, newly calculated quadratic ephemeris O-C (Eq.4.4). The two plots on the right show the RMS photometric scatter for out of transit data (top) and full transit data (bottom) . No statistically significant correlation is found between these parameters and the red noise metric. The red dashed lines indicate the mean value for each measurement, or the orbital ephemeris in the case of the O-C measurements.

5.2.3 Tracking Performance and Impact on Photometry

The OSO telescopes are operated in unguided mode, relying on the precision of the polar alignment, mechanical capability of the German Equatorial mounts and of the pointing model which automatically updates the tracking to minimise star trailing in images. This approach proved perfectly capable of ensuring no trailing was seen in individual exposures up to 3 minutes duration, the maximum exposure used. However time series observations of a full transit typically last between 3 and 5 hours and over these timescales drift in the centroid position of the target star is apparent. Conversely POST uses closed loop guiding to correct for imperfect polar alignment of the mount, Chapter 2.

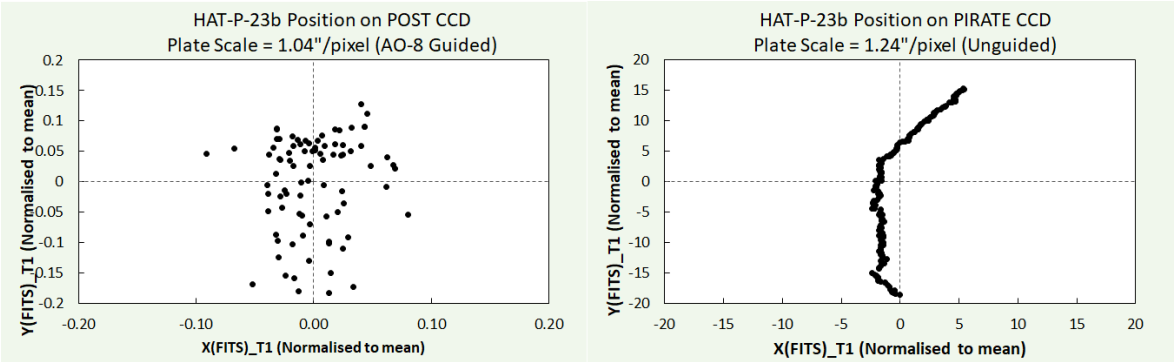

Figure 5.10: Guiding precision from a simultaneous observation of a HAT-P-23b transit from 30th June 2018. Left, POST with AO-8 fast guiding optics and right, PIRATE unguided observation. The POST fast guiding maintains the target star centriod on the same pixel for the 3 hour duration of the observation. Both CCDs were used in binning x 2 mode.

One potentially significant source of photometric noise arises from imperfect flat field correction for pixel response variations which can be mitigated by maintaining the stellar PSF on the same pixels for the duration of the observations or, to some extent, by defocusing (Southworth et al., 2009b). Maintaining a star on the same pixel for the multi-hour duration of a transit observation places high demands on a telescope system requiring closed-loop guiding. To see whether the quality of the guiding has a material effect on the quality of the photometry of transits obtained with small aperture ground-based telescopes a test observation was made of HAT-P-56b using POST on the 9th January 2021. HAT-P-56b was observed for 4.6 hours, without a pier flip, using exposures of 90 seconds (103 second cadence) through an Rc filter. The data was reduced and analysed as detailed in Chapter 2. For flat fielding a master frame was created from a median combine of 19 individual frames obtained using an artificial light source on the same night. The observations were initially guided using the AO8 fast guider with a correction rate of 1Hz. Shortly before half way through the transit observation the autoguiding guiding was switched off. Data reduction and photometry was

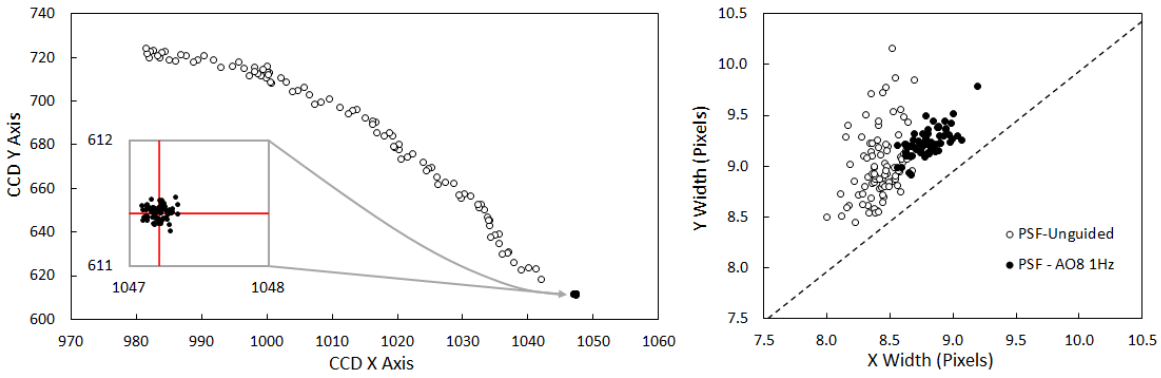

Figure 5.11: Left, stellar centriod for HAT-P-56b on the CCD. The inset shows a single pixel during AO8 guiding with the red cross indicating the mean value. On the right is the roundness of the stellar PSF where the dash line indicates perfectly round stars. It can be seen that even when guiding the PSF is slightly elongated by approximately 10% in the Y axis (RA), after guiding was disabled the X axis (Dec) shows a reduction in the mean width and an increase in the Y axis width as the stars become elongated in the RA direction. In both plots filled circles are measurements during guiding and open circles are unguided measurements.

carried out using AstroImageJ with a variable star aperture set at 1.2 × FWHM to ensure any changes in FWHM during the experiment were correctly captured in the photometry extraction.

During autoguiding at 1Hz the target star centroid was maintained on a single pixel. After guiding was disabled the field drifted due to imperfect polar alignment moving 31 arcsec in the X-direction (Declination) and 55 arcsec in the Y-direction (Right Ascension), Figure 5.11, left. The rate of drift was 0.41 arcsec per minute which equates to 1.2 pixels per exposure which is visible as an increase in the elongation of the stellar FWHM along the RA axis, Figure 5.11 right. Figure 5.12 shows the transit data along with airmass, FWHM and SNR over the observation. Airmass decreased from 1.45 at the start of the observation to 1.09 before increasing again slightly to 1.12. During the autoguided section of the observation the airmass decreased and the SNR increased as expected, the FWHM stayed constant. After guiding was disabled the FWHM mean remained the same but the scatter increased notably.

To analyse the quality of the photometry the out of transit data as indicated in Figure 5.12 was analysed. Before transit the flux value was 0.3570 ± 0.0004 and after transit 0.3570 ± 0.0006, with the uncertainties being the standard deviation on the measurements. The maximum spread in measured flux values was 1.968×10^{-3} before ingress and 2.232×10^{-3} after egress, a 13% increase. The mean photometric uncertainty calculated by AstroImageJ was $391.6 \pm 2.5 \times 10^{-6}$ before transit and improved slightly to $389.5 \pm 2.1 \times 10^{-6}$ after transit.

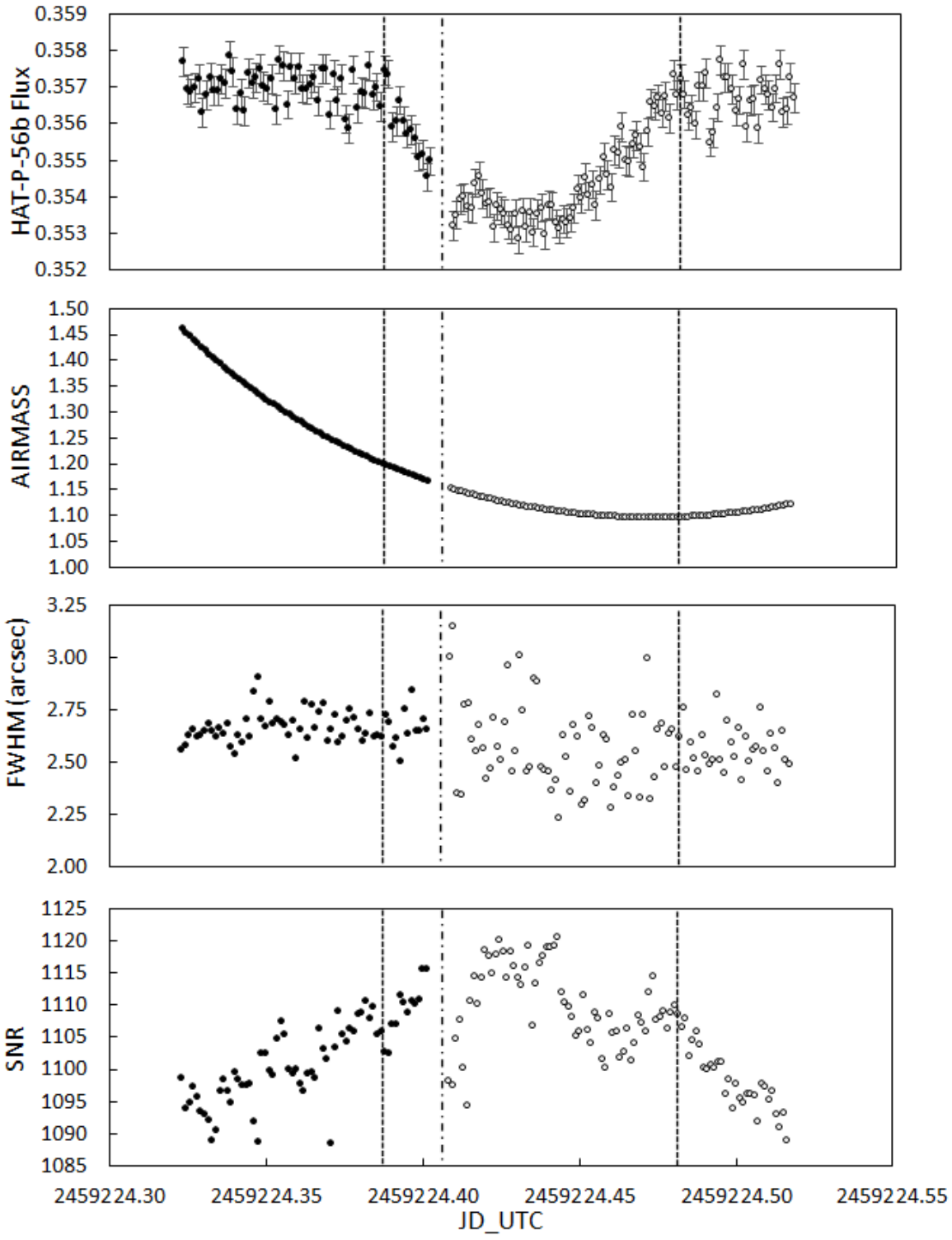

Figure 5.12: From top to bottom, the transit lightcurve, airmass, FWHM and SNR for the transit data. The vertical dashed lines indicate the cut off for the pre and post transit analysis and the dash-dot line is the point guiding was disabled. Again filled circles are guided measurements and open circles are unguided.

The increase in photometric scatter after egress while unguided is clear as is the increased scatter in FWHM. Airmass was greater before ingress excluding that as a cause. The SNR values remain similar, varying by only 3% over the duration of the 4.6 hour observation. It seems therefore that the increase in photometric scatter is a direct result of the drift of the target star on the CCD likely arising due variations in CCD pixel response not completely corrected for by the flat field process. Additional experiments testing alternative approaches to the flat field calibration, such median combining a significantly larger number of individual calibration frames or using sky flats, would determine whether the photometric scatter for unguided imaging could be reduced further. Transit photometry precision is notably improved by minimising drift of the target and ideally maintaining the target on the same pixels. While PIRATE and COAST operate unguided, the superior polar alignment means the drift on the CCD is 0.2 pixels (0.12 arcsec) per minute, over three times less than for POST. Not enough to affect the stellar PSF during typical exposures of 30-180 seconds but over a 5 hour observation this still amounts to approximately 60 pixels (43 arcsec) of drift. It therefore seems likely the photometry from PIRATE and COAST could be improved further through the implementation of sub-pixel autoguiding.

Another potential noise source arising from imperfect guiding is the transition of any hot or cold pixels, not corrected for in the data reduction process, through the photometry apertures. An example of this effect can be seen in a transit lightcurve of the hot Jupiter XO-2b obtained with COAST-STL on the 4th January 2017, Figure 5.13, where hot pixels appear close to comparison star C8 on frames 159 to 213 of 242. The cause of the hot pixels is unexplained but during the near 4 hour observation the centroid of comparison star C8 drifted across the hot pixels. AIJ provides an iterative 2σ cleaning of hot pixels from the sky annulus which successfully corrected for the effects but cannot be applied to the star aperture. The contribution from the hot pixels resulted in an increase in the measured stellar flux for the period the star aperture crossed the location of the hot pixels. The overall effect was to increase the measured transit depth by 2.8%, introducing a systematic error in transit depth measurement. The effect also resulted in a change in the measured transit mid-time by 23 seconds and increased the transit duration by 16 seconds. In this case with the anomaly occurring over the transition to egress (t_3), the greatest effect is on the full transit time from the end of ingress (t_2) to the start of egress (t_3), excluding ingress/egress, which is reduced by 36 seconds.

This type of noise, which is clear in the C8 comparison star flux measurements, highlights the importance of visually checking the photometry output.

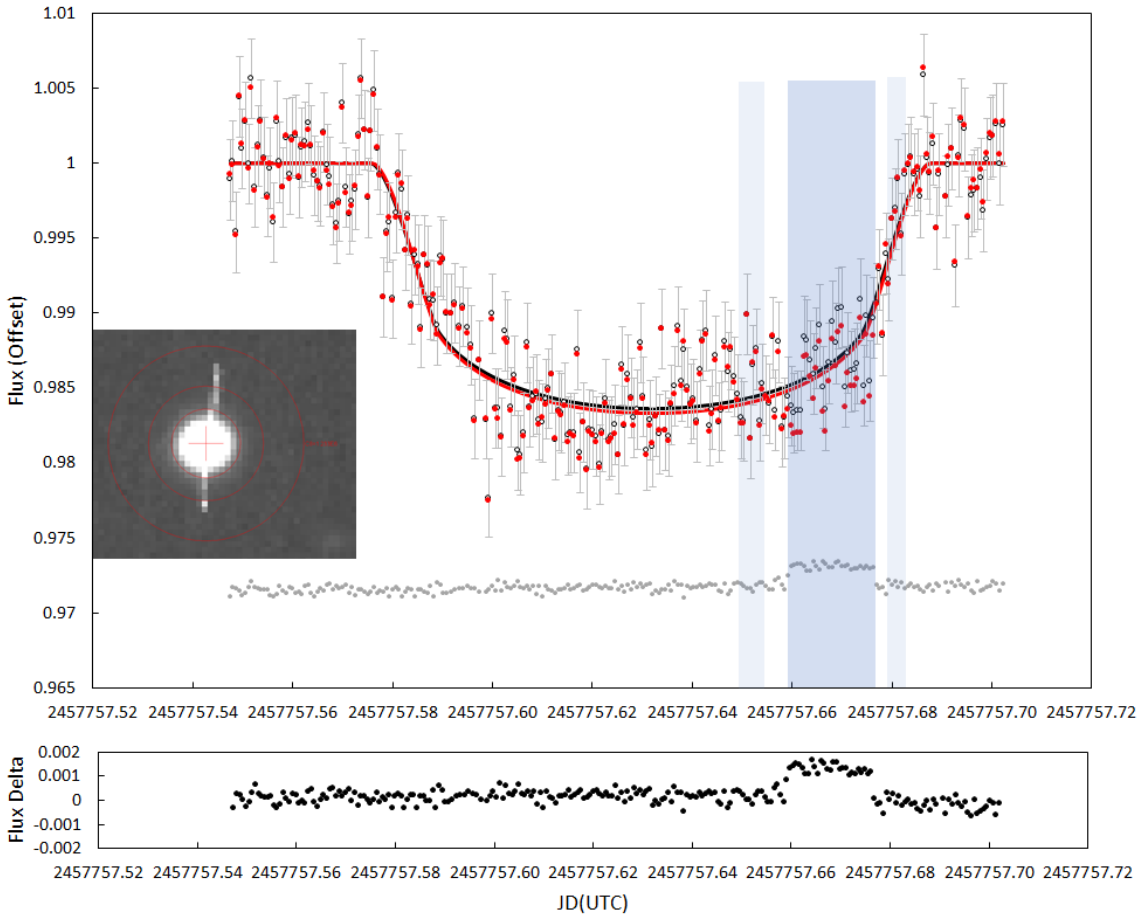

Figure 5.13: Transit of XO-2b obtained with COAST on 4th January 2017 showing the impact of uncorrected hot pixels. Top, open black data points and black AIJ transit model are without the affected star included in the photometry ensemble. The red circles and red AIJ transit model include the affected star in the photometry ensemble. Grey dots show the flux from the affected star which is shown in the inset composite image with the hot pixels crossing the sky and star apertures. The central blue band highlights the data points affected while the hot pixels were crossing the star aperture and the light blue bands either side show where the hot pixels were present in the sky annulus. Bottom, difference between the transit lightcurve calculated with and without the affected C8 comparison star.

5.2.4 Lightcurve Comparison with Published Observations

In Table 5.1 I compare the photometric precision achieved with the small aperture ground-based telescopes used in this work with those from the literature often using larger aperture telescopes. In Figure 5.14 I show the phase folded individual measurements and binned data for HAT-P-23b and WASP-52b along with previously published observations made with the telescopes compared in Table 5.1. The phase folded lightcurve for HAT-P-23b comprised 1821 individual measurements (17 full and partial transits) and a total observation time of 3337 minutes was binned by 25 data points. By comparison Mancini et al. (2017) used the Calar Alto 2.2m telescope which has a primary mirror area approximately 24 times greater than the telescopes used in this study and obtained a single transit observation of 244 minutes duration. Defining a metric of telescope mirror area multiplied by the duration of observations I find that, in the absence of spot crossing events, the binned photometric results obtained with the small aperture ground-based result in a lightcurve with the same or better photometric precision in half the mirror area $\times$ observation time of the 2.2m telescope observation. A similar result was found when the phase folded and binned WASP-52b transits were compared with those obtained using the Danish 1.54m telescope Ciceri et al. (2015).

The WASP-12b data set is larger with 42 full transits obtained through a Red filter. These 42 transits, comprising 6956 individual measurements, were phase folded and then binned to 2, 3 and 5 minute cadence achieving an out of transit RMS of 359ppm, 186ppm and 119ppm respectively. Collins et al. (2017a) published 23 lightcurves of WASP-12b obtained with the 0.6m MORC telescope and achieved an RMS precision of 183ppm for 5 minute sample bins. The precision would be expected to improve with $\sqrt{N}$ where N is number of phase folded lightcurves. The result of 119ppm for 42 lightcurves is $\sim 12\%$ better than expected from just the greater number of lightcurves used. WASP-12b was observed by the NASA Transiting Exoplanet Survey Satellite (TESS) covering 21 new transits (Turner et al., 2021). These observations were obtained from EXOMAST[1], phase folded around the same ephemeris and binned to a 5 minute cadence. The TESS observations provide full phase coverage so the out of transit RMS was measured over the same phase region used for the 42 new transits, resulting in an RMS scatter value of 204ppm. Again the difference in the two 5 minute binned RMS values is slightly better than expected from the difference in the number of transits observed. The phase folded lightcurves provide confidence that the lightcurves are not affected by a correlated noise component. These results demonstrate the capability of of small aperture ground-based telescope observations as an efficient way to collect high precision lightcurves for system characterisation while obtaining transit timing measurements.

[1] https://exo.mast.stsci.edu/

Table 5.1: Out of transit photometric RMS scatter for published observations of single transits of HAT-P-23b and WASP-52b obtained with medium class telescopes compared with the multiple phase folded and binned lightcurves from this work. For WASP-12b the comparison is made between all the available data from each source binned to the same cadence. The number in brackets after the system name is the number of phase folded lightcurves. RMS scatter is given in parts per million (ppm). The efficiency of the small versus medium aperture telescope observations is discussed further in Section 6.4.

System	**RMS Scatter**	**Observation**	**Filter**	**Source**
HAT-P-23b (1)	645	Calar Alto 2.2m	Thuan-Gunn r	Ciceri et al. (2015)
HAT-P-23b (1)	746	Calar Alto 1.23m	Rc	Ciceri et al. (2015)
HAT-P-23b (17)	415	0.4m (Binx25)	Rc	This work
WASP-52b (1)	582	DK 1.54m	Bessell r	Mancini et al. (2017)
WASP-52b (1)	768	Calar Alto 1.23m	Rc	Mancini et al. (2017)
WASP-52b (13)	616	0.4m (Binx12)	Rc	This work
WASP-12b (23)	186	MORC 0.6m (5min)	Rc	Collins et al. (2017a)
WASP-12b (21)	204	TESS 0.1m (5min)	0.6-1.0µm	Turner et al. (2021)
WASP-12b (42)	119	0.4m (5min)	Rc	This work

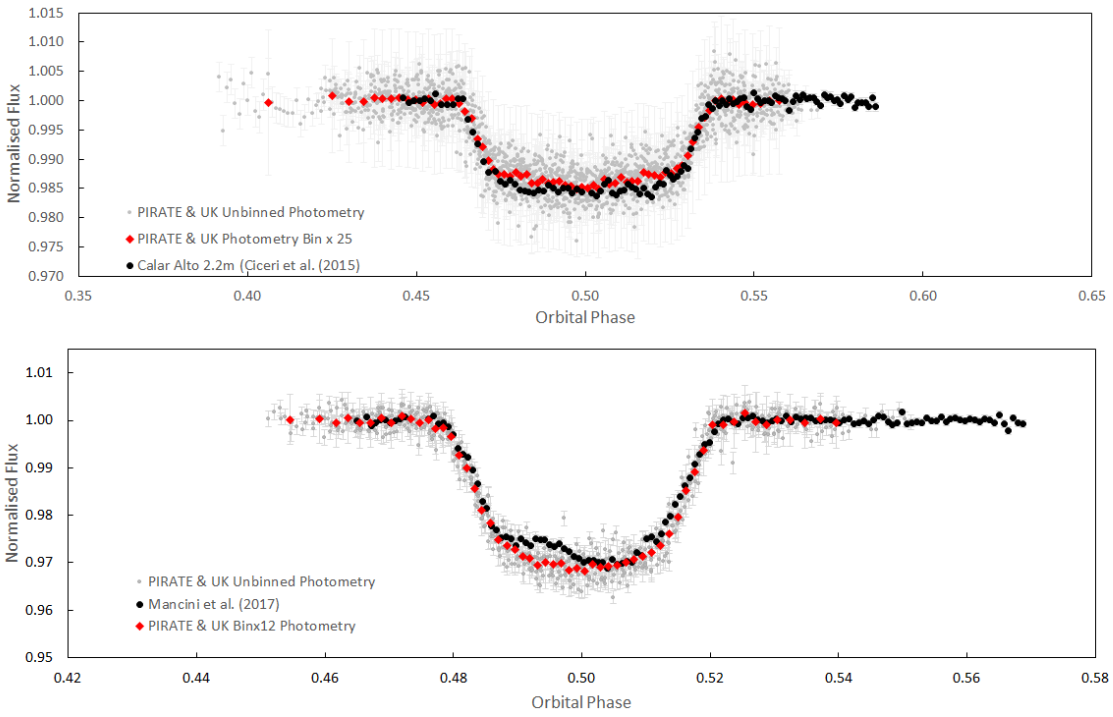

Figure 5.14: A comparison of the individual and binned photometric data for HAT-P-23 b (top) and WASP-52 b (bottom) with previously published results for medium class telescopes. Clearly visible in the WASP-52 b data from Mancini et al. (2017) is one of the spot crossing events observed.

5.2.5 On Chip CCD Binning

Lightcurves of WASP-12b and HAT-P-23b were obtained with PIRATE and POST using two different binning modes for the CCD cameras, 1×1 or unbinned where the images are obtained at the native resolution of the camera and 2×2 binning. Two archive POST observations were obtained at 3×3 binning. Binning of CCD pixels is a common practice for small aperture telescopes to increase sensitivity, reduce exposure and read-out times and decrease image file size. CCD binning allows the plate scale for individual telescopes to be matched to the Niquist sampling criterion (which states the stellar FWHM should be covered by 2 pixels), allowing matching of the plate scale to individual telescope characteristics and conditions. POST has a native plate scale of 0.52 arcsec and a typical seeing of 3 arcsec meaning, that when unbinned, 6 pixels would cover each star, considered over sampled against the Niquist criterion. Binning the CCD 2×2 doubles the plate scale to 1.04 arcsec and reduces the PSF sampling to 3 pixels, much closer to the Niquist value. PIRATE, COAST-STL and COAST have native plate scales of 0.64, 1.26 and 0.63 arcseconds respectively and better seeing of 2 arcsec. A key benefit of this method is that the resulting increase in sensitivity and reduction in readout times allow for much higher cadence imaging than is possible with the CCD unbinned. From even a brief comparison of the lighcurves for HAT-P-23b and

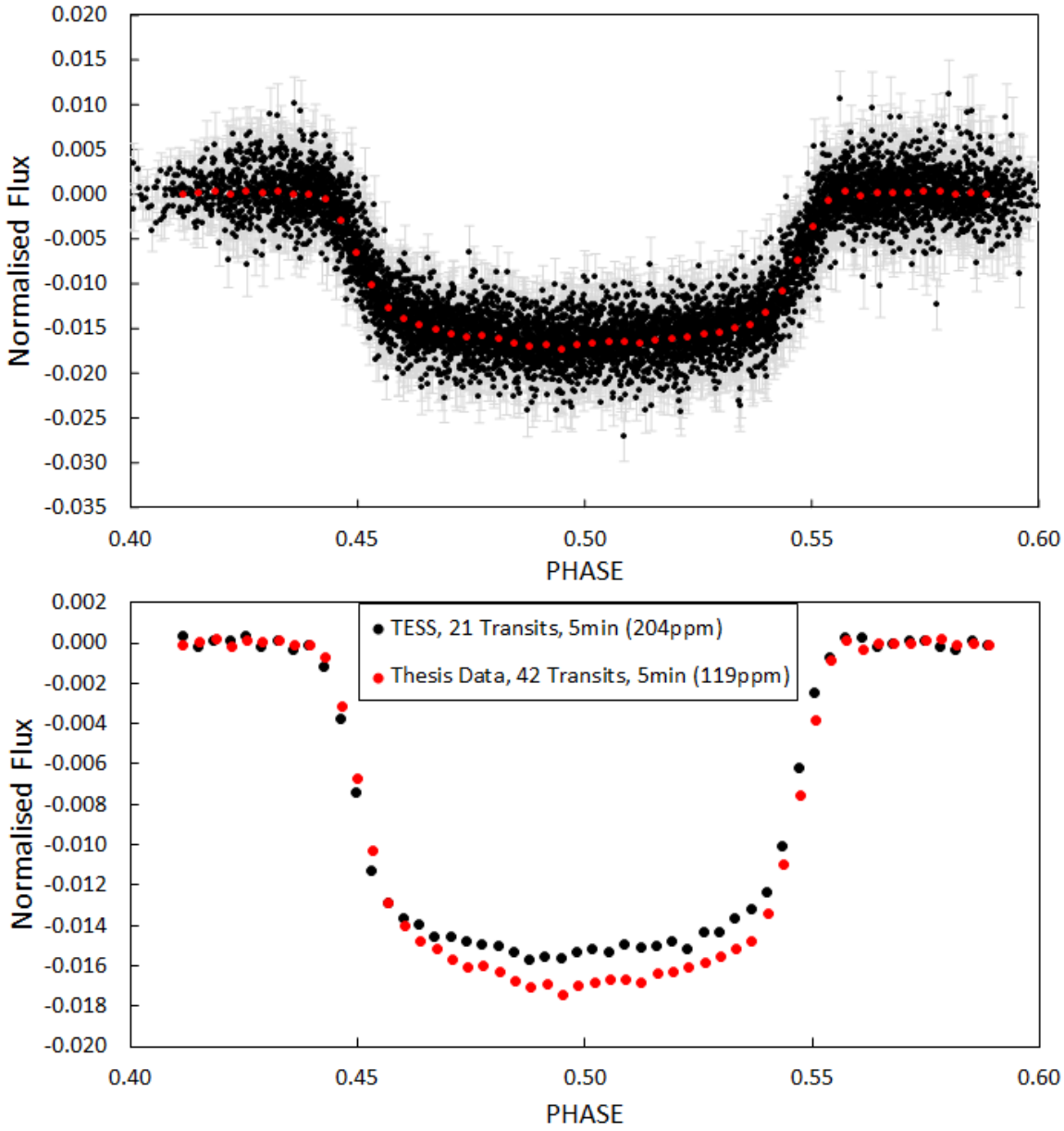

Figure 5.15: Top, 42 WASP-12b transits obtained with small aperture ground-based telescopes through Red filter in 1×1 and 2×2 CCD binning mode (black dots). Red dots are 5 minute bins achieving 119ppm out of transit RMS. Bottom, 5 min bin data from upper figure compared with 21 phase folded lightcurves from TESS binned to the same 5 min cadence. The out of transit RMS over the same phase range is 204ppm.

WASP-12b it is clear that the lightcurves obtained using on chip binning contain many more measurements but show considerably greater scatter in the photometry than those obtained unbinned. The question I address in this sub-section is whether the higher cadence/higher noise binned observations or lower cadence/lower noise un-binned observations provide more accurate and precise transit measurements for small aperture ground-based telescope follow up of transiting exoplanets. The natural assumption, my null hypothesis, is that higher cadence imaging should produce greater transit timing precision as the lightcurve is sampled more frequently.

Figure 5.16 plots the mean photometric signal versus the mean photometric noise in ADU per second of exposure (excluding download time). A clear differentiation is seen in the SNR between PIRATE 1×1 and 2×2 lightcurves for all three systems. The same trend of higher noise with higher signal is seen in both but with a lower noise value for the unbinned observations. There is a single unbinned outlying point where a lightcurve of HAT-P-23b was erroneously obtained unbinned but with the exposure settings used for the binned observation. For POST only WASP-12b was observed with 1×1 and 2×2 CCD binning but the same separation is not seen. It is clear from the plot for PIRATE that the unbinned observations provide a greater reduction in noise than signal, leading to overall higher SNR than the 2×2 binned observations. The longer exposure durations used for the unbinned observations more than offset the greater sensitivity expected for the 2×2 binned lightcurves. The increased exposure durations used for the unbinned observations were typically 2 - 3 times the 2×2 binned exposure duration rather than four times, as may be expected from additional sensitivity implied by combining the electron count from four pixels in 2×2 binning.

In Section 5.5 I compare the transit timing results in detail. Here I consider further the effect of cadence and RMS scatter on the transit timing measurements by comparing observations taken at high cadence in 2×2 mode, binned to the same cadence as the 1×1 observations. A number of lightcurves obtained using PIRATE, both unbinned and binned 2×2, are available for WASP-12b and HAT-P-23b. Two average lightcurves were selected for each system obtained in 2×2 on-chip binning mode and the lightcurves binned in software to the same lower cadence as the lightcurves obtained at the CCD native resolution.

The transit model independent out-of-transit RMS for the lightcurves is compared in Table 5.2. For both systems binning the 2×2 observations to the same cadence as the 1×1 data reduced the oot RMS by 30%. The RMS of the time binned lightcurves was still greater than the un-binned data. The result shows that time binning higher cadence single lightcurve data obtained with 2×2 on-chip binning produces inferior lightcurve precision to lower cadence lightcurves obtained in un-binned mode.

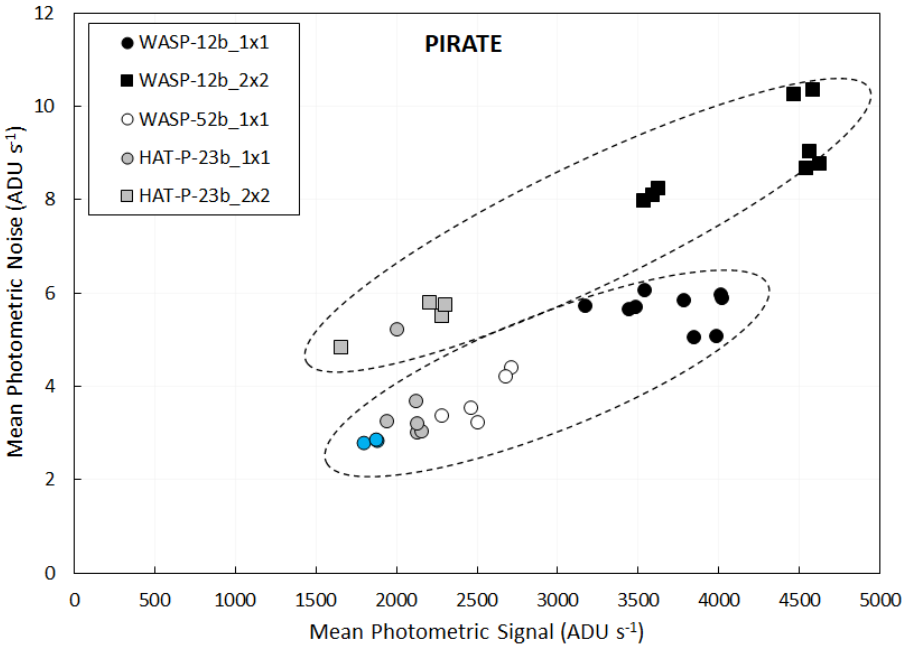

Figure 5.16: Sky subtracted signal and noise for unbinned and 2×2 binned observations of all three systems observed with PIRATE as calculated in AIJ. The values for signal and noise are in ADU's per second. The lower noise for a given signal value of unbinned over 2×2 binning is clear. Blue symbols are observations of WASP-12b made through B filter, all other observations are R filter.

The transit mid-times uncertainties and O-C values for the test lightcurves are also shown in Table 5.2. Binning the 2×2 lightcurves to the same cadence as the 1×1 lightcurves resulted in transit mid-time uncertainties that are significantly worse than the original lightcurves and worse than the control lightcurves obtained at 1×1. The scatter about the calculated ephemeris also increased or remained unchanged. This result clearly shows that lower cadence/lower noise transits obtained with the CCD read out in unbinned (1×1) mode provide more precise and accurate timing results than higher cadence/higher noise lightcurves.

5.3 Transit Parameter Determination

The majority of transit observations obtained with small aperture telescopes are used individually to determine a transit mid-time in order to calculate and improve the orbital ephemeris. In Chapters 3 and 4 I used the transit lightcurves to also derive parameters for each of the three systems observed and compared the results with those previously published, see Figures 3.4, 3.7 and 4.19.

The determination of R_* in Exofast V2 was achieved using MIST stellar models with a photometric SED and distance prior from Gaia DR2 along with dust extinction estimation.

Table 5.2: Test results for time binning PIRATE lightcurves obtained with 2×2 CCD binning to the same cadence as 1×1 observations. For each system the table includes two original 2×2 transits and the same transits time binned to the cadence of the 1×1 lightcurves. Two 'control' transits obtained with the CCD unbinned are also shown for comparison. The cadence values are the sum of the exposure and download times. All transits, including the controls were modelled together in Exofastv2. σT_C(s) is the calculated transit mid-time uncertainty and oot RMS scatter is in parts per million (ppm). O-C values are calculated against the new ephemerides calculated in Chapters 3 and 4.

System	Date	CCD Bin	Cadence (s)	oot RMS	Count	σT_C(s)	O-C (s)
WASP-12b	20180125	2×2	49	3078	349	50.98	-82.6
WASP-12b	20180125	2×2	97	1966	170	112.32	-82.6
WASP-12b	20161215	2×2	49	2921	342	57.89	-66.0
WASP-12b	20161215	2×2	97	2104	166	95.04	-124.8
WASP-12b	20181203	1×1	97	1655	133	34.56	-52.1
WASP-12b	20191231	1×1	97	1677	171	38.88	-4.3
HAT-P-23b	20180626	2×2	64	2870	199	40.61	94.5
HAT-P-23b	20180626	2×2	187	1988	69	86.4	128.2
HAT-P-23b	20180712	2×2	64	3570	196	62.21	-91.3
HAT-P-23b	20180712	2×2	187	2344	67	164.16	-123.3
HAT-P-23b	20180803	1×1	187	1621	63	50.98	-0.3
HAT-P-23b	20180809	1×1	187	1253	67	35.42	48.8

For WASP-12b the photometry used to create the SED was modified to account for the nearby companion star flux. In all three systems this approach resulted in R_* determinations with uncertainties smaller than any previously published. Not all authors publish values for R_* or even R_P, choosing instead to publish the scaled system parameters a/R_* and R_P/R_*. For HAT-P-23b and WASP-12b R_* agrees with previous published results within 1σ, for WASP-52b R_* was found to be 6% larger than the only two other independent published values, a 3.7σ difference. R_P, derived directly from the transit depth and R_* follows a similar pattern. The uncertainties on R_P for WASP-12b and WASP-52b are smaller than previously published while values for HAT-P-23b are similar to those previously published. For WASP-52b I found R_P 4% larger than the discovery paper and reversing a trend seen in more recent publications for smaller R_P (as seen in Figure 3.7).

The uncertainty determined for HAT-P-23b semi-major axis is larger than previous publications. For WASP-52b it is larger than the discovery paper, but smaller than subsequent publications. It is the smallest uncertainty for WASP-12b. The results for the scaled system parameters are slightly more mixed with the uncertainties being larger (HAT-P-23b) or comparable to previous results (WASP-12b/52b). The inclination found for WASP-52b and HAT-P-23b was slightly smaller than the published values while for WASP-12b it was slightly larger. The uncertainties on the inclination determination are toward the smaller end of the range of published values.

The results show that multiple lightcurves obtained using small aperture ground-based telescopes can be combined with published RV and photometric data within ExofastV2 to provide precise measurements of system parameters. This does require that the observations are obtained in standard photometric filters bands. Timing observations obtained unfiltered or through non standard filters (E.g. CBB) are not suitable for this purpose. This combination of multiple lightcurves obtained primarily for transit timing purposes with published RV and photometric data is a use of this data that is often overlooked. The approach benefits over single transit observations using larger aperture telescopes by providing both precise system parameter determination while also providing multi-epoch timing measurements.

Authors will often fix certain parameters to values determined previously by other authors. The obvious example is eccentricity but also values for R_*, M_* and Mp can be fixed by some authors. In this work no values were fixed which has the advantage of not relying of values obtained by other authors and thus biasing the new results. A downside is substantially increasing the ExofastV2 model calculation time required, WASP-12b for example with 47 lightcurves and five RV files, took 16 days to calculate.

5.4 Monitoring Photometry

As discussed in Chapters 3 and 4 for HAT-P-23 and WASP-12 I used the results of host star monitoring to look for any variability due to rotation. In this section I review the monitoring photometry obtained over multiple observing seasons, discuss the quality of the observations and analyse the suitability of PIRATE to undertake long term, multi season monitoring observations of exoplanet host stars. Understanding host star variability helps us understand the host star itself, identifying rotation periods and stellar cycles which in turn can be used to plan spectroscopic atmosphere observations when activity is at a minimum, E.g. inform ARIEL observation scheduling.

PIRATE was used to undertake all the monitoring observations of both systems, POST was not used for this purpose due to its semi-manual operation and small number of cloud free nights. For the HAT-P-23 field the nightly observations were made with groups of 6 frames which exhibited a typical spread of 0.007 mag for each a night. The mean photometric uncertainty was 0.002 mag. The stability of the long term photometry can be seen by studying the stable check star observed in the same field as the target star. The standard error of the nightly mean magnitude is 0.002 mag over 93 days, equal to the mean measurement uncertainty, see Figure 5.17, top panel. This is a significant improvement over the nightly spread in measurements, highlighting the importance of combining multiple observations per night. The uncertainty on the individual data points were combined in quadrature giving a nightly uncertainty of 0.005 magnitude. For HAT-P-23b the monitoring observations were supplemented with measurements obtained from the out of transit portion of the lightcurve on nights transits were observed. The magnitude measurements obtained from the out of transit data were found to have a -0.01 mag offset for the 2×2 on-chip binning compared to the un-binned monitoring observations which was corrected for prior to the analysis. The monitoring observations conducted with PIRATE were clearly able to detect the 0.011 mag variation of HAT-P-23 in measurements spanning 93 days.

As with the transit observations a different mean magnitude is observed depending on whether the optical tube is located on the East or West side of the German equatorial mount, this effect amounted to a difference of 0.002 mag for the check star which was corrected by bringing the observations made when pointing East or West together by half the difference so the resulting magnitude determined is the mean of the East and West measurements. The resulting instrumental magnitude of the check star determined was 12.351 ± 0.002 which compares with 12.349 ± 0.01 from UCAC4 but as the observations were made using Johnson-Cousins Rc filter and the comparison ensemble were measured using the SDSS r$'$ filter the measured and catalogue values cannot be directly compared.

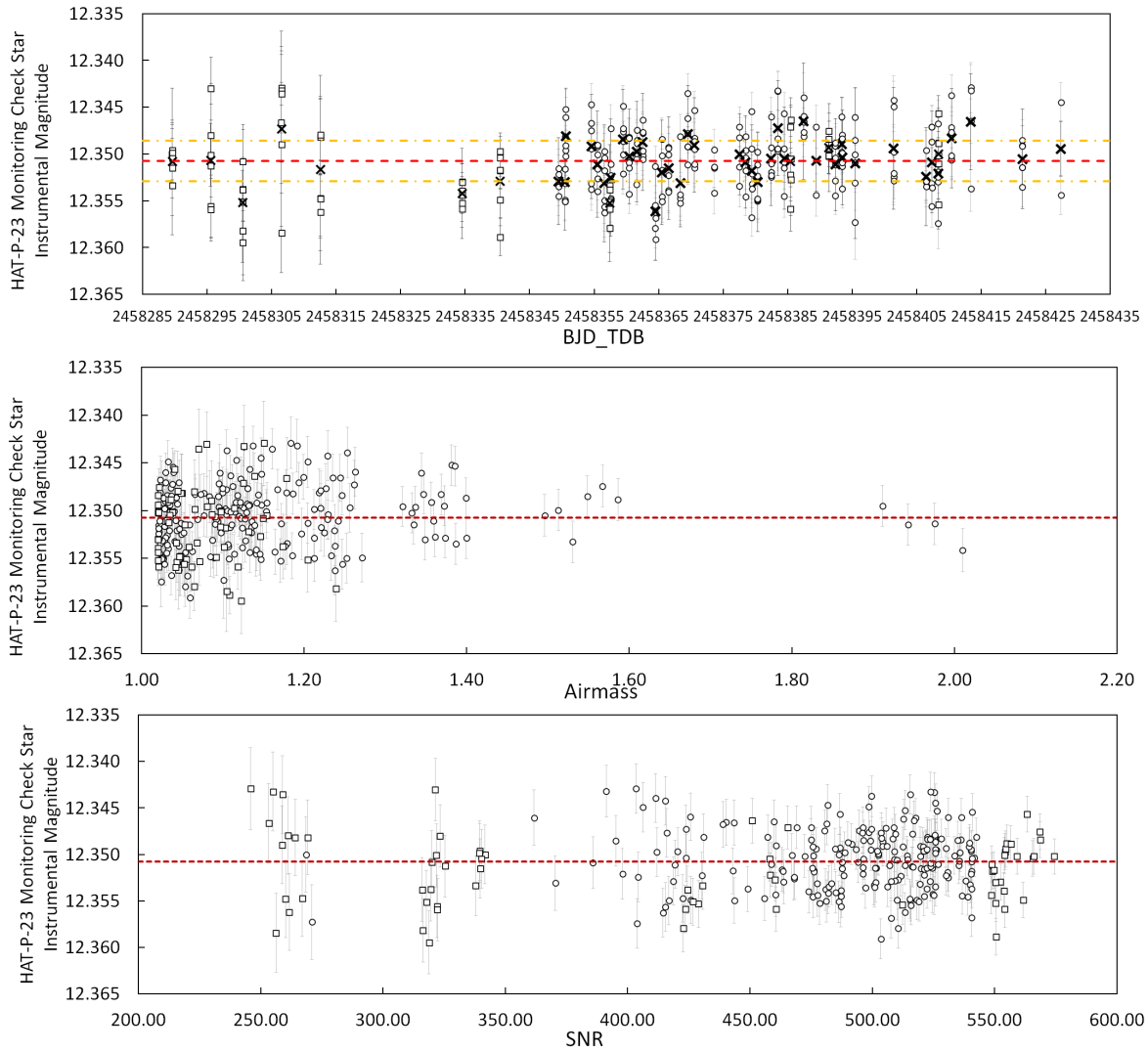

Figure 5.17: Top, individual nightly measurements of HAT-P-23 (open circles) and out of transit data (open squares) with nightly mean values shown as crosses. The mean magnitude value (red dashed line) and the 1σ uncertainties (amber dash-dot lines) are indicated. Middle, magnitude variation with airmass and bottom magnitude variation with SNR. The low and higher SNR values are dominated by the out of transit measurements made at 2×2 and 1×1 binning respectively.

The middle and bottom panels of Figure 5.17 show how the detrended check star photometry was affected by changing airmass and SNR of the observations. No trend of changing magnitude with increasing airmass is seen following detrending. The SNR plot at bottom clearly shows the out of transit measurements dominating the low and high end of the SNR range for 2×2 and 1×1 on-chip binning respectivly. Again no trend of changing magnitude is seen with SNR though the lower SNR $\lesssim 350$ show slightly increased scatter. The stability of the SNR for the monitoring observations was aided by the use of a variable star aperture in AstroImageJ which ensured all the stellar flux was contained within the photometry aperture regardless of any night to night FWHM variations.

No variability was detected in WASP-12 but previously undetected variability was found in J0630+2942. As with the HAT-P-23 data here I focus on the quality of the check star observations obtained this time over multiple seasons and with different filters, bin modes and exposure durations. For the WASP-12 monitoring observations the first two seasons data, 2016/17 and 2017/18 were obtained through Baader red and blue filters with the CCD camera operating 2×2 binning mode. Exposures for all red filter observations were 45 seconds and for the blue filter 90 seconds were used for 2016/17 season and 60 seconds for the 2017/18 season, though a small number of blue filter observations were obtained inadvertently with 45 second exposures for the second season. The data was detrended and offset corrected as described in Chapter 4. The 2016-17 season represents the densest data set with up to 169 measurements in a single night. For the 2018/19 season Johnson-Cousins Rc and B filters were used with the CCD in 1×1 binning mode. Exposures were either 120 second or 90 second for the Rc filter and 180 seconds for B filter.

The monitoring observation schedule made multiple observations per night in groups of 6 after the initial 2016-17 season. On many occasions multiple groups of observations were obtained each, sometimes with the optical tube on different sides of the mount. The aim of taking multiple observations each night being to increase photometric precision. Table 5.3 compares the spread in nightly measurements to the photometric error, the whole season standard deviation and the whole season standard deviation with the data binned to a single mean data point for each night. For the first two WASP-12 seasons the nightly spread in measurements reached almost 0.02 mag for the blue filter data, over 6 times larger than the standard deviation in the mean nightly values over the whole season. This result clearly highlights the need to make multiple monitoring observations of a given target each night. It is also clear that the WASP-12 2018-19 and HAT-P-23b 2018 seasons observations made using the CCD in 1×1 binned mode with subsequently longer exposures produced significantly more stable measurements. Fewer but longer exposures at 1×1 binning produce more stable results than a greater number of shorter exposures at 2×2 binning.

Table 5.3: Comparison of mean nightly and seasonal monitoring precision. Spread is the mean min-max spread in measurements obtained each night. The seasonal 1σ is the standard deviation in detrended measurements over the whole season and and the nightly 1σ value is the standard deviation calculated from the nightly mean magnitudes. Observations obtained with the CCD camera in 1×1 binning mode produced more consistent results. $\bar{\sigma}$ is the mean individual measurement uncertainty.

Season	Filter	Spread	Seasonal 1σ	Nightly 1σ	$\bar{\sigma}$c
WASP-12 Check Star					
2016-17	Red	0.018	0.006	0.004	0.003
2016-17	Blue	0.019	0.006	0.003	0.004
2017-18	Red	0.010	0.006	0.004	0.004
2017-18	Blue	0.019	0.008	0.005	0.006
2018-19	Rc	0.004	0.004	0.004	0.002
2018-19	B	0.004	0.004	0.004	0.002
HAT-P-23 Check Star					
2018	Rc	0.007	0.003	0.002	0.002

As with HAT-P-23 the airmass-magnitude plots show that there is no remaining trend in the magnitude measurements with increasing airmass after detrending, out to the limit of the observations around an airmass of 2. Similarly the SNR-magnitude plots also show no trend in magnitude values. It can be seen, especially in the 2016-17 season data, that observations made with an SNR < 300 show considerably greater scatter in magnitude measurement. For the Red filter observations the scatter in the magnitude measurement doubles from 0.005 to 0.01 for SNR < 300. Similarly for the blue filter the scatter increases from 0.005 to 0.007. In both cases the mean magnitude values agree within the uncertainties. For the 2018-19 season obtained in 1×1 mode a similar trend of increasing scatter in the magnitude measurements can be seen for SNR < 550. This is less apparent in the HAT-P-23 data which was all obtained with a SNR below this value. Within each nights observations the SNR value is negatively correlated with changes in airmass. Observations over multiple nights show a wide range of SNR values for a given airmass resulting from different FWHM values due in part to possible seeing changes but most likely due to different focus positions, SNR is strongly correlated with FWHM. This correlation is not seen between FWHM and determined magnitude measurement indicating the photometry aperture selection correctly accounts for changes in FWHM over a season.

Again as for HAT-P-23 the monitoring photometry was corrected for a constant offset between the magnitude measurements when the telescope was on the East or West side of

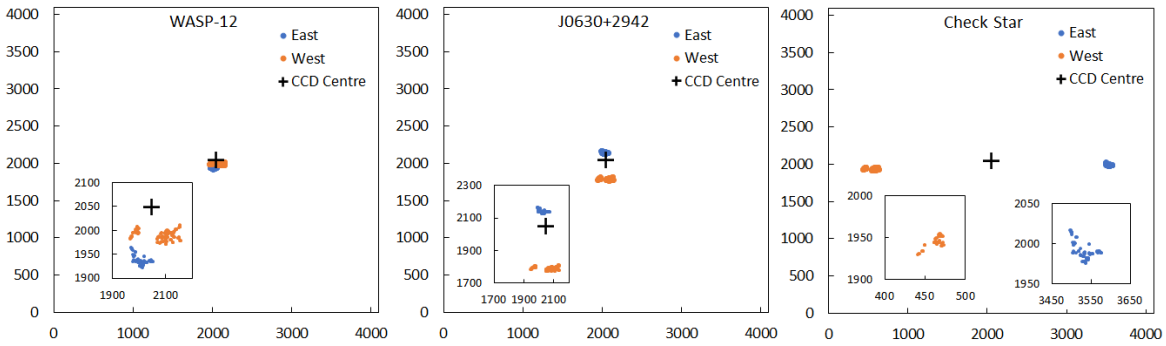

Figure 5.18: Example of the target star positioning in the PIRATE CCD frame from the 2018-19 season B filter observations showing the consistent centering of the WASP-12 target and the change in location of the check star caused by pier flips for Meridian crossing. Insets show detail of each stars position.

the mount. Individual offset corrections were calculated for each star, filter and season. For the WASP-12b 2016-17 and 2017-18 seasons the offset correction values for WASP-12, J0630+2942 and the check star in each filter are in good agreement with each other. The offset value is always greater in R than B and is greater for the check star than either WASP-12 or J0630+2942. The same results are seen for the 2018-19 season data obtained at 1×1 binning through standard filters with the exception that the offset values for Rc and B are in much closer agreement. Figure 5.18 shows an example of the target stars positioning on the CCD chip for the 2018-19 season B filter data. This shows that PIRATE exhibits excellent repeatability in placing the target star at the CCD centre, minimising position changes on the CCD before and after pier flips. J0630+2942 being located close to WASP-12 is affected slightly more by pier flip while the check star, being located closer to the edge of the frame, is affected the most. This indicates that the magnitude of the measurement offset is likely related to the amount of position change on the CCD. That the effect is greater in R filter bands than B would seem to rule out Luna illumination as the cause, the CCD camera has greater sensitivity in the red regions than in the blue. The pier flip offset effect is common in German Equatorial mounted telescopes and is also seen in transit data obtained with all three telescopes indicating any cause is not local to the PIRATE telescope. Further investigation is required to positively identify the cause.

For long term monitoring the photometric consistency between seasons is of key importance. The 2016-17 and 2017-18 season observations o WASP-12 were obtained with the same parameters allowing direct comparison, see Table 4.9. The Red filter magnitude from each season agree to 1.5σ with the same seasonal measurement uncertainty of 0.004 mag. The blue filter data similarly agree though, the uncertainty on the 2017-18 season blue data is greater where it is affected more by Luna illumination later in the season (Figure 5.20). The

2018-19 season data was obtained using different filters so is not directly comparable, though the seasonal uncertainty values are similar. The 2018-19 season data obtained through a Johnson B filter is the only data directly comparable with the UCAC4 catalogue values. The UCAC4 value for the check star used is 12.345 ± 0.05 and the seasonal mean measured with PIRATE is 12.331 ± 0.004, providing a 10 fold increase in measured magnitude precision.

The results show that

- Snapshot monitoring observations should ideally be constrained to airmass below 2.

- Multiple snap-shot observations per night are required to provide precise results, single magnitude measurements would provide significantly inferior results.

- SNR values $\gtrsim 350$ for 2×2 on-chip binned observations and $\gtrsim 550$ for un-binned observations are required to minimise the uncertainty in the magnitude measurements.

- The magnitude measurements obtained in given filters have proved to be stable over multiple seasons.

- Correction of the magnitude offset seen between observations made when the telescope is pointing to the East or West is required.

- The wide field of view of small aperture telescopes is well suited to this task, ensuring many catalogue reference stars are available and allowing monitoring of stars used in transit lightcurve comparison ensembles to also be monitored for variability.

- The scheduling methods adopted for PIRATE (also available for COAST) with the ability to schedule "filler" observations within set parameters that can be made in between observing higher priority targets makes efficient use of available telescope time for monitoring observations.

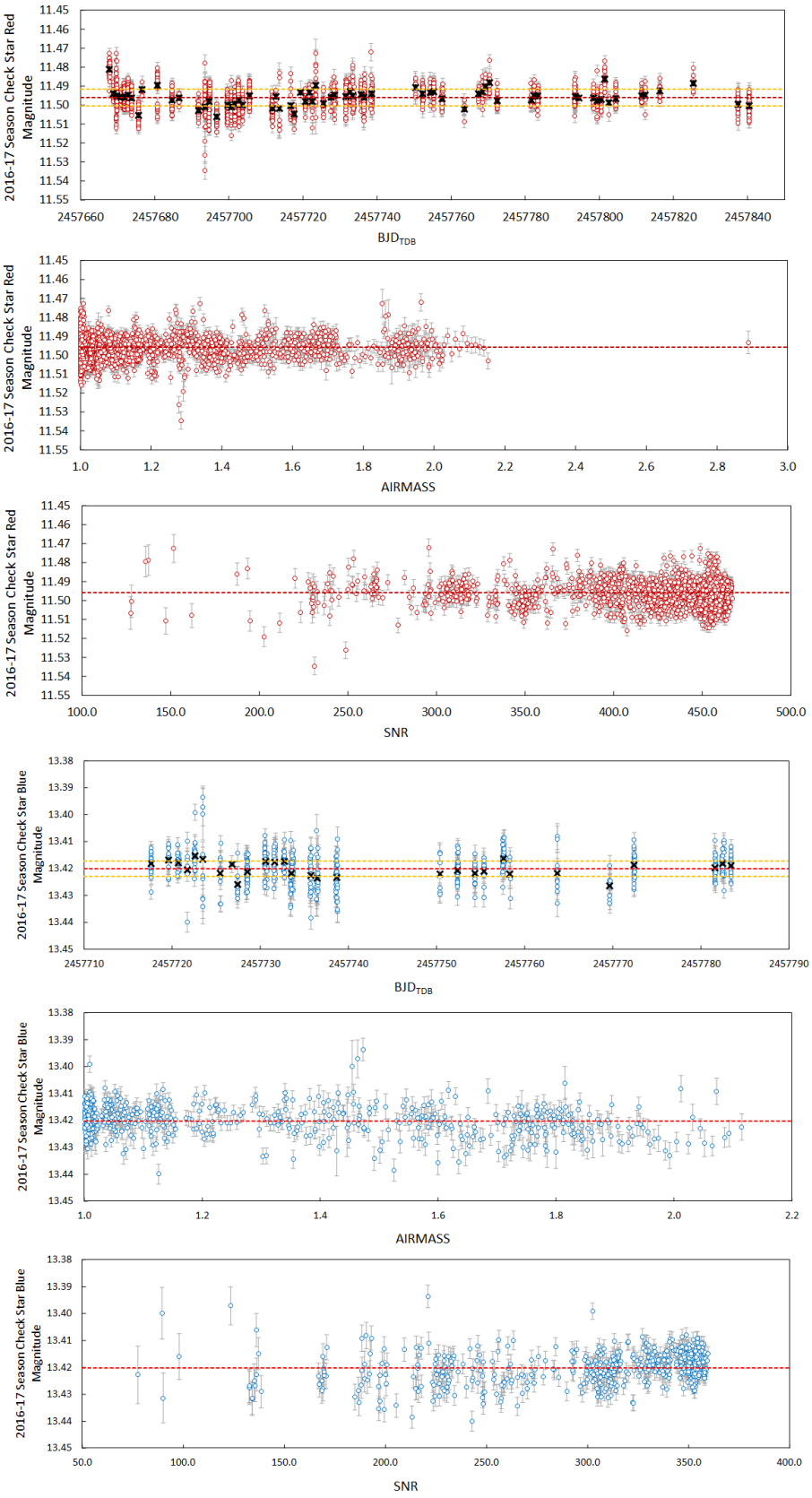

Figure 5.19: Detrended photometry for the 2016-17 season, Red filter is top, Blue filter is bottom. The red lines indicate the determined stellar magnitude and the amber lines are the 1σ deviation from the seasonal mean.

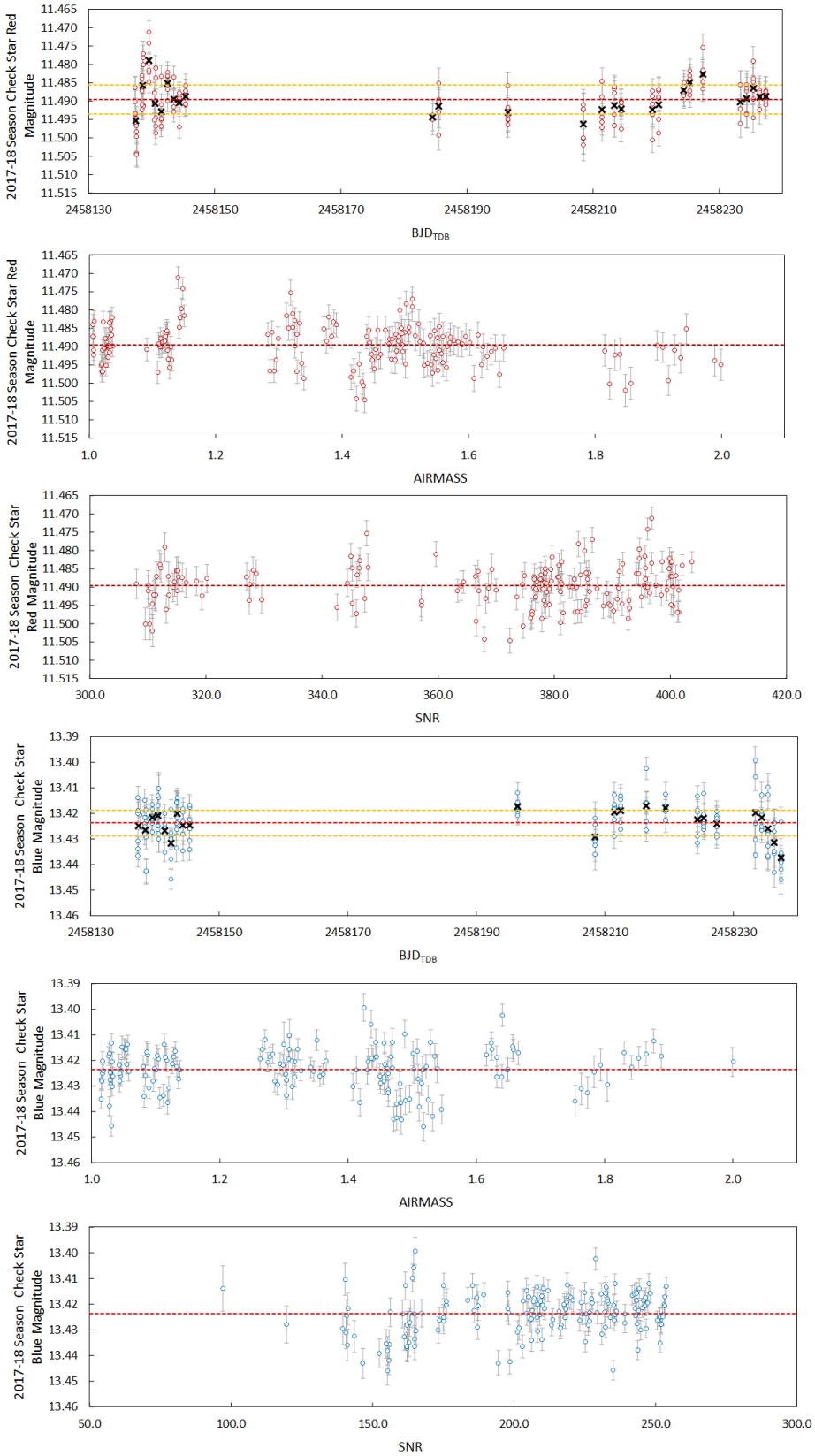

Figure 5.20: As Figure 5.19 but for the the 2017-18 season.

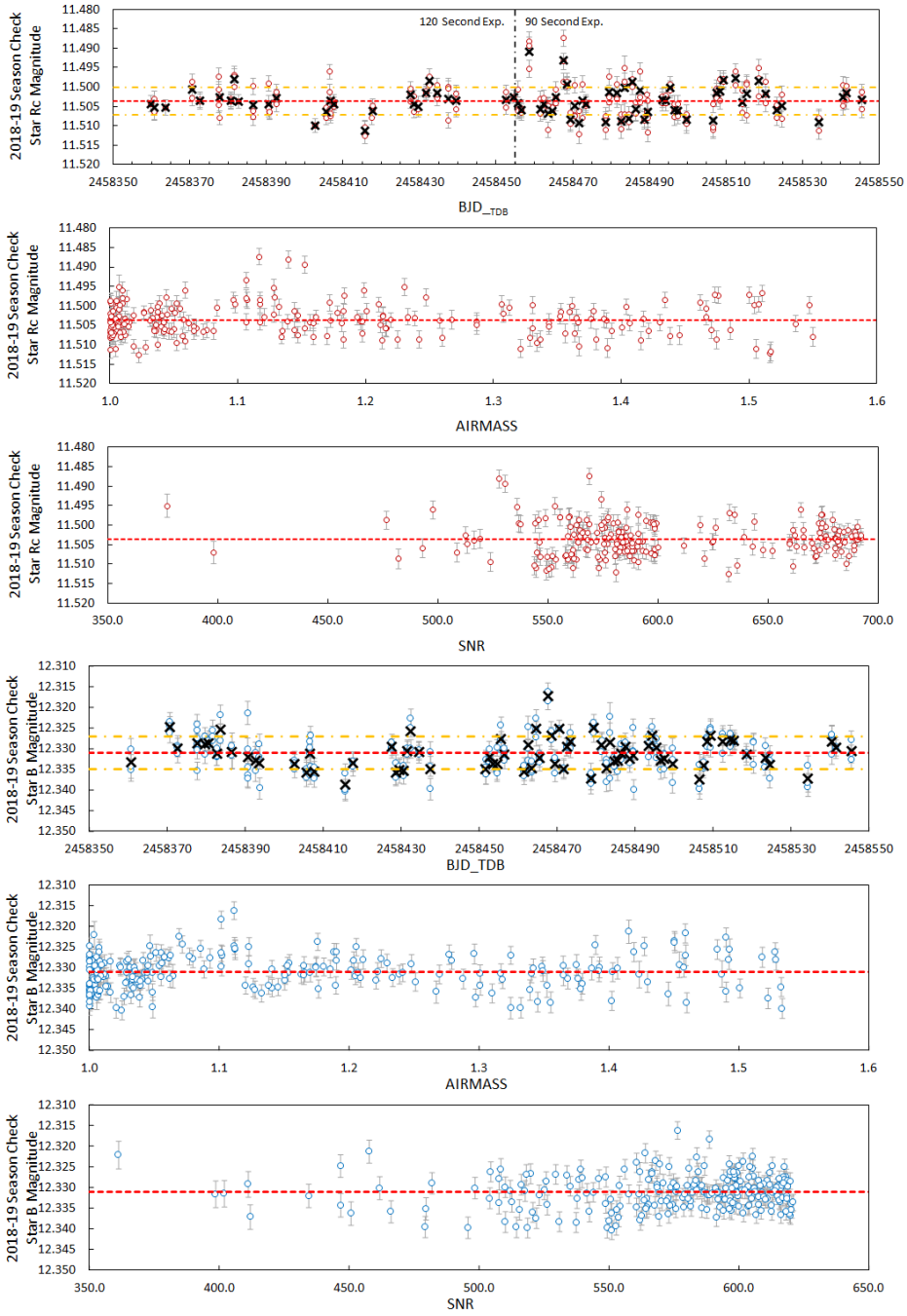

Figure 5.21: As Figure 5.19 but for the the 2018-19 season.

5.5 Transit Mid-Time Precision

5.5.1 WASP-12b

Table 5.4 summarises the mean transit timing measurements obtained for 47 transits of WASP-12b using the quadratic ephemeris from equation 4.4 from before and after the installation of GPS timing control for COAST and PIRATE and the replacement of the COAST CCD. The observations made before the GPS upgrade with all telescopes were made at 2×2 binning and after all are 1×1 binning, POST was not part of the GPS upgrade but the observing mode was changed to 1×1 binning at the same time so serves as a comparison with PIRATE and COAST. The PIRATE values include three transits obtained through the B filter and POST includes a single Ic filter transit the remainder are broadband red or Rc. The O-C measurements and change in measurement spread are plotted in Figure 5.22.

Table 5.4: Mean transit time measurements for WASP-12b from the three telescopes, shown by pre and post GPS upgrade date. $\sigma_{(O-C)}$ is the standard deviation in the O-C calculations. All values have units of day.

	PIRATE	COAST	POST
Pre upgrade O-C Mean	0.000424	0.000757	0.000230
Pre upgrade $\sigma_{(O-C)}$	0.001327	0.002088	0.000890
Mean timing error (CCD bin 2×2)	0.000520	0.000633	0.000587
Post upgrade O-C Mean	0.000098	0.000090	0.000036
Post upgrade $\sigma_{(O-C)}$	0.000606	0.000928	0.000815
Mean timing error (CCD bin 1×1)	0.000558	0.000529	0.000597

Table 5.4 shows that, following the OSO telescopes upgrade and the switch to 1×1 binning, the mean O-C value is much closer to the calculated ephemeris. The fact that this is seen for all three telescopes indicates the improvement in timing precision is due to the switch to 1×1 binning. Following the upgrade the the mean O-C value for the OSO telescopes lightcurves is ~ 8 seconds, the improvement is most obvious for COAST with the new CCD camera where this was ~ 65 seconds before the upgrade.

The values for the transit mid-time standard deviation ($\sigma_{(O-C)}$) show that for PIRATE and COAST the spread in timing measurements has more than halved following the upgrade. At the same time POST shows a minimal 9% reduction, indicating the that improvement in the measurement scatter arises from the GPS upgrade rather than the change to 1×1 binning.

For all three telescopes the measurement uncertainty remained comparable before and after the upgrade, indicating the change to 1×1 binning with the associated decrease in

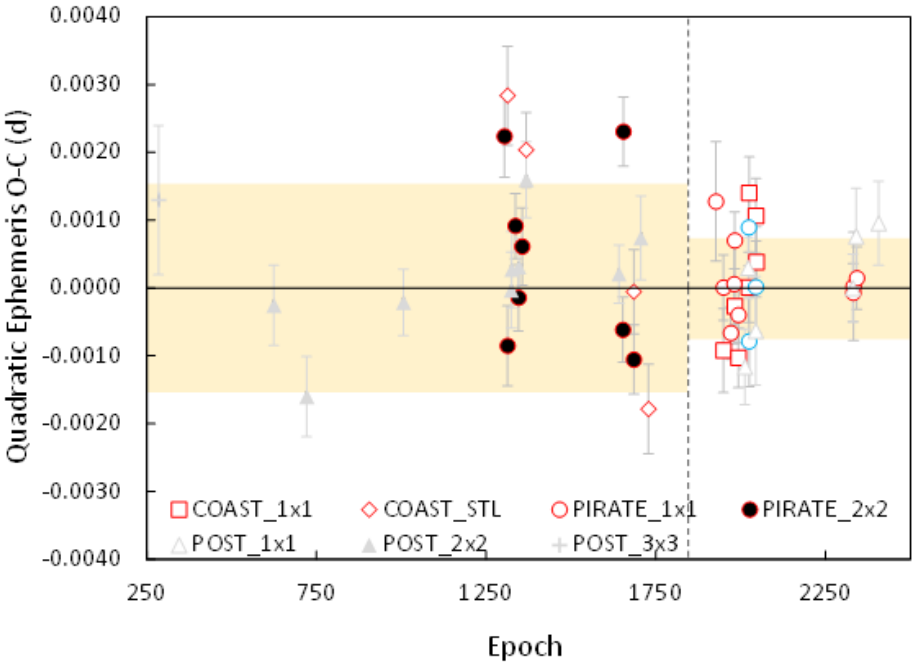

Figure 5.22: O-C plot for 47 WASP-12b transit times obtained for this project. The shaded area indicates the standard deviation in O-C measurements before and after the GPS installation and switch to 1×1 binned observing mode. POST transits are shown for context but are excluded from the standard deviation calculation.

cadence has not had a detrimental affect on the measurement uncertainty.

Table 5.5 shows the improvement in mean RMS values in the photometry for the transit lightcurves for out of transit RMS and for full transit RMS, the latter of which includes any effects arising from the transit model fit. It can be seen that the change from 2×2 to 1×1 binning (or changing CCD for COAST) has significantly reduced the measurement scatter, more so for PIRATE and COAST. The table also shows that the reduction in scatter is greater for the full transit data, the implication being the 1×1 binned observations result in an improved transit model fit which in turn may explain the accuracy improvement seen in the transit mid-time measurements for 1×1 over 2×2 observation for all three telescopes.

There are 139 transit times obtained with a variety of ground-based telescopes published for WASP-12b, Yee et al. (2019) along with a further 21 from TESS, Turner et al. (2021) allowing a comparison to made with the new observation obtained. Looking at all 139 observations obtained since discovery, the mean transit mid time uncertainty is 0.000339 ± 0.000121d and the mean deviation from the ephemeris is -0.000006 ± 0.00034d, where the uncertainties quoted are the standard deviation in the measurements. Of particular interest within this data set are 23 transit mid-time measurements obtained by Collins et al. (2017a) using a 0.6m telescope and analysed with AstroImageJ and an earlier version of Exofast. Their measurements show a mean transit mid-time uncertainty of 0.000375 ± 0.000093d and a mean

Table 5.5: Mean values by telescope for WASP-12b residual RMS values before and after the change to 1×1 binning showing the greater improvement in the full transit RMS than seen in the out of transit RMS.

Scope	Bin Mode	oot mean RMS	FT mean RMS	oot RMS Reduction	FT RMS Reduction
COAST(STL)	1×1	0.00284	0.00293		
PIRATE	2×2	0.00282	0.00279		
POST	2×2	0.00207	0.00197		
COAST	1×1	0.00162	0.00152	43%	48%
PIRATE	1×1	0.0020	0.00186	29%	33%
POST	1×1	0.00183	0.00164	12%	17%

deviation from the ephemeris of 0.000160 ± 0.000369d. Finally the 21 TESS transits observed in two continuous blocks have a transit mid-time uncertainty of 0.000505 ± 0.000059d and a mean deviation from the ephemeris of 0.000233 ± 0.000459d.

The ground-based observations in the published literature show mean T_C transit mid-time uncertainties on average 40% smaller than those for the 47 new WASP-12b observations and in general a smaller spread in values. The TESS T_C uncertainties are comparable those of the new observations. Compared to the new observations the standard deviation in the O-C values is 5 times smaller for the published ground-based observations while the TESS values standard deviation of 0.000459 is comparable to the best PIRATE data but half that from COAST.

While it is clear the implementation of a GPS time control and change of observing strategy to produce lower noise lightcurves has significantly improved the transit mid-time measurements they are still someway short of the precision achieved with generally larger telescopes from the published literature. It is therefore worth considering the lightcurve quality to see if any factors are driving this larger scatter seen in Tc measurement.

Transit signal noise ratio (Ioannidis et al., 2016) as discussed in Section 5.2.1, which is simply the transit depth divided by the summed pre and post transit RMS photometric scatter, is one method of measuring the quality of a group of lightcurves of a given target. The transit mid-time uncertainty shows a negative correlation with TSNR, lightcurves with small TNSR values show a higher Tc measurement uncertainty (Kendall Tau statistic = -0.24, p-value = 0.019). This same correlation is not seen when looking O-C value which although showing a negative trend is found not to be statistically significant (Kendall tau = -0.13, p-value = 0.18). No statistically significant correlation is found between O-C and Tc, the red noise metric, changing airmass, mean FWHM or SNR. When looking at the absolute O-C

value , i.e. just the magnitude of the deviation from the ephemeris without its sign, more of the lightcurve quality measures show a statistically significant correlation. For example TSNR, red noise metric, total out of transit coverage and the change in airmass over the duration of the observation are all correlated with the magnitude of the O-C. This indicates that these quality factors do affect the precision of the transit mid-time measurements by increasing the spread in measurement value but they do so in a way that affects the amplitude of the spread without preference for whether the derived O-C value is positive or negative. This provides confidence that although the timing measurements exhibit a greater spread than seen in the literature, their mean value is a true representation of the transit ephemeris.

With a fixed transit depth (for a given filter) the TSNR depends only on the out of transit RMS scatter in the measurements taken as a mean from the pre and post transit coverage. The TSNR metric does not take into account how this RMS may change during an observation, for example from changing airmass which may result in significantly different RMS values either side of the transit. Excluding transits with two or fewer data points on either side of transit, the individual WASP-12b transits exhibit the same RMS value (to 5dp). No correlation is seen between the ratio of pre to post RMS and the O-C value or with the transit mid-time uncertainty.

Having out of transit coverage is important for the transit model fitting solution. It is conceivable that the duration of out of transit coverage or differences between pre and post transit coverage could affect the T_C measurement. The T_C uncertainty shows no statistically significant correlation with the pre-transit, post transit or total out-of-transit duration. The O-C measurements do show a statistically significant negative correlation with the post transit coverage duration (Kendall tau = -0.24, p-value = 0.016) that is not seen with the pre-transit or total out of transit duration. As a result the pre-transit to post transit coverage ratio show shows a moderate correlation with O-C, (Kendall tau = 0.18, p-value = 0.071).

Of the 19 transits observed with the OSO telescopes in the 2018-20 seasons after the GPS upgrade and all using 1×1 binning, 12 have pre-transit coverage shorter than the ingress/egress duration, Table 5.6. These 12 transits have a mean absolute O-C value that is double the value for the 7 transits where pre-transit coverage exceeds the ingress/egress duration and the spread in O-C is 77% greater. This result confirms that transit times are more consistent where pre-transit coverage duration equals or exceeds the ingress duration.

Finally the data was analysed to see if the occurrence of a pier flip for a meridian crossing during the transit observation affected the O-C mean or scatter. 21 of the 47 transits contained a pier flip and they show a mean closer to the ephemeris than those transits without a flip with a smaller scatter in the O-C measurements, Table 5.7. Therefore the pier flip detrending carried out in ExofastV2 does not adversely affect the derived transit times.

Table 5.6: Mean O-C values for WASP-12b transit measurements obtained with the OSO telescopes after the GPS upgrade. The top row includes all post GPS upgrade and COAST CCD replacement measurements. The other rows below show the results for the two cases where pre-transit coverage is less than and greater than the transit ingress/egress duration. The spread in O-C determination is significantly reduced where pre-transit coverage exceeds ingress/egress duration.

O-C Data Set	Qty.	Mean	ABS Mean	StdDev
After GPS - all transits	19	0.00010	0.00053	0.00072
After GPS - pre coverage $<$ ingress	12	0.00000	0.00068	0.00083
After GPS - pre coverage $>$ ingress	7	0.00025	0.00027	0.00047

Table 5.7: Mean O-C values for lightcurves with and without a pier flip. Transits with Meridian crossings have a smaller mean, standard deviation and total spread, indicating correctly detrended pier flips do not adversely affect transit mid-time measurements.

	Without Flip	With Flip
O-C Mean	0.000277	0.000169
O-C StdDev	0.001190	0.000757
O-C Min-Max Range	0.004621	0.003290

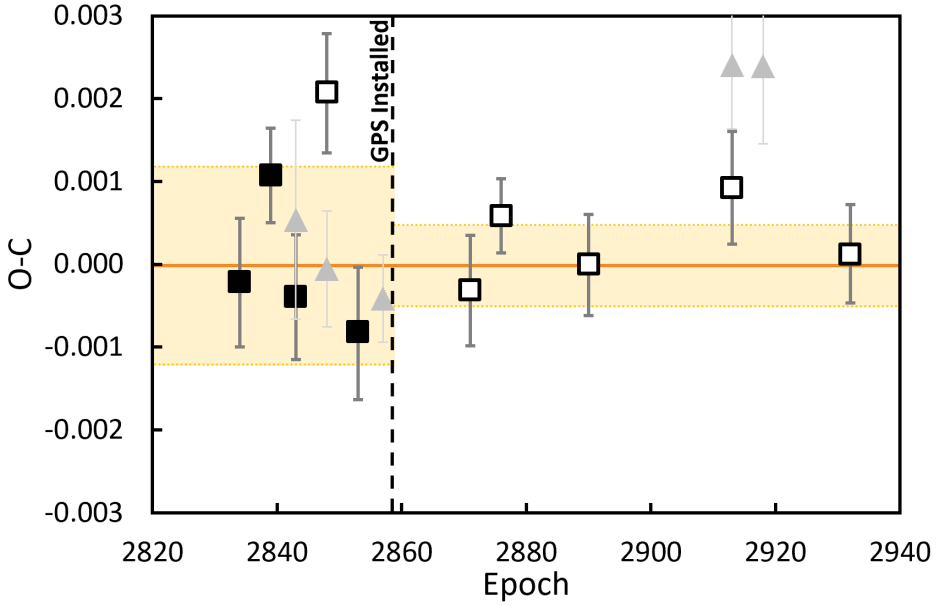

Figure 5.23: O-C values for PIRATE transit observations of HAT-P-23b before and after GPS upgrade (vertical line). The PIRATE observations are shown as black symbols with 2×2 CCD binning as filled symbols and 1×1 binning as open symbols. POST transits are shown in grey for context. The shaded area indicates the standard deviation in PIRATE O-C measurements. The scatter in measured O-C values reduces after the GPS installation and the switch to 1×1 CCD binning.

5.5.2 HAT-P-23b and WASP-52b

The other set of transit observations that spanned either side of the GPS upgrade for PIRATE and COAST were those for HAT-P-23b which was observed intensively with both PIRATE and POST between 20$^{\text{th}}$ June and 16$^{\text{th}}$ October2018. Before the GPS upgrade all but one PIRATE observation were obtained in 2×2 binning mode and in 1×1 binning mode after the upgrade. All POST observations were made at 2×2 CCD binning. From Figure 5.23 the reduction in scatter of O-C values around the calculated ephemeris after the upgrade is clear, reducing by 2.4 times from 1.017×10^{-3}d to 4.38×10^{-4}d. The pre upgrade standard deviation includes the transit obtained inadvertently at 1×1 binning but with the same exposure duration as the 2×2 observations, resulting in a reduced SNR. Over the duration of the observations the standard deviation in POST O-C measurements was 1.26×10^{-3}.

The observations of WASP-52b were all obtained after the GPS upgrade. The mean O-C values determined for the six PIRATE Rc filter observations is -0.000074d and the spread is 0.000194d. This a much smaller spread in measurement times than seen for either WASP-12b or HAT-P-23b. The spread in O-C measurements from POST is greater than from PIRATE but still half that seen for HAT-P-23b and 25% smaller than seen for WASP-12b.

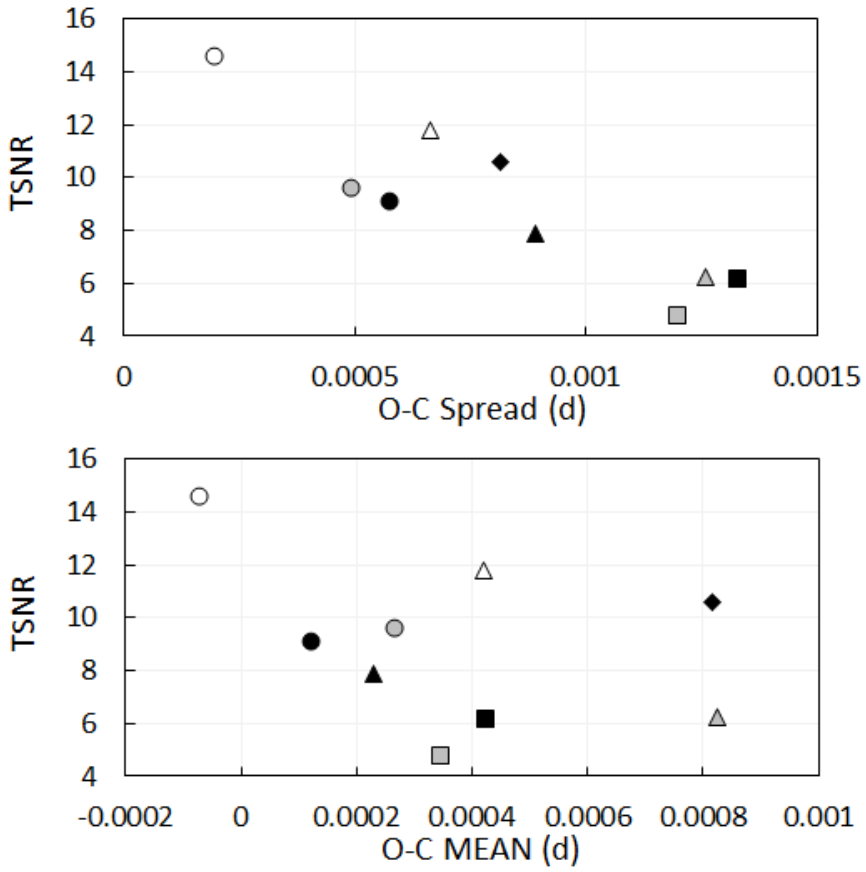

Figure 5.24: Plots of TSNR against O-C spread and O-C mean values. Black fill symbols are WASP-12b, grey are HAT-P-23b and open symbols are WASP-52b. Square symbols are OSO measurements obtained before the GPS upgrade and circles are after. The triangles are POST 2×2 CCD binning and the diamond is POST 1×1. The plots clearly show increasing TSNR values reduce the spread in measurements but have minimal effect on the mean O-C values.

Returning to the question of the impact of TSNR on the timing results for all three systems, figure 5.24 shows the strong correlation between TSNR and measured O-C spread and between TSNR and O-C scatter where no correlation is found for all three systems and observing modes. This implies that that high TSNR is required to provide precise results explaining the reduced scatter seen for WASP-52b with its 3% deep transits.

TSNR is significantly negatively correlated with O-C spread (Kendall Tau = -0.66, p-value=0.012) while no significant correlation is seen with O-C mean value (Kendall Tau = -0.22, p-value=0.4). The O-C scatter increases three fold for halving the TSNR (where TSNR =12, O-C spread is approximately 400ppm, where TSNR =6 the O-C spread is approximately 1200ppm).

5.5.3 Transit Mid-Time Uncertainty

The measured transit mid-time uncertainty (σTc) for all telescopes and observing modes varies between 0.0004d to 0.0008d (35 to 70 seconds) with a mean of 0.00056d (48 seconds). The Transit Error Estimator (TEE) (Deeg and Tingley, 2017), provides a method to calculate an expected timing precision, providing an opportunity to compare the theoretical expectation with the σTc measured using the small aperture ground-based telescopes. The parameters required to calculated the expected measurement uncertainty using TEE are the out of transit RMS, the number of data points covering ingress/egress, the duration over which the RMS noise is measured, the ingress/egress duration and the transit depth. The uncertainty can then be calculated using the general form of TEE (Eq.5, Deeg and Tingley (2017)).

$$\sigma_{\mathrm{t}} = \frac{\sigma F_{\tau}}{2\Delta F}\sqrt{\tau T_{\nabla}} \tag{5.3}$$

where σ_{t} is the calculated transit mid-time uncertainty, σF_{τ} is the RMS noise measured over duration τ. ΔF is the transit depth and T_{∇} is the ingress and egress duration summed.

To calculate the theoretical timing uncertainties using TEE the transit ingress/egress duration and depth in a given filter band were taken from the results for each system. The RMS white noise was calculated from the out of transit coverage and the number of data points covering ingress/egress was calculated from the ingress duration divided by the observing cadence. The TEE timing uncertainty was calculated for all new transits of WASP-12b, WASP-52b and HAT-P-23b used to determine the ephemerides in Chapters 3 and 4.

Figure 5.25 plots the measured values of σTc against those calculated using TEE. The left hand plot shows the uncertainties by telescope and observing mode while on the right the same data is shown by exoplanet system. It can be seen that for σTc values below 0.005, TEE underestimates the measured uncertainties observed. For greater values of σTc the values are widely spread around the diagonal indicating agreement between measured and calculated values. It can also be seen that as the uncertainty increases so does the scatter between measured σTc and TEE. The plot on the right in Figure 5.25 shows that overall the σTc magnitude is governed by the transit depth with increasing values for σTc and TEE as we moves from WASP-52b with a 2.6% transit depth, through WASP-12b (1.4%) to HAT-P-23b at 1.3%.

Although the measured and TEE calculated uncertainties have a large scatter looking at the mean values by telescope and observing mode reveals a more stable picture. The mean σTc varies between being 7% less to 20% greater than the value from TEE, Table 5.8. The largest mean difference occurring for the POST 3x3 observations, it is noted that there are

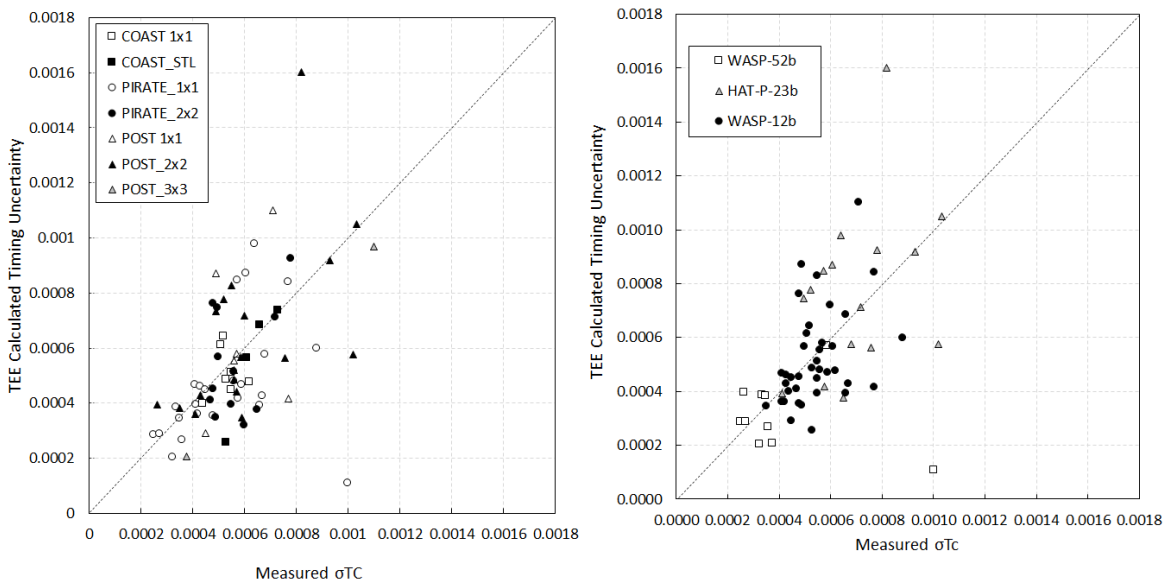

Figure 5.25: Plots of measured σTc against the mid-time uncertainty calculated using TEE Eq. 5.3. On the left the data is shown by telescope and observing mode. On the right the data is shown by system observed. The diagonal line indicate perfect agreement between TEE and the measured values.

only two observations made in this mode. Excluding the POST 3x3 observation the range of mean value agreement is -7% to 11%. Both COAST and PIRATE show a mean σTc larger than calculated using TEE while the values measured with POST are slightly smaller. Transit time uncertainty calculated using TEE shows a significantly greater spread of values than seen in the measured results for all observing modes, in the most extreme cases the standard deviation in the mean for TEE results is 2.5 times greater than the mean in the measured values.

Plotting the ratio of σTc measured to calculated using TEE against the total out of transit duration we can see that the values are best agreement for out of transit coverage values between approximately 0.05 to 0.07 days (72 to 100 minutes), Figure 5.26. Less total coverage than this leads to a larger σTc than estimated using TEE. Where out of transit coverage is longer TEE over estimates the uncertainty. The power law nature of the plot shows lightcurves with little out of transit coverage will be most affected.

The results indicate that the measured σTc values are more stable than the calculations using TEE would suggest, either the values calculated using Eq.5 have some factor that affects the timing uncertainty missing or the observations are in some way limited to a smaller range of possible σTc values. The value of the RMS noise is the most significant factor as the number of data points covering ingress/egress resulting from the observing cadence enters Eq. 5.3 only as the square root. TEE also makes the assumption that the RMS noise is

Table 5.8: Mean values for measured σTc and σTc calculated using TEE. The uncertainties are the standard deviation on the mean which shows a much greater spread for the the values calculated using TEE.

Mode	Measured Mean	TEE Mean
COAST 1×1	0.000531 ± 0.000054	0.000510 ± 0.000088
COAST-STL	0.000633 ± 0.000084	0.000560 ± 0.000215
PIRATE 1×1	0.000529 ± 0.000190	0.000469 ± 0.000219
PIRATE 2×2	0.000565 ± 0.000103	0.000544 ± 0.000198
POST 1×1	0.000592 ± 0.000125	0.000635 ± 0.000300
POST 2×2	0.000613 ± 0.000218	0.000650 ± 0.000313
POST 3x3	0.000738 ± 0.000513	0.000588 ± 0.000537

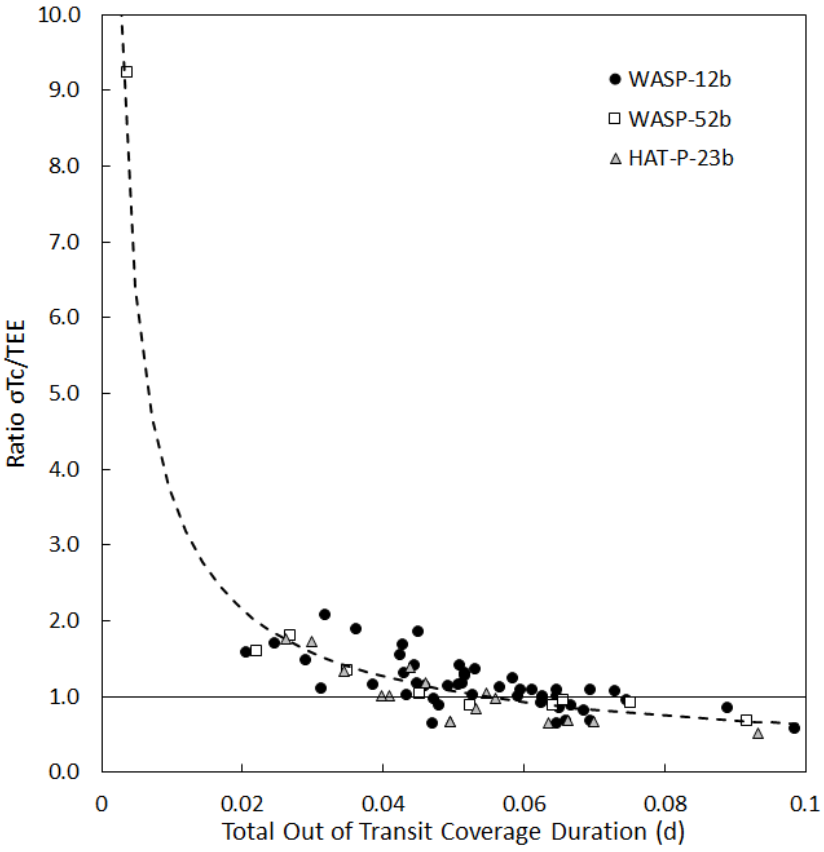

Figure 5.26: Plot of the ratio of σTc/TEE to the total duration over which the out of transit RMS noise was measured for each system observed

white noise with no red noise component. No correlation is seen with the calculated TEE uncertainty or its difference from the measured value with the red noise metric for the WASP-12b data, indicating this is a safe assumption for the WASP-12b data set. The oot RMS and ratio of σTc/TEE is significantly correlated for all three systems (tau=-0.23, p-value=0.004), the ratio of σTc/TEE decreases as RMS noise increases.

5.6 Simultaneous Transit Observations

Observations of the same transit with two or more telescopes allow us to compare the timing results and potentially understand any systematic effects that influence these results. There are a number of simultaneous transit time observations which occur in the combined transit timing data sets for WASP-12b and HAT-P-23b, Figures 5.27 and 5.28. These fall into three categories, simultaneous transit times in the already published results, simultaneous transit times for published and new observations and simultaneous transit times for observations made by two telescopes in the newly obtained data. The HAT-P-23b timing data contains only the second and third categories, no simultaneous observations are available between previously published results, Tables 5.9 and 5.10. The WASP-52b timing data set does not contain any true simultaneous observations.

In the set of transit times for WASP-12b published by Yee et al. (2019), which pulls together 139 previously published primary transit times from multiple sources, there are 5 pairs of observations made of the same transit by the same or different observers. This includes three pairs of measurements made of the same transits with the MuSCAT telescope in g' and r', obtained by Patra et al. (2020). In four of these five measurements the difference in reported transit mid time is greater than largest of the two quoted transit time uncertainties, and in two cases the uncertainties do not overlap, see Table 5.9. For the three simultaneous transits observed by Patra et al. (2020) the exposure time for the r' band is half that of the g', resulting in correspondingly smaller uncertainties on the transit mid-time reported for the r' measurements. It is noted that the authors transit observation on 12$^{\text{th}}$ February 2018 missed the t_1 ingress transition point and has no pre-transit data which would be expected to result in a poorer transit mid-time determination. Instead the full transit observations made on 27$^{\text{th}}$ January 2017 have the largest transit mid-time uncertainties and a 3σ mid time difference, explained by the authors as being due to transparency variations during egress and having to exclude several data points as outliers.

Two simultaneous transit observations between the new data obtained for this project and published observations made by (Maciejewski et al., 2016, 2018) occur at epochs 624 (POST) and 1345 (PIRATE). The difference in reported transit mid-times for the two pairs are 38

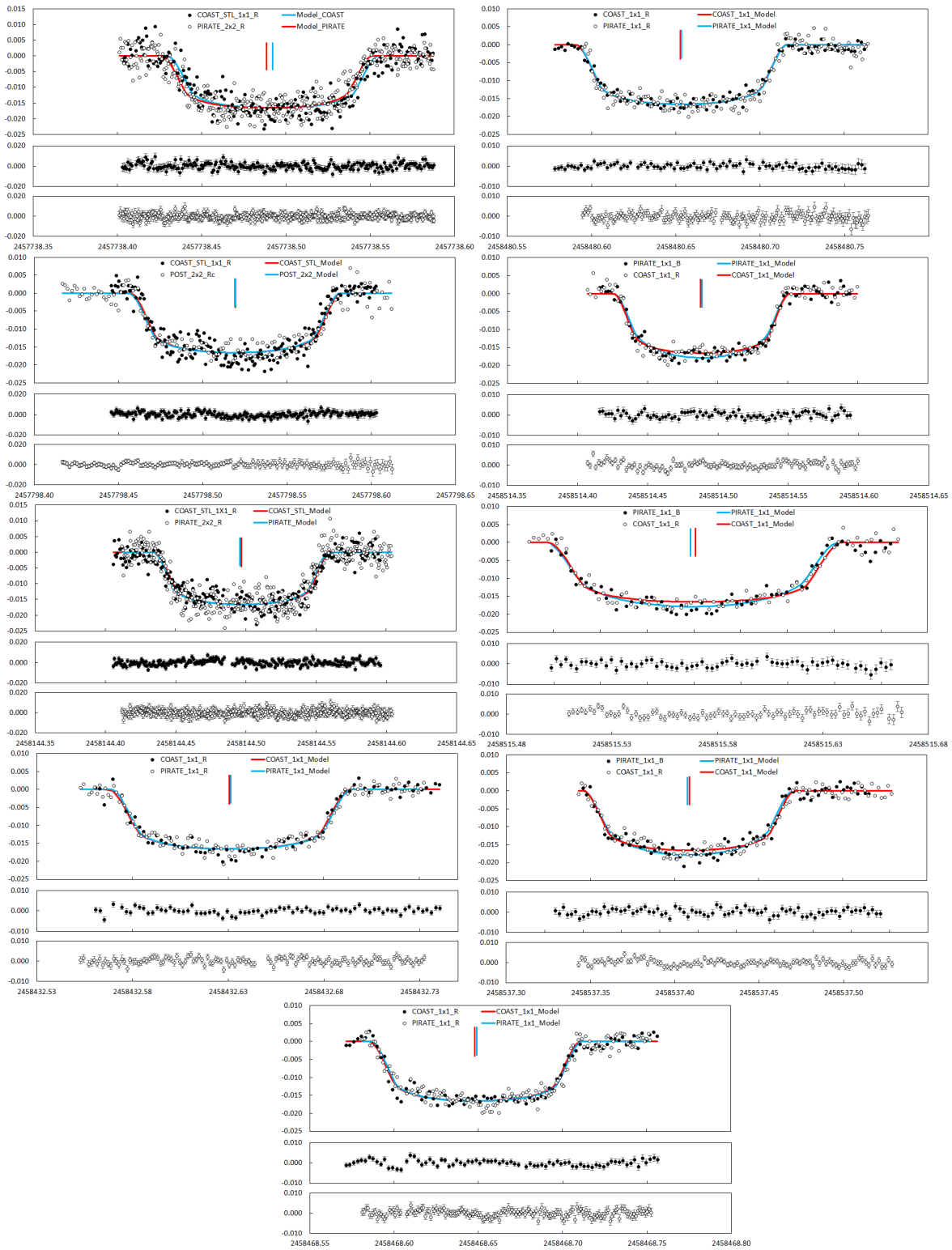

Figure 5.27: Pairs of simultaneous lightcurves obtained with the small aperture ground-based telescopes. The short vertical lines indicate the mid-time determined for each transit.

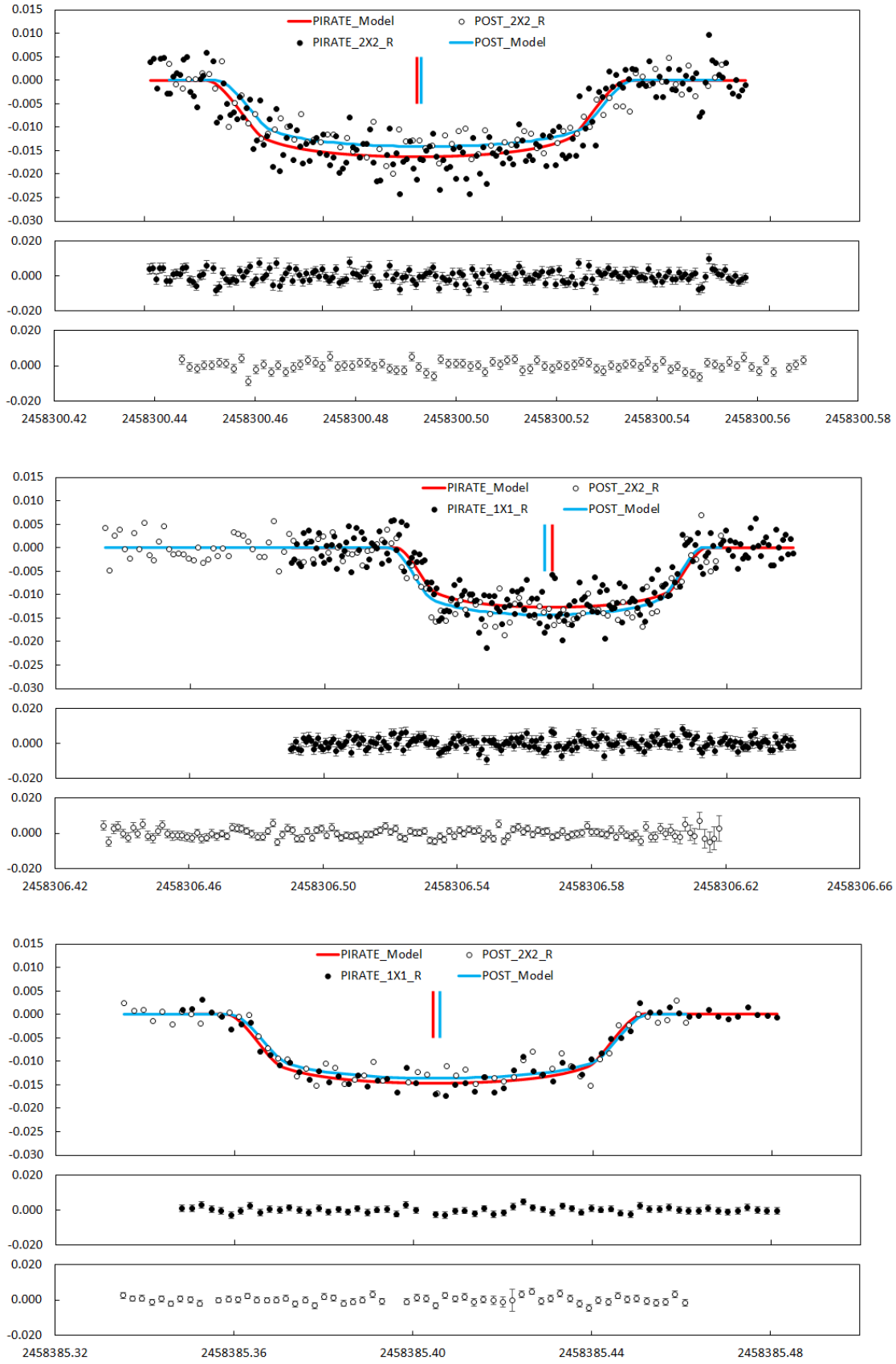

Figure 5.28: As Figure 5.27 but for HAT-P-23b simultaneous lightcurves.

seconds and 32 seconds respectively. This is smaller than the transit mid-time uncertainties from the POST and PIRATE observations and smaller than the exposure time used in any of the observations so these simultaneous observations can be considered in good agreement. The PIRATE observation was obtained prior to the GPS timing control upgrade install in Summer 2018. WASP-12b was observed by TESS for 21 transits in two continuous blocks in sector 20, Turner et al. (2021) and three simultaneous observation were obtained, two with PIRATE and one with POST over three adjacent epochs (2030, 2031 and 2032). Again all three pairs of observations were in excellent agreement with the largest difference being 0.00048d (41 seconds), Figure 5.29.

For HAT-P-23b there are two pairs of observations obtained simultaneously with those from Maciejewski et al. (2018), one with POST and one with PIRATE after the GPS upgrade. As with WASP-12b the two pairs of observations are in good agreement with the largest difference being 49 seconds, comparable to the uncertainty on the PIRATE and POST observations, Figure 5.30.

For WASP-12b there are a further nine simultaneous transits observations obtained as part of this project, one transit was observed with COAST and POST, five with COAST and PIRATE using the same filter and three with PIRATE and COAST through different filters. Of the eight observations obtained simultaneously with COAST and PIRATE, two were obtained prior to the GPS upgrade and six after. The difference in derived transit mid-times ranges from 0.8σ to 5.1σ with the only pair of observations agreeing within 1σ being between COAST and POST obtained in February 2017. This is also the pair of observations exhibiting the greatest mean departure from the ephemeris. The greatest mid-time difference occurs between the pair of PIRATE and COAST observations made before the GPS installation (epoch 1313) while the second greatest difference is seen between a pair of observations made after the upgrade (epoch 2025). The remaining six pairs of transit times agree to within 2σ. Six of the nine time differences are smaller than the exposure time used which varied between 45 to 180 seconds depending on telescope, filter and CCD binning used. It can clearly be seen from Figure 5.29 that the observations made after the GPS upgrade are more clustered around the ephemeris value than those obtained before the upgrade but that all the pairs of observations obtained show greater differences than those obtained simultaneously with published results. This is a pattern that is also seen in the HAT-P-23b simultaneous observations where two pairs of new observations were obtained prior to the GPS upgrade and one after with the timing differences of 80, 184 and 128 seconds, Figure 5.30.

Table 5.9: Simultaneous transit times obtained through the observation of the same transit by the same or different observers. Δ(d) is the difference in determined transit mid time from the two observations in days and σ is the transit mid time difference divided by the larger of the two transit time uncertainties.

BJD_{TDB}	Uncertainty (d)	Source	Δ(d)	σ
2455542.55210	0.00040	Cowan et al. (2012)		
2455542.55273	0.00028	Maciejewski et al. (2013a)	0.00063	1.58
2458155.41040	0.00050	Öztürk and Erdem (2019)		
2458155.41152	0.00031	Maciejewski et al. (2018)	0.00112	2.24
2457781.05418	0.00043	Patra et al. (2020)(g′)		
2457781.05566	0.00036	Patra et al. (2020)(r′)	0.00148	3.44
2458161.95991	0.00035	Patra et al. (2020)(g′)		
2458161.95964	0.00026	Patra et al. (2020)(r′)	0.00024	0.77
2458163.05089	0.00034	Patra et al. (2020)(g′)		
2458163.05125	0.00021	Patra et al. (2020)(r′)	0.00036	1.06
2456986.50195	0.00043	Maciejewski et al. (2016)		
2456986.50151	0.00059	POST, 2 × 2, (R)	-0.00044	0.75
2457773.41517	0.00022	Maciejewski et al. (2018)		
2457773.41480	0.00049	PIRATE, 2 × 2, (R)	-0.00037	0.76
2457738.49238	0.00073	COAST-STL1001, 1 × 1, (R)		
2457738.48869	0.00059	PIRATE, 2 × 2, (R)	0.00369	5.05
2457798.51961	0.00055	COAST-STL1001, 1 × 1, (R)		
2457798.51917	0.00056	POST, 2 × 2, (R)	0.00044	0.79
2458144.49720	0.00062	COAST-STL1001, 1 × 1, (R)		
2458144.49620	0.00051	PIRATE, 2 × 2, (R)	0.0010	1.61
2458432.63075	0.00062	COAST, 1 × 1, (R)		
2458432.63168	0.00048	PIRATE, 1 × 1, (R)	0.00093	1.5
2458468.64820	0.00055	COAST, 1 × 1, (R)		
2458468.64917	0.00042	PIRATE, 1 × 1, (R)	0.00097	1.76
2458480.65304	0.00044	COAST, 1 × 1, (R)		
2458480.65367	0.00041	PIRATE, 1 × 1, (R)	0.00063	1.43
2458514.48892	0.00056	PIRATE, 1 × 1, (B)		
2458514.48804	0.00052	COAST, 1 × 1, (R)	0.00088	1.57
2458515.57866	0.00067	PIRATE, 1 × 1, (B)		
2458515.58085	0.00053	COAST, 1 × 1, (R)	0.00219	3.27
2458537.40782	0.00068	PIRATE, 1 × 1, (B)		
2458537.40887	0.00055	COAST, 1 × 1,(R)	0.00105	1.54

Table 5.10: As for Table 5.9 but for the HAT-P-23b simultaneous observations.

BJD_{TDB}	Uncertainty (d)	Source	Δ(d)	σ
2458317.481360	0.00054	POST, 2×2, (R)		
2458317.481929	0.00046	Maciejewski et al. (2018)	0.00057	1.05
2458334.461870	0.00066	PIRATE, 1×1, (R)		
2458334.462413	0.00035	Maciejewski et al. (2018)	0.00054	0.82
2458300.500970	0.00075	PIRATE, 2×2, (R)		
2458300.501900	0.00120	POST, 2×2, (R)	0.00093	0.78
2458306.565740	0.00070	POST, 2×2, (R)		
2458306.567870	0.00071	PIRATE, 1×1, (R)	0.00213	3.0
2458385.404340	0.00068	PIRATE, 1×1, (R)		
2458385.405820	0.00075	POST, 2×2, (R)	0.00148	1.97

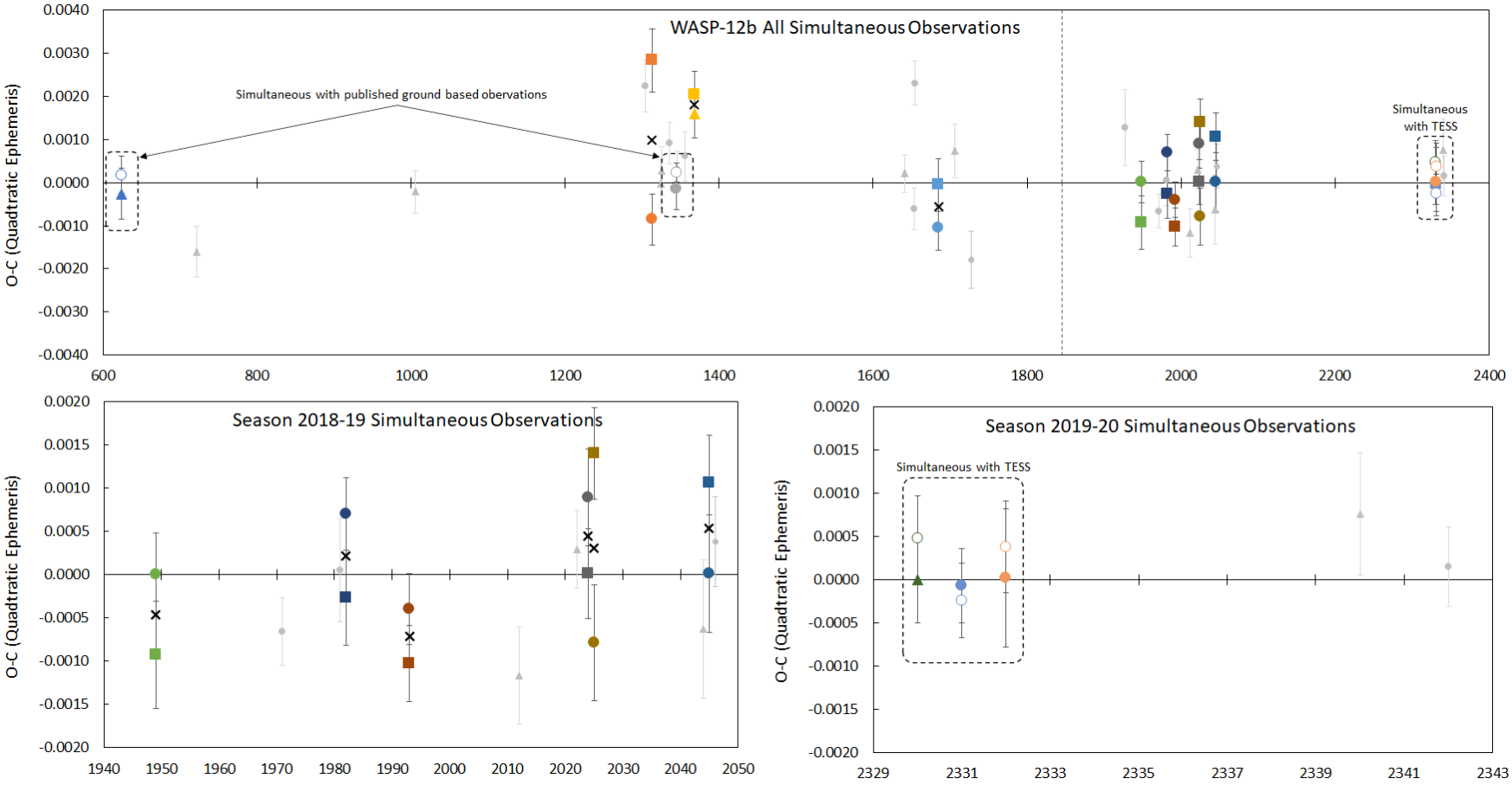

Figure 5.29: O-C plot for WASP-12b highlighting the simultaneous transit pairs. Fill squares are from COAST, filled circles from PIRATE and filled triangles from POST. Open symbols are taken from the literatures where they are simultaneous with a new observation. The lower two plots cover just the 2018-19 and 2019-20 seasons. Single observations are indicated with small grey symbols.

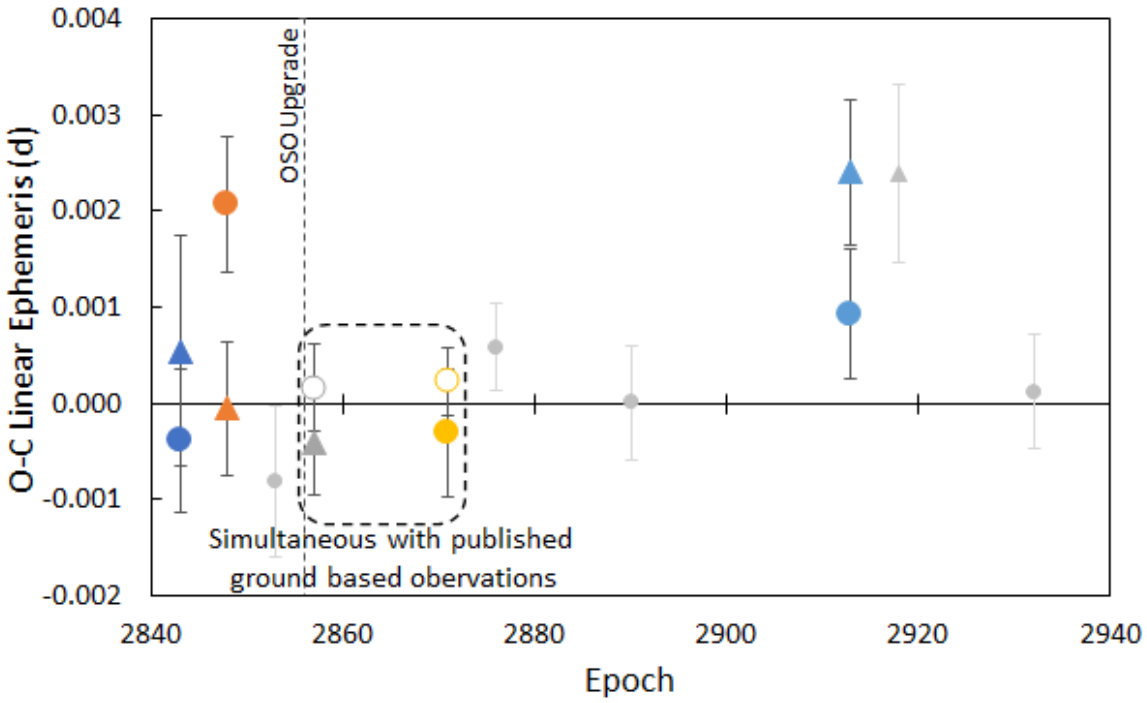

Figure 5.30: As Figure 5.29 but for HAT-P-23b simultaneous pairs.

Of the newly obtained simultaneous pairs of observations for WASP-12b and HAT-P-23b, eight pairs have overlapping uncertainties while four pairs exhibit a greater difference, only two out of twelve agree within 1σ. This level of difference, especially in the timing pairs obtained after the OSO GPS upgrade appears at odds with the transit timing measurement pairs simultaneous with published values, which are in closer agreement. The mean mid-time difference between pairs of new observations is 0.00136 ± 0.00026d whereas for observations simultaneous with published results the mean timing difference is 0.00042 ± 0.00004d. This result motivated a more detailed analysis of the new transit observations timing measurement and lightcurve quality metrics to better understand whether there is an underlying reason for the larger per-pair timing difference.

The standard deviation in measured T_C seen between all pairs of observations before the GPS timing system was installed at the OSO telescopes is 113 seconds, compared with 45 seconds for the pairs obtained after the GPS upgrade. This indicates that the pre upgrade timing difference could be the result of differences in the precision of the timing control at all three telescopes. It is worth noting however that the majority of this difference results from the single largest timing difference pair from the WASP-12b data set (epoch 1313), if this one pair is removed the pre-upgrade standard deviation drops to 62 seconds.

Figure 5.31, left shows that there is an imbalance between the occurrence of late vs early transit mid times by telescope for COAST and PIRATE. Before the GPS upgrade COAST transit times were always later than PIRATE but after the upgrade twice many PIRATE

times are later than COAST. This effect is not seen in POST observations simultaneous with one of the OSO telescopes which are evenly split between late and early. Figure 5.31 right shows how the mean O-C and spread in pair timing measurements between COAST and PIRATE changes dramatically after the GPS upgrade with a mean significantly closer to the ephemeris as is also seen for all the single observations timing results as well. The standard deviation in COAST measurements is reduced by half but increases for PIRATE, possible due to the smaller number of before upgrade observations. After the upgrade the standard deviation in COAST time measurements is approximately 60% greater than for PIRATE measurements. This could be attributable to the smaller aperture of COAST (0.35m vs 0.425m), however the COAST mean photometric SNR value is 50% greater than PIRATE (resulting from longer exposures and the use of the B filter in 3 PIRATE observations) and the TSNR values are comparable which argue against aperture alone being the cause of this difference. The red noise metric is an indicator of the extent to which individual transits are affected by correlated noise, the mean red noise metric for COAST is almost double that of PIRATE, while the spread in PIRATE red noise metric is greater than seen for COAST. The timing SNR values calculated using Eq.2 from Deeg and Tingley (2017) are comparable for COAST and PIRATE.

A search for correlations between the transit time difference for each pair of simultaneous observations and the available lightcurve quality measures was undertaken. For each lightcurve pair the Kendall-Tau statistical test (due to the small sample size) was used to look at the difference, sum and ratio of the lightcurve quality measures. Only two correlations were found to be statistically significant, the difference between TSNR values, ΔTSNR, (tau = -0.6, p-value = 0.007) for each pair and difference in pre-transit RMS, (tau = 0.5, p-value = 0.023). The negative correlation of ΔTSNR with timing difference results in a smaller timing difference as the difference between TSNR increases, intuitively it would be expected for the time difference be less when the lightcurves were of a similar quality, whereas this result implies the difference is less where one lightcurve is a lower quality than the other. The correlation between ΔTc and pre-transit RMS shows that the timing difference reduces as the pre transit RMS for the early transit in each pair increases or equivalently as the RMS noise for the late transit decreases. No significant correlation with transit RMS values (post transit, all out of transit and full transit measurements) is found. Both correlations become statistically insignificant when considering only the post GPS install data for PIRATE and COAST. Although not having the greatest per-pair time difference the three pairs with greatest mean O-C value also have the greatest TSNR difference, WASP-12b epochs 1368 and 1993 and HAT-P-23b epoch 2913 have ΔTSNR of 4.0, 5.3 and 3.6 respectively. The mean ΔTSNR value for the other nine pairs is 1.06. Further simultaneous observations using

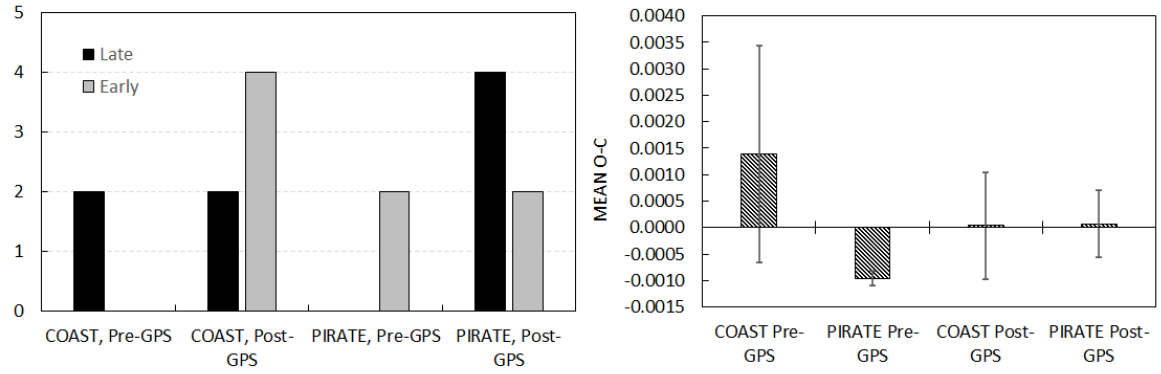

Figure 5.31: Left, pairs of COAST-PIRATE simultaneous WASP-12b transit observations. Before the GPS upgrade and switch to CCD 1×1 binning there were only two pairs of observations and in both the PIRATE transit mid-time was earlier than than for COAST. After the GPS installation there were six pairs of observations where for four COAST was earlier than PIRATE and two where COAST was later than PIRATE. Right, plot showing change in mean transit mid-time and spread in measurements before and after the GPS upgrade/switch to CCD 1×1 binning showing the significant improvement in accuracy and reduction in spread for COAST.

the OSO telescopes would be required to determine if any correlation with lightcurve quality factors are real.

Of note are the three Blue filter PIRATE observations simultaneous with Rc filter COAST observations. All three PIRATE observations are missing any pre transit data. However the spread of the B filter O-C values is smaller than for the Rc filter COAST measurements. This was also seen in the simultaneous MUSCAT measurements (Patra et al., 2020) where one transit had no pre-ingress data but doesn't show the largest timing discrepancy which arises from a transit with good coverage but higher noise.

For WASP-12b the mean timing difference in six previously published simultaneous observation pairs is 0.0019d (164s). Three of these pairs were observed by same telescope through different filters and as a result the mean difference is much reduced at 0.0007d, but still larger than the typical mid-time measurement uncertainty. By contrast for the five pairs of transits where one is from the published literature and the other from a new observation (including three from TESS) the timing difference is 0.00036d (31s), less than the typical transit mid-time uncertainty. Across both WASP-12b and HAT-P-23b the pairs of observations obtained before the GPS upgraded at the OSO telescopes was 0.00164d (142s) and after the upgrade was 0.00116 (100s). While this is a 30% reduction in timing spread and an improvement over the values seen between published pairs of observations it is still almost double the typical mid-time measurement uncertainty. At the same time it can be seen the three individual

PIRATE observations obtained over 12 days in the 2019-20 season have a mean O-C value of 0.00003d (2.6s). No upgrades or changes were made at the OSO telescopes between these observing seasons. Comparing the WASP-12b data sets from the 2018-19 and 2019-2020 season two factors stand out as potential causes for the larger spread in O-C values seen in the 2018-19 season. Firstly it can be seen from looking at Figures 4.4 and 4.5 that the transit observations during 2018-19 season (transit numbers 28 to 58) have in general much less pre-transit data than those obtained in the 2019-20 season (transit numbers 60-65). Of the 19 full transits obtained with all telescopes during the 2018-19 season, including the 6 simultaneous pairs, 14 have pre-transit data coverage shorter than the ingress duration and 5 have none or only 2 measurements before ingress. As was shown in Table 5.6 transits with pre-ingress coverage less than ingess/egress duration show a greater scatter in O-C. All 2019-2020 observations have pre-transit data coverage at least twice the ingress duration. This may also explain why no correlation was seen between the transit time spread and out of transit coverage for the simultaneous pairs, as all transits had little or no pre-transit coverage. The second point of note is that the PIRATE observation obtained during the 2019-20 season were more defocussed than those from the 2018-19 season with an FWHM typically 3 times greater.

5.7 Summary of Key Findings

Analysis of the transit timing measurements before and after the implementation of the GPS timing control for PIRATE and COAST has shown that the timing accuracy improved significantly. Observations of HAT-P-23b clearly show the scatter in O-C measurements reducing by 2.4× after the GPS upgrade. At the same time the results show that making observations with a longer cadence in 1×1 binning mode provide more precise results than faster cadence in 2×2 binning mode.

TSNR is a useful measure of the precision with which transit times can be measured and the results show that a higher TSNR gives a lower spread in transit mid-time measurement. Out-of-transit RMS has been shown to be proportional to $\mathrm{SNR}^{-0.95}$ providing a guide that photometric SNR greater than 600 is required to provide the best timing precision for observations in 1×1 binning mode using an Rc filter. Transit photometry with PIRATE and COAST regularly achieved oot RMS of 0.0015 showing that 3σ detection of transits with a depth of 0.5% can be achieved in single a observation. With a few exceptions observations made with all telescopes show minimal red noise and no correlation is found between a calculated red noise metric and the transit timing results. A test of guiding precision has shown precise guiding will reduce the RMS scatter in the photometric measurements by 13%.

Using multiple transit observations obtained and analysed in a homogeneous way can be combined with catalogue data to provide high precision system parameters. Long term photometric monitoring with PIRATE is stable over multiple seasons and provides precision sufficient to measure periodicity's in exoplanet host star at least at the 0.01 magnitude level.

In this chapter I have quantified the performance capabilities of the small aperture ground-based telescopes used to make short and long term timing observations of transiting exoplanets and how those observations can be used, in combination with published data, to provide high precision system parameters. I have also quantified the ability of PIRATE to undertake long term monitoring observations over multiple seasons to search for and quantify Exoplanet host star variability. In the final chapter I review the key finding from the study of the selected transiting exoplanets with small aperture ground-based telescopes, identify best practice approaches for obtaining the most accurate and precise system parameters and at future developments and possibilities for the OpenScience Observatories and small aperture ground-based telescopes to contribute to the field of exoplanet research.

Chapter 6

Conclusion and Discussion

In this thesis I used multiple small aperture ground-based telescopes to look for transiting timing variations, refine orbital ephemerides and provide high precision system parameters. I also undertook long term monitoring of selected exoplanet host stars to search for variability in order to better understand the host stars of transiting hot Jupiter planets.

Here I summarise the key findings for the systems observed and then consider the suitability of small aperture ground-based telescopes for undertaking follow-up observations of transiting exoplanets. I'll finish by looking ahead to potential future exoplanet observation projects suitable for small aperture ground-based telescopes including developments planned for the OpenScience Observatories.

6.1 Transit timing

New observations of three transiting hot Jupiter systems were obtained. HAT-P-23b and WASP-52b were observed over a single season in 2018 while WASP-12b was observed over four seasons between 2016 and 2020. Where available, archive observations obtained using the POST observatory were used to extend the observation baselines.

No periodic variation in the transit timing measurements was seen in the new measurements for any of the three systems observed. This is in agreement with studies that have suggested hot Jupiter planets are likely to be isolated (E.g. Huang et al., 2016; Lillo-Box et al., 2016; Hamer and Schlaufman, 2019). However it also remains possible that short periods of observation along with generally sparse coverage are preventing the detection of TTVs. The calculated linear ephemeris for HAT-P-23b agrees well with that independently published shortly after my observations were obtained (Maciejewski et al., 2018).

Combining new and published transit times for WASP-52b initially resulted an ephemeris with a high χ^2_ν of 2.5. This motivated an analysis of the transit times from different authors which highlighted the transits times with very small uncertainties published by Mancini et al.

(2017) which were responsible increasing the χ^2_ν of the calculated ephemeris.

The authors noted that their linear ephemeris had a high χ^2_ν of 8.98 and they subsequently multiplied the uncertainties on their final linear ephemeris by this value. Multiplying the individual transit time uncertainties by this χ^2_ν value of 8.98 prior to re-calculating the ephemerides reduced the χ^2_ν of the ephemeris fit from 2.4 to 1.51. This also resulted in a slight preference for a quadratic ephemeris with a rate of change of $\delta P/\delta t = -38.6 \pm 4\text{ms yr}^{-1}$. This highlights the care required when combining transit time data from multiple sources. Forward projecting the linear and quadratic ephemerides shows that this period change could be confirmed by transit timing observations made in the 2021 season.

In early 2016 observations started to show evidence for a non linear ephemeris for WASP-12b (Maciejewski et al., 2016). A subsequent analysis postulated either apsidal precession or orbital decay as the cause (Patra et al., 2017). A flurry of published results have confirmed the period change is due to orbital decay (Weinberg et al., 2017; Maciejewski et al., 2018; Bailey and Goodman, 2019; Baluev et al., 2019; Öztürk and Erdem, 2019; Yee et al., 2019; Turner et al., 2021). Transit times from the 47 new transits with full coverage obtained with the three telescopes used for this project were insufficient to detect the quadratic ephemeris on their own. This was due to very sparse coverage of archive transit observation from POST with only 4 transits available between 2013 to 2016. The first two seasons of observations with PIRATE and COAST showed a significant scatter in the timing measurements, being greater than double the scatter in published values, see Figure 4.17. The final two seasons of observation, 2018 to 2020, showed less scatter in timing measurements.

The improvement in timing measurements is attributed to two changes in the way the transit lightcurves were obtained. Firstly, in the Summer of 2018, the OSO telescopes were upgraded with GPS time controllers connected to the CCD camera shutter trigger to give precise time stamps for when the shutter opens and closes. The control PCs were also slaved to the GPS controllers to ensure they maintained accurate UTC time. Prior to this the observatories had relied on the control PC operating systems to update system times from an Internet time server. The second key change was from using the CCD in 2x2 on-chip binning mode to unbinned (1x1). The improvement in transit time measurements obtained using COAST and PIRATE is clearly seen in the results for both HAT-P-23b and WASP-12b. The standard deviation for HAT-P-23b transit times reduced by 2.4 times following the changes, while for WASP-12b the standard deviation halved.

The installation of the GPS controller along with higher precision lightcurves resulting from making unbinned observations combined to improve both the accuracy and precision of the timing measurements. The GPS time controller provides milli-second accurate timing stamps for exposures made using PIRATE and COAST while the higher precision photometric

measurements resulting from using the CCD camera unbinned increased the transit signal to noise ratio (TSNR). The results show that while increased TSNR had minimal effect on individual transit mid-time uncertainty, it was correlated with reducing scatter in the transit time measurements. Figure 7.24 shows that for the spread in O-C measurements to match typical measurement uncertainty of 0.0005 day, a minimum TSNR of 10-12 is required. For a given transit depth the TSNR depends only on the out of transit photometric scatter; Figure 5.2 can be used to estimate the photometric SNR required to achieve a TSNR of 10-12 for a target transit observation.

The theoretical transit timing uncertainties (σTc) were calculated using TEE (Deeg and Tingley, 2017) and showed that the measured uncertainty achieved using the three small aperture telescopes is in generally good agreement with theoretical predictions. Figure 5.25 shows that for $\sigma\text{Tc} < 0.0005$d the measured σTc is approximately 10% greater than predicted by TEE. Measured transit uncertainties showed less scatter than suggested by the theoretical calculations. The standard deviation in the measured uncertainties were smaller for all telescopes and observing modes.

The importance of out-of-transit (oot) coverage is highlighted by the 2018-19 season observations of WASP-12b where 15 out of 19 transits have oot coverage less than the ingress/egress duration and a greater scatter in Tc determination. Figure 5.26 shows that transits with little total oot coverage show much greater σTc, with measured and theoretical values reaching agreement for oot coverage in the range 0.05 to 0.07d, indicating 30 to 50 minutes of oot coverage is required either site of transit. Little improvement in σTc is seen for longer oot coverage.

6.2 Parameter Determination

Multiple lightcurves obtained over extended periods of time for the primary purpose of transit timing have been analysed in conjunction with published radial velocity and photometric data to provide updated system parameters. Combining multiple transit lightcurves in this way enables the extraction of the maximum information from the available observations making the most efficient use of the telescope time used to obtain these data sets

The same care was taken in selecting and incorporating previously published data used in the analyses as was applied to the gathering of new data. Radial velocity data sets were treated individually to allow independent zero point and jitter determinations. Where authors suggested zero points may vary over long durations the data sets were separated into short time spans. Timestamps were updated to BJD_{TDB} where required. Photometric data used in the building of the SEDs was taken from multiple trusted sources and where required de-

blended to remove the contribution from unresolved companions. Distance information was taken from Gaia DR2 parallax data corrected for known systematics (E.g. Stassun et al., 2017) and V-band extinction values applied from dust reddening maps. To minimise any potential bias resulting from previous results all parameters were freely determined. No stellar, orbital or planetary parameters were fixed based on previously published results. This is in contrast to previous studies of these systems which often do this (E.g. Öztürk and Erdem, 2019). The analysis of the new transit data using ExofastV2 produced an homogenous set of results for transit times and system parameters.

The analysis for HAT-P-23b provide the most precise measurements yet for the stellar radius and result in stellar and planetary radii between the values previously published, confirming its inflated nature. The analysis for WASP-52b finds somewhat larger values for R_* and $R_{\rm P}$ than previous studies. No close companion to WASP-52 is identified in the literature however Hébrard et al. (2013) note a 'hint' of an approximately $+40$ ms^{-1} RV drift over 15 months which could be due to an unresolved companion. A blend with the host star cannot be ruled out without high resolution imaging, not possible with small aperture ground-based telescopes. The distance to WASP-52 was found to be 24% greater than that estimated in the discovery paper. The combined analysis shows both systems have an eccentricity within 2.4σ of zero and are therefore consistent with circular orbits (Eastman et al., 2019).

Similarly the newly presented results for WASP-12b provide the most precise determinations yet for R_*, $R_{\rm P}$, a, M_* and $M_{\rm P}$. The determinations of e and ω^* are in agreement with the values reported by Maciejewski et al. (2020) who suggest the apparent eccentricity of WASP-12b results from tidal bulges being raised by the planet on the host star.

The transit depth measured for WASP-12b was 4σ deeper than the small number of depth values published on the NASA Exoplanet Archive. The two different red filters used both cover the same key NaI and Hα absorption bands and hence cannot be the cause of this difference. Phase folding the lightcurves did not reveal any depth differences. WASP-12b has been observed by amateur astronomers for many years with the results being recorded on the Exoplanet Transit Database. Taking 21 of the most precise (data quality 1 and 2) R filter lightcurves the mean transit depth measured is 0.0186 ± 0.003. This is greater still than the 0.01439 ± 0.00012 measured from the 47 new transits and the mean value from the exoplanet archive of 0.01390 ± 0.00016.

Combining data from small aperture ground-based telescopes to provide precise exoplanet system parameters is an often overlooked use of large number of transit data obtained for timing purposes. The results presented have demonstrated that results achievable are comparable with those obtained from single or small number transit observations using significantly

larger telescopes.

6.3 Host Star Monitoring

Monitoring of exoplanet host stars concurrently with transit observations is a generally neglected task that has the capability to reveal further information about exoplanet systems not provided by observing transit events alone. This activity is well suited to small aperture automated telescopes such as PIRATE and COAST with schedulers capable of obtaining monitoring observations in a way that makes most efficient use of available telescope time.

Monitoring of HAT-P-23 over a single season in 2018 through an Rc filter detected variation with a period of 7.015 days and an amplitude of 0.011 magnitude. This is interpreted as the rotation period of HAT-P-23 at the latitude of surface spots. The measured amplitude was much lower than a previous tentative detection of variation of 0.03 magnitude seen by Sada and Ramón-Fox (2016), suggesting evolution of amplitude over time possibly due to HAT-P-23's ongoing stellar cycle. Further monitoring over multiple seasons would be required to detect any periodic variation in the amplitude to support this hypothesis.

Three years of monitoring of WASP-12 detected no definitive sign of periodic variation. The previously measured very slow rotational velocities for a late F spectral type star (Hebb et al., 2009; Albrecht et al., 2012) imply a rotation period in the range 21-66 days for WASP-12. Periodicities between 27-30 days seen in some seasons data are attributed to a systematic effect arising from lunar illumination. The conclusion reached by Albrecht et al. (2012) that we are seeing WASP-12 at a high stellar inclination, just 6.7° from pole explains the observed slow rotational velocity, the previous non-detections of the Rossiter McLaughlin effect and non-detection of photometric modulation in this work. Modelling with SOAP suggests that in order to detect rotational modulation due to spots with PIRATE on WASP-12b the spots need to be larger than 3% of the stellar surface (with an 80% flux level) and residing between latitudes 15°to 60°to generate a photometric variation. The possibility that WASP-12 was simply in a quiescent stage of its stellar cycle during the observations could be confirmed or refuted by ongoing monitoring.

Another reason to monitor exoplanet host star fields is to confirm, or otherwise, the stability of photometric comparison stars. Small aperture ground-based telescopes with a wide field of view are well suited to this task. Periodic variation was detected in J0630+2942, just $2'$ from WASP-12, the amplitude of which was seen to vary over multiple observing seasons. This star is of similar brightness and colour index to WASP-12 and was previously thought to be a photometrically stable comparison star. The maximal rate of flux variation indicated by the period and greatest amplitude measured during the 2016-17 season indicates a change in

brightness of up to 2.3 millimag over a 6 hour observation capturing a complete WASP-12b transit. This change in brightness amounts to $\sim 15\%$ of the transit depth of WASP-12b and is greater than the scatter in transit measurements for the higher quality lightcurves obtained as part of this project. For high precision transit lightcurves obtained with large telescopes and their small field of view, using solely J0630+2492 could have a significant detrimental effect on the measured lightcurve. This would become significantly more pronounced for the much shallower occultation lightcurve measurements and could potentially account for variations seen in secondary eclipse depths (see Section 6.5) if J0630+2942 is used as a photometric comparison.

The monitoring observations made using PIRATE have shown the observatory is capable of detecting variation at the 0.01 magnitude level in observations made over single and multiple observing seasons. Observations obtained in the 2018-2019 seasons were made using the CCD in 1x1 binned mode with subsequently longer exposures producing significantly more stable measurements, see Tables 4.9 and 5.3. Stability of measurement was aided by obtaining multiple measurements per night above an airmass of 2. Where multiple measurements were obtained each night the standard deviation in the check star measurements was generally less than half the spread in measurement values indicating single measurements per night would produce significantly inferior results. Making fewer observations using 1x1 binning with longer exposures produced more stable results than a larger number of shorter exposures at 2x2 binning. This is especially clearly seen in the reduced nightly spread in measurement values of the check star, Table 5.3. The spread in measurement values increased significantly where an SNR < 300 was achieved when observations were made in 2x2 binning and where SNR < 550 in 1x1 binning mode, providing minimum SNR values to be targeted for monitoring observations.

Our understanding of exoplanets is built on our understanding of the host stars they orbit. Ongoing photometric monitoring by small aperture ground-based telescopes can provide key information on the long term photometric modulations of these stars adding to our baseline of knowledge for each individual system. Observing host stars over extend periods of time in support of ground and space based spectroscopy measurements is another area where the small aperture ground-based telescopes have an important role to play. Precise spectroscopic measurements can be significantly adversely affected by the presence of star spots where activity cycles can induce radial velocity variations up to 25 ms^{-1} (Lovis et al., 2011). Such monitoring observations can be used to identify stellar cycles and inform optimum scheduling of spectroscopic observations. Parallel monitoring during ground and space based spectroscopic observations to provide a variability baseline will be especially important where multiple observations of a given system are required. Small aperture ground-based

telescope monitoring of host stars therefore has an important role even where the planet transit is not detectable or where the planets do not transit at all.

6.4 Monitoring Transiting Exoplanet Systems with Small aperture ground-based Telescopes

Throughout the observing programme undertaken for this thesis significant improvements were made in the precision of the lightcurves obtained when measured as the RMS scatter in the oot measurements. The best practice developed for the three telescopes used here can be extended more generally for small aperture ground-based telescopes.

Transit timing results from observations of HAT-P-23b and WASP-12b before and after implementation of GPS timing control have highlighted the requirement for accurate, consistent timing control for observations. Control systems based on standard PCs in an observatory can be subject to large temperature variations which they were not designed for, leading to significant variations in internal clocks. Relying on operating systems to keep clocks updated via the Internet can lead to synchronisation delays, adding up to unpredictable variations in timing measurements. GPS controlled timing is the gold standard and as a result of this work POST has subsequently been upgraded with GPS timing control. GPS systems may not be viable for all small aperture ground-based telescopes often owned by individuals, in which case dedicated software such as D4 to manage timing synchronisation is the next best approach. Portable telescopes without GPS control and where no Internet connectivity is available can present problems. Mobile Internet connectivity is commonly available and cost effective but where this is not available control laptops should be time synchronised before travelling to the observing site.

The second change implemented was to use the CDD in unbinned mode with longer exposures, resulting in improved photometric precision. This observing mode results in an oversampling of the stellar PSF akin to defocusing (Collins et al., 2017a) which is an often used method to improve the photometric precision (E.g. Southworth et al., 2004; Hinse et al., 2015). Spreading the flux over a larger number of pixels reduces the impact of inter-pixel variations not completely corrected for if the flat fielding is imperfect. Secondary terms in the standard CCD equation (E.g. Collins et al., 2017b) show that noise increases with the number of pixels in the photometry aperture. In modern low noise cooled CCDs, the decrease in interpixel variations more than offsets the increase in noise resulting from a greater number of pixels, see Figure 5.16.

Another approach for improving photometric precision gaining in popularity is the use of engineered diffusers (Stefansson et al., 2017; von Essen et al., 2019). These devices provide a

controlled PSF with a square profile, unlike defocusing which typically results in a "donut" profile to the PSF. Oversampling has two key benefits over both defocusing and engineered diffusers. Firstly in crowded fields these methods can lead to overlapping of the extended PSFs, blending the flux of multiple stars resulting in shallower transit depth determinations. Secondly well focused oversampled imaging allows the use of on-axis guiding to further reduce the effect of inter-pixel variations by maintaining the stellar centroid on the same pixels throughout an observation. A test undertaken using POST to compare unguiding imaging with precise autoguiding showed a 13% reduction in photometric scatter where a stellar centroid was maintained on the same pixel. This improvement would be expected to be greater where flat fielding is not perfect which may arise for PIRATE and COAST master flat fields as these are built from individual flat field frames obtained over multiple nights (Jackson et al., 2021).

To further minimise photometric scatter the photometry analysis used an iterative approach, testing multiple target and sky aperture radii along with removing comparison stars from the ensemble in turn to test for reductions in RMS scatter and BIC. Implemented in AstroImageJ (Collins et al. (2017b) this was a manual process for the lightcurves analysed in this thesis but this approach should be adopted into any automated photometry pipeline.

As discussed in Section 6.1, a TSNR of 10-12 should be considered the minimum for consistent transit timing retrieval along with out of transit coverage that exceeds the ingress/egress duration either side of the transit. Later lightcurves obtained with PIRATE and COAST in this work have out of transit RMS scatter in the region of 0.0013 to 0.0015. Transit depths of 1.3% to 1.5% are detectable with TSNR of 10-12 and transits depths of 0.5% are detectable at TSNR = 3 for single observations.

Phase folding of multiple observations has shown that the observations are an efficient way of obtaining extremely high precision transit lightcurves compared to single transit measurements from much larger 2m class ground-based telescopes. To achieve these results requires a greater time investment for the small telescopes to obtain the multiple observations required, which automation greatly simplifies. Using a metric of telescope mirror area multiplied by the duration of observations the results show that, in the absence of spot crossing events, the binned photometric results obtained with the small telescopes result in a lightcurve with the same or better out of transit photometric precision in half the mirror area $\times$ observation time of the 2m class telescopes.

Phase folding 42 Red filter lightcurves obtained for WASP-12b in this thesis resulted in an out of transit RMS of 119ppm, which I compared to a similar phase fold of 21 TESS lightcurves which result in an out of transit RMS of 204ppm.

Table 6.1: Comparison of mean transit mid uncertainty and mean absolute O-C for HAT-P-23b.

	ETD	ExoClock	PIRATE
Number of measurements	121	24	5
Mean Tc Uncertainty (d)	0.001	0.00075	0.0006
Mean —O-C— (d)	0.0056	0.001	0.0004

6.5 Looking Forward

A number of further improvements are planned to upgrade the capability for the Open University OpenScience Observatories. Chief amongst these is the replacement of the current 0.45m PIRATE OTA with a new 0.6m OTA of the same optical type while the 0.45m OTA from PIRATE will replace the 0.35m f11 optical tube on COAST. Taking the greater secondary mirror into consideration this will provide a mirror area 2.5 times greater than the current COAST telescope and twice as large as PIRATE. Other developments are planed including the implementation of a focus offset for automated observing of bright targets and a data reduction pipeline tailor-made for transit observations.

Zellem et al. (2020) showed that our ability to accurately predict transit mid-times in the future is most dependent on the precision of the period determination which requires multiple transit mid-time measurements with low scatter in order to calculate precise ephemerides. The example of HAT-P-23b in table 6.1 compares the results obtained using PIRATE after the GPS installation with measurements from ETD and Exoclock. The results demonstrate the capability of PIRATE/COAST to contribute accurate and precise timing measurements to programmes such as ExoClock in support of the ESA ARIEL mission.

Combined analysis of transit lightcurves, RV and photometric data with accurate distances now available from Gaia was used in Exofastv2 to determine accurate stellar radii. This approach will produce a discrepant result where the flux of the target star is blended with that of close, unresolved companion(s). This fact could be used to systematically identify systems exhibiting "excess" stellar radii over other methods used to determine stellar radius such as the Torres relationship. These systems would make suitable follow up targets for high resolution or "lucky" imaging to identify close companions contaminating the photometric data which would also impact precision spectroscopic studies.

The level of lightcurve precision achieved when phase folding multiple observations opens the possibility for the detection of very shallow primary transits or even secondary occultations. Using the results from phase folding the 42 Red filter lightcurves of WASP-12b a transit depth of 0.06% would be detectable with a TSNR of 5. This is equivalent to a $2.7R_{\oplus}$

planet orbiting a Sun like star, or an Earth radius planet orbiting a red dwarf host star.

Occultations of WASP-12b have been measured using ground-based telescopes in the filter bandpasses available for PIRATE and COAST and appear to indicate significant variability in the occultation depths. Hooton et al. (2019) observed two occultations a year apart in the i' band using 2m class telescopes and measured single event depths of 0.97 ± 0.14 mmag and 0.44 ± 0.21 mmag. Using an engineered diffuser on the 2.5m Nordic Optical Telescope, von Essen et al. (2019) measured three occultations in the V band separated by 24 days and with varying depths of 1.16 ± 0.17 parts per thousand (ppt), -0.03 ± 0.17ppt and 0.28 ± 0.1ppt. Hooton et al. (2019) speculate that while systematic errors are likely leading to some of the variation seen they cannot rule out temperature variations of several hundred Kelvin in the dayside temperature of WASP-12b. A potential cause of systematic errors in occulatation depth measurement separated by years could arise from the use of J0630+2942 as a comparison. Hooton et al. (2019) used an ensemble of 5 comparison stars, it is unclear if this ensemble included J0630+2942.

Occultation depths of 0.97 and 0.44 mmag could be detected at the 8σ and 3.7σ level respectively with PIRATE given the precision achieved in this work. The quantum efficiency of the FLI PL16803 camera on PIRATE at 800nm, in the centre of the Ic band, is about 40% lower than at 600nm in the Rc band, a deficit more than made up for with the aperture increase when moved to the new 0.6m telescope. The level of lightcurve precision achieved required the phase folding of many lightcurves over several seasons, not an optimal approach for a time variable target. Due to its 1.09 day orbit transits (and occultations) occur in groups of three on successive nights where all three occur when WASP-12b is above 30° altitude for the entire transit/occultation. The best single night PIRATE lightcurve achieved an out of transit RMS precision of 0.85 mmag when binned to 5 minute cadence, which could be expected to be improved to 0.49 mmag by phase folding three similar quality lightcurves. This would enable a 2σ detection of the occultation at the greatest depth seen by Hooton et al. (2019) over 3 successive nights, minimising the likelihood of intrinsic variability.

The study of transiting exoplanets is one of the few areas of astronomical research where observations made with small aperture ground-based telescopes, whether as part of a dedicated professional project, individual educational facility or amateurs are able to make a worthwhile contribution to the field. Groups of interested amateurs with access to small aperture ground-based telescopes are being organised around specific projects such the ARIEL Exoclock project or around existing national amateur astronomy societies such as the BAA and AAVSO exoplanet groups. These groups provide a level of organisation and education outreach, bringing like minded observers together and providing training in the specifics of

exoplanet transit observation. This in turn helps increase awareness of the field with the general public and science educators. As these groups grow in size and capability the opportunity to undertake specific targeted projects, especially those that foster international collaboration, will be a natural outcome. Such projects include transit timing and host star monitoring, micro-lensing event follow-up, long duration (multi-day) transit coverage, single transit event follow-up and combining observations of occultations to name just a few.

As was shown in Chapter 5, combining multiple transit observations from small aperture ground-based telescopes is an efficient way to obtain high precision lightcurves for follow up observations of known transiting exoplanets.

A typical commercial, off the shelf, 0.6m observatory telescope provides $0.22m^2$ unobstructed mirror area while a medium class 4m ground-based telescope such as the 4m Lowell Discovery Channel Telescope (LDCT)[1] or the planned New Robotic Telescope (NRT)[2] provide in the region of $13m^2$, an aperture ratio of 59/1. The costs of medium class telescopes are undoubtedly reducing with the adoption of modern technologies such as segmented mirrors but they are still significant investments with the LDCT having a price tag of $53m while the NRT is expected to cost $24m. A typical cost for an off the shelf 0.6m observatory telescope including OTA, mount, camera system and enclosure would be in the region of $150,000. 59 such telescopes would the same mirror area as the 4m class telescopes for a sixth of the LDCT cost and a third the NRT cost. Projects such as MEarth[3] based on two automated observatories each with eight 0.6m telescopes already exist for specific purposes. Combining small aperture ground-based telescopes into similar observatory groups would, in principle, allow 10 such observatories (80 telescopes) to be set up around the globe for half the NRT cost. Spread over a range of latitude and longitude multiple observatories could provide almost continuous coverage of the entire night sky, with overlap redundancy for weather conditions at individual locations. Such an observatory capability would be very flexible providing high quality, multi-filter transit follow-up, host and comparison star monitoring and other transient target follow-up such as for micro-lensing events, over a longer duration than could be achieved with a satellite observatory. This approach would provide significant opportunities for education and outreach, a model used by the Las Cumbres Observatory (LCO), a global network of 0.4m to 2m class robotic telescopes for transient follow up with a strong focus on education and outreach[4]. Such a network of observatories could be operated on a day-to-day basis by educational groups or even volunteer groups such national astronomical societies.

[1] `https://en.wikipedia.org/wiki/Lowell_Discovery_Telescope`

[2] https://www.roboticstelescope.org

[3] `https://lweb.cfa.harvard.edu/MEarth/Welcome.html`

[4] https://lco.global/about/

Bibliography

F. C. Adams and G. Laughlin. Long-Term Evolution of Close Planets Including the Effects of Secular Interactions. *The Astrophysical Journal*, 649(2):1004–1009, 2006. ISSN 0004-637X. doi: 10.1086/506145.

E. Agol and K. Deck. Transit timing to first order in eccentricity. *The Astrophysical Journal*, 818(2), 2016. URL `http://arxiv.org/abs/1509.01623`.

E. Agol, J. Steffen, W. Clarkson, R. Sari, and W. Clarkson. On detecting terrestrial planets with timing of giant planet transits. *Monthly Notices of the Royal Astronomical Society*, 359(2):567–579, 5 2005. ISSN 0035-8711. doi: 10.1111/j.1365-2966.2005.08922.x. URL `http://mnras.oxfordjournals.org/cgi/doi/10.1111/j.1365-2966.2005.08922.xhttp://mnras.oxfordjournals.org/content/359/2/567.short`.

S. Albrecht, J. N. Winn, J. A. Johnson, A. W. Howard, G. W. Marcy, R. P. Butler, P. Arriagada, J. D. Crane, S. A. Shectman, I. B. Thompson, T. Hirano, G. Bakos, and J. D. Hartman. Obliquities of hot jupiter host stars: Evidence for tidal interactions and primordial misalignments. *Astrophysical Journal*, 757(1), 2012. ISSN 15384357. doi: 10.1088/0004-637X/757/1/18.

J. Applegate, J; Patterson. Magnetic activity, tides, and orbital period changes in close binaries. *ASTROPHYSICAL JOURNAL*, 322:99–102, 1987.

J. H. Applegate. A mechanism for orbital period modulation in close binaries. *The Astrophysical Journal*, 385(2):621, 1992. ISSN 0004-637X. doi: 10.1086/170967. URL `http://stacks.iop.org/1538-4357/669/i=2/a=L93%5Cnhttp://adsabs.harvard.edu/abs/1992ApJ...385..621A%5Cnhttp://adsabs.harvard.edu/doi/10.1086/170967`.

D. J. Armstrong, D. Veras, S. C. C. Barros, O. Demangeon, J. McCormac, H. P. Osborn, J. Lillo-Box, A. Santerne, M. Tsantaki, J.-M. Almenara, D. Barrado, I. Boisse, A. S. Bonomo, F. Bouchy, D. J. a. Brown, G. Bruno, J. R. Cerda, B. Courcol, M. Deleuil, R. F. Díaz, A. P. Doyle, G. Hébrard, J. Kirk, K. W. F. Lam, D. L. Pollacco, A. Rajpurohit, J. Spake, and S. R. Walker. One of the closest planet pairs to the 3:2

Mean Motion Resonance, confirmed with K2 observations and Transit Timing Variations: EPIC201505350. *Astronomy & Astrophysics*, 33(582), 2015. ISSN 14320746. doi: 10.1051/0004-6361/201526008. URL http://arxiv.org/abs/1503.00692.

A. Bailey and J. Goodman. Understanding WASP-12b. *Monthly Notices of the Royal Astronomical Society*, 482(2):1872–1882, 2019. ISSN 13652966. doi: 10.1093/mnras/sty2805.

A. G. Bakos, J. Hartman, G. Torres, D. W. Latham, G. Kovcs, R. W. Noyes, D. A. Fischer, J. A. Johnson, G. W. Marcy, A. W. Howard, D. Kipping, G. A. Esquerdo, A. Shporer, B. Béky, L. A. Buchhave, G. Perumpilly, M. Everett, D. D. Sasselov, R. P. Stefanik, J. Lázár, I. Papp, and P. Sári. HAT-P-20b-HAT-P-23b: Four massive transiting extrasolar planets. *Astrophysical Journal*, 742(2), 2011. ISSN 15384357. doi: 10.1088/0004-637X/742/2/116.

G. A. Bakos, A. W. Howard, R. W. Noyes, J. Hartman, G. Torres, G. Kovacs, D. A. Fischer, D. W. Latham, J. A. Johnson, G. W. Marcy, D. D. Sasselov, R. P. Stefanik, B. Sipocz, G. Kovacs, G. A. Esquerdo, A. Pal, J. Lazar, I. Papp, and P. Sari. HAT-P-13b,c: A Transiting Hot Jupiter with a Massive Outer Companion on an Eccentric Orbit. *The Astrophysical Journal*, 707(1):446–456, 2009. ISSN 0004-637X. doi: 10.1088/0004-637X/707/1/446. URL http://adsabs.harvard.edu/cgi-bin/nph-data_query?bibcode=2009ApJ...707..446B&link_type=ABSTRACT%5Cnpapers2://publication/doi/10.1088/0004-637X/707/1/446.

R. V. Baluev, E. N. Sokov, V. S. Shaidulin, I. A. Sokova, H. R. A. Jones, M. Tuomi, G. Anglada-escud, P. Benni, C. A. Colazo, M. E. Schneiter, C. S. V. D. Angelo, A. Y. Burdanov, and E. Fern. Benchmarking the power of amateur observatories for the TTV exoplanets detection. *Monthly Notices of the Royal Astronomical Society*, 450(January): 3101, 2015.

R. V. Baluev, E. N. Sokov, H. R. A. Jones, V. S. Shaidulin, I. A. Sokova, L. D. Nielsen, P. Benni, E. M. Schneiter, C. V. D Angelo, E. Fernandez-Lajus, R. P. Di Sisto, O. Basturk, M. Bretton, A. Wunsche, V. P. Hentunen, S. Shadick, Y. Jongen, W. Kang, T. Kim, E. Pakstiene, J. K. T. Qvam, C. R. Knight, P. Guerra, A. Marchini, F. Salvaggio, R. Papini, P. Evans, M. Salisbury, F. Garcia, D. Molina, J. Garlitz, N. Esseiva, Y. Ogmen, Y. Karavaev, S. Rusov, M. A. Ibrahimov, and R. G. Karimov. Homogeneously derived transit timings for 17 exoplanets and reassessed TTV trends for WASP-12 and WASP-4. *Monthly Notices of the Royal Astronomical Society*, 490(1):1294 – 1312, 2019. doi: 10.1093/mnras/stz2620. URL http://arxiv.org/abs/1908.04505.

S. Barros, G. Boue, N. P. Gibson, D. L. Pollacco, A. Santerne, F. P. Keenan, I. Skillen, and R. A. Street. Transit timing variations in WASP-10b induced by stellar activity. *Monthly Notices of the Royal Astronomical Society*, 430(4):3032–3047, 2013. ISSN 00358711. doi: 10.1093/mnras/stt111.

O. Basturk, E. M. Esmer, S. Torun, S. Yalcınkaya, F. E. Helweh, E. Karamanli, M. Oncu, H. O. Albayrak, F. A. M. Akram, M. G. Kahraman, S. Sufi, M. Uzumcu, and F. Davoudi. Transit Timing Variations of Five Transiting Planets. *American Institute of Physics Conference Series*, 2019.

K. Batygin, P. H. Bodenheimer, and G. P. Laughlin. In Situ Formation and Dynamical Evolution of Hot Jupiter Systems. *The Astrophysical Journal*, 829(2):1–17, 2016. URL http://arxiv.org/abs/1511.09157.

T. G. Beatty and S. Seager. Transit Probabilities for Stars With Stellar Inclination Constraints. *The Astrophysical Journal*, 712(2):1433–1442, 2010. ISSN 0004-637X. doi: 10.1088/0004-637X/712/2/1433. URL http://stacks.iop.org/0004-637X/712/i=2/a=1433?key=crossref.2ee4753be6fa36acc6c34e3a1277cadc.

E. B. Bechter, J. R. Crepp, H. Ngo, H. a. Knutson, K. Batygin, S. Hinkley, P. S. Muirhead, J. A. Johnson, A. W. Howard, B. T. Montet, C. T. Matthews, and T. D. Morton. WASP-12b AND HAT-P-8b ARE MEMBERS OF TRIPLE STAR SYSTEMS. *The Astrophysical Journal*, 788:2, 2014. ISSN 0004-637X. doi: 10.1088/0004-637X/788/1/2.

J. C. Becker, A. Vanderburg, F. C. Adams, S. A. Rappaport, and H. M. Schwengeler. Wasp-47: a Hot Jupiter System With Two Additional Planets Discovered By K2. *The Astrophysical Journal*, 812(2):L18, 2015. ISSN 2041-8213. doi: 10.1088/2041-8205/812/2/L18. URL http://stacks.iop.org/2041-8205/812/i=2/a=L18?key=crossref.5f4173b9e2b0879f176c0aa9e1c6a45a.

B. Beky. Development and Application of Tools to Characterize Transiting Astrophysical Systems. *PHD Thesis*, 2014. URL http://dash.harvard.edu/handle/1/12274130.

L. Ben-Jaffel and G. Ballester. Hubble Space Telescope detection of carbon and oxygen in the atmosphere of exoplanet HD 189733b. *Astronomy & Astrophysics*, 52:1–12, 2013. ISSN 0004-6361. doi: 10.1051/0004-6361/201221014. URL http://arxiv.org/abs/1303.4232.

C. Bergfors, W. Brandner, S. Daemgen, B. Biller, S. Hippler, M. Janson, N. Kudryavtseva, K. Gei??ler, T. Henning, and R. K??hler. Stellar companions to exoplanet host stars: Lucky Imaging of transiting planet hosts. *Monthly Notices of the Royal Astronomical Society*, 428 (1):182–189, 2013. ISSN 00358711. doi: 10.1093/mnras/sts019.

J. Blecic, J. Harrington, N. Madhusudhan, K. B. Stevenson, R. a. Hardy, P. E. Cubillos, M. Hardin, O. Bowman, S. Nymeyer, D. R. Anderson, C. Hellier, A. M. S. Smith, and A. C. Cameron. SPITZER OBSERVATIONS OF THE THERMAL EMISSION FROM WASP-43b. *The Astrophysical Journal*, 781:116, 2014. ISSN 0004-637X. doi: 10.1088/0004-637X/781/2/116. URL http://stacks.iop.org/0004-637X/781/i=2/a=116?key=crossref.f5300a03c9e6b83bed1f503d8665fdde.

E. Bohm-Vitense. Chromospheric Activity in G and K Main-Sequence Stars, and What It Tells Us about Stellar Dynamos. *The Astrophysical Journal*, 657(1):486–493, 2007. ISSN 0004-637X. doi: 10.1086/510482. URL http://stacks.iop.org/0004-637X/657/i=1/a=486.

I. Boisse, F. Bouchy, G. Hébrard, X. Bonfils, N. Santos, and S. Vauclair. Disentangling between stellar activity and planetary signals. *Astronomy & Astrophysics*, 6(S276):A4, 2011. ISSN 1743-9213. doi: 10.1017/S1743921311020515. URL http://adsabs.harvard.edu/abs/2011A&A...528A...4B%5Cnhttp://adsabs.harvard.edu/abs/2011IAUS..273..281B%5Cnhttp://adsabs.harvard.edu/abs/2011IAUS..276..399B.

A. C. Boley, A. P. G. Contreras, and B. Gladman. The In Situ Formation of Giant Planets at Short Orbital Periods. *The Astrophysical Journal Letters*, 817(2):1–17, 2016. URL http://arxiv.org/abs/1510.04276.

A. S. Bonomo, S. Desidera, S. Benatti, F. Borsa, S. Crespi, M. Damasso, A. F. Lanza, A. Sozzetti, G. Lodato, F. Marzari, C. Boccato, R. U. Claudi, R. Cosentino, E. Covino, R. Gratton, A. Maggio, G. Micela, E. Molinari, I. Pagano, G. Piotto, E. Poretti, R. Smareglia, L. Affer, K. Biazzo, A. Bignamini, M. Esposito, P. Giacobbe, G. Hébrard, L. Malavolta, J. Maldonado, L. Mancini, A. M. Fiorenzano, S. Masiero, V. Nascimbeni, M. Pedani, M. Rainer, and G. Scandariato. The GAPS Programme with HARPS-N@TNG XIV. Investigating giant planet migration history via improved eccentricity and mass determination for 231 transiting planets. *Astronomy & Astrophysics*, 602(A107):1–16, 2017. ISSN 0004-6361. doi: 10.1051/0004-6361/201629882. URL http://arxiv.org/abs/1704.00373%0Ahttp://dx.doi.org/10.1051/0004-6361/201629882.

L. Borsato, F. Marzari, V. Nascimbeni, G. Piotto, V. Granata, L. R. Bedin, and L. Malavolta. TRADES: A new software to derive orbital parameters from observed transit times and radial velocities. *Astronomy & Astrophysics*, 571:A38, 2014. ISSN 0004-6361. doi: 10.1051/0004-6361/201424080. URL http://labs.adsabs.harvard.edu/adsabs/abs/2014A&A...571A..38B/%5Cnhttp://arxiv.org/abs/1408.2844%5Cnhttp://www.aanda.org/10.1051/0004-6361/201424080.

L. G. Bouma, J. N. Winn, C. Baxter, W. Bhatti, F. Dai, T. Daylan, J. M. Désert, M. L. Hill, S. R. Kane, K. G. Stassun, J. Villasenor, G. R. Ricker, R. Vanderspek, D. W. Latham, S. Seager, J. M. Jenkins, Z. Berta-Thompson, K. Colón, M. Fausnaugh, A. Glidden, N. Guerrero, J. E. Rodriguez, J. D. Twicken, and B. Wohler. WASP-4b Arrived Early for the TESS Mission. *Astronomical Journal*, 157(6):217, 2019. URL `http://arxiv.org/abs/1903.02573`.

A. G. A. Brown and Gaia Collaboration. Gaia Data Release 1 Summary of the astrometric, photometric, and survey properties. *Astronomy & Astrophysics*, 2016. doi: 10.1051/0004-6361/201629512.

A. G. A. Brown and Gaia Collaboration. Astrophysics Special issue Gaia Data Release 2. *Astronomy & Astrophysics*, 616(A1):1–22, 2018.

D. J. Brown. Discrepancies between isochrone fitting and gyrochronology for exoplanet host stars? *Monthly Notices of the Royal Astronomical Society*, 442(2):1844–1862, 2014. ISSN 13652966. doi: 10.1093/mnras/stu950.

G. Bruno, M. Deleuil, J. M. Almenara, S. C. Barros, A. F. Lanza, M. Montalto, I. Boisse, A. Santerne, A. M. Lagrange, and N. Meunier. Disentangling planetary and stellar activity features in the CoRoT-2 light curve. *Astronomy and Astrophysics*, 595:1–14, 2016. ISSN 14320746. doi: 10.1051/0004-6361/201527699. URL `http://arxiv.org/abs/1608.01855`.

G. Bruno, N. K. Lewis, K. B. Stevenson, J. Filippazzo, M. Hill, J. D. Fraine, H. R. Wakeford, D. Deming, M. López-Morales, and M. K. Alam. Starspot Occultations in Infrared Transit Spectroscopy: The Case of WASP-52b. *The Astronomical Journal*, 156(3):124, 2018. ISSN 1538-3881. doi: 10.3847/1538-3881/aac6db. URL `http://stacks.iop.org/1538-3881/156/i=3/a=124?key=crossref.d4ef34444f840a2904934c8407a92cf0`.

M. L. Bryan, H. A. Knutson, A. W. Howard, H. Ngo, K. Batygin, J. R. Crepp, B. J. Fulton, S. Hinkley, H. Isaacson, J. A. Johnson, G. W. Marcy, and J. T. Wright. Statistics of Long Period Gas Giant Planets in Known Planetary Systems. *The Astrophysical Journal*, 821(2):89, 2016. ISSN 1538-4357. doi: 10.3847/0004-637X/821/2/89. URL `http://stacks.iop.org/0004-637X/821/i=2/a=89?key=crossref.39863e2249694376455eca5eb6d7630d`.

C. J. Campo, J. Harrington, R. A. Hardy, K. B. Stevenson, S. Nymeyer, D. Ragozzine, N. B. Lust, D. R. Anderson, A. Collier-Cameron, J. Blecic, C. B. Britt, W. C. Bowman, P. J. Wheatley, T. J. Loredo, D. Deming, L. Hebb, C. Hellier, P. F. Maxted, D. Pollaco, and R. G. West. On the orbit of exoplanet WASP-12b. *Astrophysical Journal*, 727(2), 2011. ISSN 15384357. doi: 10.1088/0004-637X/727/2/125.

B. Carroll and D. Ostile. *An Introduction to Modern Astrophysics*. Pearson International, second edition, 2007. ISBN 0-321-44284-9.

A. Chakrabarty and S. Sengupta. Precise Photometric Transit Follow-up Observations of Five Close-in Exoplanets: Update on Their Physical Properties. *The Astronomical Journal*, 158 (1):39, 2019. ISSN 0004-6256. doi: 10.3847/1538-3881/ab24dd. URL `http://dx.doi.org/10.3847/1538-3881/ab24dd`.

G. Chen, L. Nortmann, F. Murgas, H. Parviainen, and G. Nowak. The GTC exoplanet transit spectroscopy survey VI . Detection of sodium in WASP-52b ' s cloudy atmosphere. *Astrophysics Letter to the E ditor*, 11:1–6, 2017.

S. V. Chernov, P. B. Ivanov, and J. C. Papaloizou. Dynamical tides in exoplanetary systems containing hot Jupiters: Confronting theory and observations. *Monthly Notices of the Royal Astronomical Society*, 470(2):2054–2068, 2017. ISSN 13652966. doi: 10.1093/mnras/stx1234.

A. Chontos, D. Huber, D. W. Latham, A. Bieryla, V. Van Eylen, T. R. Bedding, T. Berger, L. A. Buchhave, T. L. Campante, W. J. Chaplin, I. L. Colman, J. L. Coughlin, G. Davies, T. Hirano, A. W. Howard, and H. Isaacson. The Curious Case of KOI 4: Confirming Kepler's First Exoplanet. *Astronomical Journal*, 157(5):192, 2019. URL `http://arxiv.org/abs/1903.01591`.

D. J. Christian, N. P. Gibson, E. K. Simpson, R. a. Street, I. Skillen, D. Pollacco, A. Collier Cameron, Y. C. Joshi, F. P. Keenan, H. C. Stempels, C. a. Haswell, K. Horne, D. R. Anderson, S. Bentley, F. Bouchy, W. I. Clarkson, B. Enoch, L. Hebb, G. Hébrard, C. Hellier, J. Irwin, S. R. Kane, T. a. Lister, B. Loeillet, P. Maxted, M. Mayor, I. McDonald, C. Moutou, a. J. Norton, N. Parley, F. Pont, D. Queloz, R. Ryans, B. Smalley, a. M. S. Smith, I. Todd, S. Udry, R. G. West, P. J. Wheatley, and D. M. Wilson. WASP-10b: A 3M J, gas-giant planet transiting a late-type K star. *Monthly Notices of the Royal Astronomical Society*, 392:1585–1590, 2009. ISSN 00358711. doi: 10.1111/j.1365-2966.2008.14164.x.

S. Ciceri, L. Mancini, J. Southworth, I. Bruni, N. Nikolov, G. D'Ago, T. Schröder, V. Bozza, J. Tregloan-Reed, and T. Henning. Physical properties of the HAT-P-23 and WASP-48 planetary systems from multi-colour photometry. *Astronomy & Astrophysics*, 577(A54), 2015. ISSN 0004-6361. doi: 10.1051/0004-6361/201425449. URL `http://www.aanda.org/10.1051/0004-6361/201425449`.

a. Claret and S. Bloemen. Gravity and limb-darkening coefficients for the Kepler , CoRoT, Spitzer , uvby , UBVRIJHK , and Sloan photometric systems. *Astronomy & Astro-*

physics, 529:A75, 2011. ISSN 0004-6361. doi: 10.1051/0004-6361/201116451. URL http://adsabs.harvard.edu/abs/2011A&A...529A..75C.

K. A. Collins, J. F. Kielkopf, and K. G. Stassun. Transit Timing Variation Measurements of WASP-12b and Qatar-1b: No Evidence for Additional Planets. *The Astronomical Journal*, 153(2), 2017a.

K. A. Collins, J. F. Kielkopf, and K. G. Stassun. AstroImageJ: Image Processing and Photometric Extraction for Ultra-Precise Astronomical Light Curves. *The Astronomical Journal*, 153(2), 2017b.

N. B. Cowan, P. MacHalek, B. Croll, L. M. Shekhtman, A. Burrows, D. Deming, T. Greene, and J. L. Hora. Thermal phase variations of WASP-12b: Defying predictions. *Astrophysical Journal*, 747(1), 2012. ISSN 15384357. doi: 10.1088/0004-637X/747/1/82.

B. Croll, D. Lafreniere, L. Albert, R. Jayawardhana, J. J. Fortney, and N. Murray. Near-infrared thermal emission from wasp-12b: Detections of the secondary eclipse in Ks, H, and J. *Astronomical Journal*, 141(2), 2011. ISSN 00046256. doi: 10.1088/0004-6256/141/2/30.

R. Cutri. VizieR Online Data Catalog: AllWISE Data Release. *VizieR Online Data Catalog: AllWISE Data Releas*, II/328, 2013.

F. Dai, J. N. Winn, P. Arriagada, R. P. Butler, J. D. Crane, J. A. Johnson, S. A. Shectman, J. K. Teske, I. B. Thompson, A. Vanderburg, and R. A. Wittenmyer. Doppler Monitoring of the Wasp-47 Multiplanet System. *The Astrophysical Journal*, 813(1):L9, 2015. ISSN 2041-8213. doi: 10.1088/2041-8205/813/1/L9. URL http://stacks.iop.org/2041-8205/813/i=1/a=L9?key=crossref.4ff04386ebc5999f7e4a30bb111198dc.

K. M. Deck and E. Agol. Transit timing variations for planets near eccentricity-type mean motion resonances. *The Astrophysical Journal*, 821(2), 2016. URL http://arxiv.org/abs/1509.08460.

K. M. Deck, E. Agol, M. J. Holman, and D. Nesvorny. TTVFast: An efficient and accurate code for transit timing inversion problems. *The Astrophysical Journal*, 787 (2), 2014. ISSN 0004-637X. doi: 10.1088/0004-637X/787/2/132. URL http://arxiv.org/abs/1403.1895http://dx.doi.org/10.1088/0004-637X/787/2/132http://arxiv.org/abs/1403.1895%0Ahttp://dx.doi.org/10.1088/0004-637X/787/2/132.

H. J. Deeg and B. Tingley. TEE, a simple estimator for the precision of eclipse and transit minimum times. *Astronomy & Astrophysics*, 599(A93):1–7, 2017. ISSN 14320746. doi: 10.1051/0004-6361/201629350. URL http://arxiv.org/abs/1612.02237%0Ahttp://dx.doi.org/10.1051/0004-6361/201629350.

J. Eastman, B. S. Gaudi, and E. Agol. EXOFAST: A fast exoplanetary fitting suite in IDL. *Publications of the Astronomical Society of the Pacific*, 125(923):83–112, 2013. ISSN 00046280. doi: 10.1086/669497. URL http://adsabs.harvard.edu/cgi-bin/nph-data_query?bibcode=2012arXiv1206.5798E&link_type=ABSTRACT%5Cnpapers://ada43e77-f677-4abf-a73e-6493805a76d2/Paper/p23857.

J. D. Eastman, J. E. Rodriguez, E. Agol, K. G. Stassun, T. G. Beatty, A. Vanderburg, B. S. Gaudi, K. A. Collins, and R. Luger. EXOFASTv2: A public, generalized, publication-quality exoplanet modeling code. *arXiv preprint arXiv:1907.09480*, 2019. URL http://arxiv.org/abs/1907.09480.

M. T. Eibe, L. Cuesta, A. Ullán, A. Pérez-Verde, and J. Navas. Analysis of variations in transit time and transit duration in WASP-3. Evidence of secular perturbations reconsidered. *Monthly Notices of the Royal Astronomical Society*, 423:1381–1389, 2012. ISSN 00358711. doi: 10.1111/j.1365-2966.2012.20962.x.

N. Espinoza, B. V. Rackham, A. Jordán, D. Apai, M. López-Morales, D. J. Osip, S. L. Grimm, J. Hoeijmakers, P. A. Wilson, A. Bixel, C. McGruder, F. Rodler, I. Weaver, N. K. Lewis, J. J. Fortney, and J. Fraine. Access: A featureless optical transmission spectrum for WASP-19b from Magellan/IMACS. *Monthly Notices of the Royal Astronomical Society*, 482(2):2065–2087, 2019. ISSN 13652966. doi: 10.1093/mnras/sty2691.

D. C. Fabrycky and S. Tremaine. Shrinking Binary and Planetary Orbits by Kozai Cycles with Tidal Friction. *The Astrophysical Journal*, 669:1298, 2007. ISSN 1538-4357. doi: 10.1086/521702. URL http://adsabs.harvard.edu/cgi-bin/nph-data_query?bibcode=2007ApJ...669.1298F&link_type=ABSTRACT%5Cnpapers://0be24a46-325a-4116-a3c6-fd8a3b614472/Paper/p9420.

D. C. Fabrycky, J. J. Lissauer, D. Ragozzine, J. F. Rowe, J. H. Steffen, E. Agol, T. Barclay, N. Batalha, W. Borucki, D. R. Ciardi, E. B. Ford, T. N. Gautier, J. C. Geary, M. J. Holman, J. M. Jenkins, J. Li, R. C. Morehead, R. L. Morris, A. Shporer, J. C. Smith, M. Still, and J. Van Cleve. Architecture of Kepler 'S Multi-Transiting Systems. Ii. New Investigations With Twice As Many Candidates. *The Astrophysical Journal*, 790(2):146, 2014. ISSN 0004-637X. doi: 10.1088/0004-637X/790/2/146. URL http://ads.nao.ac.jp/abs/2014ApJ...790..146F.

E. B. Ford. Architectures of planetary systems and implications for their formation. *Proceedings of the National Academy of Sciences of the United States of America*, 111(35):12616–21, 9 2014. ISSN 1091-6490. doi: 10.1073/pnas.

1304219111. URL http://www.pubmedcentral.nih.gov/articlerender.fcgi?artid=4156699&tool=pmcentrez&rendertype=abstract.

J. J. Fortney, M. S. Marley, and J. W. Barnes. Planetary Radii across Five Orders of Magnitude in Mass and Stellar Insolation: Application to Transits. *The Astrophysical Journal*, 659(2):1661–1672, 2007. ISSN 0004-637X. doi: 10.1086/512120.

L. Fossati, S. Bagnulo, A. Elmasli, C. A. Haswell, S. Holmes, O. Kochukhov, E. L. Shkolnik, D. V. Shulyak, D. Bohlender, B. Albayrak, C. Froning, and L. Hebb. A detailed spectropolarimetric analysis of the planet-hosting star WASP-12. *Astrophysical Journal*, 720 (1):872–886, 2010. ISSN 15384357. doi: 10.1088/0004-637X/720/1/872.

B. J. Fulton, A. Shporer, J. N. Winn, M. J. Holman, A. Pál, and J. Zachary Gazak. LONG-TERM TRANSIT TIMING MONITORING AND REFINED LIGHT CURVE PARAMETERS OF HAT-P-13b. *The Astronomical Journal*, 142(3):84, 2011. ISSN 0004-6256. doi: 10.1088/0004-6256/142/3/84. URL http://stacks.iop.org/1538-3881/142/i=3/a=84?key=crossref.f8cc879018b2910b99568da2ecb96dd0.

Gaia_Collaboration. Special Issue Gaia Early Data Release 3. *Astronomy & Astrophysics*, 649(A1):1–20, 2021.

E. García-Melendo, M. López-Morales, E. Garcia-Melendo, and M. Lopez-Morales. Potential biases in the detection of planetary systems with large transit timing variations. *Monthly Notices of the Royal Astronomical Society Letters*, 20:no–no, 2011. ISSN 17453925. doi: 10.1111/j.1745-3933.2011.01111.x. URL http://doi.wiley.com/10.1111/j.1745-3933.2011.01111.x.

M. Gillion, A. Triaud, B.-O. Demory, E. Jehin, E. Agol, NASA, University of Bern, and STAR Institute. Seven temperate terrestrial planets around the nearby ultracool dwarf star TRAPPIST-1. *NATURE*, 452:456–460, 2017. doi: 10.1038/nature21360. URL https://www.ncbi.nlm.nih.gov/labs/articles/28230125/.

P. Goldreich and S. Soter. Q in the solar system. *Icarus*, 5(1-6):375–389, 1966. ISSN 10902643. doi: 10.1016/0019-1035(66)90051-0.

S. Hadden and Y. Lithwick. Numerical and Analytical Modelling of Transit Time Variations. *The Astrophysical Journal*, 828(1), 2016. URL http://arxiv.org/abs/1510.02476.

J. H. Hamer and K. C. Schlaufman. Hot Jupiters are Destroyed by Tides While Their Host Stars are on the Main Sequence. *The Astronomical Journal*, 158(5):190–198, 2019. ISSN 1538-3881. doi: 10.3847/1538-3881/ab3c56. URL http://arxiv.org/abs/1908.06998.

C. A. Haswell. *Transiting Exoplanets*. Cambridge University Press in association with THE OPEN UNIVERSITY, 2010. ISBN 9780521133203.

C. A. Haswell. WASP-12b: A Mass-Losing Extremely Hot Jupiter. *Handbook of Exoplanets*, pages 2585–2602, 2018. doi: 10.1007/978-3-319-55333-7{_}97.

C. A. Haswell, L. Fossati, T. Ayres, K. France, C. S. Froning, S. Holmes, U. C. Kolb, R. Busuttil, R. A. Street, L. Hebb, A. C. Cameron, B. Enoch, V. Burwitz, J. Rodriguez, R. G. West, D. Pollacco, P. J. Wheatley, and A. Carter. Near-Ultraviolet Absorption, Chromospheric Activity, and Star-Planet Interactions in the Wasp-12 System. *The Astrophysical Journal*, 760(1):79, 2012. ISSN 0004-637X. doi: 10.1088/0004-637X/760/1/79.

D. H. Hathaway. The solar cycle. *Living Reviews in Solar Physics*, 12(1), 2015. ISSN 16144961. doi: 10.1007/lrsp-2015-4.

L. Hebb, A. Collier-Cameron, B. Loeillet, D. Pollacco, G. Hébrard, R. a. Street, F. Bouchy, H. C. Stempels, C. Moutou, E. Simpson, S. Udry, Y. C. Yoshi, R. G. West, I. Skillen, D. M. Wilson, I. McDonald, N. P. Gibson, and t. S. Consortium. WASP-12b: The hottest transiting planet yet discovered. *The Astrophysical Journal*, 693(2):1920–1928, 2009. ISSN 0004-637X. doi: 10.1088/0004-637X/693/2/1920. URL `http://arxiv.org/abs/0812.3240`.

G. Hébrard, A. Collier Cameron, D. J. A. Brown, R. F. Díaz, F. Faedi, B. Smalley, D. R. Anderson, D. Armstrong, S. C. C. Barros, J. Bento, F. Bouchy, A. P. Doyle, B. Enoch, Y. Gomez Maqueo Chew, E. M. Hebrard, C. Hellier, M. Lendl, T. A. Lister, P. F. L. Maxted, J. McCormac, C. Moutou, D. Pollacco, D. Queloz, A. Santerne, I. Skillen, J. Southworth, J. Tregloan-Reed, A. H. M. J. Triaud, S. Udry, M. Vanhuysse, C. A. Watson, R. G. West, and P. J. Wheatley. WASP-52b, WASP-58b, WASP-59b, and WASP-60b: Four new transiting close-in giant planets. *Astronomy & Astrophysics*, 549:A134, 2013. ISSN 0004-6361. doi: 10.1051/0004-6361/201220363. URL `http://www.aanda.org/10.1051/0004-6361/201220363`.

G. Hebrard, R. Diaz, A. Correia, A. Collier Cameron, J. Laskar, D. Pollacco, and al. Discovery and characterization of the exoplanets WASP-148b and c. A transiting system with two interacting giant planets. *Astronomy & Astrophysics*, 2020. ISSN 0004-6361. doi: 10.1051/0004-6361/202038296.

A. Henden. APASS DR10. *JAVSO*, 47(1), 2019.

E. Herrero, I. Ribas, C. Jordi, J. C. Morales, and A. F. Lanza. Modelling the photosphere of active stars. *Highlights in Spanish Astrophysics*, VII(July 9-13):699–707, 2012.

T. C. Hinse, W. Han, J.-n. Yoon, and S. R. Mar. Photometric defocus observations of transiting extrasolar planets. *Journal of Astronomy ans Space Sciences*, 32(1):1–12, 2015. doi: http://dx.doi.org/10.5140/JASS.2015.32.1.21.

T. Hirano, N. Narita, E. Sato, Y. H. Takahashi, K. Masuda, Y. Takeda, W. Aoki, M. Tamura, and Y. Suto. PLANET–PLANET ECLIPSE AND THE ROSSITER–McLAUGHLIN EFFECT OF A MULTIPLE TRANSITING SYSTEM: JOINT ANALYSIS OF THE SUBARU SPECTROSCOPY AND THE KEPLER PHOTOMETRY. *The Astrophysical Journal Letters*, 759:36–5, 2012. ISSN 2041-8205. doi: 10.1088/2041-8205/759/2/L36.

E. Høg, C. Fabricius, V. V. Makarov, S. Urban, T. Corbin, G. Wycoff, U. Bastian, P. Schwekendick, and A. Wicenec. The Tycho-2 Catalogue of the 2.5 million brightest stars. *Astronomy and Astrophysics*, 363(1):27–30, 2000. ISSN 00046361.

T. Holczer, T. Mazeh, G. Nachmani, D. Jontof-Hutter, E. B. Ford, D. Fabrycky, D. Ragozzine, M. Kane, and J. H. Steffen. Transit Timing Observations from Kepler. IX. Catalog of the Full Long-Cadence Data Set. *The Astrophysical Journal Supplement Series*, 225(1), 2016. URL `http://arxiv.org/abs/1606.01744`.

M. J. Hooton, E. J. De Mooij, C. A. Watson, N. P. Gibson, F. J. Galindo-Guil, R. Clavero, and S. R. Merritt. Storms or systematics the changing secondary eclipse depth of WASP-12b. *Monthly Notices of the Royal Astronomical Society*, 486(2):2397–2406, 2019. ISSN 13652966. doi: 10.1093/mnras/stz966.

S. Hoyer, E. Pallé, D. Dragomir, and F. Murgas. Ruling Out the Orbital Decay of the Wasp-43B Exoplanet. *The Astronomical Journal*, 151(6):137, 2016. ISSN 1538-3881. doi: 10.3847/0004-6256/151/6/137. URL `http://stacks.iop.org/1538-3881/151/i=6/a=137?key=crossref.0ca20778df25db88df65c08cbfa50804`.

C. Huang, Y. Wu, and A. H. M. J. Triaud. Warm Jupiters Are Less Lonely Than Hot Jupiters: Close Neighbors. *The Astrophysical Journal*, 825(2):98, 2016. ISSN 1538-4357. doi: 10.3847/0004-637X/825/2/98. URL `http://stacks.iop.org/0004-637X/825/i=2/a=98?key=crossref.d35c4d2422977bef07e354ad7a23a97e`.

N. Husnoo, F. Pont, G. Hébrard, E. Simpson, T. Mazeh, F. Bouchy, C. Moutou, L. Arnold, I. Boisse, R. F. Díaz, A. Eggenberger, and A. Shporer. Orbital eccentricity of WASP-12 and WASP-14 from new radial velocity monitoring with SOPHIE. *Monthly Notices of the Royal Astronomical Society*, 413(4):2500–2508, 2011. ISSN 00358711. doi: 10.1111/j.1365-2966.2011.18322.x.

N. Husnoo, F. Pont, T. Mazeh, D. Fabrycky, G. Hébrard, F. Bouchy, and A. Shporer. Observational constraints on tidal effects using orbital eccentricities. *Monthly Notices of the Royal Astronomical Society*, 422(4):3151–3177, 2012. ISSN 00358711. doi: 10.1111/j.1365-2966.2012.20839.x.

P. Ioannidis, K. F. Huber, and J. H. M. M. Schmitt. How do starspots influence the transit timing variations of exoplanets? Simulations of individual and consecutive transits. *Astronomy & Aastrophysics*, 585:A72, 2016. URL http://arxiv.org/abs/1510.03276.

S. L. Jackson, U. C. Kolb, and S. F. Green. Asteroid Photometry with PIRATE: Optimisations and Techniques for Small Aperture Telescopes. *In preparation*, 2021.

A. G. Jensen, P. W. Cauley, S. Redfield, W. D. Cochran, and M. Endl. HYDROGEN AND SODIUM ABSORPTION IN THE OPTICAL TRANSMISSION SPECTRUM OF WASP-12b. *The Astronomical Journal*, 156(4), 2018.

I.-G. Jiang, C.-Y. Lai, A. Savushkin, D. Mkrtichian, K. Antonyuk, E. Griv, H.-F. Hsieh, and L.-C. Yeh. The Possible Orbital Decay and Transit Timing Variations of the Planet WASP-43b. *The Astronomical Journal*, 151(1), 2016. URL http://arxiv.org/abs/1511.00768.

D. Jontof-Hutter, E. B. Ford, J. F. Rowe, J. J. Lissauer, D. C. Fabrycky, C. Van Laerhoven, E. Agol, K. M. Deck, T. Holczer, and T. Mazeh. Robust TTV Mass Measurements: Ten Kepler Exoplanets between 3 and 8 Earth Masses with Diverse Densities and Incident Fluxes. *The Astrophysical Journal*, 830(39):39, 2016. ISSN 1538-4357. doi: 10.3847/0004-637X/820/1/39. URL http://arxiv.org/abs/1512.02003.

I. G. Juvan, M. Lendl, P. E. Cubillos, L. Fossati, H. Lammer, E. W. Guenther, and A. Hanslmeier. PyTranSpot: A tool for multiband light curve modeling of planetary transits and stellar spots. *Astronomy & Astrophysics*, 15:1–17, 2018.

C. Karoff, T. S. Metcalfe, W. J. Chaplin, Y. Elsworth, H. Kjeldsen, T. Arentoft, and D. Buzasi. Sounding stellar cycles with Kepler - I. Strategy for selecting targets. *Monthly Notices of the Royal Astronomical Society*, 399(2):914–923, 2009. ISSN 00358711. doi: 10.1111/j.1365-2966.2009.15323.x.

D. M. Kipping. The Transits of Extrasolar Planets with Moons. *PHD Thesis*, 2011. doi: 10.1007/978-3-642-22269-6. URL http://books.google.com/books?hl=en&lr=&id=qXVi-zJ__7cC&oi=fnd&pg=PR9&dq=The+Transits+of+Extrasolar+Planets+with+Moons&ots=EF8jcqlx-N&sig=YKOKWG8vl9j8ROIPaqsgaFCAMOghttp://books.google.com/books?hl=en&lr=&id=qXVi-zJ__7cC&oi=fnd&pg=PR9&dq=The+transits+of+.

D. M. Kipping. In Search of Exomoons. *Frank N. Bash Symposium 2013: New Horizons in Astronomy (BASH 2013)*, page 18, 2013. URL `http://arxiv.org/abs/1405.1455`.

J. Kirk, P. J. Wheatley, T. Louden, S. P. Littlefair, C. M. Copperwheat, D. J. Armstrong, T. R. Marsh, and V. S. Dhillon. Transmission spectroscopy of the inflated exoplanet WASP-52b, and evidence for a bright region on the stellar surface. *Monthly Notices of the Royal Astronomical Society*, 463(3):2922–2931, 2016. ISSN 13652966. doi: 10.1093/mnras/stw2205.

H. A. Knutson, D. Charbonneau, R. W. Noyes, T. M. Brown, and R. L. Gilliland. Using Stellar Limb-Darkening to Refine the Properties of HD 209458b. *The Astrophysical Journal*, 655(1):564–575, 2007. ISSN 0004-637X. doi: 10.1086/510111.

H. a. Knutson, B. J. Fulton, B. T. Montet, M. Kao, H. Ngo, W. Andrew, K. Batygin, J. A. Johnson, J. R. Crepp, S. Hinkley, A. Gaspar, T. D. Morton, P. S. Muirhead, A. W. Howard, J. R. Crepp, S. Hinkley, G. A. Bakos, K. Batygin, J. A. Johnson, T. D. Morton, and P. S. Muirhead. Friends of hot jupiters i: a radial velocity search for massive, long-period companions to close-in gas giant planets. *ASTROPHYSICAL JOURNAL*, 785(2):126–148, 2014. ISSN 0004-637X. doi: 10.1088/0004-637X/785/2/126.

A. Kokori, A. Tsiaras, B. Edwards, M. Rocchetto, G. Tinetti, A. Wünsche, N. Paschalis, V. K. Agnihotri, M. Bachschmidt, M. Bretton, H. Caines, M. Caló, R. Casali, M. Crow, S. Dawes, M. Deldem, D. Deligeorgopoulos, R. Dymock, P. Evans, C. Falco, S. Ferratfiat, M. Fowler, S. Futcher, P. Guerra, F. Hurter, A. Jones, W. Kang, T. Kim, R. Lee, C. Lopresti, A. Marino, M. Mallonn, F. Mortari, M. Morvan, L. V. Mugnai, A. Nastasi, V. Perroud, C. Pereira, M. Phillips, P. Pintr, M. Raetz, F. Regembal, J. Savage, D. Sedita, N. Sioulas, I. Strikis, G. Thurston, A. Tomacelli, and A. Tomatis. ExoClock project: an open platform for monitoring the ephemerides of Ariel targets with contributions from the public. *Experimental Astronomy*, 2021. ISSN 15729508. doi: 10.1007/s10686-020-09696-3.

U. Kolb, M. Brodeur, N. Braithwaite, and S. Minocha. A Robotic Telescope For University-Level Distance Teaching. *RTSRE Proceedings*, 1(1):127–136, 2018. URL `http://adsabs.harvard.edu/abs/2018RTSRE...1..127K`.

V. Kornilov, M. Sarazin, A. Tokovinin, T. Travouillon, and O. Voziakova. Comparison of the scintillation noise above different observatories measured with MASS instruments. *Astronomy and Astrophysics*, 546(A41):1–13, 2012. ISSN 00046361. doi: 10.1051/0004-6361/201219954.

Y. Kozai. Secular Perturbations of Asteroids with High Inclination and Eccentricity. *Astronomical Journal*, 67(9):591–598, 1962.

A. L. Kraus and L. A. Hillenbrand. The Stellar Populations of Praesepe and Coma Berenices. *The Astronomical Journal*, 134(6):2340–2352, 2007. ISSN 0004-6256. doi: 10.1086/522831. URL http://stacks.iop.org/1538-3881/134/i=6/a=2340.

D. Lai, C. Helling, and E. P. J. van den Heuvel. Mass Transfer, Transiting Stream, and Magnetopause in Close-in Exoplanetary Systems With Applications To Wasp-12. *The Astrophysical Journal*, 721(2):923–928, 2010. ISSN 0004-637X. doi: 10.1088/0004-637X/721/2/923. URL http://stacks.iop.org/0004-637X/721/i=2/a=923?key=crossref.f6b5fd92a65e3e9ecf2370b1828eab3b.

D. Lang, D. W. Hogg, K. Mierle, M. Blanton, and S. Roweis. Astrometry.net: Blind astrometric calibration of arbitrary astronomical images. *Astronomical Journal*, 139(5):1782–1800, 2010. ISSN 00046256. doi: 10.1088/0004-6256/139/5/1782.

B. Levrard, C. Winisdoerffer, and G. Chabrier. Falling transiting extrasolar giant planets. *Astrophysical Journal*, 692(1), 2009. ISSN 15384357. doi: 10.1088/0004-637X/692/1/L9.

S.-L. Li, N. Miller, D. N. C. Lin, and J. J. Fortney. WASP-12b as a prolate, inflated and disrupting planet from tidal dissipation. *Nature*, 463(February):1054–1056, 2010. ISSN 0028-0836. doi: 10.1038/nature08715.

M. L. Lidov. The evolution of orbits of artificial satellites of planets under the action of gravitational perturbations of external bodies. *Planetary and Space Science*, 9(10):719–759, 1962. ISSN 00320633. doi: 10.1016/0032-0633(62)90129-0.

J. Lillo-Box, D. Barrado, and A. C. M. Correia. Close-in planets around giant stars. Lack of hot-Jupiters and prevalence of multi-planetary systems. *Astronomy & Astrophysics*, 589 (A124), 2016. ISSN 0004-6361. doi: 10.1051/0004-6361/201527683. URL http://arxiv.org/abs/1603.09719.

D. N. C. Lin, P. H. Bodenheimer, and D. C. Richardson. Orbital migration of the planetary companion of 51 Pegasi to its present location, 1996. ISSN 1476-4687. URL http://adsabs.harvard.edu/cgi-bin/nph-data_query?bibcode=1996Natur.380..606L&link_type=ABSTRACT%5Cnpapers://0be24a46-325a-4116-a3c6-fd8a3b614472/Paper/p6202.

Y. Lithwick, J. Xie, and Y. Wu. Extracting Planet Mass and Eccentricity From Ttv Data. *The Astrophysical Journal*, 761(2):122, 2012. ISSN 0004-637X. doi: 10.1088/0004-637X/

761/2/122. URL http://stacks.iop.org/0004-637X/761/i=2/a=122?key=crossref.71ade8fc1fd6ef7aabcd47995e424736.

J. Llama, K. Wood, M. Jardine, A. A. Vidotto, C. Helling, L. Fossati, and C. A. Haswell. The shocking transit of WASP-12b: Modelling the observed early ingress in the near-ultraviolet. *Monthly Notices of the Royal Astronomical Society: Letters*, 416(1):1–4, 2011. ISSN 17453933. doi: 10.1111/j.1745-3933.2011.01093.x.

J. Llama, A. A. Vidotto, M. Jardine, K. Wood, R. Fares, and T. I. Gombosi. Exoplanet transit variability: Bow shocks and winds around HD 189733b. *Monthly Notices of the Royal Astronomical Society*, 436(3):2179–2187, 2013. ISSN 00358711. doi: 10.1093/mnras/stt1725.

T. Louden, P. J. Wheatley, P. G. Irwin, J. Kirk, and I. Skillen. A precise optical transmission spectrum of the inflated exoplanet WASP-52b. *Monthly Notices of the Royal Astronomical Society*, 470(1):742–754, 2017. ISSN 13652966. doi: 10.1093/mnras/stx984.

C. Lovis, X. Dumusque, N. C. Santos, F. Bouchy, M. Mayor, F. Pepe, D. Queloz, D. Ségransan, S. Udry, and W. Benz. The HARPS search for southern extra-solar planets. XXXI. Magnetic activity cycles in solar-type stars: statistics and impact on precise radial velocities. *Astronomy & Astrophysics*, 534(Harvey 1985):A58, 2011. ISSN 0004-6361. doi: 10.1051/0004-6361/201117055. URL http://arxiv.org/abs/1107.5325v1%5Cnpapers2://publication/uuid/FC27F4BF-61A3-4F1A-A335-74E897BE3511%5Cnhttp://adsabs.harvard.edu/cgi-bin/nph-data_query?bibcode=2011A&A...534A..58P&link_type=ABSTRACT%5Cnpapers2://publication/doi/10.1051/0004-6361/201117055.

L. B. Lucy and M. A. Sweeney. Spectroscopic binaries with circular orbits. *Astronomical Journal*, 76(6):544–556, 1971.

R. Luger, M. Sestovic, E. Kruse, S. L. Grimm, B.-O. Demory, E. Agol, E. Bolmont, D. Fabrycky, C. S. Fernandes, V. Van Grootel, A. Burgasser, M. Gillon, J. G. Ingalls, E. Jehin, S. N. Raymond, F. Selsis, A. H. M. J. Triaud, T. Barclay, G. Barentsen, S. B. Howell, L. Delrez, J. de Wit, D. Foreman-Mackey, D. L. Holdsworth, J. Leconte, S. Lederer, M. Turbet, Y. Almleaky, Z. Benkhaldoun, P. Magain, B. M. Morris, K. Heng, and D. Queloz. A seven-planet resonant chain in TRAPPIST-1. *Nature Astronomy*, 1(May):0129, 2017. ISSN 2397-3366. doi: 10.1038/s41550-017-0129. URL http://www.nature.com/articles/s41550-017-0129.

G. Maciejewski, D. Dimitrov, R. Neuhäuser, A. Niedzielski, S. Raetz, C. Ginski, C. Adam, C. Marka, M. Moualla, and M. Mugrauer. Transit timing variation in exoplanet WASP-

3b. *Monthly Notices of the Royal Astronomical Society*, 407(June):2625–2631, 2010. ISSN 00358711. doi: 10.1111/j.1365-2966.2010.17099.x. URL http://mnras.oxfordjournals.org/content/407/4/2625.short.

G. Maciejewski, D. Dimitrov, R. Neuhäuser, N. Tetzlaff, A. Niedzielski, St. Raetz, W. P. Chen, F. Walter, C. Marka, S. Baar, T. Krejcová, J. Budaj, V. Krushevska, K. Tachihara, H. Takahashi, and M. Mugrauer. Transit timing variation and activity in the WASP-10 planetary system, 2011a. ISSN 00358711. URL http://arxiv.org/pdf/1009.4567v1.pdf.

G. Maciejewski, R. Errmann, S. Raetz, M. Seeliger, I. Spaleniak, and R. Neuhaeuser. High-precision photometry of WASP-12 b transits. *ASTRONOMY & ASTROPHYSICS*, 65:5, 2011b. ISSN 0004-6361. doi: 10.1051/0004-6361/201016268. URL http://arxiv.org/abs/1102.2421.

G. Maciejewski, D. Dimitrov, M. Seeliger, S. Raetz, L. Bukowiecki, M. Kitze, R. Errmann, G. Nowak, A. Niedzielski, V. Popov, C. Marka, K. Goździewski, R. Neuhäuser, J. Ohlert, T. C. Hinse, J. W. Lee, C.-U. Lee, J.-N. Yoon, A. Berndt, H. Gilbert, C. Ginski, M. M. Hohle, M. Mugrauer, T. Röll, T. O. B. Schmidt, N. Tetzlaff, L. Mancini, J. Southworth, M. Dall'Ora, S. Ciceri, R. Zambelli, G. Corfini, H. Takahashi, K. Tachihara, J. M. Benkő, K. Sárneczky, G. M. Szabo, T. N. Varga, M. Vaňko, Y. C. Joshi, and W. P. Chen. Multi-site campaign for transit timing variations of WASP-12 b: possible detection of a long-period signal of planetary origin. *Astronomy & Astrophysics*, 551:A108, 2013a. ISSN 0004-6361. doi: 10.1051/0004-6361/201220739. URL http://www.aanda.org/10.1051/0004-6361/201220739.

G. Maciejewski, A. Niedzielski, A. Wolszczan, G. Nowak, R. Neuhäuser, J. N. Winn, B. Deka, M. Adamów, M. Górecka, M. Fernández, F. J. Aceituno, J. Ohlert, R. Errmann, M. Seeliger, D. Dimitrov, D. W. Latham, G. a. Esquerdo, L. McKnight, M. J. Holman, E. L. N. Jensen, U. Kramm, T. Pribulla, S. Raetz, T. O. B. Schmidt, C. Ginski, S. Mottola, S. Hellmich, C. Adam, H. Gilbert, M. Mugrauer, G. Saral, V. Popov, and M. Raetz. Constraints on a Second Planet in the Wasp-3 System. *The Astronomical Journal*, 146:147, 2013b. ISSN 0004-6256. doi: 10.1088/0004-6256/146/6/147. URL http://iopscience.iop.org/1538-3881/146/6/147/article/.

G. Maciejewski, D. Dimitrov, M. Fernandez, A. Sota, G. Nowak, J. Ohlert, G. Nikolov, L. Bukowiecki, T. C. Hinse, E. Palle, B. Tingley, D. Kjurkchieva, J. W. Lee, and C.-U. Lee. Departure From The Constant-Period Ephemeris For The Transiting Exoplanet WASP-

12b. *Astronomy & Astrophysics Letters*, 588(L6):1–6, 2016. doi: 10.1051/0004-6361/201628312. URL http://arxiv.org/pdf/1602.09055v1.pdf.

G. Maciejewski, M. Fernández, F. Aceituno, S. Martín-Ruiz, J. Ohlert, D. Dimitrov, K. Szyszka, C. VonEssen, M. Mugrauer, R. Bischoff, K. U. Michel, M. Mallonn, M. Stangret, and D. Moździerski. Planet-star interactions with precise transit timing. I. The refined orbital decay rate for WASP-12 b and initial constraints for HAT-P-23 b, KELT-1 b, KELT-16 b, WASP-33 b, and WASP-103 b. *Acta Astronomica*, 68(4):371–401, 2018. doi: 10.32023/0001-5237/68.4.4. URL http://arxiv.org/abs/1812.02438.

G. Maciejewski, A. Niedzielski, E. Villaver, M. Konacki, and R. K. Pawlaszek. An apparently eccentric orbit of the exoplanet WASP-12 b as a radial velocity signature of planetary-induced tides in the host star. *The Astrophysical Journal*, 889(1):54, 2020. doi: 10.3847/1538-4357/ab5e87. URL http://arxiv.org/abs/1912.01360.

L. Mancini, J. Southworth, G. Raia, J. Tregloan-Reed, P. Mollière, V. Bozza, M. Bretton, I. Bruni, S. Ciceri, G. D'Ago, M. Dominik, T. C. Hinse, M. Hundertmark, U. G. Jørgensen, H. Korhonen, M. Rabus, S. Rahvar, D. Starkey, S. Calchi Novati, R. Figuera Jaimes, T. Henning, D. Juncher, T. Haugbølle, N. Kains, A. Popovas, R. W. Schmidt, J. Skottfelt, C. Snodgrass, J. Surdej, and O. Wertz. Orbital alignment and star-spot properties in the WASP-52 planetary system. *Monthly Notices of the Royal Astronomical Society*, 465(1):843–857, 2017. ISSN 13652966. doi: 10.1093/mnras/stw1987.

K. Mandel and E. Agol. Analytic light curves for planetary transit searches. *The Astrophysical Journal Letters*, 2002. URL http://iopscience.iop.org/1538-4357/580/2/L171.

P. F. Maxted, A. M. Serenelli, and J. Southworth. Comparison of gyrochronological and isochronal age estimates for transiting exoplanet host stars. *Astronomy and Astrophysics*, 577:1–11, 2015. ISSN 14320746. doi: 10.1051/0004-6361/201525774.

M. Mayor and D. Queloz. A Jupiter-mass companion to a solar-type star. *Nature*, 378:355–359, 1995. ISSN 0028-0836. doi: 10.1038/378355a0.

T. Mazeh, G. Nachmani, T. Holczer, D. C. Fabrycky, E. B. Ford, R. Sanchis-Ojeda, G. Sokol, J. F. Rowe, S. Zucker, E. Agol, J. A. Carter, J. J. Lissauer, E. V. Quintana, D. Ragozzine, J. H. Steffen, and W. Welsh. TRANSIT TIMING OBSERVATIONS FROM KEPLER . VIII. CATALOG OF TRANSIT TIMING MEASUREMENTS OF THE FIRST TWELVE QUARTERS. *The Astrophysical Journal Supplement Series*, 208(2):16, 2013. ISSN 0067-0049. doi: 10.1088/0067-0049/208/2/16. URL http://stacks.iop.org/0067-0049/208/i=2/a=16?key=crossref.a5f885d44d3a737e622a8cc66a4cea74.

F. Middelkoop. Magnetic structure in cool stars. *Astronomy & Astrophysics*, 107:31–35, 1982.

S. Millholland, S. Wang, and G. Laughlin. on the Detection of Non-Transiting Hot Jupiters in Multiple-Planet Systems. *The Astrophysical Journal*, 823(1):L7, 2016. ISSN 2041-8213. doi: 10.3847/2041-8205/823/1/L7. URL http://stacks.iop.org/2041-8205/823/i=1/a=L7?key=crossref.12a97172ee6e3d3db3c6f07adf500f1d.

M. Montalto, J. Gregorio, G. Boué, A. Mortier, I. Boisse, M. Oshagh, M. Maturi, P. Figueira, S. Sousa, and N. C. Santos. A new analysis of the WASP-3 system: No evidence for an additional companion. *Monthly Notices of the Royal Astronomical Society*, 427:2757–2771, 2012. ISSN 00358711. doi: 10.1111/j.1365-2966.2012.21926.

C. Moutou, R. F. Díaz, S. Udry, G. Hébrard, F. Bouchy, A. Santerne, D. Ehrenreich, L. Arnold, I. Boisse, X. Bonfils, X. Delfosse, A. Eggenberger, T. Forveille, A.-M. Lagrange, C. Lovis, P. Martinez, F. Pepe, C. Perrier, D. Queloz, N. C. Santos, D. Ségransan, D. Toublanc, J. P. Troncin, M. Vanhuysse, and A. Vidal-Madjar. Spin-orbit inclinations of the exoplanetary systems HAT-P-8b, HAT-P-9b, HAT-P-16b, and HAT-P-23b. *Astronomy & Astrophysics*, 533:A113, 2011. ISSN 0004-6361. doi: 10.1051/0004-6361/201116760. URL http://www.aanda.org/10.1051/0004-6361/201116760.

S. Naoz, W. M. Farr, Y. Lithwick, F. A. Rasio, and J. Teyssandier. Hot Jupiters from secular planet-planet interactions. *Nature*, 473(7346):187–189, 2011. ISSN 0028-0836. doi: 10.1038/nature10076. URL http://dx.doi.org/10.1038/nature10076.

V. Nascimbeni, G. Piotto, L. R. Bedin, M. Damasso, L. Malavolta, and L. Borsato. TASTE. II. A new observational study of transit time variations in HAT-P-13b. *Astronomy & Aastrophysics*, 532:5, 2011. ISSN 0004-6361. doi: 10.1051/0004-6361/201116830. URL http://www.aanda.org/index.php?option=com_article&access=doi&doi=10.1051/0004-6361/201116830&Itemid=129.

V. Nascimbeni, A. Cunial, S. Murabito, P. V. Sada, A. Aparicio, G. Piotto, L. R. Bedin, a. P. Milone, A. Rosenberg, L. Borsato, M. Damasso, V. Granata, and L. Malavolta. TASTE. III. A homogeneous study of transit time variations in WASP-3b. *Astronomy & Astrophysics*, 30:10, 2012. ISSN 00046361. doi: 10.1051/0004-6361/201219601. URL http://arxiv.org/abs/1210.3045.

D. Nesvorný. Dynamical Evolution of the Early Solar System. *Annual Review of Astronomy and Astrophysics*, 56:137–174, 2018. ISSN 00664146. doi: 10.1146/annurev-astro-081817-052028.

D. Nesvorný and A. Morbidelli. Mass and Orbit Determination from Transit Timing Variations of Exoplanets. *The Astrophysical Journal*, 688:636–646, 2008. ISSN 0004-637X. doi: 10.1086/592230.

D. Nesvorny, D. Kipping, D. Terrell, J. Hartman, G. A. Bakos, and L. A. Buchhave. Koi-142, the King of Transit Variations, Is a Pair of Planets Near the 2:1 Resonance. *The Astrophysical Journal*, 777(1):3, 2013. ISSN 0004-637X. doi: 10.1088/0004-637X/777/1/3. URL http://stacks.iop.org/0004-637X/777/i=1/a=3?key=crossref.fce3e49bce2ae77779104a784d8e271c.

M. Neveu-VanMalle, D. Queloz, D. Anderson, D. Brown, A. Collier Cameron, L. Delrez, R. Diaz, M. Gillon, C. Hellier, E. Jehin, T. Lister, F. Pepe, P. Rojo, D. Ségransan, A. H. M. J. Triaud, and O. D. Turner. Hot Jupiters with relatives : discovery of additional planets in orbit around WASP-41 and WASP-47. *Astronomy & Astrophysics*, 586(A93), 2016.

E. R. Newton, J. Irwin, D. Charbonneau, Z. K. Berta-Thompson, and J. A. Dittmann. the Impact of Stellar Rotation on the Detectability of Habitable Planets Around M Dwarfs. *The Astrophysical Journal*, 821(1):L19, 2016. ISSN 2041-8213. doi: 10.3847/2041-8205/821/1/L19. URL http://stacks.iop.org/2041-8205/821/i=1/a=L19?key=crossref.0d5836e5a79602634f48ede8311416ab.

H. Ngo, H. A. Knutson, S. Hinkley, J. R. Crepp, E. B. Bechter, K. Batygin, A. W. Howard, J. A. Johnson, T. D. Morton, and P. S. Muirhead. Friends of Hot Jupiters. Ii. No Correspondence Between Hot-Jupiter Spin-Orbit Misalignment and the Incidence of Directly Imaged Stellar Companions. *The Astrophysical Journal*, 800(2):138, 2015. ISSN 1538-4357. doi: 10.1088/0004-637X/800/2/138. URL http://stacks.iop.org/0004-637X/800/i=2/a=138?key=crossref.ab38ac455dedffad91d5f83518699a4f.

H. Ngo, H. A. Knutson, S. Hinkley, M. Bryan, J. R. Crepp, K. Batygin, I. Crossfield, B. Hansen, A. W. Howard, J. A. Johnson, D. Mawet, T. D. Morton, P. S. Muirhead, and J. Wang. FRIENDS OF HOT JUPITERS. IV. STELLAR COMPANIONS BEYOND 50 au MIGHT FACILITATE GIANT PLANET FORMATION, BUT MOST ARE UNLIKELY TO CAUSE KOZAI–LIDOV MIGRATION. *The Astrophysical Journal*, 827(1):8, 2016. ISSN 1538-4357. doi: 10.3847/0004-637X/827/1/8. URL http://arxiv.org/abs/1606.07102http://stacks.iop.org/0004-637X/827/i=1/a=8?key=crossref.8fb98170bdefb0584cf6c47b8dca4cb4.

M. B. Nielsen, L. Gizon, H. Schunker, and C. Karoff. Rotation periods of 12 000 main-sequence Kepler stars: Dependence on stellar spectral type and comparison with v sin i

observations. *Astronomy & Astrophysics*, 557:L10, 2013. ISSN 0004-6361. doi: 10.1051/0004-6361/201321912. URL http://www.aanda.org/10.1051/0004-6361/201321912.

F. T. O'Donovan, D. Charbonneau, G. A. Bakos, G. Mandushev, E. W. Dunham, T. M. Brown, D. W. Latham, G. Torres, A. Sozzetti, G. Kovács, M. E. Everett, N. Baliber, M. G. Hidas, G. a. Esquerdo, M. Rabus, H. J. Deeg, J. a. Belmonte, L. a. Hillenbrand, and R. P. Stefanik. TrES-3: A Nearby, Massive, Transiting Hot Jupiter in a 31-Hour Orbit. *The Astrophysical Journal*, 663(1):37–40, 2007. ISSN 0004-637X. doi: 10.1086/519793. URL http://arxiv.org/abs/0705.2004.

J. G. O'Rourke, H. A. Knutson, M. Zhao, J. J. Fortney, A. Burrows, E. Agol, D. Deming, J. M. Désert, A. W. Howard, N. K. Lewis, A. P. Showman, and K. O. Todorov. Warm spitzer and palomar near-ir secondary eclipse photometry of two hot jupiters: Wasp-48b and hat-p-23b. *Astrophysical Journal*, 781(2), 2014. ISSN 15384357. doi: 10.1088/0004-637X/781/2/109.

J. Osborn, D. Föhring, V. S. Dhillon, and R. W. Wilson. Atmospheric scintillation in astronomical photometry. *Monthly Notices of the Royal Astronomical Society*, 452(2):1707–1716, 2015. ISSN 13652966. doi: 10.1093/mnras/stv1400.

M. Oshagh, N. C. Santos, I. Boisse, G. Boué, M. Montalto, X. Dumusque, and N. Haghighipour. Effect of stellar spots on high-precision transit light-curve. *Astronomy & Astrophysics*, 556:A19, 2013. ISSN 0004-6361. doi: 10.1051/0004-6361/201321309. URL http://arxiv.org/abs/1306.0739.

O. Öztürk and A. Erdem. New photometric analysis of five exoplanets: CoRoT-2b, HAT-P-12b, TrES-2b, WASP-12b and WASP-52b. *Monthly Notices of the Royal Astronomical Society*, 2, 2019. ISSN 0035-8711. doi: 10.1093/mnras/stz747. URL https://academic.oup.com/mnras/advance-article/doi/10.1093/mnras/stz747/5380787.

A. Pál, K. Sárneczky, G. M. Szabó, A. Szing, L. L. Kiss, G. Mező, Z. Regály, and G. Mezö. Transit timing variations in the HAT-P-13 planetary system. *Monthly Notices of the Royal Astronomical Society: Letters*, 46:5, 2011. ISSN 17453925. doi: 10.1111/j.1745-3933.2011.01029.x. URL http://arxiv.org/abs/1102.0525%5Cnhttp://doi.wiley.com/10.1111/j.1745-3933.2011.01029.x.

K. C. Patra, J. N. Winn, M. J. Holman, L. Yu, D. Deming, and F. Dai. The Apparently Decaying Orbit of WASP-12. *The Astronomical Journal*, 154(1), 2017. URL http://arxiv.org/abs/1703.06582.

K. C. Patra, J. N. Winn, M. J. Holman, M. Gillon, A. Burdanov, E. Jehin, L. Delrez, F. J. Pozuelos, K. Barkaoui, Z. Benkhaldoun, N. Narita, A. Fukui, N. Kusakabe, K. Kawauchi,

Y. Terada, L. G. Bouma, N. N. Weinberg, and M. Broome. The continuing search for evidence of tidal orbital decay of hot Jupiters. *The Astronomical Journal*, 159(4), 2020. URL http://arxiv.org/abs/2002.02606.

K. Penev, J. D. Hartman, G. A. Bakos, S. Ciceri, R. Brahm, D. Bayliss, J. Bento, A. Jordan, Z. Csubry, W. Bhatti, M. d. Val-Borro, N. Espinoza, G. Zhou, L. Mancini, M. Rabus, V. Suc, T. Henning, B. Schmidt, R. W. Noyes, J. Lazar, I. Papp, and P. Sari. Hats-18B: an Extreme Short-Period Massive Transiting Planet Spinning Up Its Star. *The Astronomical Journal*, 152(5):127, 2016. ISSN 1538-3881. doi: 10.3847/0004-6256/152/5/127. URL http://dx.doi.org/10.3847/0004-6256/152/5/127.

K. Penev, L. G. Bouma, J. N. Winn, and J. D. Hartman. Empirical Tidal Dissipation in Exoplanet Hosts From Tidal Spin-up. *The Astronomical Journal*, 155(4):165, 2018. ISSN 1538-3881. doi: 10.3847/1538-3881/aaaf71. URL http://dx.doi.org/10.3847/1538-3881/aaaf71.

M. Perryman. Resource Letter Exo-1: Exoplanets. *American Journal of Physics*, 82(6): 552–563, 2014. ISSN 0002-9505. doi: 10.1119/1.4830455. URL http://scitation.aip.org/content/aapt/journal/ajp/82/6/10.1119/1.4830455.

R. Petrucci, E. Jofr, M. Chew, T. C. Hinse, M. Maˇ, and T. Tan. Discarding orbital decay in WASP-19b after one decade of transit observations. *Monthly Notices of the Royal Astronomical Society*, 491(1):1243–1259, 2020. doi: 10.1093/mnras/stz3034. URL Decay.

S. Poddaný, L. Brát, and O. Pejcha. Exoplanet Transit Database. Reduction and processing of the photometric data of exoplanet transits. *New Astronomy*, 15(September 2009):297–301, 2010. ISSN 13841076. doi: 10.1016/j.newast.2009.09.001.

K. Poppenhaeger. Tidal effects on stellar activity. *Proceedings of the International Astronomical Union*, 12(328):308–314, 2016. ISSN 17439221. doi: 10.1017/S1743921317004045.

K. Poppenhaeger and S. J. Wolk. Indications for an influence of hot Jupiters on the rotation and activity of their host stars. *Astronomy & Astrophysics*, 565:L1, 2014. ISSN 0004-6361. doi: 10.1051/0004-6361/201423454. URL http://www.aanda.org/articles/aa/full_html/2014/05/aa23454-14/aa23454-14.html.

A. M. Price-Whelan, B. M. Sipocz, H. M. Gunther, and P. L. Lim. The Astropy Project: Building an Open-science Project and Status of the v2.0 Core Package. *The Astronomical Journal*, 156(3):123, 2018. ISSN 0004-6256. doi: 10.3847/1538-3881/aabc4f.

G. Privitera. Star-planet interactions II. *Astronomy & Aastrophysics*, 593(A128), 2019. doi: 10.1051/0004-6361/201628758.

G. Privitera, G. Meynet, P. Eggenberger, A. A. Vidotto, E. Villaver, and M. Bianda. Star-planet interactions: I. Stellar rotation and planetary orbits. *Astronomy & Astrophysics*, pages 1–14, 2016. URL `http://arxiv.org/abs/1604.06005`.

D. Ragozzine and M. J. Holman. The Value of Systems with Multiple Transiting Planets. *Bulletin of the American Astronomical Society*, 41:929, 2010. URL `http://arxiv.org/abs/1006.3727`.

D. Ragozzine and A. S. Wolf. Probing the Interiors of Very Hot Jupiters Using Transit Light Curves. *The Astrophysical Journal*, 698(2):1778–1794, 2009. ISSN 0004-637X. doi: 10.1088/0004-637X/698/2/1778.

F. G. Ramon-Fox and P. V. Sada. Parameters of recent transits of HAT-P-23b. *Revista Mexicana de Astronomia y Astrofisica*, 49(1):71–77, 2013. ISSN 01851101.

S. N. Raymond, A. M. Mandell, and S. Sigurdsson. Exotic Earths Forming Habitable Worlds-Giant Planet.pdf. *Science*, 313(5792):1413–1416, 2006.

W. K. M. Rice, J. Veljanoski, and a. C. Cameron. Tidal evolution of close-in giant planets: Evidence of type II migration? *Monthly Notices of the Royal Astronomical Society*, 425: 2567–2575, 2012. ISSN 00358711. doi: 10.1111/j.1365-2966.2012.21728.x.

T. P. Robitaille, E. J. Tollerud, and P. Greenfield. Astropy: A community Python package for astronomy. *Astronomy and Astrophysics*, 558:1–9, 2013. ISSN 00046361. doi: 10.1051/0004-6361/201322068.

P. V. Sada and F. G. Ramón-Fox. Exoplanet Transits Registered at the Universidad de Monterrey Observatory. Part I: HAT-P-12b, HAT-P-13b, HAT-P-16b, HAT-P-23b and WASP-10b. *Publications of the Astronomical Society of the Pacific*, 128(960), 2016. ISSN 00046280. doi: 10.1088/1538-3873/128/960/024402. URL `http://arxiv.org/abs/1601.02292`.

M. Salisbury. An investigation into the precision with which exoplanet transit timing can be measured with two small telescopes . *SXP390 Project, Unpublished*, 2015.

M. A. Salisbury, U. C. Kolb, A. J. Norton, and C. A. Haswell. Monitoring of transiting exoplanets and their host stars with small aperture telescopes. *New Astronomy*, 83(April 2020):101477, 2021. ISSN 13841076. doi: 10.1016/j.newast.2020.101477. URL `https://doi.org/10.1016/j.newast.2020.101477`.

E. F. Schlafly and D. P. Finkbeiner. Measuring reddening with Sloan Digital Sky Survey

stellar spectra and recalibrating SFD. *Astrophysical Journal*, 737(2), 2011. ISSN 15384357. doi: 10.1088/0004-637X/737/2/103.

K. C. Schlaufman. Evidence of possible spin-orbit misalignment along the line of sight in transiting exoplanet systems. *Astrophysical Journal*, 719(1):602–611, 2010. ISSN 15384357. doi: 10.1088/0004-637X/719/1/602.

F. Seward and P. Charles. *Exploring the X-ray Universe*. Cambridge University Press, second edition, 2010.

I. I. Shevchenko. The Lidov-Kozai Effect - Applications in Exoplanet Research and Dynamical Astronomy. *Astrophysics and Space Science Library*, pages 139–159, 2017. ISSN 0067-0057. doi: 10.1007/978-3-319-43522-0.

M. F. Skrutskie, R. M. Cutri, R. Stiening, M. D. Weinberg, S. Schneider, J. M. Carpenter, C. Beichman, R. Capps, T. Chester, J. Elias, J. Huchra, J. Liebert, C. Lonsdale, D. G. Monet, S. Price, P. Seitzer, T. Jarrett, J. D. Kirkpatrick, J. E. Gizis, E. Howard, T. Evans, J. Fowler, L. Fullmer, R. Hurt, R. Light, E. L. Kopan, K. A. Marsh, H. L. McCallon, R. Tam, S. Van Dyk, and S. Wheelock. The Two Micron All Sky Survey (2MASS). *The Astronomical Journal*, 131(2):1163–1183, 2006. ISSN 0004-6256. doi: 10.1086/498708.

a. M. S. Smith, L. Hebb, a. Collier Cameron, D. R. Anderson, T. a. Lister, C. Hellier, D. Pollacco, D. Queloz, I. Skillen, and R. G. West. A SuperWASP search for additional transiting planets in 24 known systems. *Monthly Notices of the Royal Astronomical Society*, 398:1827–1834, 2009. ISSN 00358711. doi: 10.1111/j.1365-2966.2009.15262.x.

E. N. Sokov, I. A. Sokova, V. V. Dyachenko, D. A. Rastegaev, A. Burdanov, S. A. Rusov, P. Benni, S. Shadick, V. P. Hentunen, M. Salisbury, N. Esseiva, J. Garlitz, M. Bretton, Y. Ogmen, Y. Karavaev, A. Ayiomamitis, O. Mazurenko, D. Alonso, and S. F. Velichko. Transit timing analysis of the exoplanet TrES-5 b. Possible existence of the exoplanet TrES-5 c. *Monthly Notices of the Royal Astronomical Society*, 480(1):291–301, 2018. ISSN 13652966. doi: 10.1093/mnras/sty1615.

J. Southworth. Homogeneous studies of transiting extrasolar planets - III. Additional planets and stellar models. *Monthly Notices of the Royal Astronomical Society*, 408(3):1689–1713, 2010. ISSN 00358711. doi: 10.1111/j.1365-2966.2010.17231.x.

J. Southworth. The solar-type eclipsing binary system LL Aquarii. *Astronomy & Aastrophysics*, 557(A119):1–8, 2013. ISSN 00046361. doi: 10.1051/0004-6361/201322195.

J. Southworth. Observational studies of transiting extrasolar planets (invited review). *Invited review paper presented at Living Together: Planets, Host Stars and Binaries (Litomysl,*

Czech Republic, September 2014), pages 1–15, 11 2014. URL `http://arxiv.org/abs/1411.5517v1`.

J. Southworth and L. Mancini. Orbital obliquities of transiting planets from starspot occultations. *The 19th CambridgeWorkshop on Cool Stars, Stellar Systems, and the Sun Edited by G. A. Feiden*, 1:3–8, 2016. URL `http://arxiv.org/abs/1608.03095`.

J. Southworth, P. F. L. Maxted, and B. Smalley. Eclipsing binaries in open clusters - II. V453 Cyg in NGC 6871. *Monthly Notices of the Royal Astronomical Society*, 351(4):1277–1289, 2004. ISSN 00358711. doi: 10.1111/j.1365-2966.2004.07871.x.

J. Southworth, T. C. Hinse, M. J. Burgdorf, M. Dominik, a. Hornstrup, U. G. Jørgensen, C. Liebig, D. Ricci, C. C. Thöne, T. Anguita, V. Bozza, S. C. Novati, K. Harpsøe, L. Mancini, G. Masi, M. Mathiasen, S. Rahvar, G. Scarpetta, C. Snodgrass, J. Surdej, and M. Zub. High-precision photometry by telescope defocussing - II. the transiting planetary system WASP-4. *Monthly Notices of the Royal Astronomical Society*, 399:287–294, 2009a. ISSN 00358711. doi: 10.1111/j.1365-2966.2009.15283.x.

J. Southworth, T. C. Hinse, U. G. Jørgensen, M. Dominik, D. Ricci, M. J. Burgdorf, A. Hornstrup, P. J. Wheatley, T. Anguita, V. Bozza, S. C. Novati, K. Harpsøe, P. Kjærgaard, C. Liebig, L. Mancini, G. Masi, M. Mathiasen, S. Rahvar, G. Scarpetta, C. Snodgrass, J. Surdej, C. C. Thöne, and M. Zub. High-precision photometry by telescope defocusing - I. the transiting planetary system WASP-5. *Monthly Notices of the Royal Astronomical Society*, 396(2):1023–1031, 2009b. ISSN 00358711. doi: 10.1111/j.1365-2966.2009.14767.x.

J. Southworth, I. Bruni, L. Mancini, and J. Gregorio. Refined physical properties of the HAT-P-13 planetary system. *Monthly Notices of the Royal Astronomical Society*, 420(3): 2580–2587, 2012. ISSN 00358711. doi: 10.1111/j.1365-2966.2011.20230.x.

J. Southworth, M. Dominik, U. G. Jørgensen, M. I. Andersen, V. Bozza, M. J. Burgdorf, G. D'Ago, S. Dib, R. F. Jaimes, Y. I. Fujii, S. Gill, L. K. Haikala, T. C. Hinse, M. Hundertmark, E. Khalouei, H. Korhonen, P. Longa-Peña, L. Mancini, N. Peixinho, M. Rabus, S. Rahvar, S. Sajadian, J. Skottfelt, C. Snodgrass, P. Spyratos, J. Tregloan-Reed, E. Unda-Sanzana, and C. von Essen. Transit timing variations in the WASP-4 planetary system*. *Monthly Notices of the Royal Astronomical Society*, 490(3):4230–4236, 2019. ISSN 0035-8711. doi: 10.1093/mnras/stz2602.

J. J. Spake, D. J. Brown, A. P. Doyle, G. Hébrard, J. McCormac, D. J. Armstrong, D. Pollacco, Y. G. M. Chew, D. R. Anderson, S. C. Barros, F. Bouchy, P. Boumis, G. Bruno, A. Collier Cameron, B. Courcol, G. R. Davies, F. Faedi, C. Hellier, J. Kirk, K. W. Lam,

A. Liakos, T. Louden, P. F. Maxted, H. P. Osborn, E. Palle, J. Prieto Arranz, S. Udry, S. R. Walker, R. G. West, and P. J. Wheatley. WASP-135b: A highly irradiated, inflated hot jupiter orbiting a G5V star. *Publications of the Astronomical Society of the Pacific*, 128(960):24401, 2016. ISSN 00046280. doi: 10.1088/1538-3873/128/960/024401. URL http://dx.doi.org/10.1088/1538-3873/128/960/024401.

K. G. Stassun and G. Torres. Evidence for a Systematic Offset of 80 micro arcsec in the Gaia DR2 Parallaxes. *The Astrophysical Journal*, 862(61), 2018. doi: 10.3847/1538-4357/aacafc.

K. G. Stassun, K. A. Collins, and B. S. Gaudi. Accurate, Empirical Radii and Masses of Planets and their Host Stars with Gaia Parallaxes. *The Astronomical Journal*, 153(136), 2017. ISSN 1538-3881. doi: 10.3847/1538-3881/aa5df3. URL http://arxiv.org/abs/1609.04389%0Ahttp://dx.doi.org/10.3847/1538-3881/aa5df3.

G. Stefansson, S. Mahadevan, L. Hebb, J. Wisniewski, J. Huehnerhoff, B. Morris, S. Halverson, M. Zhao, J. Wright, J. O'rourke, H. Knutson, S. Hawley, S. Kanodia, Y. Li, L. M. Z. Hagen, L. J. Liu, T. Beatty, C. Bender, P. Robertson, J. Dembicky, C. Gray, W. Ketzeback, R. McMillan, and T. Rudyk. Towards Space-like Photometric Precision from the Ground with Beam-Shaping Diffusers. *The Astrophysical Journal*, 848(1):9, 2017. ISSN 1538-4357. doi: 10.3847/1538-4357/aa88aa. URL http://arxiv.org/abs/1710.01790%0Ahttp://dx.doi.org/10.3847/1538-4357/aa88aa.

J. H. Steffen. Sensitivity bias in the mass-radius distribution from Transit Timing Variations and Radial Velocity measurements. *Monthly Notices of the Royal Astronomical Society*, 457, 2016. URL http://arxiv.org/abs/1510.04750.

J. H. Steffen, B. S. Gaudi, E. B. Ford, E. Agol, and M. J. Holman. Detecting and Characterizing Planetary Systems with Transit Timing. *White paper submitted to the Exoplanet Task Force*, 2007. URL http://arxiv.org/abs/0704.0632.

J. H. Steffen, D. Ragozzine, D. C. Fabrycky, J. a. Carter, E. B. Ford, M. J. Holman, J. F. Rowe, W. F. Welsh, W. J. Borucki, A. P. Boss, D. R. Ciardi, and S. N. Quinn. Kepler constraints on planets near hot Jupiters. *Proceedings of the National Academy of Sciences of the United States of America*, 109(21):7982–7, 5 2012. ISSN 1091-6490. doi: 10.1073/pnas.1120970109. URL http://www.pubmedcentral.nih.gov/articlerender.fcgi?artid=3361435&tool=pmcentrez&rendertype=abstract.

J. H. Steffen, D. C. Fabrycky, E. Agol, E. B. Ford, R. C. Morehead, W. D. Cochran, J. J. Lissauer, E. R. Adams, W. J. Borucki, S. Bryson, D. a. Caldwell, A. Dupree, J. M. Jenkins, P. Robertson, J. F. Rowe, S. Seader, S. Thompson, and J. D. Twicken. Transit timing

observations from Kepler - VII. Confirmation of 27 planets in 13 multiplanet systems via transit timing variations and orbital stability. *Monthly Notices of the Royal Astronomical Society*, 428(2):1077–1087, 10 2013. ISSN 00358711. doi: 10.1093/mnras/sts090. URL http://mnras.oxfordjournals.org/cgi/doi/10.1093/mnras/sts090.

M. Swain, P. Deroo, G. Tinetti, M. Hollis, M. Tessenyi, M. Line, H. Kawahara, Y. Fujii, A. P. Showman, and S. N. Yurchenko. Probing the extreme planetary atmosphere of WASP-12b. *Icarus*, 225(1):432–445, 2013. ISSN 00191035. doi: 10.1016/j.icarus.2013.04.003. URL http://dx.doi.org/10.1016/j.icarus.2013.04.003.

J. J. Swift, J. A. Johnson, J. T. Wright, R. A. Wittenmyer, P. S. Muirhead, C. H. Blake, T. G. Beatty, S. I. Barnes, S. R. Gibson, P. Gardner, C. Robinson, D. H. Sliski, J. D. Vera, and A. Szentgyorgyi. Miniature Exoplanet Radial Velocity Array I : design , commissioning , and early photometric results Miniature Exoplanet Radial Velocity Array I : design , commissioning , and early photometric results. *Journal of Astronomical Telescopes, Instruments, and Systems*, 1(2), 2015. doi: 10.1117/1.JATIS.1.2.027002.

P. W. Sybilski, R. Pawłaszek, S. K. Kozłowski, M. Konacki, M. Ratajczak, and K. G. Hełminiak. Software for autonomous astronomical observatories: challenges and opportunities in the age of big data. *Software and Cyberinfrastructure for Astronomy III*, 9152: 91521C, 2014. doi: 10.1117/12.2055836.

G. M. Szabó, L. L. Kiss, J. M. Benkő, G. Mező, J. Nuspl, Z. Regály, K. Sárneczky, A. E. Simon, G. Leto, R. Z. Sanchez, C.-C. C. Ngeow, Z. Kővári, R. Szabó, and R. Zanmar Sanchez. HAT-P-13: a multi-site campaign to detect the transit of the second planet in the system. *Astronomy and Astrophysics*, 523:5, 2010. ISSN 0004-6361. doi: 10.1051/0004-6361/201015172. URL http://www.aanda.org/index.php?option=com_article&access=doi&doi=10.1051/0004-6361/201015172&Itemid=129.

A. Teachey and D. M. Kipping. Evidence for a large exomoon orbiting Kepler-1625b. *Science Advances*, 4(10):1–10, 2018. ISSN 23752548. doi: 10.1126/sciadv.aav1784.

G. Torres, J. Andersen, and A. Giménez. Accurate masses and radii of normal stars: Modern results and applications. *Astronomy & Astrophysics Review*, 18(1), 2010. ISSN 09354956. doi: 10.1007/s00159-009-0025-1.

A. H. Triaud. The rossiter-McLaughlin effect in exoplanet research. *Handbook of Exoplanets*, pages 1375–1401, 2018. doi: 10.1007/978-3-319-55333-7{_}2.

D. E. Trilling, W. Benz, T. Guillot, J. I. Lunine, W. B. Hubbard, and A. Burrows. Orbital Evolution and Migration of Giant Planets: Modeling Extrasolar Planets. *The*

Astrophysical Journal, 500:428, 1998. ISSN 15384357 0004637X. doi: 10.1086/305711. URL http://adsabs.harvard.edu/cgi-bin/nph-data_query?bibcode=1998ApJ...500..428T&link_type=ABSTRACT%5Cnpapers2://publication/doi/10.1086/305711.

J. D. Turner, K. A. Pearson, L. I. Biddle, B. M. Smart, R. T. Zellem, J. K. Teske, K. K. Hardegree-Ullman, C. C. Griffith, R. M. Leiter, I. T. Cates, M. N. Nieberding, C.-T. W. Smith, R. M. Thompson, R. Hofmann, M. P. Berube, C. H. Nguyen, L. C. Small, B. C. Guvenen, L. Richardson, A. McGraw, B. Raphael, B. E. Crawford, A. N. Robertson, R. Tombleson, T. M. Carleton, A. P. M. Towner, A. M. Walker-LaFollette, J. R. Hume, Z. T. Watson, C. K. Jones, M. J. Lichtenberger, S. R. Hoglund, K. L. Cook, C. A. Crossen, C. R. Jorgensen, J. M. R. A. R. Thompson, C. F. Villegas, A. A. Wilson, B. Sanford, and J. M. Taylor. Ground-based near-UV observations of 15 transiting exoplanets: Constraints on their atmospheres and no evidence for asymmetrical transits. *Monthly Notices of the Royal Astronomical Society*, 819(459):789–819, 2016. ISSN 0035-8711. doi: 10.1093/mnras/stw574. URL http://arxiv.org/abs/1603.02587.

J. D. Turner, A. Ridden-Harper, and R. Jayawardhana. Decaying Orbit of the Hot Jupiter WASP-12b: Confirmation with TESS Observations. *Astrobiology*, 161(2), 2021. URL http://arxiv.org/abs/2012.02211.

F. Valsecchi and F. A. Rasio. Planets on the edge. *Astrophysical Journal Letters*, 787(1): 2010–2015, 2014. ISSN 20418213. doi: 10.1088/2041-8205/787/1/L9.

A. H. Vaughan, G. W. Preston, and O. C. Wilson. Flux measurements of CA II H and K emission. *Publications of the Astronomical Society of the Pacific*, 90(June):267, 1978. ISSN 0004-6280. doi: 10.1086/130324.

K. Vida, L. Kriskovics, and K. Oláh. A quest for activity cycles in low mass stars. *Astronomische Nachrichten*, 334(9):972–975, 2013. doi: 10.1002/asna.201211973. URL http://arxiv.org/abs/1306.6845v1%5Cnpapers2://publication/uuid/333A783A-46B8-4ACC-B402-445C7F40E108.

A. A. Vidotto. Different types of star-planet interactions. *IAU Symposium 354, Solar and Stellar Magnetic Fields: Origins and Manifestations.*, 1(354):1–10, 2019. doi: 00.0000/X000000000000000X. URL http://arxiv.org/abs/1911.10915.

C. von Essen, G. Stefansson, M. Mallonn, T. Pursimo, A. A. Djupvik, S. Mahadevan, H. Kjeldsen, J. Freudenthal, and S. Dreizler. First light of engineered diffusers at the Nordic Optical Telescope reveal time variability of the optical eclipse depth of WASP-12b. *Astronomy & Astrophysics*, 628:A115, 2019. ISSN 0004-6361. doi: 10.1051/0004-6361/201935312.

K. J. Walsh, A. Morbidelli, S. N. Raymond, D. P. O'Brien, and A. M. Mandell. A low mass for Mars from Jupiter's early gas-driven migration. *Nature*, 475(7355):206–209, 2011. ISSN 0028-0836. doi: 10.1038/nature10201. URL http://dx.doi.org/10.1038/nature10201.

C. A. Watson and T. R. Marsh. Orbital period variations of hot Jupiters caused by the Applegate effect. *Monthly Notices of the Royal Astronomical Society*, 405:2037–2043, 2010. ISSN 00358711. doi: 10.1111/j.1365-2966.2010.16602.x.

N. N. Weinberg, M. Sun, P. Arras, and R. Essick. Tidal Dissipation in WASP-12. *The Astrophysical Journal Letters*, 849(1):L11, 2017. ISSN 20418213. doi: 10.3847/2041-8213/aa9113. URL http://arxiv.org/abs/1710.00858%0Ahttp://dx.doi.org/10.3847/2041-8213/aa9113.

L. M. Weiss, G. W. Marcy, J. F. Rowe, A. W. Howard, H. Isaacson, J. J. Fortney, N. Miller, B. O. Demory, D. A. Fischer, E. R. Adams, A. K. Dupree, S. B. Howell, R. Kolbl, J. A. Johnson, E. P. Horch, M. E. Everett, D. C. Fabrycky, and S. Seager. The mass of koi-94d and a relation for planet radius, mass, and incident flux. *Astrophysical Journal*, 768(1), 2013. ISSN 15384357. doi: 10.1088/0004-637X/768/1/14.

R. C. Willson and H. S. Hudson. The sun's luminosity over a complete solar cycle. *Nature*, 351:42–44, 1991. ISSN 0028-0836. doi: 10.1038/351042a0.

J. N. Winn. The Occurrence and Architecture of Exoplanetary Systems. *Annu. Rev. Astron. Astrophys.*, 2015. URL http://arxiv.org/pdf/1410.4199v1.pdf.

J. N. Winn, J. A. Johnson, A. W. Howard, G. W. Marcy, G. A. Bakos, J. Hartman, G. Torres, S. Albrecht, and N. Narita. The HAT-P-13 Exoplanetary System: : Evidence for Spin-Orbit Alignment and a Third Companion. *The Astrophysical Journal*, 718(1):575–582, 2010. ISSN 0004-637X. doi: 10.1088/0004-637X/718/1/575. URL http://adsabs.harvard.edu/abs/2010ApJ...718..575W.

J. T. Wright, G. W. Marcy, A. W. Howard, J. A. Johnson, T. D. Morton, and D. A. Fischer. The frequency of hot jupiters orbiting nearby solar-type stars. *Astrophysical Journal*, 753 (2):1–5, 2012. ISSN 15384357. doi: 10.1088/0004-637X/753/2/160.

J.-W. Xie. Transit Timing Variation of Near-Resonance Planetary Pairs: Confirmation of 12 Multiple-Planet Systems. *The Astrophysical Journal Supplement Series*, 208(2):22, 10 2013. ISSN 0067-0049. doi: 10.1088/0067-0049/208/2/22. URL http://stacks.iop.org/0067-0049/208/i=2/a=22?key=crossref.7c45faa5f93d6f4a1f34d8352a05241f.

J.-W. Xie. Transit Timing Variation of Near-Resonance Planetary Pairs. Ii. Confirmation of 30 Planets in 15 Multiple-Planet Systems. *The Astrophysical Journal*

Supplement Series, 210(2):25, 2 2014. ISSN 0067-0049. doi: 10.1088/0067-0049/210/2/25. URL http://stacks.iop.org/0067-0049/210/i=2/a=25?key=crossref.b63e0f52dfd795cb873a7d637b2284bb.

H. Yang, J. Liu, Q. Gao, X. Fang, J. Guo, Y. Zhang, Y. Hou, Y. Wang, and Z. Cao. The Flaring Activity of M Dwarfs in the Kepler Field. *The Astrophysical Journal*, 849(1):36, 2017. ISSN 1538-4357. doi: 10.3847/1538-4357/aa8ea2. URL http://dx.doi.org/10.3847/1538-4357/aa8ea2.

S. W. Yee, J. N. Winn, H. A. Knutson, K. C. Patra, S. Vissapragada, M. M. Zhang, M. J. Holman, A. Shporer, and J. T. Wright. The Orbit of WASP-12b is Decaying. *The Astrophysical Journal Letters*, 888(1), 2019. URL http://arxiv.org/abs/1911.09131.

Young. Photometric error analysis. VI. Confirmation of Reiger's theory of scintillation. *Astronomical Journal*, 72(747), 1967.

N. Zacharias, C. T. Finch, T. M. Girard, A. Henden, J. L. Bartlett, D. G. Monet, and M. I. Zacharias. The fourth US naval observatory ccd astrograph catalog (UCAC4). *Astronomical Journal*, 145(2), 2013. ISSN 00046256. doi: 10.1088/0004-6256/145/2/44.

R. T. Zellem, K. A. Pearson, E. Blaser, M. Fowler, D. R. Ciardi, A. Biferno, B. Massey, F. Marchis, R. Baer, C. Ball, M. Chasin, M. Conley, S. Dixon, E. Fletcher, S. Hernandez, S. Nair, Q. Perian, F. Sienkiewicz, K. Tock, V. Vijayakumar, M. R. Swain, G. M. Roudier, G. Bryden, D. M. Conti, D. H. Hill, C. W. Hergenrother, M. Dussault, S. R. Kane, M. Fitzgerald, P. Boyce, L. Peticolas, W. Gee, L. Cominsky, R. Zimmerman-Brachman, D. Smith, M. J. Creech-Eakman, J. Engelke, A. Iturralde, D. Dragomir, N. Jovanovic, B. Lawton, E. Arbouch, M. Kuchner, and A. Malvache. Utilizing Small Telescopes Operated by Citizen Scientists for Transiting Exoplanet Follow-up. *Publications of the Astronomical Society of the Pacific*, 132(1011):054401, 2020. ISSN 0004-6280. doi: 10.1088/1538-3873/ab7ee7. URL http://dx.doi.org/10.1088/1538-3873/ab7ee7.